STABILITY OF NONLINEAR OSCILLATORY SYSTEMS WITH APPLICATION TO SHIP DYNAMICS

by

Néstor E. Sánchez

Dissertation submitted to the Faculty of the
Virginia Polytechnic Institute and State University
in partial fulfillment of the requirements for the degree of
Doctor Of Philosophy
in
Engineering Mechanics

APPROVED:

Ali H. Nayfeh, Chairman

Dean T. Mook

Mahendra P. Singh

Saad A. Ragab

William T. Baumann

July, 1989

Blacksburg, Virginia

STABILITY OF NONLINEAR OSCILLATORY SYSTEMS WITH APPLICATION TO SHIP DYNAMICS

by

Néstor E. Sánchez

Ali H. Nayfeh, Chairman

Engineering Mechanics

(ABSTRACT)

A procedure to generate an approximate bifurcation diagram for a single-degree-of-freedom system in a selected parameter space is developed. The procedure is based on the application of Floquet analysis to determine the stability of second-order perturbation approximations of the solutions of the system in the neighborhoods of specific resonances. As a control parameter is varied, a combination of elementary concepts of bifurcation theory and the proposed method are used to detect the first bifurcation from the periodic solutions and hence infer the qualitative changes that the system experiences. Codimension-one bifurcations are investigated in a two-dimensional parameter space composed of the amplitude and frequency of the excitation. The behavior of a softening Duffing oscillator is analyzed under external and parametric excitation. The dynamics of a ship rolling in waves is also considered and three types of excitations are treated: external, parametric, and a combination of both.

Analog- and digital-computer simulations are used to verify the accuracy of the analytical predictions. It is found that the predictions based on the first bifurcation of the analytical solution give a good estimate of the actual behavior of the system. The stability regions of the solutions near each of the resonances display a self-similar structure in the parameter space. The physical implications of these bifurcation patterns are important for the prediction of the capsizing of ships. The dangerous regions of the parameter space where capsizing might occur are identified for a given system.

Capsizing is found to occur via two distinct scenarios: one evolving from a large oscillation through a disappearance of a chaotic attractor (crises) and a second, potentially more dangerous, developing from a small oscillation through a sudden tangent instability. These scenarios agree with previous experimental studies.

Acknowledgements

I wish to express my appreciation and gratitude to Professor Ali H. Nayfeh for the teaching, guidance, support, and advice that he provided as my advisor through the years that this work was in progress. I like to thank the committee members : Professor Dean Mook, Professor Saad Ragab, Professor Mahendra Singh, and Professor William Baumann for their comments and valuable advice. I am also grateful to Professors Scott Hendricks and John Burns who were not in the final committee due to scheduling problems, but provided me with teaching and advice. In addition, I appreciate the friendship and assistance from fellow graduate students : , , , , , and . Thanks are also due to whose patience and expert typing skills were always of great help.

I appreciate the financial assistance that the department of Mechanical Engineering gave me in the form of teaching-assistant appointments for two academic years. This work was supported by the Office of Naval Research under Grant No. N00014-83-k-0184, NR 4322753 and the National Science Foundation under Grant No. MSM-8521748.

The difficulties, pressures, and anxiety were sorted out with the help of my friend who has the ability to make everything enjoyable and keep the priorities in life straight. The support, encouragement, and understanding from my family was always motivation to continue. I dedicate this work to my mother and the memory of my father who passed away only one month after I began the program.

Table of Contents

Chapter 1

INTRODUCTION

1.1. General description and motivation of this work

The current work deals with the stability of deterministic dissipative dynamical systems that display oscillatory behavior. We are interested in characterizing the long-term behavior of a system in terms of the number and type of existing solutions and the qualitative changes that these solutions undergo as a control parameter is slowly varied. Our aim is to present analytical tools that can be used to approximately predict the stability regions of specific solutions in a selected parameter space. The systems that we treat are all modeled by second-order nonlinear ordinary differential equations, which are typical of rigid-body oscillations in single-degree-of-freedom systems. However, the techniques that we use to analyze and predict the behavior are not restricted to this particular class of systems; they are rather general and should equally apply to higher-order systems.

The continuously growing interest in nonlinear systems can be explained by the confluence of a number of factors: there is a wealth of evidence on the importance of nonlinear phenomena in all branches of engineering and science [1], there is a strong mathematical background [2] that is bringing a good deal of order and understanding into dynamical systems, there is an emerging new paradigm that relates determinism and ergodicity through what is called deterministic chaos, and finally there are available powerful computer codes to manipulate symbols and perform numerical simulations. We have attempted to benefit as much as possible from all of these factors, and the material presented here will reveal this effort.

The nonlinear nature of the differential equations governing the states of the systems under consideration makes closed-form solutions in general unavailable. Therefore, we have to resort to the following approaches :

- Approximate analytical solutions
- Direct numerical integration
- Qualitative or topological analysis

One or more of these approaches can be use to analyze a particular system. In this work, we rely primarily on the first and second approaches, although in the process of analysis we also use some qualitative tools, such as phase-space representations and Poincaré maps.

Perturbation techniques have been at the heart of nonlinear analyses from the time of Poincaré [3]. It has been shown (e.g., [4-6]) that approximate analytical solutions can accurately model the behavior of weakly nonlinear systems in the neighborhoods of the resonances of the system. Nayfeh and Mook [6], among many others, have successfully applied perturbation techniques to a large number of discrete and continuous dynamical systems. The method of multiple time scales [4] as well as the method of averaging [7] have been found to be useful techniques to determine approximate uniform solutions. Therefore, the derivation of approximate solutions for weakly nonlinear systems near a specific resonance is in many cases a standard procedure.

Periodically forced systems by either an external or a parametric load are very commonly found in engineering applications. The dynamics of these systems is often complicated, even when the system itself is very simple. These complicated behaviors include phenomena such as period-multiplying bifurcations, coexistence of solutions, a sudden jump from one solution to another, and chaotic solutions. A large number of studies has analyzed the forced Duffing oscillator and simple pendulums, which are among the simplest nonlinear systems, but at the same time model many physical systems of significance in various diciplines.

Huberman and Crutchfield [8] found period-doubling sequences and chaotic behaviors in a Duffing-type oscillator of the form

$$\ddot{\theta} + \mu\dot{\theta} + \theta - 4\,\theta^3 = \Gamma\cos(\Omega t)$$

The analog-computer simulation showed that by varying the frequency of the excitation, the system could be driven into a region where the response displayed a period-doubling sequence and then a broad-band frequency spectrum, characteristic of a chaotic behavior. This confirmed the predictions of Morozov [9,10] who had analyized the complex structure of the solutions near a homoclinic bifurcation. Huberman, Crutchfield, and Packard [11] studied the behavior of the equation

$$\ddot{\theta} + \mu\dot{\theta} + \omega_0^2\sin\theta = \Gamma\cos(\Omega t)$$

in the context of plasma oscillations in the presence of microwave radiation. Using a hybrid digital-analog computer, they generated a bifurcation diagram by varying the amplitude and frequency of the excitation and locating the regions of the parameter space $\Gamma - \Omega$ where periodic and chaotic responses can be found. The resulting diagram showed a Y shaped region where clear boundaries for the chaotic responses could be identified. Parlitz and Lauterborn [12] used digital-computer simulations to construct the bifurcation diagram of a forced Duffing oscillator with a hardening nonlinearity taking the amplitude and frequency of excitation as control parameters. The resulting diagram showed what they conjectured to be a superstructure that might be universal for a large class of oscillatory systems. Using analog-computer simulations, Zavodney, Nayfeh, and Sanchez [13] found a similar bifurcation structure for the equation

$$\ddot{u} + 2\varepsilon\mu\dot{u} + [\omega_0^2 + \varepsilon\delta u + \varepsilon^2\alpha u^2 + \varepsilon g \cos\Omega t]u = 0$$

which is a parametrically excited oscillator. The bifurcation diagram (some times called state diagram) in the parameter space $g - \Omega$ showed that over twenty qualitatively different solutions could be found. These solutions were stable in a tongue-like region that usually had period-doubling instabilities, leading to a chaotic response on one side and tangent instabilities on the other. In regions of the parameter space where two or more tongues overlap, there would be multistability of solutions and the initial conditions would take the system to a particular solution, depending on the domain of attraction of that solution. A key feature of the behavior observed was that complicated responses such as period-multiplications and chaotic solutions were confined to a small region of the parameter space.

Approximate solutions are effective in modeling periodic behavior that can be represented as a summation of a few terms, usually harmonic, that progresively improve the approximation. As the frequency content of a solution increases, the likelihood of obtaining a good approximate solution decreases due to the large number of terms in the expansion that is needed. This fact makes the approximation of complicated behavior very difficult. However, due to the observation that complicated behaviors are confined to a narrow region of the parameter space, we were motivated to generate an approximation of the bifurcation diagram by analyzing the stability of perturbation solutions in the neighborhoods of the resonances of the system.

Expanding the work of Nayfeh and Khdeir [14,15], we use Floquet theory and elementary concepts of bifurcation theory to determine the regions of the parameter space where the approximate analytical solutions are stable and the type of instabilities that take place when they become unstable. A second-order approximate analytical solution near each resonance is obtained by the method of multiple scales [5]. The complicated algebra involved in this process was performed by a symbolic manipulator. The asymptotic stability of the solution is determined by perturbing it and studying the evolution of this perturbation, which is governed by a linear differential equation with periodic coefficients. A computer code was written to solve the algebraic system of equations generated from the multiple-scales analysis and to perform a numerical integration for determining the stability of the solution at every point in the parameter space. The parameters selected were the frequency and amplitude of the excitation, which are common control parameters in physical applications.

We begin by presenting in Chapter 2 a general approach for treating problems that show time evolution, which is the dynamical system's point of view. Basic concepts and definitions are also given, which are used in the following chapters. In Chapter 3, we concentrate on the analysis of a softening Duffing oscillator with an external excitation. In Chapter 4, we consider a similar Duffing oscillator with a parametric excitation. It is shown that these simple systems display a complex but organized structure of solutions.

1.2. Analysis of ship motions

Although the dynamic behavior that we study is common to many physical systems governed by analogous equations, we have a specific problem that motivates this work, which is the prediction of the dynamics and capsizing of ships rolling in seas. The latter phenomenon, which is of fundamental importance for safety and design considerations, is still not well understood primarily because of its inherent nonlinear nature. There have been recent cases [16] where the inadequacy of the current design regulations has been documented unfortunately with loss of lives and equipment. In other situations [17], casualties have occurred in not very unusual sea conditions. These facts point to a basic lack of understanding of the specific mechanisms that cause a vessel to capsize. Considerable effort has been dedicated to the formulation of mathematical models that capture the main features of the dynamics [18]. These models have to a good extent been successful (e.g., [19]) in representing some characteristics of the real phenomena. However, the difficulty remains in relating geometrical characteristics to the dynamic performance for design evaluation.

The initial developments of the theory of ship motions are due to Leonhard Euler, who in 1737 first postulated the theory of motions in still water. Euler derived the equations of motion of a ship by neglecting the hydrodynamic terms and reducing the mathematical model to the equations of a pendulum. Daniel Bernoulli also made contributions by studying the forced oscillations resulting from the motion of a vessel in waves. The first complete theory was formulated by the English scientist-ship designer W. Froude [20] and published in 1861. In this analysis Froude treated the case of rolling in beam seas, assuming the dimensions of the ship to be small compared to the wavelength. The wave was considered to be sinusoidal and the direction of the buoyancy force was assumed to be not vertical, but normal to the wave. A. N. Krilov [21] was the first to apply the variational methods developed by Lagrange to ship motion.

In spite of the fact that shipbuilding is an ancient art, only recently have analytical methods been used to scientifically improve the techniques. Particularly, the developments in the basic understanding of capsizing are quite new. The effect of nonlinear coupling between the modes has been postulated only in the past forty years. The work of Grim [22], Kerwin [23], Pauling and Rosenberg [24], and Nayfeh, Mook, and Marshal [25] have shown the vital role of the nonlinear terms in the stability of the motion.

In Chapter 5, we present some basic concepts in the theory of ship motions. We derive the general equations of motion for the six-degree-of-freedom system and give the assumptions used to reduce this system to the one-degree-of-freedom model that we finally analyzed. In Chapter 6, we study the rolling motion of a ship in beam seas; that is, when the waves approach the ship from the side, including the case of a ship having a bias angle. In Chapter 7, we consider the case of rolling of ships in longitudinal waves; that is, when the waves are directed in a direction normal to the longitudinal axis of the ship. In this case the governing equation has a parametric excitation; that is, a time-varying coefficient. In Chapter 8, we consider a general case having both parametric and external excitations. This situation arises for a ship moving in a quartering seas; that is, when the waves move at an angle to the longitudinal axis of the ship, or when a biased ship rolls in longitudinal waves, or when variations of pressure within the waves are taken into account in the rolling in beam seas.

Chapter 2

DYNAMICAL SYSTEMS

In this chapter we present a short review of basic concepts from the theory of dynamical systems to bring new insight into the problems of stability of systems. At the same time, it provides a solid ground for the analysis of the behaviors that we encounter in this work and a test of their universality for larger classes of systems that share the dominant features of the governing equations.

2.1 Description of time evolution

The theory of dynamical systems deals with systems that experience time evolution. The description of the evolution of the states of a system from a known previous history is given by a set of equations. The theory applies to cases in which, independently of the physical characteristics of the system, the time evolution can be described mathematically in the form of equations. This classification covers all time varying phenomena for which states can be identified and governing equations, or some sort of descriptive tools, can be applied to model their change. Therefore, the field of applications of dynamical systems is immense and the unification of the treatment for phenomena originating from diverse fields, such as mechanics, chemistry, biology, and economics not only provides common tools of analysis but reveals the presence of universal features shared by these systems.

The earliest problems on dynamic evolution are those dealing with the motion of the planets in the solar system, which date back to Newton (1642-1727). However, it was Poincaré (1854-1912) [3] who laid the foundation for the qualitative analysis of dynamical systems. His early ideas, which included the study of the topological structure of the orbits in the phase space, were later expanded by Liapunov (1857-1918) [26], Birkhoff [27], Andronov [28], Kolmogorov [29], Moser [30], Arnold [31], and Smale [32], among others. who shaped the core of the mathematical apparatus available today.

In the study of dynamical systems we must first distinguish between conservative (Hamiltonian) and dissipative systems due to the large differences in the qualitative structure of the solutions in these cases. Hamiltonian systems have the characteristic of being frictionless; that is, energy is conserved. In systems of this type the initial conditions have a profound effect on the long term behavior. On the contrary, dissipative systems possess a mechanism for dissipating energy. This fact implies that, as time increases, the solutions decay in the phase space to a space having a dimension lower than that of the initial conditions; this space is known as an attractor. Once the system is on the attractor the initial conditions have no direct influence on the behavior. These systems display an initial transient behavior. These characteristics are typical of most engineering applications. Therefore, we are mostly concerned with this latter type.

The time evolution of dissipative systems is usually described by a set of nonlinear equations which can be algebraic, ordinary-differential, partial-differential, difference, or integral equations. In most common applications in engineering, the governing equations can be reduced to either ordinary-differential or partial-differential equations. These equations are obtained by applying the physical laws to the state variables of the system. In the case of dynamics, these laws reduce to Newton's second law or some equivalent statement, usually in the form of an extended Hamilton's principle. If the system under consideration has state variables with continuous spatial dependence, the resulting equations are partial-differential equations, such as those describing the vibration of an elastic beam. On the other hand, if the state variables are discrete or lumped, the governing equations are ordinary-differential equations, such as those describing rigid-body dynamics. In many instances the infinite-dimensional phase space of a continuous system is contracted due to dissipation to a finite-dimensional phase space. This fact allows us to solve these problems by using the Galerkin procedure or a similar technique to transform the problem from continuous to discrete. Therefore, we are mostly interested in discrete systems.

In the following subsections we describe general characteristics of dissipative dynamical systems. Some of the definitions and terminology are used throughout this work. Some others are included just for the sake of completeness, although the description is very brief. We hope that the basic concepts are discussed in enough detail to make the material of the later chapters self-contained. Most of the concepts presented in this chapter have been discussed in books and articles published in the past ten years. Specific references have been given in a few sections, but most of the ideas in one way or another can be traced to books and articles by Eckmann [33], Bergé, Pomeau, and Vidal [34], Kubicek and Marek [35], Nayfeh and Mook [6], Guckenheimer and Holmes [36], Thompson and Stewart [37], Jordan and Smith [38], Arnold [39], Seydel [40], Lichtenberg and Lieberman [41], Iooss and Joseph [42], and Schuster [43].

2.2 *Dissipative systems and their attractors*

In a typical situation the evolution of a system is described by a system of first order ordinary-differential equations of the form

$$\frac{d}{dt}X(t) = F(X,\gamma) \qquad X\in\mathbb{R}^n \quad \gamma\in\mathbb{R}^k \tag{2.1}$$

where X(t) is a vector that represents the state of the system at time t and γ is a vector of control parameters whose effect on the dynamics is being sought. If the n observable scalars contained in X(t) completely characterize a system at each time t and (2.1) determines its evolution, then the geometry of the phase space contains important information about the dynamics of the system that we can interpret. The right-hand side of (2.1) defines a vector field in the phase space, which is tangent at every point to the solution X(t); it is often referred to as the flow of the differential equation. Considering the analogy of a flow, we can apply the Eulerian description of a velocity field, in which the rate of change of a property Υ, is given by the transport theorem

$$\frac{D}{Dt}\int_V \Upsilon dV = \int_V \left(\frac{\partial\Upsilon}{\partial t} + \Upsilon\nabla\bullet v\right)dV \tag{2.2}$$

where V denotes the volume of a region in the phase space and v is the velocity field. For the flow in phase space, we can consider $\Upsilon = 1$ everywhere and $v = F(X,\gamma)$, which renders (2.2) as

$$\frac{d}{dt}V(t) = \int_V (\nabla.F)dV \tag{2.3}$$

Therefore, the change in the volume of the phase space is described by the divergence of the velocity field. This important conclusion is stated in Liouville's theorem (see Arnold [39]) for the case of a Hamiltonian system which reads, "The phase flow of Hamilton's equations preserves the phase volume." In the case of dissipative systems we have

$$\nabla.F = \sum_{i=1}^{n} \frac{\partial F_i}{\partial X_i}(X) < 0 \tag{2.4}$$

which implies that the local phase volume decreases. This reduction of volume as time goes to infinity shrinks any initial volume to zero. This is the essential idea of the attractor : any set of initial conditions has to evolve until it reaches a set of zero volume. Figure 2.1 illustrates this concept for a particular case of a periodic attractor.

Considering the flow as a transformation T^t that acts on a set of initial conditions Y in the form $T^tY = X(Y, t)$ to generate the trajectory in the phase space, Eckmann [33] defines the properties of an attractor $\tilde{X}$ as :

1. $\tilde{X}$ is an invariant set under the transformation T^t: $T^t\tilde{X} = \tilde{X}$.

2. $\tilde{X}$ has a shrinking neighborhood in the sense that there is an open neighborhood U of $\tilde{X}$, $U \supset \tilde{X}$ such that $T^tU \subset U$ for $t > 0$ and $\tilde{X} = \bigcap_{t>0}^{\infty} T^tU$.

3. The flow T^t on $\tilde{X}$ is recurrent and indecomposable

where the operator $\bigcap$ represents the intersection of the sets generated after applying the function T^t an infinite number of times. Recurrent means that the flow is never transient on $\tilde{X}$, and indecomposable means that $\tilde{X}$ cannot be split into two nontrivial closed invariant pieces.

Associated with each attractor there is a basin of attraction, which can be defined as the set of initial points X such that T^tX approaches $\tilde{X}$ as t goes to infinity; or in other words, it is the set of initial conditions that leads to the attractor. This is a set of nonzero volume that contains the attractor. A nonlinear system can have many attractors (even a countable infinity) each with its own basin of attraction. The basins of attraction are mutually exclusive, but they can be interlaced, leading to sensitive dependence on the initial conditions.

Usually the analysis of the long-term behavior of the dynamical system can be reduced to the study of the behavior of its attractors. In general terms four different types of attractors can be identified : a point attractor, a limit cycle, a torus or quasiperiodic attractor, and a chaotic attractor. A description of each type is given in the next subsections.

2.2.1. Point attractor

This type of solution is often associated with equilibrium or fixed points of the system; that is, for some specific value of γ (2.1) becomes

$$F(X, \gamma) = 0 \tag{2.5}$$

This expression represents a system of algebraic equations, which can have many solutions. Although a solution X_0 of (2.5) is an invariant set, it is not necessarily an attractor unless it possesses a shrinking neighborhood. This issue can be settled by considering an infinitesimal perturbation of the equilibrium point in the form

$$\hat{X} = X_0 + \xi(t) \qquad\qquad \xi \in \mathbb{R}^n \tag{2.6}$$

Then, X_0 is an attractor provided that ξ(t) goes to zero as $t \to \infty$. Substituting (2.6) into (2.1), we obtain

$$\dot{\xi} = F(X_0 + \xi, \gamma) - F(X_0, \gamma) \tag{2.7}$$

Expanding $F(X_0 + \xi, \gamma)$ in a Taylor series around X_0 and keeping only linear terms, we obtain

$$\dot{\xi} = [\frac{\partial F_i(X_{0,}\gamma)}{\partial X_j}]\xi + \cdots \tag{2.8}$$

Terms of higher order can be neglected based on the assumption that ξ(t) is small. The matrix of the derivatives of F in (2.8) is known as the Jacobian matrix J. Thus, ξ(t) is governed by a system of linear differential equations having constant coefficients; they have solutions of the form $\xi(t) = r\exp(\lambda t)$, where λ and r are constant provided that [38]

$$\det(J - \lambda I) = 0 \tag{2.9}$$

Therefore, ξ(t) will decay as $t \to \infty$ and hence X_0 is an attractor if and only if the real parts of all eigenvalues of J are negative; that is, if and only if

$$Re(\lambda_i) < 0 \qquad for \quad i = 1, 2, \dots, n \tag{2.10}$$

In a two-dimensional phase space the point attractor is often called a focus when the eigenvalues are complex and a node when the eigenvalues are real. If the condition (2.10) is not satisfied, the two-dimensional fixed point is not an attractor. It is called saddle if one eigenvalue has a positive real part and the other a negative real part and a center when both eigenvalues are purely imaginary. The latter case, in which the perturbation has oscillatory behavior without decay, displays a structure sensitive to small perturbations. This structure is so atypical that in a general way fixed points are classified as hyperbolic or non-hyperbolic, depending on the absence or presence of complex eigenvalues with zero real parts. In the same way, a flow near an equilibrium point is called hyperbolic when all eigenvalues of the Jacobian have nonzero real parts, which makes it decomposable into a contracting flow and an expanding flow.

2.2.2. Limit cycle

This type of attractor represents a periodic motion. It is of fundamental importance because of the significance of oscillatory behavior in all physical systems, including biological cycles and vibrations in bodies and structures. In this case the basic characteristic is that the system returns to a state after a period of time T; that is

$$X(t+T) = X(t) \tag{2.11}$$

In the phase space this behavior corresponds to closed trajectories or orbits.

To determine whether or not a particular periodic solution is an attractor, we again disturb the solution with an arbitrary infinitesimal perturbation $\xi(t)$ in the form $\hat{X}(t) = X(t) + \xi(t)$. After substituting $\hat{X}(t)$ into the governing equation (2.1), we obtain

$$\dot{\xi}(t) = F[(X(t) + \xi, \gamma)] - F[(X(t), \gamma)] \tag{2.12}$$

Expanding $F(X(t) + \xi(t), \gamma)$ in a Taylor series for small ξ and linearizing, we obtain an equation of the form [42]

$$\dot{\xi}(t) = P(t)\xi \tag{2.13}$$

where $P(t) = \frac{\partial F_i[X(t), \gamma]}{\partial X_j}$. The solutions of (2.13) determine the stability of X(t). This is a linear ordinary-differential equation with periodic coefficients. According to Floquet's theorem [6], (2.13) possesses solutions of the form

$$\xi(t + T) = \lambda\xi(t) \tag{2.14}$$

where λ is called the Floquet multiplier. Thus, after m periods $\xi(t + mT) = \lambda^m\xi(t)$. Therefore, if $|\lambda| < 1$, $\xi(t + mT) \rightarrow 0$ *as* $m \rightarrow \infty$ and hence X(t) is an attracting limit cycle. The Floquet multipliers λ are the eigenvalues of the so called monodromy matrix C, which is related to a fundamental solution matrix Φ(t) as

$$\Phi(t + T) = \Phi(t)C \tag{2.15}$$

In addition, it can be easily shown [38] that for a system, such as (2.13) where $P(t)$ has the principal period T, the eigenvalues of the monodromy matrix are related by

$$\lambda_1\lambda_2 \ldots \lambda_n = \exp\left(\int_0^T \mathrm{tr}[\,P(\tau)\,]d\tau\right) \tag{2.16}$$

There are some particular limit sets called homoclinic and heteroclinic orbits, which are not attractors, but play important roles in characterizing the dynamic behavior. These trajectories connect saddles. Heteroclinic orbits connect distinct saddles. Homoclinic orbits connect saddles to themselves. Both types of orbits have infinite periods and it is common to find complicated behavior in their neighborhoods. They are also known as separatrices because usually they represent boundaries separating distinct types of solutions in the phase space.

2.2.3. Torus or quasiperiodic attractor

A third type of attractor is the so-called torus T^r, which represents a periodic motion modulated by one or more basic frequency. The attractor lies on the surface of a torus of dimension r, where r is the number of incommensurate frequencies present in the response. Newhouse, Ruelle, and Takens [44] have conjectured that quasi-periodicity of degree greater than two may be difficult to observe in nature because under fairly general conditions a torus T^3 can lose stability to be replaced by a strange attractor. This scenario has been proposed by Ruelle and Takens [45] as a possible mechanism for turbulence.

2.2.4. Strange attractors

An important remark regarding the contraction of volumes in the phase space is that although T^t contracts volume it does not need to contract lengths in all dimensions. Snapshots of T^t at times t = 0,1,2, may give the sequences shown in Figure 2.2 . In (a) there is contraction in all directions, in (b) one dimension remains constant, and in (c) there can even be stretching and folding provided that the other dimensions are contracted enough to make the final volume smaller than the initial one. This latter case shows that even if trajectories converge to a single attractor, one might find that points that are arbitrarily close initially may get macroscopically separated on the attractor after sufficient time. An attractor displaying this property is called strange.

The following important features characterize chaotic attractors and can be used to identify this type of solution. The power spectrum of one of the variables of the dynamical system contains a continuous part, reflecting the presence of an infinite number of frequencies necessary to approximate the erratic behavior. In the same way the autocorrelation function tends to zero as time increases, expressing the fact that knowledge of the variable at time t does not give any information about it in the future at time $t + \tau$. Another property related to the stretching of the attractor is the exponential divergence of neighboring trajectories, which makes the chaotic solution critically sensitive to initial conditions.

2.3. *Invariant subspaces*

The stability of a fixed point X_0 of the system defined by (2.1) was determined by considering the behavior of small perturbations near it. This procedure is equivalent to linearizing the flow in the neighborhood of the fixed point and studying the behavior of the approximate system (2.8) (see [36]). This linearized system contains the local behavior of the flow T^t near the fixed point. The solutions of this system can be expressed in the form

$$\xi(Y_0, t) = e^{tJ} Y_0 \tag{2.17}$$

where Y_0 is the set of initial conditions and J is the Jacobian matrix. Therefore, e^{tJ} is the linearized flow that we can call L^t. Alternatively, the general solution of (2.8) can be expressed as the linear superposition of n linearly independent solutions $\{\xi^1(t), \dots, \xi^n(t)\}$ in the form

$$\xi(t) = \sum_{i=1}^{n} a_i \xi^i(t) \tag{2.18}$$

where the constants a_i are determined from the specific initial conditions. If J has n linearly independent eigenvectors u^i, $i = 1, \dots, n$, then a basis for the space of solutions is

$$\xi^i(t) = e^{\lambda_i t} u^i \tag{2.19}$$

where λ_i is the eigenvalue associated with u^i. A set of n independent solutions forms what is called the fundamental solution matrix

$$\Phi(t) = [\xi^1(t), \dots, \xi^n(t)] \tag{2.20}$$

Some of the solutions in the flow L^t have the characteristic of being invariant under the transformation e^{tJ}, in particular, if u^i is a real eigenvector of J, then a solution beginning at $a_i u^i$ remains in this subspace for all times. It is useful to divide the space spanned by the eigenvectors into three groups and thereby to generate separate manifolds; that is, subspaces with some smoothness properties that insure that the implicit function theorem applies. The result is

Stable manifold, $E^s = \text{span}\{v^1, \dots, v^{n_s}\}$

Unstable manifold, $E^u = \text{span}\{u^1, \dots, u^{n_u}\}$

Center manifold, $E^c = \text{span}\{w^1, \dots, w^{n_c}\}$

where $\{v^i\},\{u^i\}$, and $\{w^i\}$ are the eigenvectors corresponding to the eigenvalues that have negative real parts, positive real parts, and zero real parts, respectively.

In the neighborhood of a saddle the invariant manifolds give essential information about the structure of the phase space. The stable manifold, or inset, approaches the saddle as $t \rightarrow +\infty$ while the unstable manifold, or outset, approaches the saddle as $t \rightarrow -\infty$. The determination of these invariant sets is important because the other trajectories near the saddle can be inferred once the asymptotic trajectories are known.

Carr [46] proved that for fixed points having local stable and unstable manifolds the local properties of the linearized system (2.8) carry over to the nonlinear system (2.1), and the local stable and unstable manifolds of (2.8) are tangent to those of (2.1) at X_0.

2.4. Bifurcations of attractors

We have so far considered the attractors for a system of the form (2.1) for some given values of the parameters γ. However, this approach does not have great interest because the specific values used in the differential equations might have some discrepancies with those that best model the behavior of the physical system at some point in time. Perhaps, these coefficients may change with time due to the action of some environmental conditions or even as a reaction to a deliberate attempt to control the dynamics of the system. For these reasons, the best understanding of the behavior of the system can be obtained when the key coefficients of the differential equation are used as parameters and the qualitative effects of slow changes in these parameters are understood.

In general, the attractors change smoothly for small variations of a parameter, and the changes show mostly scaled versions of the same thing; that is, quantitative changes. A point attractor might move slightly as one parameter is changed, or a limit cycle might grow as another parameter is changed. Sometimes, however, the qualitative nature of the attractor might change as the parameter crosses a critical point. This point is a bifurcation point. The bifurcation points are of fundamental importance because changes in the behavior might bring catastrophic consequences in the physical system. For the case of a beam subjected to an axial static load, there exists a critical load, infinitesimal changes of which might cause the beam to buckle suddenly. Moreover, as we show later, there exists conditions under which infinitesimal changes in the frequency or height of a wave might cause the ship to capsize. Therefore, characterization of the bifurcations for some particular control parameters of interest defines stability limits for each particular type of behavior displayed by the system.

In this work we mostly deal with what is known as local bifurcations, which originate from small perturbations of attractors in the neighborhood of the instability point. The qualitative changes occurring in the attractors affect a small region of the phase space. However, small changes in the parameters might also have associated changes that affect the configuration of the phase space in a global way, such as transformations of the invariant manifolds involving the creation or destruction of homoclinic orbits. These critical points are called global bifurcations.

The dimension of the parameter space in (2.1) is k; however, a particular bifurcation may need variations in a different number of parameters to be observed. This fact is reflected in the definition of codimension, which is defined [34] as the smallest dimension of the parameter space in which a particular bifurcation can occur. Therefore, the number of parameters used in (2.1) might not necessarily be the codimension of the bifurcation taking place. In this work we have only considered bifurcations of codimension one; that is, any of the changes considered can be observed by changing a single control parameter.

2.4.1. Bifurcations of a point attractor

In this case we are concerned with qualitative changes on the attractor as the parameter γ in (2.1) is varied, where $\gamma \in \mathbb{R}^1$. The attractor loses stability when part of the spectrum of the Jacobian matrix moves into the right half-plane. This can happen by when a real eigenvalue becomes positive or when the real part of a complex pair of eigenvalues becomes positive.

Saddle-node

In general the crossing of a real eigenvalue into the right half-plane originates a saddle-node or fold bifurcation unless some particular characteristics of the system are present in which case it could cause a transcritical or a pitchfork bifurcation [36]. The saddle-node, as indicated by the name, represents the collision of a stable node and an unstable fixed point (saddle) causing the disappearance of the attractor. Therefore, after a saddle-node bifurcation takes place a jump to another attractor is observed.

For a system in which the trivial solution is a fixed point for all values of the parameter, when the real eigenvalue becomes positive the trivial attractor loses stability and a nontrivial fixed point becomes an attractor. There is an exchange of stability between the trivial and nontrivial fixed points at the bifurcation point. This bifurcation is called transcritical.

Some systems exhibit symmetries under particular transformations which prevent the occurrence of either the saddle-node or the transcritical bifurcations to occur. In this case the bifurcation takes the form of a pitchfork. At the bifurcation point a new pair of equilibria (two solutions appear), related by the specific symmetry, appear. The pitchfork is called subcritical or supercritical if the branches are stable after or before the bifurcation point, respectively.

Hopf bifurcation

The bifurcations of a point attractor generated by a real eigenvalue crossing into the right half-plane of the complex plane are called static or stationary, because the system goes from one type of equilibrium to another. On the other hand, bifurcations generated by a pair of complex eigenvalues crossing the imaginary axis transversely into the right-half of the complex plane are characterized by generating motion from equilibria. At the bifurcation (Hopf bifurcation) point the Jacobian matrix has a pair of purely imaginary eigenvalues. A theorem, which Hopf postulated in 1942 [46], summarizes the conditions as

1. $F(X_h, \gamma_h) = 0 \qquad X \in \mathbb{R}^n \qquad \gamma \in \mathbb{R}^1$

2. The Jacobian has a simple pair of purely imaginary eigenvalues $\lambda(\gamma_h) = \pm i\beta$ and no other eigenvalue with a zero real part.

3. $\frac{d}{d\gamma}[Re(\lambda)] \neq 0$.

Then there is a birth of limit cycles at (X_h, γ_h). The initial period of oscillation is $T_h = \frac{2\pi}{\beta}$.

We did not observe Hopf bifurcations in this work because it is impossible for a dissipative one-degree-of-freedom (J is rank 2) system to have a pair of purely imaginary eigenvalues, because the trace of the Jacobian is the divergence of $F(X, \gamma)$ which must remain less than zero to satisfy (2.4).

2.4.2. Bifurcations of limit cycles

We previously used Floquet theory to determine the stability of a periodic solution of (2.1) under small perturbations for a given value of the parameter γ. To study bifurcations in these periodic solutions, we let γ slowly change and determine the location where qualitative changes take place. The Floquet multipliers must remain inside the unit circle for the orbit to be an attractor. Therefore, a bifurcation occurs when a Floquet multiplier λ leaves the unit circle. There are three possible situations:

1. A real eigenvalue leaves the unit circle through $+1$.

2. A real eigenvalue leaves the unit circle through -1.

3. A pair of complex eigenvalues leave the unit circle.

In the first case, at the bifurcation point, in general, there is a collision of a stable and an unstable orbit, and as in the case of fixed points, the result is the disappearance of the attractor and a jump to another stable solution. This bifurcation is called a saddle-node or a cyclic fold bifurcation. We show in a later chapter that under some particular conditions the interpretation of the bifurcations resulting from a Floquet multiplier going through +1 might not lead to a jump.

The second case does not have a similarity to the bifurcation of a fixed point. When λ leaves the unit circle through -1, it follows from (2.14) that $\xi(t+2T)=\xi(t)$. A solution with period 2T is generated. This bifurcation is called period-doubling or flip (because the Poincaré map flips between two points). Again, there exist conditions under which this interpretation does not hold.

The third case is known as the Hopf, secondary Hopf, or Neimark bifurcation. This case is somewhat similar to the one for fixed points, where a limit cycle is born. At this bifurcation a new basic frequency of oscillation is born, causing the limit cycle to break into a torus. Following the bifurcation the attractor is contained on the surface of a torus. This bifurcation leads either to phase locking when the two frequencies involved are commensurable or to quasi-periodicity when they are irrational [34].

Chapter 3

BIFURCATIONS IN A FORCED SOFTENING DUFFING OSCILLATOR

3.1. Introduction

A large number of studies has been dedicated to the Duffing oscillator with softening nonlinearity [e.g., 8,10,47-49]. The interest in this system lies in the variety of physical phenomena that it models, such as the rolling motion of a ship [14,50], and the fact that it is isomorphic to other systems of importance in physics and engineering (e.g., Josephson junction oscillators [51] and Foucault's pendulum). Particularly interesting is the response of the Duffing oscillator to a harmonic excitation in the presence of viscous damping, which has been found [8,47] to exhibit, among other features, hysteretic and chaotic behaviors. Thus, we consider a nondimensional differential equation of the form

$$\begin{aligned} &\ddot{x} + 2\mu\dot{x} + x - \alpha x^3 = f\cos\Omega t \\ &\mu, \alpha > 0 \quad f \in F \quad \Omega \in W \quad F, W \subseteq \mathbb{R}^1 \end{aligned} \tag{3.1}$$

where F and W represent appropriate domains for the analysis of the dependence of the solution on the parameters f and Ω, which can be alternatively changed. Our aim is to identify the regions of the parameter space $\mathbb{P} = FxW$ where qualitative changes in the solution occur (i.e., bifurcations) using approximate analytical techniques and simple numerics. Additionally, to assess the merits of the bifurcation analysis in predicting the behavior of a physical system, we carried out detailed analog-computer simulations on a system governed by (3.1).

Figure 3.1 shows the potential and the phase diagram of the Hamiltonian system associated with (3.1) when $\alpha = 1$. It is evident that in the absence of the excitation all initial conditions inside the heteroclinic orbit (orbit consisting of the separatrices connecting the saddle points) yield bounded solutions and all initial conditions outside the heteroclinic orbit yield unbounded solutions. It is also possible for a stable bounded solution of a system modeled by (3.1) in the presence of the excitation to become unbounded. We are especially interested in this event due to the catastrophic implications that it has for a physical system, such as, the capsizing of a vessel. Previous studies focused attention on the regions of the parameter space $\mathbb{P}$, where bounded solutions exist. Huberman and Crutchfield [8] observed the existence of a period-doubling sequence to chaos in a region where the coexistence of two solutions generated a hysteretic effect. Räty et al. [47] observed the symmetry-breaking precursor to period-doubling bifurcations and confirmed the consistency of the behavior with the universal features of noninvertible one-dimensional maps. Rasband [45] calculated an approximate bifurcation diagram by numerically calculating the stability of perturbations in a Hamiltonian system whose first term involved Jacobi elliptic functions. The resulting bifurcation diagram showed Y-shape curves [1,53] (see Section 3.3), previously identified in other forced oscillators [11,54,55] and iterative maps [56], which Parlitz and Lauterborn [12] conjectured to be universal for a large class of nonlinear oscillators.

To determine the dependence of $x(t)$ on the parameters f and Ω we develop in Section 3.2 an approximate second-order solution using perturbation techniques. In Sections 3.3-3.5, the stability of this solution is then determined by Floquet theory, which signals the location of bifurcation points. By sequentially applying this procedure, we generate a bifurcation diagram in the parameter space $\mathbb{P}$ for the T-periodic approximate solution, where $T = 2\pi/\Omega$. In Section 3.6, we present the results of analog-computer simulations and compare these observations with those obtained by a perturbation method and Floquet theory. The analog-computer simulations show solutions escaping from the potential well in two different scenarios, which form the sides of a Y-shape region. On the right side, escape is observed after the destruction of a chaotic attractor at the end of a cascade of period-doubling bifurcations. On the left side, escape is observed suddenly and with no previous warning as a consequence of a tangent instability. In Section 3.7, we comment on results from digital-computer simulations and point out difficulties that may arise in implementing this approach.

3.2. Perturbation Solution

An approximate analytical solution of (3.1) is obtained by assuming that the coefficients μ, α, and f are small. This smallness can be characterized using a single coefficient ε , where $\varepsilon << 1$, as a scaling factor. Thus, we rewrite (3.1) as

$$\ddot{x} + x = \varepsilon(- 2\mu\dot{x} + \alpha x^3 + f\cos\Omega t) \tag{3.2}$$

$$\mu, \alpha > 0 \quad f \in F \quad \Omega \in W \quad F, W \subseteq \mathbb{R}^1$$

A second-order straightforward expansion [5] of the type

$$x(t; \varepsilon) = x_0(t) + \varepsilon x_1(t) + \varepsilon^2 x_2(t) + \ldots \tag{3.3}$$

quickly identifies the resonances $\Omega \approx 1, \Omega \approx \frac{1}{3}$, and $\Omega \approx 3$, which render expansion (3.3) nonuniform and consequently inappropriate.

In the following section, we determine a uniform second-order approximate solution for the case of primary resonance $\Omega \approx 1$ using the method of multiple scales [5]. Because the subharmonic ($\Omega \approx 3$) and superharmonic $\left(\Omega \approx \frac{1}{3}\right)$ resonances produce considerably smaller amplitude responses than the primary resonance, they are excluded from the frequency interval considered.

The proximity of Ω to unity is expressed as

$$\Omega^2 = 1 + \varepsilon\sigma \tag{3.4}$$

where σ is a detuning parameter. The natural frequency of the linear oscillator in (3.2) can be written in terms of Ω by using (3.4). The resulting equation has the following form:

$$\ddot{x} + \Omega^2 x = \varepsilon\left(\sigma x + \alpha x^3 - 2\mu\dot{x} + f\cos\Omega t\right) \tag{3.5}$$

We let

$$x(t;\varepsilon) = x_0(T_0, T_1, T_2) + \varepsilon x_1(T_0, T_1, T_2) + \varepsilon^2 x_2(T_0, T_1, T_2) + \ldots \tag{3.6}$$

where $T_0 = t$ is a fast scale, characterizing changes occurring at the frequencies 1.0 and Ω, and $T_1 = \varepsilon t$ and $T_2 = \varepsilon^2 t$ are slow scales, characterizing the modulation of the amplitude and phase caused by the nonlinearity, damping, and resonance. The time derivatives become

$$\frac{d}{dt} = D_0 + \varepsilon D_1 + \varepsilon^2 D_2 + \ldots \tag{3.7a}$$

$$\frac{d^2}{dt^2} = D_0^2 + 2\varepsilon D_0 D_1 + \varepsilon^2(2D_0D_2 + D_1^2) + \ldots \tag{3.7b}$$

where $D_n = \frac{\partial}{\partial T_n}$. Substituting (3.6) and (3.7) into equation (3.5) and equating coefficients of like powers of ε, we obtain

$$D_0^2 x_0 + \Omega^2 x_0 = 0 \tag{3.8}$$

$$D_0^2 x_1 + \Omega^2 x_1 = -2D_0D_1x_0 + \sigma x_0 - 2\mu D_0 x_0 + \alpha x_0^3 + f\cos\Omega t \tag{3.9}$$

$$\begin{aligned} D_0^2 x_2 + \Omega^2 x_2 = & -2D_0D_2x_0 - 2D_0D_1x_1 - D_1^2x_0 - 2\mu D_0x_1 \\ & -2\mu D_1x_0 + \sigma x_1 + 3\alpha x_0^2 x_1 \end{aligned} \tag{3.10}$$

It is convenient to express the solution of (3.8) in the complex form

$$x_0(T_0, T_1, T_2) = A(T_1, T_2)e^{i\Omega T_0} + \bar{A}(T_1, T_2)e^{-i\Omega T_0} \tag{3.11}$$

where A is an arbitrary complex function of T_1 and T_2 at this level of approximation. It is determined by imposing solvability conditions at the next levels of approximation. Substituting (3.11) into (3.9) yields

$$\begin{aligned} D_0^2 x_1 + \Omega^2 x_1 = & \left[-2i\Omega D_1 A - 2i\mu\Omega A + \sigma A\right]e^{i\Omega T_0} + \alpha A^3 e^{3i\Omega T_0} \\ & + 3\alpha A^2\bar{A}e^{i\Omega T_0} + \frac{1}{2}fe^{i\Omega T_0} + cc \end{aligned} \tag{3.12}$$

where cc stands for the complex conjugate of the preceding terms and Ω is near 1.0. Depending on the function A the particular solutions of (3.12) may contain secular terms. The condition for the elimination of these secular terms is

$$-2i\Omega D_1 A + (\sigma - 2i\mu\Omega)A + 3\alpha A^2\overline{A} + \frac{1}{2}f = 0 \tag{3.13}$$

To this order, A is considered to be a function of T_1 only. Therefore, a first-order approximation can be obtained by expressing A in the polar form

$$A = a(T_1)\exp[i\beta(T_1)] \tag{3.14}$$

where $a(T_1)$ and $\beta(T_1)$ are the amplitude and phase of the fundamental frequency. Substituting (3.14) into (3.13) and separating real and imaginary parts, we find that [16]

$$\dot{a} = -\mu a - \frac{F}{2\Omega}\sin\beta \tag{3.15}$$

$$a\dot{\beta} = -\frac{\sigma}{2\Omega}a - \frac{3\alpha}{8\Omega}a^3 - \frac{f}{2\Omega}\cos\beta \tag{3.16}$$

The first-order solution then becomes

$$x(t) = a\cos(\Omega t + \beta) + \ldots \tag{3.17}$$

where a and β are given by (3.15) and (3.16).

To proceed to second order, we need to determine a particular solution for $x_1(T_0, T_1, T_2)$. With (3.13) the solution of (3.12) can be expressed as

$$x_1 = -\frac{\alpha A^3}{8\Omega^2} e^{3i\Omega T_0} + cc \tag{3.18}$$

Substituting (3.11) and (3.18) into (3.10) yields

$$\begin{aligned} D_0^2 x_2 + \Omega^2 x_2 = &\left(-2i\Omega D_2 A - D_1^2 A - 2\mu D_1 A\right) e^{i\Omega T_0} \\ &- \frac{3\alpha^2}{8\Omega^2} A^3 \bar{A}^2 e^{i\Omega T_0} + NST + cc \end{aligned} \tag{3.19}$$

where NST stands for terms that do not produce secular terms in any particular solution for x_2. To eliminate secular terms from x_2, we must put

$$-2i\Omega D_2 A - D_1^2 A - 2\mu D_1 A - \frac{3\alpha^2}{8\Omega^2} A^3 \bar{A}^2 = 0 \tag{3.20}$$

To solve (3.13) and (3.20), we find it convenient to combine them into a single first-order ordinary-differential equation. This procedure is usually referred to as the method of reconstitution [57] and gives

$$\begin{aligned} &-2i\Omega \frac{dA}{dt} + \varepsilon\left[(\sigma - 2i\mu\Omega)A + 3\alpha A^2 \bar{A} + \frac{1}{2} f\right] + \varepsilon^2\left[\left(\mu^2 + \frac{\sigma^2}{4\Omega^2}\right)A\right. \\ &- \frac{3\alpha f}{8\Omega^2} A^2 + \left(\frac{3\alpha\sigma}{2\Omega^2} - \frac{3i\alpha\mu}{\Omega}\right) A^2 \bar{A} + \frac{3\alpha f}{4\Omega^2} A\bar{A} + \frac{15\alpha^2}{8\Omega^2} A^3 \bar{A}^2 \\ &\left.+ \frac{i\mu f}{4\Omega} + \frac{\sigma f}{8\Omega^2}\right] = 0 \end{aligned} \tag{3.21}$$

Next, the function A in this case is expressed in the polar form

$$A = \frac{1}{2} a(t) \exp[i\beta(t)] \tag{3.22}$$

Substituting (3.22) into (3.21) and separating real and imaginary parts, we obtain

$$\begin{aligned} \dot{a} = & -\varepsilon\mu a - \varepsilon^2 \frac{3\alpha\mu}{8\Omega^2} a^3 + \varepsilon^2 \frac{\mu f}{4\Omega^2} \cos\beta \\ & - \left(\varepsilon \frac{f}{2\Omega} + \varepsilon^2 \frac{\sigma f}{8\Omega^3} + \varepsilon^2 \frac{9\alpha f}{32\Omega^3} a^2 \right) \sin\beta \end{aligned} \tag{3.23}$$

$$\begin{aligned} a\dot{\beta} = & -\left(\varepsilon \frac{\sigma}{2\Omega} + \varepsilon^2 \frac{\mu^2}{2\Omega} + \varepsilon^2 \frac{\sigma^2}{8\Omega^3} \right) a - \left(\varepsilon \frac{3\alpha}{8\Omega} + \varepsilon^2 \frac{3\alpha\sigma}{16\Omega^3} \right) a^3 \\ & - \varepsilon^2 \frac{15\alpha^2}{256\Omega^3} a^5 - \left(\varepsilon \frac{f}{2\Omega} + \varepsilon^2 \frac{\sigma f}{8\Omega^3} + \varepsilon^2 \frac{3\alpha f}{32\Omega^3} a^2 \right) \cos\beta \\ & - \varepsilon^2 \frac{\mu f}{4\Omega^2} \sin\beta \end{aligned} \tag{3.24}$$

Substituting (3.22), (3.11), and (3.18) into (3.6), we find that the second-order approximation to the solution of (3.2) for the primary resonant case ($\Omega \approx 1.0$) is

$$x(t) = a \cos(\Omega t + \beta) - \varepsilon \frac{\alpha a^3}{32\Omega^2} \cos(3\Omega t + 3\beta) + \ldots \tag{3.25}$$

where a and β are given by (3.23) and (3.24).

Equations (3.15)-(3.17) define the first-order approximation while (3.23)-(3.25) define the second-order approximation. For steady-state periodic responses $\dot{a} = 0$ and $\dot{\beta} = 0$ so that (3.15) and (3.16) and (3.23) and (3.24) become sets of algebraic equations that can be solved numerically to determine a and β. Figure 3.2 shows the frequency-response curve of a system governed by (3.1) when $\varepsilon = 1$, $\mu = 0.2, \alpha = 1.0$, and $f = 0.3$. The results obtained from the first-order and second-order approximations and the direct numerical integration of (3.2) by a Runge-Kutta routine are displayed. In spite of the fact that μ, α, and f are not relatively small compared with $x(t)$, the agreement between the solution predicted by the second-order perturbation solution and that obtained using the numerical integration is remarkable. The first-order approximation gives acceptable values for the amplitudes, but the stability predictions are considerably off. Nayfeh and Khdeir [14] found cases in which the first-order approximation produces even unacceptable amplitudes. Therefore, only the second-order approximation will be used.

3.3. *Stability Analysis*

To ascertain the stability of the approximate solution (3.25), we examine the time evolution of the orbit after the application of an arbitrary infinitesimal disturbance $\xi(t)$ in the form

$$\hat{x}(t) = x(t) + \xi(t) \tag{3.26}$$

If $\xi(t) \to 0$ as $t \to \infty$, $x(t)$ is asymptotically stable; otherwise, it is unstable. Substituting $\hat{x}(t)$ into (3.2) and keeping only linear terms in $\xi(t)$, we obtain

$$\ddot{\xi}(t) + 2\varepsilon\mu\dot{\xi}(t) + \left[1 - 3\varepsilon\alpha x^2(t)\right]\xi(t) = 0 \tag{3.27}$$

which is a linear ordinary-differential equation with periodic coefficients. Because $x(t+T) = x(t)$, where $T = 2\pi/\Omega$, and $x(t + \frac{1}{2}T) = -x(t)$, $x^2(t)$ is periodic with the period $\frac{1}{2}T$. Therefore, it follows from Floquet theory [6,42] that (3.27) has solutions of the form

$$\xi(t + \frac{1}{2}T) = \lambda\xi(t) \tag{3.28}$$

where λ is an eigenvalue (also called Floquet multiplier) of the monodromy matrix C associated with a fundamental matrix solution $\Phi(t)$ of (3.27) through the relation

$$\Phi(t + \frac{1}{2}T) = \Phi(t)C \tag{3.29}$$

The solution $x(t)$ is stable if $\xi(t)$ does no grow with t . Thus, the eigenvalues of C must remain inside the unit circle in the complex plane for the solution given by (3.25) to be asymptotically stable.

The stability of the periodic orbit (3.25) or its Poincare map when a parameter is varied can be determined by characterizing its codimension-one bifurcations [36] from the information provided by the Floquet multipliers λ.

For the dissipative one-degree-of-freedom system described by (3.2), there are two ways in which λ can leave the unit circle. They create independent patterns of instability in a T-periodic orbit. An eigenvalue can leave the unit circle through the real axis at -1, originating a saddle-node (tangent) bifurcation. A second way to exit the unit circle is through the real axis at +1, originating a pitchfork bifurcation.

The preceding procedure allows us to predict instabilities in the T-periodic solutions of (3.2) when either f or Ω is being changed. Therefore, the dynamic behavior of the system in a broad portion of the parameter space $\mathbb{P} = FxW$ is dictated by the eigenvalues of C. They can be found by choosing a fundamental matrix solution with the initial conditions $\Phi(0) = I$ so that (3.29) becomes

$$C = \Phi\left(\frac{1}{2}T\right) \tag{3.30}$$

The matrix Φ can be computed numerically by integrating (3.27) in the interval $\left[0, \frac{1}{2}T\right]$ subject to the two sets of initial conditions: (a) $\xi(0) = 1.0$ and $\xi(0) = 0$ and (b) $\xi(0) = 0$ and $\xi(0) = 1.0$ for each set of parameters (f, Ω). The periodic coefficient of (3.27) that depends on $x(t)$ is evaluated by using (3.25).

A traditional alternate approach to the solution of (3.27) has been to transform the equation into a Mathieu-type equation and then find an asymptotic approximation for this new equation [60,61]. Although some insight is gained in this manner, the scope of analysis has to be limited to simple cases such as the one under consideration.

3.4. Bifurcation of Symmetric Solutions

The Duffing oscillator defined in (3.1) is symmetric under parity inversion [49]. This suggests that $x(t)$ also has this property, in the sense that

$$x(t+\frac{1}{2}T) = -x(t) \tag{3.31}$$

The multiple-scales approximation (3.25) satisfies condition (3.31) so it is called symmetric.

Recently [40,52,53], a good deal of attention has been given to the role of symmetry in the bifurcation of periodic orbits. In particular, period-doubling bifurcations have been found to be absent when the symmetry of the system is shared by the solution, which implies that the inversion symmetry of the solution must be first broken before the system undergoes bifurcation. This fact has been exploited [58-61] for the development of techniques that predict the appearance of period-doubling bifurcations in a symmetric orbit. Establishing conditions for the onset of even harmonics in the Fourier expansion of the solution identifies the symmetry-breaking precursor to period-doubling bifurcations. The symmetry of $x(t)$ in (3.25) implies that this periodic orbit can only undergo saddle-node or pitchfork bifurcations. However, the proximity to period-doubling bifurcations can be detected by the appearance of the pitchfork instability, indicating the symmetry-breaking precursor and the loss of the stability of the symmetric solution.

As mentioned earlier, the solution $x(t)$ loses stability when one of the eigenvalues of $\Phi\left(\frac{1}{2}T\right)$ leaves the unit circle in the complex plane through + 1 or -1. If one of the eigenvalues leaves the unit circle through -1, we have

$$\xi\left(t+\frac{1}{2}T\right)=-\,\xi(t) \text{ and } \xi(t+T)=\xi(t) \tag{3.32}$$

at the bifurcation point. Therefore, it follows from (3.26) and (3.32) that

$$\hat{x}(t+T)=\hat{x}(t) \tag{3.33}$$

Thus, $\hat{x}(t)$ is a periodic attractor with period T and the system is expected to display a saddle-node instability and the solution is expected to jump to either another attractor or to an unbounded motion. On the other hand, if one of the eigenvalues of $\Phi\left(\frac{1}{2}T\right)$ leaves the unit circle through $+1$, we have

$$\xi\left(t+\frac{1}{2}T\right)=\xi(t) \tag{3.34}$$

Then, it follows from (3.26), (3.31), and (3.34) that

$$\hat{x}\left(t+\frac{1}{2}T\right) = -x(t) + \xi(t) \neq -\hat{x}(t) \qquad (3.35)$$

and hence the inversion symmetry of the solution is lost through a pitchfork bifurcation. This characterizes the precursor to period-doubling bifurcations.

To illustrate and validate the previous statements we solve (3.1) numerically using a fifth- and sixth-order Runge-Kutta routines for $\mu = 0.2, \alpha = 1$, and increasing values of f. We then apply Floquet analysis to this numerical solution and observe the behavior of the Floquet multipliers as f is increased. Figures 3.3 and 3.4 show the behavior of the Floquet multipliers for $\Omega = 0.8$ and $\Omega = 0.4$: (a) and (c) depict the variation of λ_1 and λ_2 in the complex plane, while (b) and (d) show the variation of their real and imaginary parts with f. In (a) and (c) as f changes, λ_1 and λ_2 move inside the unit circle at constant radius when they are complex, one along the top semicircle, and the other along the bottom semicircle. Figure 3.3(d) shows the signature of the symmetry-breaking precursor to period-doubling bifurcations when the multiplier crosses +1. Similarly, Figure 3.4(b) shows the signature of the saddle-node instability when the multiplier crosses -1. Figure 3.5 shows the effect of f on the phase portrait and power spectrum of the digital-computer simulations at selected points that display symmetric, asymmetric, and period-doubled orbits.

A computer code is developed to find all real values of a and β that satisfy (3.23) and (3.24) in the steady-state (i.e., when $\dot{a} = 0$ and $\dot{\beta} = 0$). The corresponding number of feasible solutions is computed from (3.25) and their stability is determined by the procedure described in the preceding section. The coefficients in (3.1) are taken again as $\mu = 0.2$ and $\alpha = 1.0$, and the parameters Ω and f are varied in the intervals $W = [0.4, 1.0]$ and $F = [0.2, 0.6]$. Figure 3.2 illustrates typical results (second-order solutions) when f is kept constant. For this portion of the domain of Ω two bounded stable attractors are found that form the branches of the response curve. We note that in a portion of the domain of Ω no bounded solutions are found, so we expect the system to diverge to infinity in this region. The two bounded attractors and infinity are reached by specifying appropriate initial conditions. Important qualitative information about the behavior of the system can be obtained by defining the regions of instability of the bounded attractors. This can be achieved by latching onto the attractor and studying its stability as one of the parameters is changed. In this case Ω is increased along the lower branch until a saddle-node bifurcation is observed at point 1, or it is decreased along the upper branch until a pitchfork bifurcation is observed at point 2. The locus of the bifurcation points obtained when f and Ω are alternatively changed is shown in Figure 3.6, where the inserts (a), (b), and (c) correspond to the stable attractors found in regions A, B, and C of the parameter space $\mathbb{P}$. These regions can be defined as follows:

$$A = \left\{(F, \Omega) \in \mathbb{P} \,|\, x(t) \rightarrow \Gamma_1 \quad \text{as} \quad t \rightarrow \infty \quad (x(0), \dot{x}(0)) \in \Psi_1\right\} \tag{3.36}$$

where Γ_1 is the invariant set representing the large attractor and Ψ_1 is its basin of attraction. A similar definition holds for B, with its invariant set being Γ_2 and its basin of attraction being Ψ_2. Consequently, C has an invariant set $\Gamma_1 \bigcup \Gamma_2$ and a basin of attraction $\Psi_1 \bigcup \Psi_2$. The large attractor (upper branch of response curve) in insert (a) is then stable in regions A and C. On the other hand, the small attractor (lower branch of response curve) in insert (b) is stable in regions B and C. Therefore, we observe bistability in C, where the two attractors coexist. In this case the domains of stable solutions are separated by curves of saddle-node or pitchfork bifurcations, which indicate the loss of stability of the T-periodic solution as either of the two parameters undergoes a change across the bifurcation line. Attractor a undergoes pitchfork bifurcations across the top solid line and saddle-node instabilities across the bottom solid line, while attractor b loses stability when the parameters are changed across the dashed line. The arrows point the direction in which the bifurcations are active; that is, attractor b is lost when the dashed line is crossed by increasing either Ω or f. Similarly, attractor a undergoes a pitchfork bifurcation when the solid line is crossed by either decreasing Ω or increasing f. Region C corresponds to the case in which solutions corresponding to the upper branch of the response curve coexist with solutions corresponding to the lower branch for some values of Ω. Therefore, when one solution loses stability the system jumps to the other, creating a hysteretic loop.

3.5. Bifurcation of Asymmetric Solutions

To investigate the behavior of the system after the symmetry-breaking bifurcation has taken place, we need to calculate the asymmetric solution. To this end, we modify the form of the solution in (3.25) to allow for the appearance of even harmonics. Thus, we seek an expansion in the form

$$\tilde{x}(t) \approx \sum_{k=0}^{3} A_k \cos(k\Omega t + k\beta) \tag{3.37}$$

where we denote by $x(t)$, a solution that contains some even harmonics, and therefore is asymmetric. Figures 3.5 (a) and (b), obtained by digital-computer simulation, illustrate the appearance of even harmonics in the frequency content of the solution as it becomes asymmetric. The method of harmonic balance [6] is used to determine the values of the constants A_k and β that satisfy (3.1). Substituting (3.37) into (3.1) and equating the coefficients of each of the harmonics and the constant term to zero, we obtain

$$-\alpha A_0^3 - \frac{3}{2}\alpha\left[A_0 A_1^2 + A_0 A_2^2 + A_0 A_3^2 + \frac{1}{2} A_1^2 A_2 + A_1 A_2 A_3\right] + A_0 = 0 \tag{3.38}$$

$$\begin{aligned} -3\alpha\Big[A_0^2 A_1 + A_0 A_1 A_2 + A_0 A_2 A_3 + \frac{1}{4} A_1^3 + \frac{1}{4} A_1^2 A_3 + \frac{1}{2} A_1 A_2^2 \\ + \frac{1}{2} A_2 A_3^2 + \frac{1}{4} A_2^2 A_3\Big] - f\cos(\beta) - A_1\Omega^2 + A_1 = 0 \end{aligned} \tag{3.39}$$

$$f \sin(\beta) + 2\mu\Omega A_1 = 0 \tag{3.40}$$

$$\begin{aligned} -3\alpha\Big[& A_0^2A_2 + \frac{1}{2}A_0A_1^2 + A_0A_1A_3 + \frac{1}{2}A_1^2A_2 + \frac{1}{2}A_1A_2A_3 + \frac{1}{4}A_2^3 \\ & + \frac{1}{2}A_2\,A_3^2\Big] - 4\Omega^2A_2 + A_2 = 0 \end{aligned} \tag{3.41}$$

$$\begin{aligned} -3\alpha\Big[& A_0^2A_3 + A_0A_1A_2 + \frac{1}{4}A_1^3 + \frac{1}{2}A_1^2A_3 + \frac{1}{4}A_1A_2^2 + \frac{1}{2}A_2^2A_3 \\ & + \frac{1}{4}\,A_3^3\Big] - 9\Omega^2A_3 + A_3 = 0 \end{aligned} \tag{3.42}$$

This set of equations can be solved numerically to determine the A_k and β for any given set of parameters $(f, \Omega) \in \mathbb{P}$. The stability of expansion (3.37) in the parameter space can be determined by the procedure described in Section 3.3 when $x(t)$ is replaced by $\tilde{x}(t)$ in (3.27) and $\Phi\left(\frac{1}{2}T\right)$ by $\Phi(T)$ in (3.29). The results are summarized in Figure 3.7, which shows the occurrence of period-doubling bifurcations (solid curve) and, as before, the tangent instabilities (dashed). The circles mark the results obtained in Section 3.4 for the symmetric orbit. The sequence of events observed when f is increased at constant Ω in the region of period-doubling bifurcations is similar to that obtained in the digital-computer simulation and described in Section 3.4 (Figure 3.5). A pitchfork bifurcation makes the symmetric solution unstable, and shortly afterwards, two stable asymmetric orbits appear displaying small-amplitude even harmonics in their frequency content. After a brief interval of stability these asymmetric solutions undergo period-doubling bifurcations. Our ability to predict bifurcations beyond this point is impaired by the fact that we only have a T-periodic solution which is unstable, while the stable solution is 2T-periodic. As shown in Figure 3.7, the use of the asymmetric orbit has improved our capacity to discern the nature of the events taking place after the symmetry-breaking bifurcation and confirm that indeed it is a precursor to period-doubling bifurcations. On the other hand, the results for the tangent instabilities can be considered equivalent to those of the symmetric solution. Although the beginning of a period-doubling sequence can be foreseen, prediction of the 2nT bifurcation requires an analytical knowledge of the $2(n-1)$ T-periodic asymmetric solution. However, using analog-computer simulations we show in the next section that prediction of these latter bifurcations might not be necessary given the small region where they occur.

3.6. Analog-Computer Simulations

As a means to verify the behaviors predicted in the previous sections, we use an analog computer to model the system described by (3.1). This type of simulation is useful because it brings into play features from the physical system. In spite of their moderate accuracy, analog-computer simulations contribute important qualitative information about the behavior of nonlinear systems.

The results obtained are summarized in Figure 3.8, where we can observe the characteristic Y-shaped zones [1] encountered in many phase-locking systems and obtained previously from the T-periodic solution (Figure 3.7). However, this time we have a complete picture of the events that take place after the T-periodic solution loses stability.

The region marked B remains as defined earlier. It lies below the arm of the Y-shaped zone with negative slope, that we denote by y_1. Tangent instabilities take place when any of the parameters crosses y_1, and the future fate of the system is determined by the attracting set existing in the subset of the parameter space where it lands and the state of the system. When f and Ω are initially in B and then varied to cross y_1 into A, we observe the small orbit becoming unstable and the response of the system jumping to the large attractor, which is the attracting set in this domain. On the other hand, if y_1 is crossed into D, where

$$D = \left\{(f, \Omega) \in \mathbb{P} \mid x(t) \to \infty \ \text{as} \ t \to \infty \ \ (x(0), \dot{x}(0)) \in \mathbb{R}^2\right\} \tag{3.42}$$

the solution becomes unbounded, because infinity is the only attracting set with a nonzero basin of attraction.

Region A contains a good deal of new behaviors unobserved in the analysis of Sections 3.3-3.5. Nevertheless, the size of the domain has not changed considerably. Two curves y_2 and y_3 lie on the side of the Y-shaped zone with positive slope. The curve y_2 marks the locus of the period-doubling bifurcations as observed on an oscilloscope and confirmed by the appearance of one-half frequency components in the frequency content of an FFT (fast Fourier transform) of the solution. The symmetry-breaking precursor is observed but given the small region of transition, the bifurcation curve is not included to avoid obscuring the diagram. Shortly after the first period-doubling bifurcation occurs across y_2 a period-doubling sequence appears to take place. Only a few period multiplications can be observed before a broad-band spectrum appears in the FFT, indicating the presence of a chaotic attractor. When any of the parameters crosses the curve y_3, the existing chaotic attractor vanishes, causing the system to jump to one of the attractors in the new domain. In this case the jump is to the small attractor if the crossing goes into B and the initial conditions are appropriate, or to infinity otherwise. The former situation was observed previously by Huberman and Crutchfield [8], among others. The last curve bordering domain A is y_4, which represents the locus of tangent instabilities causing the large attractor to jump to the small attractor. The small arrows in Figure 3.8 mark the direction in which the bifurcation curves y_k are active.

It is important to point out a few more details from Figure 3.8. The first is the complicated behavior arising in the small area in the parameter space between y_2 and y_3. Because of the symmetry of (3.1), $x(t)$ and $-x(t)$ are solutions; thus, two attractors like the ones in Figure 3.9 coexist and each undergoes a period-doubling sequence to chaos. Figure 3.10 shows spectra (FFT) of a transition from an asymmetric orbit in (a) to a period-doubling bifurcation in (b) to a chaotic attractor in (c). Finally, we note that below Ω = 0.3 we observe a small Y notch replicating in small scale all the behavior previously described, but this time in the superharmonic-frequency range where the system (3.1) has another resonance.

Figure 3.11 shows the data points (stars) obtained from the analog-computer simulations for comparison with the predictions from Sections 3.3-3.5. Although the computed diagram only indicates the occurrence of saddle-node, pitchfork, and period-doubling bifurcations on the arms of the Y-shaped zone, the fact that no other attractor is present in D should hint the possibility of unbounded motions.

3.7. *Digital-Computer Simulations*

Direct numerical integration of the equation of motion is always an attractive option in finding the solution of a nonlinear ordinary-differential equation, and very remarkable algorithms have been developed [e.g., 62] to find the dependence of the solution on the parameters. In some cases it is possible to map completely the branches of the solution $x(t)$ for large portions of the parameter space. However, the singularities at the branch points, and particularly the metamorphoses that the basins of attraction undergo as the parameters are varied, can often prove to be formidable obstacles.

The results obtained in the previous sections have been verified using a fifth- and sixth-order Runge-Kutta routine at selected points in the parameter space. Good agreement has been obtained among the digital-and analog-computer simulations and the analytical predictions. Nevertheless, in some regions of the parameter space it is very cumbersome to find appropriate initial conditions for the numerical routine.

Figure 3.12 shows a series of basin-boundary metamorphoses as the level of f is increased for $\Omega = 0.8$. We note that as f increases from 0.3, the once smooth basin boundary develops fingers (Figures 3.12a and 3.12b) following the scenario described by Grebogi et al. [63]. The white region represents the basin of attraction of bounded solutions while the dark one indicates the set of initial conditions that take the system to an unbounded solution. The entanglement of the two regions becomes complicated and possibly fractal as f increases as shown in Figures 3.12c-3.12e, and the basin of attraction of bounded solutions fades away as shown in Figure 3.12f.

The disappearance of the basin of attraction of bounded solutions is associated with the point of escape from the potential well, since no initial conditions can take the system to an attractor other than infinity. The sequence of basins in Figure 3.12 is generated with a grid of 500x500 initial conditions. This type of identification of the proper initial condition is not generally feasible, but perhaps other techniques such as cell-to-cell mapping [64] would be more appropriate. In any case, the computational effort is considerable.

Chapter 4

PREDICTION OF BIFURCATIONS IN A PARAMETRICALLY EXCITED DUFFING OSCILLATOR

4.1. Introduction

The Duffing oscillator with softening nonlinearity has been extensively studied in the context of a large variety of physical systems [e.g., 8,10,14,47-50,65], such as the oscillation of a pendulum, the rolling motion of a ship, or charge oscillations in superionic conductors. In spite of its simplicity this system has been shown to exhibit complex behaviors in the presence of harmonic forcing and damping, including, among other features, bistability, period-doubling sequences, chaos, and sometimes, unbounded motions.

The above behaviors, apart from interesting, must be considered because they can describe catastrophic consequences for the physical system being modeled. Therefore, prediction of the regions of instability of the system when a parameter is varied becomes critical. In Chapter 3, We predicted the instability regions of a damped Duffing oscillator subject to an external sinusoidal excitation in a parameter space composed of the frequency and amplitude of the excitation. Using an algorithm based on Floquet theory to determine the stability of a second-order approximate analytical solution, we showed that prediction of the first instability was sufficient to characterize the behavior of the system. To further demonstrate this point, we now consider another simple Duffing-type oscillator of considerable importance; namely, a parametrically excited one degree-of-freedom system governed by the nondimensional differential equation

$$\ddot{x} + 2\mu\dot{x} + x - \alpha x^3 + gx\cos\Omega t = 0 \tag{4.1}$$

$$g \in G, \quad \Omega \in W, \quad G, \quad W \subseteq \mathbb{R}$$

where μ, α, g, and Ω are positive constant parameters, and G and W are appropriate domains of the parameters g and Ω; they can be alternately changed.

Nonlinear parametrically excited oscillators have been extensively analyzed [e.g., 6,66-68]. Recently, Zavodney et al. [13] found, through digital- and analog-computer simulations, complicated behaviors near the principal and fundamental parametric resonances of an oscillator with quadratic and cubic nonlinearities. Additional analog-computer simulations in a broader frequency range revealed consistent patterns in the shape of the stability regions of the many attractors of the system. Our aim this time is to use analytical techniques, based on high-order perturbation methods and Floquet theory, to predict some of the bifurcations observed in the numerical simulations. The procedure is applied to a simple parametrically excited single-degree-of-freedom system with cubic nonlinearity. This type of analysis is extremely useful for the characterization of the dynamic behavior of a system when a parameter is slowly varied as a result of either a control or an external action. The resulting bifurcation diagrams can be used during design stages to define safe operating conditions by avoiding dangerous instabilities. Digital- and analog-computer simulations are used to assess the accuracy of the predictions.

Equation (4.1) models, among other systems, the rolling motion of a ship in a regular sea [69] and, for small x, a parametrically excited pendulum [70]. Figure 3.1 shows the potential and the phase diagram of the Hamiltonian system associated with (4.1) when $\alpha = 1.0$. It is evident that under some conditions the system can escape the potential well, and an unbounded response would result. We are especially interested in this event due to the catastrophic implications that it has for a physical system, such as the capsizing of a vessel. Previous studies of the softening Duffing oscillator have dealt with the response of an externally excited system for constant amplitude and varying frequency of excitation. Huberman and Crutchfield [8] observed a period-doubling sequence culminating in chaos for a level of external excitation where the coexistence of two solutions produces a hysteretic effect. Räty, et al. [47] observed in the same region a symmetry-breaking precursor to period-doubling bifurcations and confirmed the consistency of this behavior with the universal features of noninvertible one-dimensional maps.

The response x(t) of the system described by (4.1) depends on both the parameters g and Ω and the initial conditions. To determine the dependence of x(t) on the parameters, in Section 4.2 we develop second-order approximate solutions in the neighborhoods of the nonlinear resonances of (4.1) using perturbation techniques. We then proceed to determine the instability regions of these solutions in the g-Ω plane using an algorithm based on Floquet theory. By sequentially applying this procedure, we generate a bifurcation diagram for the analytically predicted periodic solutions in the parameter space $\mathbb{P} = G \times W$. In Section 4.3 we present the results of detailed analog-computer simulations of the system, locating the attractors and their bifurcations in the parameter space. Finally, in Section 4.4 we present the results of digital integration using a Runge-Kutta routine and compare them with the analytical and analog-computer results.

4.2. Perturbation solutions

Equation (4.1) can be recast as a perturbed linear oscillator by assuming that the parameters μ, α, and g are small. Using a single coefficient ε, where $\varepsilon << 1$, to represent this smallness, we rewrite (4.1) as

$$\ddot{x} + x = -\varepsilon(2\mu\dot{x} - \alpha x^3 + gx\cos\Omega t) \tag{4.2}$$

Carrying out a second-order straightforward expansion [5], we find that resonances occur when $\Omega \approx 1, 2$, and 4. The first two cases are known as the fundamental and principal parametric resonances, respectively. They are treated in the following two subsections, where we use the method of multiple scales, as presented by Nayfeh [57], to determine second-order uniform solutions, which we found to be considerably more accurate than the first-order solutions. The analytical solutions are in close agreement with digital-computer simulations even when ϵ approaches unity. We assume that Ω is away from 4 so that the last resonant case is not treated.

4.2.1 Fundamental parametric resonance

In this case the proximity of Ω to unity can be expressed as

$$\Omega^2 = 1 + \varepsilon\sigma_1 \tag{4.3}$$

where σ_1 is a detuning parameter. The natural frequency of the linear oscillator defined in (4.2) can be written in terms of Ω using (4.3), resulting in the following form:

$$\ddot{x} + \Omega^2 x = \varepsilon(\sigma_1 x - 2\mu\dot{x} + \alpha x^3 - gx\cos\Omega t) \tag{4.4}$$

We let

$$x(t;\varepsilon) = x_0(T_0, T_1, T_2) + \varepsilon x_1(T_0, T_1, T_2) + \varepsilon^2 x_2(T_0, T_1, T_2) + \ldots \tag{4.5}$$

where $T_0 = t$ is a fast scale, characterizing motions occurring at the frequency Ω, and $T_1 = \varepsilon t$ and $T_2 = \varepsilon^2 t$ are slow scales, characterizing the modulation in the amplitude and phase caused by the nonlinearity, damping and resonances. The time derivatives become

$$\frac{d}{dt} = D_0 + \varepsilon D_1 + \varepsilon^2 D_2 + \ldots \tag{4.6a}$$

$$\frac{d^2}{dt^2} = D_0^2 + 2\varepsilon D_0 D_1 + \varepsilon^2(2D_0 D_2 + D_1^2) + \ldots \tag{4.6b}$$

where $D_n = \dfrac{\partial}{\partial T_n}$. Substituting (4.5) and (4.6) into (4.4) and equating coefficients of like powers of ε, we obtain

$$D_0^2 x_0 + \Omega^2 x_0 = 0 \tag{4.7}$$

$$D_0^2 x_1 + \Omega^2 x_1 = \sigma_1 x_0 - 2D_0 D_1 x_0 - 2\mu D_0 x_0 + \alpha x_0^3 - g x_0 \cos\Omega T_0 \tag{4.8}$$

$$D_0^2 x_2 + \Omega^2 x_2 = \sigma_1 x_1 - 2D_0D_2x_0 - D_1^2 x_0 - 2D_0D_1x_1 - 2\mu D_0 x_1 - 2\mu D_1 x_0 + 3\alpha x_0^2 x_1 - g x_1 \cos \Omega T_0 \tag{4.9}$$

It is convenient to express the solution of (4.7) in the complex form

$$x_0(T_0, T_1, T_2) = A(T_1, T_2)e^{i\Omega T_0} + \bar{A}(T_1, T_2)e^{-i\Omega T_0} \tag{4.10}$$

where $\bar{A}$ is the complex conjugate of A, which is an arbitrary complex function of T_1 and T_2 at this level of approximation. It is determined by imposing the solvability conditions at the next levels of approximation. Substituting (4.10) into (4.8) yields

$$D_0^2 x_1 + \Omega^2 x_1 = (-2i\Omega D_1 A - 2i\mu\Omega A + \sigma_1 A)e^{i\Omega T_0} + \alpha A^3 e^{3i\Omega T_0} + 3\alpha A^2 \bar{A} e^{i\Omega T_0} - \frac{1}{2} g A e^{2i\Omega T_0} - \frac{1}{2} g A + cc \tag{4.11}$$

where cc is the complex conjugate of the preceding terms. Depending on the function A, the particular solutions of (4.11) may contain secular terms. The condition for the elimination of these secular terms is

$$-2i\Omega D_1 A + (\sigma_1 - 2i\mu\Omega)A + 3\alpha A^2 \bar{A} = 0 \tag{4.12}$$

Then, the particular solution of (4.11) can be written as

$$x_1 = -\frac{gA}{2\Omega^2} + \frac{gA}{6\Omega^2} e^{2i\Omega T_0} - \frac{\alpha A^3}{8\Omega^2} e^{3i\Omega T_0} + cc \tag{4.13}$$

Substituting (4.10) and (4.13) into (4.9) yields

$$D_0^2 x_2 + \Omega^2 x_2 = \left(-2i\Omega D_2 A - D_1^2 A - 2\mu D_1 A - \frac{3}{8\Omega^2}\alpha^2 A^3 \bar{A}^2 + \frac{g^2 A}{6\Omega^2} + \frac{g^2 \bar{A}}{4\Omega^2} \right) e^{i\Omega T_0} + NST + cc \tag{4.14}$$

where NST stands for terms that do not produce secular terms. Eliminating secular terms from x_2 (4.14), we obtain

$$-2i\Omega D_2 A - D_1^2 A - 2\mu D_1 A - \frac{3}{8\Omega^2}\alpha^2 A^3 \bar{A}^2 + \frac{g^2 A}{6\Omega^2} + \frac{g^2 \bar{A}}{4\Omega^2} = 0 \tag{4.15}$$

To solve (4.12) and (4.15), we find it convenient to combine them into a single first-order ordinary-differential equation. This procedure is usually referred to as the method of reconstitution [57] and gives

$$-2i\Omega \dot{A} + \varepsilon\left[(\sigma_1 - 2i\mu\Omega)A + 3\alpha A^2 \bar{A}\right] + \varepsilon^2\left[\left(\frac{\sigma_1^2}{4\Omega^2} + \mu^2 + \frac{g^2}{6\Omega^2}\right)A + \frac{g^2}{4\Omega^2}\bar{A} + \left(\frac{3\sigma_1\alpha}{2\Omega^2} - \frac{3i\mu\alpha}{\Omega}\right)A^2\bar{A} + \frac{15\alpha^2}{8\Omega^2}A^3\bar{A}^2\right] = 0 \tag{4.16}$$

Next the function A is expressed in the polar form

$$A = \frac{1}{2} a e^{i\beta} \tag{4.17}$$

where a and β are the amplitude and phase of the fundamental frequency. Substituting (4.17) into (4.16) and separating real and imaginary parts, we obtain

$$\dot{a} = -\varepsilon\mu a - \frac{3\varepsilon^2}{8\Omega^2}\mu\alpha a^3 - \frac{\varepsilon^2 g^2}{8\Omega^3} a \sin 2\beta \tag{4.18}$$

$$\begin{aligned} a\dot{\beta} = & -\left(\frac{\varepsilon\sigma_1}{2\Omega} + \frac{\varepsilon^2\sigma_1^2}{8\Omega^3} + \frac{\varepsilon^2\mu^2}{2\Omega} + \frac{\varepsilon^2 g^2}{12\Omega^3}\right)a - \left(\frac{3\varepsilon\alpha}{8\Omega} + \frac{3\varepsilon^2\sigma_1\alpha}{16\Omega}\right)a^3 \\ & - \frac{\varepsilon^2 15}{256\Omega^3}\alpha^2 a^5 - \frac{\varepsilon^2 g^2 a}{8\Omega^3}\cos 2\beta \end{aligned} \tag{4.19}$$

Substituting (4.17), (4.10), and (4.13) into (4.5), we find that the second-order approximation to the solution of (4.4) for the fundamental resonant case ($\Omega \approx 1$) is

$$\begin{aligned} x_f(t) = & \, a\cos(\Omega t + \beta) + \varepsilon\left[\frac{ga}{6\Omega^2}\cos(2\Omega t + \beta)\right. \\ & \left. - \frac{\alpha a^3}{32\Omega^2}\cos(3\Omega t + 3\beta) - \frac{ga}{2\Omega^2}\cos\beta\right] + \ldots \end{aligned} \tag{4.20}$$

where a and β are given by (4.18) and (4.19). For steady-state periodic responses $\dot{a} = 0$ and $\dot{\beta} = 0$ so that (4.18) and (4.19) become a set of algebraic equations that can be solved numerically to determine a and β.

4.2.2 Principal parametric resonance

In this case $\Omega \approx 2$ and we introduce the detuning parameter σ_2 defined according to

$$\frac{1}{4}\Omega^2 = 1 + \varepsilon\sigma_2 \tag{4.21}$$

Using (4.21) to express the natural frequency in (4.2), we obtain

$$\ddot{x} + \frac{1}{4}\Omega^2 x = \varepsilon\left(\sigma_2 x - 2\mu\dot{x} + \alpha x^3 - gx\cos\Omega t\right) \tag{4.22}$$

Following the procedure used in the previous section, we substitute (4.5) and (4.6) into (4.22), equate coefficients of like powers of ε, and obtain

$$D_0^2 x_0 + \frac{1}{4}\Omega^2 x_0 = 0 \tag{4.23}$$

$$D_0^2 x_1 + \frac{1}{4}\Omega^2 x_1 = \sigma_2 x_0 - 2D_0 D_1 x_0 - 2\mu D_0 x_0 + \alpha x_0^3 - g x_0 \cos\Omega T_0 \tag{4.24}$$

$$\begin{aligned} D_0^2 x_2 + \frac{1}{4}\Omega^2 x_2 = {} & \sigma_2 x_1 - 2D_0 D_2 x_0 - 2D_0 D_1 x_1 - D_1^2 x_0 - 2\mu D_0 x_1 \\ & - 2\mu D_1 x_0 + 3\alpha x_0^2 x_1 - g x_1 \cos\Omega T_0 \end{aligned} \tag{4.25}$$

The solution of (4.23) is expressed in the form

$$x_0(T_0, T_1, T_2) = A(T_1, T_2)e^{\frac{1}{2}i\Omega T_0} + \bar{A}(T_1, T_2)e^{-\frac{1}{2}i\Omega T_0} \tag{4.26}$$

Substituting (4.26) into (4.24) yields

$$\begin{aligned} D_0^2 x_1 + \frac{1}{4}\Omega^2 x_1 = {} & \left(\sigma_2 A - i\Omega D_1 A - i\mu\Omega A + 3\alpha A^2\bar{A} - \frac{1}{2}g\bar{A}\right)e^{\frac{1}{2}i\Omega T_0} \\ & + \left(\alpha A^3 - \frac{1}{2}gA\right)e^{\frac{3}{2}i\Omega T_0} + cc \end{aligned} \tag{4.27}$$

Eliminating the terms that produce secular terms in x_1 yields

$$-i\Omega D_1 A+(\sigma_2-i\mu\Omega)A+3\alpha A^2\bar{A}-\frac{1}{2}g\bar{A}=0 \tag{4.28}$$

This leaves (4.27) with the particular solution

$$x_1=\left(\frac{gA}{4\Omega^2}-\frac{\alpha A^3}{2\Omega^2}\right)e^{\frac{3}{2}i\Omega T_0}+cc \tag{4.29}$$

Substituting (4.26) and (4.29) into (4.25) yields

$$\begin{aligned}D_0^2x_2+\frac{1}{4}\Omega^2x_2=\Bigg(&-i\Omega D_2A-D_1^2A-2\mu D_1A-\frac{3\alpha^2}{2\Omega^2}A^3\bar{A}^2+\frac{3\alpha}{4\Omega^2}gA\bar{A}^2\\&+\frac{\alpha g}{4\Omega^2}A^3-\frac{g^2}{8\Omega^2}A\Bigg)e^{\frac{1}{2}i\Omega T_0}+NST+cc\end{aligned} \tag{4.30}$$

Elimination of secular terms from x_2 demands that

$$\begin{aligned}-i\Omega D_2A-D_1^2A-2\mu D_1A-\frac{3\alpha^2}{2\Omega^2}A^3\bar{A}^2+\frac{3\alpha g}{4\Omega^2}A\bar{A}^2+\frac{\alpha g}{4\Omega^2}A^3&\\-\frac{g^2}{8\Omega^2}A=0&\end{aligned} \tag{4.31}$$

Combining (4.28) and (4.31) in the manner mentioned in the preceding section, we obtain

$$\begin{aligned} & - i\Omega \dot{A} + \varepsilon\left[(\sigma_2 - i\mu\Omega)A - \frac{1}{2}g\overline{A} + 3\alpha A^2\overline{A}\right] + \varepsilon^2\left[\left(\frac{\sigma_2^2}{\Omega^2} - \frac{3g^2}{8\Omega^2} + \mu^2\right) A \right. \\ & \left. + \left(\frac{6\sigma_2\alpha}{\Omega^2} - \frac{6i\mu\alpha}{\Omega}\right)A^2\overline{A} + \frac{15\alpha^2}{2\Omega^2} A^3\overline{A}^2 + \frac{7\alpha}{4\Omega^2} A^3 - \frac{3\alpha g}{4\Omega^2} A\overline{A}^2\right] = 0 \end{aligned} \tag{4.32}$$

Using (4.17) and separating real and imaginary parts in (4.32), we have

$$\dot{a} = - \varepsilon\mu a - \varepsilon^2 \frac{3\mu}{2\Omega^2}\alpha a^3 + \varepsilon\frac{ga}{2\Omega}\sin(2\beta) + \varepsilon^2\frac{5\alpha}{8\Omega^3} g a^3 \sin(2\beta) \tag{4.33}$$

$$\begin{aligned} a\dot{\beta} = & -\left(\frac{\varepsilon\sigma_2}{\Omega} + \varepsilon^2\frac{\sigma_2^2}{\Omega^3} + \varepsilon^2\frac{\mu^2}{\Omega} - \varepsilon^2\frac{3g}{8\Omega^3}\right)a - \left(\frac{\varepsilon 3\alpha}{4\Omega} + \frac{\varepsilon^2 3\sigma_2\alpha}{2\Omega^3}\right)a^3 \\ & - \varepsilon^2\frac{15}{32\Omega^3}\alpha^2 a^5 + \left(\frac{\varepsilon a}{2\Omega} - \varepsilon^2\frac{\alpha a^3}{4\Omega^3}\right)g\cos(2\beta) \end{aligned} \tag{4.34}$$

Substituting (4.17), (4.26), and (4.29) into (4.5), we obtain the following approximate solution for the case of principal parametric resonance ($\Omega \approx 2$):

$$\begin{aligned} x_p(t) = a\cos\left(\frac{1}{2}\Omega t + \beta\right) + \varepsilon\left[\frac{ga}{4\Omega^2}\cos\left(\frac{3}{2}\Omega t + \beta\right) \right. \\ \left. - \frac{\alpha a^3}{8\Omega^2}\cos\left(\frac{3}{2}\Omega t + 3\beta\right)\right] + \ldots \end{aligned} \tag{4.35}$$

where a and β are given by (4.33) and (4.34). In this case again, periodic responses correspond to $a = 0$ and $\dot{\beta} = 0$ so that (4.33) and (4.34) form a set of algebraic equations that can be solved numerically to obtain a and β.

Figure 4.1 shows typical trajectories for $x_f(t)$ and $x_p(t)$ to which we refer as the T_f-periodic and T_p-periodic solutions where $T_f = 2\pi/\Omega$ when $\Omega \approx 1$ and $T_p = 4\pi/\Omega$ when $\Omega \approx 2$.

4.2.3 Stability of trivial solutions near $\Omega = 1$

In the previous two subsections, expressions (4.20) and (4.35) were developed to approximate the responses of the system when Ω is near 1 and 2, respectively. Both $x_f(t)$ and $x_p(t)$ are functions of a and β, which in turn are described by the differential equations (4.18) and (4.19) and (4.33) and (4.34), respectively. Steady-state periodic solutions correspond to $\dot{a} = \dot{\beta} = 0$, that is, to the fixed points of these equations. We note that $a = 0$ (i.e., the trivial response) is a possible fixed point of both sets of (4.18) and (4.19) and (4.33) and (4.34). To determine whether these fixed points correspond to realizable solutions, we need to determine their stability by analyzing the behavior of the differential equations (4.16) and (4.32) which determine A.

Neglecting the nonlinear terms in (4.16), we obtain

$$2i\Omega\dot{A} + \left(-\varepsilon\sigma_1 + 2i\varepsilon\mu\Omega - \frac{\varepsilon^2\sigma_1^2}{4\Omega^2} - \varepsilon^2\mu^2 - \frac{\varepsilon^2 g^2}{6\Omega^2} \right)A - \frac{\varepsilon^2 g^2}{4\Omega^2}\bar{A} = 0 \quad (4.36)$$

A closed-form solution of (4.36) can be obtained by letting

$$A = B_r + iB_i \quad (4.37)$$

where B_r and B_i are real. Substituting (4.37) into (4.36) and separating real and imaginary parts, we have

$$2\Omega\dot{B}_r + 2\varepsilon\mu\Omega B_r + \left(-\varepsilon\sigma_1 - \frac{\varepsilon^2\sigma_1^2}{4\Omega^2} - \varepsilon^2\mu^2 + \frac{\varepsilon^2 g^2}{12\Omega^2} \right) B_i = 0 \tag{4.38}$$

$$2\Omega\dot{B}_i + 2\varepsilon\mu\Omega B_i + \left(\varepsilon\sigma_1 + \frac{\varepsilon^2\sigma_1}{4\Omega^2} + \varepsilon^2\mu^2 + \frac{5\varepsilon^2 g^2}{12\Omega^2} \right) B_r = 0 \tag{4.39}$$

Equations (4.38) and (4.39) admit solutions of the form

$$(B_r, B_i) = (b_r, b_i)e^{\varepsilon\lambda t} \tag{4.40}$$

provided that

$$\lambda = -\mu \pm \left[\frac{\varepsilon^2 g^4}{64\Omega^6} - \frac{1}{4\Omega^2}\left(\sigma_1 + \frac{\varepsilon\sigma_1^2}{4\Omega^2} + \varepsilon\mu^2 + \frac{\varepsilon g^2}{6\Omega^2} \right)^2 \right]^{\frac{1}{2}} \tag{4.41}$$

Hence, the trivial solution is stable if and only if the real part of each of the roots of λ is less than or equal to zero, and it is unstable if the real part of any of these roots is greater than zero. Thus, the vanishing of one of the roots in (4.41) yields a curve in the $g - \Omega$ plane, which separates stable from unstable trivial solutions.

4.2.4 Stability of trivial solution near $\Omega = 2$

Linearization of (4.32) yields the following differential equation governing the stability of the null solution:

$$i\Omega\dot{A} + \left(- \varepsilon\sigma_2 + i\varepsilon\mu\Omega - \frac{\varepsilon^2\sigma_2^2}{\Omega^2} - \varepsilon^2\mu^2 + \frac{3\varepsilon^2}{8\Omega^2}g^2 \right)A + \frac{1}{2}\varepsilon g\bar{A} = 0 \quad (4.42)$$

Substituting (4.37) into (4.42) and separating real and imaginary parts, we obtain

$$\Omega(\dot{B}_r + \varepsilon\mu B_r) + \left(- \varepsilon\sigma_2 - \frac{\varepsilon^2\sigma_2^2}{\Omega^2} - \varepsilon^2\mu^2 + \frac{3\varepsilon^2 g^2}{8\Omega^2} \right)B_i - \frac{1}{2}\varepsilon g B_i = 0 \quad (4.43)$$

$$\Omega(\dot{B}_i + \varepsilon\mu B_i) + \left(- \varepsilon\sigma_2 - \frac{\varepsilon^2\sigma_2^2}{\Omega^2} - \varepsilon^2\mu^2 + \frac{3\varepsilon^2 g^2}{8\Omega^2} \right)B_r - \frac{1}{2}\varepsilon g B_r = 0 \quad (4.44)$$

Equations (4.43) and (4.44) admit solutions of the form (4.40) provided that

$$\lambda = - \mu \pm \left[\frac{g^2}{4\Omega^2} - \frac{1}{\Omega^2}\left(\sigma_2 + \frac{\varepsilon\sigma_2^2}{\Omega^2} + \varepsilon\mu^2 - \frac{3\varepsilon g^2}{8\Omega^2} \right)^2 \right]^{\frac{1}{2}} \quad (4.44)$$

In this case, again $\lambda = 0$ gives the equation of the curve separating stable from unstable trivial solutions.

4.2.5 Orbital Stability

To ascertain the stability of the periodic orbits $x_r(t)$ and $x_p(t)$ found in Sections 4.2.1 and 4.2.2, we examine the time evolution of the orbit after the application of an arbitrary infinitesimal disturbance $\xi(t)$ in the form

$$\hat{x}(t) = x(t) + \xi(t) \tag{4.45}$$

where $x(t)$ is any of the two solutions previously found. The stability of $x(t)$ then depends on whether $\xi(t)$ grows or decays with t. Substituting (4.46) into (4.2) and keeping linear terms in $\xi(t)$, we obtain

$$\ddot{\xi} + 2\varepsilon\mu\dot{\xi} + \left[1 - 3\varepsilon\alpha x^2(t) + \varepsilon g \cos \Omega t\right]\xi = 0 \tag{4.46}$$

which is a linear ordinary-differential equation with periodic coefficients having the period $T = 2\pi/\Omega$. The existence of nontrivial solutions can be determined using Floquet's theorem [6,34], which calls for solutions of the form

$$\xi(t + T) = \lambda\xi(t) \tag{4.47}$$

where λ is an eigenvalue (also called Floquet multiplier) of the monodromy matrix C whose elements are associated with (4.47) through the relations

$$\xi_1(t + T) = c_{11}\xi_1(t) + c_{12}\xi_2(t) \tag{4.48}$$

$$x_2(t+T) = c_{21}\xi_1(t) + c_{22}\xi_2(t) \tag{4.49}$$

The functions $\xi_1(t)$ and $\xi_2(t)$ are two linearly independent solutions of (4.47); they can be determined by the initial conditions

$$\xi_1(0) = 1, \quad \dot{\xi}_1(0) = 0 \tag{4.50}$$

$$\xi_2(0) = 0, \quad \dot{\xi}_2(0) = 1 \tag{4.51}$$

The solution $x(t)$ is an asymptotically stable orbit if and only if $\xi(t)$ does not grow with t. This requires that

$$|\lambda| < 1 \tag{4.52}$$

that is, the eigenvalues of C must remain inside the unit circle in the complex plane. The monodromy matrix C can be obtained by numerically integrating (4.47) for fixed values of g and Ω in the interval [0,T] subject to the initial conditions (4.51) and (4.52). It follows from (4.49)-(4.52) that

$$C = \begin{bmatrix} \xi_1(T) & \dot{\xi}_1(T) \\ \xi_2(T) & \dot{\xi}_2(T) \end{bmatrix} \tag{4.53}$$

Therefore,

$$\lambda^2 - \left[\xi_1(T) + \dot{\xi}_2(T)\right]\lambda + \left[\xi_2(T)\dot{\xi}_2(T) - \dot{\xi}_1(T)\xi_2(T)\right] = 0 \tag{4.54}$$

The values of λ determine the stability of the approximate solutions $x_p(t)$ and $x_f(t)$ according to the criterion (4.53).

Determination of the stability of the periodic orbits (4.20) and (4.35) when a parameter is varied can be accomplished by computing the Floquet multipliers. Furthermore, the manner in which the eigenvalue λ leaves the unit circle characterizes the local qualitative changes (bifurcations) occurring to the orbit. For the dissipative one-degree-of-freedom system described by (4.2) there are two ways in which λ can leave the unit circle [36], each of which creates independent patterns of instability in the periodic orbit. An eigenvalue can leave the unit circle through the real axis at either -1 or +1. When λ leaves the unit circle through -1 (the disturbance has a period of 2T), it originates a period-doubling or flip bifurcation for x_f and a saddle-node (tangent) bifurcation for x_p. When λ leaves the unit circle through +1 (the disturbance has a period T), it originates a saddle-node bifurcation for x_f and a pitchfork (symmetry-breaking) bifurcation for x_p.

Figure 4.2 shows the bifurcation diagram generated by sequentially applying Floquet theory to the analytically calculated periodic solutions in the parameter space $\mathbb{P} = GxW$, where $W = [0.3.0]$ and $G = [0.8.0]$, for $\varepsilon\mu = 0.2$ and $\varepsilon\alpha = 1.0$. All curves represent stability boundaries, and bifurcations occur across them when the parameters change in the direction indicated by the arrows. The inserts (a)-(c) show the corresponding attractors (stable orbits) present in this region of the parameter space. Attractor (a) is stable in the dotted region on the right, which corresponds to the $x_p(t)$ solution. This solution undergoes either symmetry breaking (at $\lambda = 1$) or saddle-node ($\lambda = -1$) bifurcations across the boundaries of the wedge. Attractor (b) is stable in the narrow dotted region on the left, which corresponds to the $x_f(t)$ solution. This asymmetric solution undergoes a period-doubling bifurcation across the dashed curve on the top ($\lambda = -1$) and a saddle-node bifurcation ($\lambda = +1$) across the bottom curve. The segments 1-2-3 and 4-5 represent stability boundaries for trivial solutions, which were obtained by evaluating (4.41) and (4.45) for $\lambda = 0$. Under these segments the trivial solution is stable.

The behavior predicted by the stability analysis can take three forms corresponding to the attractors shown in the inserts of Figure 4.2. First, a solution with the period $T_p = 4\pi/\Omega$ when $\Omega \approx 1$ that is stable in region A, which can be associated with the principal parametric resonance $x_p(t)$. Second, a solution with the period $T_f = 2\pi/\Omega$ when $\Omega \approx 1$ that is stable in region B, which is associated with the fundamental parametric resonance $x_f(t)$. Third, a trivial solution. To predict subsequent bifurcations, we need to calculate the periodic solutions subsequent to x_f and x_p. However, the type of bifurcation taking place of the $T_f -$ and $T_p -$periodic solutions gives valuable qualitative information on the subsequent behavior. Saddle-node bifurcations are associated with jumps to a neighboring attractor, symmetry-breaking bifurcations are commonly known precursors to period-doubling bifurcations, and period-doubling bifurcations in turn are usually followed by a full sequence of similar bifurcations leading to chaos [34].

4.3. Analog-computer simulations

As a means to verify the behaviors predicted by analyzing the stability of the analytically determined periodic solutions in the parameter space $\mathbb{P}$, we used an analog computer to model the system described by (4.1). The results obtained are summarized in Figure 4.3, where inserts (a)-(e) show the attractors present in this portion of the parameter space. The nontrivial solutions can be classified into three types depending on the nature of the resonance that produced them: principal parametric, fundamental parametric, or superharmonic resonance. These solutions can be obtained in the regions indicated by arrows departing from the inserts (A,B,C) when the proper initial conditions are specified.

The bifurcation diagram in Figure 4.3 can now be compared with the one in Figure 4.2 obtained by using the analytical solutions. This time, we can get a complete picture of the events that take place after the first periodic solution becomes unstable. The principal parametric response can be obtained in region A between the segments 1-2 and 2-4, which mark its stability boundaries; across 1-2 this attractor undergoes saddle-node bifurcations and a jump to the trivial solution is observed; as g is increased from 1-2 approaching 2-4 the frequency content in the FFT (Fast Fourier Transform) begins to show the presence of even′ harmonics indicating a symmetry-breaking bifurcation, across 2-4 period-doubling bifurcations take place and a stable $2T_p$ −periodic attractor is obtained. In the narrow region between 2-4 and 5-3 a sequence of period-doubling bifurcations is observed. After a few period-multiplications take place, a broad-band frequency content appears in the FFT indicating the presence of a chaotic attractor. This chaotic attractor disappears when 5-3 is crossed, and an unbounded solution results, overloading the amplifiers of the computer. As the value of g increases and $\Omega = 2$, Figures 4.4(a)-(c) show quantitative changes of the principal parametric response, while figures 4.5(d) and (e) show qualitative changes in the response corresponding to a $2T_p$ − periodic orbit and a chaotic attractor.

The fundamental parametric response can be obtained in region B (between 8-9 and 7-6) of Figure 4.3 where we observe the attractors shown in inserts (b) and (c), which are inversions of each other. These attractors coexist in a narrow band within B where a hysteretic loop between the two can be observed. In the remaining part of B only one attractor is stable. However, both undergo period-doubling sequences, as shown in Figure 4.5 for $\Omega = 1$ and increasing values of g. Figures 4.5(a)- (c) depict the period-doubling sequence to chaos for the bottom attractor in region B. This sequence ends with the disappearance of the chaotic attractor and a jump to the top inverted attractor shown in Figure 4.5(d). A new sequence of period-doubling bifurcations is undergone by this attractor, leading to the chaotic attractor in

Figure 4.5(e) which also disappears as g is further increased; this time the system escapes to infinity (across 8-9 in Figure 4.3).

The trivial solution is shown as the point attractor (e) in Figure 4.3. This attractor loses stability across the curve 1-6-7 through pitchfork and reverse pitchfork bifurcations that take the system to a periodic attractor (across 1-5) or to an unbounded solution (across 5-6- 7). This latter behavior has physical significance because, as a parameter is changed, the system would go from a trivial response to an unbounded solution without a previous warning.

In region C of Figure 4.3, the system displays superharmonic responses. Insert (d) shows one of the various attractors that can be found. The transition from a bounded to an unbounded response in this region (across 9-10) takes place through either period-doubling cascades ending in the disappearance of the chaotic attractor (solid line), or tangent instabilities (dashed line).

Comparing the analytically predicted behavior in Figure 4.2 with the actual response from Figure 4.3 confirms that the top boundary of the right wedge in Figure 4.2 is the locus of pitchfork bifurcations triggering the symmetry-breaking precursor to period-doubling bifurcations. Furthermore, it confirms the assumption that in the absence of any bounded stable attractor in a neighborhood of $\mathbb{P}$ the system escapes to infinity. The existence of a full period-doubling sequence leading to chaos is also verified. Nevertheless, it should be noted that complicated behaviors arise in very narrow regions of the parameter space, so that the stability of the analytically calculated periodic solutions yields an adequate prediction of the onset of complicated responses including the occurrence of unbounded motions. Figure 4.6 compares the analytical predictions from Figure 4.2 with the results of the analog-computer simulation; the agreement is very good.

4.4. Digital-computer simulations

Very remarkable algorithms have been developed [e.g., 62] for finding the dependence of the solution of a system of differential equations on the parameters through direct numerical integration, which traces the solution branches throughout the parameter space. However, singularities at branch points and particularly the metamorphoses that the basins of attraction undergo as the parameters are varied can often create great difficulties in practical applications.

The results obtained in the preceding sections were verified using a fifth- and sixth-order Runge-Kutta routine. Excellent agreement was found between the analytical solutions $x_p(t)$ and $x_r(t)$ and the numerical simulations. Figure 4.7 compares the results obtained using the analog-computer simulations with the numerically observed locations of the point of escape from the potential well for selected values of Ω . The dotted area represents the region of bounded solutions.

The sensitivity of the solution to initial conditions was analyzed by using a grid of 280x500 initial conditions in the phase space. By integrating (4.1) for a sufficiently long period of time to determine the boundedness of the solution, we generated Figure 4.8 for $\Omega = 2$ and increasing values of g. The white regions correspond to bounded solutions and the black regions correspond to unbounded solutions. For g = 1.15 a smooth basin of attraction is obtained as shown in Figure 4.8(a). As the parameter g is increased to g = 1.2 in (b), the once smooth basin boundary develops fingers following the scenario described by Grebogi et al. [63]. Further increases in g cause the regions to develop entanglement and the boundary becomes possibly fractal, as seen in Figures 4.8(c) and (d). Eventually the basin of bounded solutions vanishes and the system goes to infinity for any set of initial conditions. Similarly, Figure 4.9 shows a basin of attraction for $\Omega = 1$ and g = 2.0, where fingers begin to appear.

Chapter 5

SHIP MOTIONS

In this chapter we present the equations of rigid-body motion of a ship moving through water. The general form of the equations is applicable to the motion of other bodies under the action of gravity and hydrodynamic forces, but some of the particular assumptions are specific to the case of vessels. We follow the notation and basic assumptions specified in reference [71] and discuss the derivation of the equations from a Newtonian point of view as well as from a variational approach. The presentation develops from a general six-degree-of-freedom motion to the more specific one-degree-of-freedom motion that we treat in the following chapters. The purpose here is to give a general perspective to the specific derivations that we perform in later chapters. In the third section, we include some concepts from static stability that are widely used in naval architecture and have influenced codes and design regulation to the present time. Finally, in the last section we append a brief note on nonlinear damping.

5.1 Equations of motion : Newtonian approach

Figure 5.1 shows the body axes that we use throughout and the principal plane of symmetry of the ship. The body axes $\{\bar{x}, \bar{y}, \bar{z}\}$ coincide with the principal axes of inertia at the origin O. A right-handed, orthogonal set of fixed axes $\{\bar{x}_0, \bar{y}_0, \bar{z}_0\}$ coincides with body axes at equilibrium. The angles of rotation between the body axes and the fixed axes are defined by Euler angles : θ, the angle of trim (or pitch) is measured between $O\bar{x}$ and the horizontal plane $\bar{x}_0\bar{y}_0$; ψ, the angle of yaw is measured from the vertical plane $\bar{z}_0\bar{x}_0$ to the vertical plane $\bar{z}_0\bar{x}$; ϕ, the angle of roll is measured from the vertical plane $\bar{x}\bar{z}_0$ to the principal plane of symmetry $\bar{x}\bar{z}$. The two coordinate systems are related by the coordinate transformation representing the rotation sequence $R_\phi R_\theta R_\psi$:

$$\begin{bmatrix} x_0 \\ y_0 \\ z_0 \end{bmatrix} = \begin{bmatrix} c\theta c\psi & -c\phi s\psi + s\theta s\phi c\psi & s\phi s\psi + s\theta c\phi c\psi \\ c\theta s\psi & c\phi c\psi + s\theta s\phi s\psi & -s\phi c\psi + s\theta c\phi s\psi \\ -s\theta & c\theta s\phi & c\theta c\phi \end{bmatrix} \begin{bmatrix} x \\ y \\ z \end{bmatrix} \tag{5.1}$$

where c and s stand for the sine and cosine functions. Let p (roll), q (pitch), and r (yaw) be the components of the angular velocity vector relative to the body axes $\{\bar{x}, \bar{y}, \bar{z}\}$, and let u, v, and w be the corresponding components of the linear velocity of O relative to the fluid. The angular velocities are related to the derivatives of the Euler angles by the transformation

$$\begin{bmatrix} p \\ q \\ r \end{bmatrix} = \begin{bmatrix} 1 & 0 & -\sin\theta \\ 0 & \cos\phi & \cos\theta\sin\phi \\ 0 & -\sin\phi & \cos\theta\cos\phi \end{bmatrix} \begin{bmatrix} \dot{\phi} \\ \dot{\theta} \\ \dot{\psi} \end{bmatrix} \tag{5.2}$$

The rotational motion around the center of mass is governed by Euler's equations of motion while the translational motion is governed by the standard form of Newton's second law for a rotating reference frame. Together, they give the equations of motion for the six degree-of-freedom problem in the form

$$\begin{aligned} I_x\dot{p} + (I_z - I_y)pr &= \overline{K} \\ I_y\dot{q} + (I_x - I_z)rp &= \overline{M} \\ I_z\dot{r} + (I_y - I_x)pq &= \overline{N} \\ m(\dot{u} + wq - vr) &= \overline{X} \\ m(\dot{v} + ur - wp) &= \overline{Y} \\ m(\dot{w} + vp - uq) &= \overline{Z} \end{aligned} \tag{5.3}$$

where $\overline{K}$, $\overline{M}$, $\overline{N}$, $\overline{X}, \overline{Y}$, and $qq\overline{Z}$ are the resultant hydrodynamic and external moments and forces acting on the center of mass. Our analysis is oriented to the prediction of capsizing, and previous works by Paulling and Rosenberg [24] and Nayfeh, Mook, and Marshal [25] have shown the importance of nonlinear coupling, particularly between heave - roll and pitch

- roll motions. Thus, we follow Blocki [72] and assume the following orders of magnitude for the amplitudes of oscillation :

heave $z = O(\varepsilon)$

roll $\phi = O(1)$

pitch $\theta = O(\varepsilon)$

surge $x = O(\varepsilon^2)$

sway $y = O(\varepsilon^2)$

yaw $\psi = O(\varepsilon^2)$

Therefore, x, y, and ψ, their velocities, and accelerations can be assumed to be negligible, so that (5.3) become

$$\begin{aligned} p &= \dot{\phi} \\ q &= \dot{\theta} \cos \phi \end{aligned} \tag{5.4}$$

and the equations of motion for heave, roll, and pitch become

$$\begin{aligned} & m\dot{w} = \overline{Z} \\ & I_x\ddot{\phi} - (I_z - I_y)\dot{\theta}^2 \cos \phi \sin \phi = \overline{K} \\ & I_y(\dot{\theta} \cos \phi - \dot{\theta}\dot{\phi} \sin \phi) - (I_x - I_z)\dot{\phi}\dot{\theta} \sin \phi = \overline{M} \end{aligned} \tag{5.5}$$

We assume that the force $\bar{Z}$ and the moments $\bar{K}$ and $\bar{M}$ are analytic functions of z, ϕ, and θ and their derivatives in the form

$$\begin{aligned}\bar{Z} &= Z(q_1, \dots, q_9) + Z(t)\\ \bar{K} &= K(q_1, \dots, q_9) + K(t)\\ \bar{M} &= M(q_1, \dots, q_9) + M(t)\end{aligned} \tag{5.6}$$

where q_i, $i = 1, 2, 3$, are the displacements $\{z, \phi, \theta\}$, and similarly for $i = 4, 5, 6$ and $i = 7, 8, 9$ we have the corresponding velocities and accelerations. In the neighborhood of the initial flotation position, we can expand these functions in Taylor series of the form

$$\begin{aligned}Z &= Z_0 + \frac{\partial Z}{\partial q_i} q_i + \frac{1}{2}\frac{\partial^2 Z}{\partial q_i \partial_j} q_i q_j + \cdots\\ K &= K_0 + \frac{\partial K}{\partial q_i} q_i + \frac{1}{2}\frac{\partial^2 K}{\partial q_i \partial_j} q_i q_j + \cdots\\ M &= M_0 + \frac{\partial M}{\partial q_i} q_i + \frac{1}{2}\frac{\partial^2 M}{\partial q_i \partial_j} q_i q_j + \cdots\end{aligned} \tag{5.7}$$

From physical considerations about the coupling among displacements, velocity, and accelerations Blocki [72] assumed the functional form

$$\begin{aligned}Z &= Z_1(q_1, q_2, q_3) + Z_2(q_4, q_5, q_6) + Z_3(q_7, q_8, q_9)\\ K &= K_1(q_1, q_2, q_3) + K_2(q_4, q_5, q_6) + K_3(q_7, q_8, q_9)\\ M &= M_1(q_1, q_2, q_3) + M_2(q_4, q_5, q_6) + M_3(q_7, q_8, q_9)\end{aligned} \tag{5.8}$$

which specifically eliminates cross coupling among displacements, velocities, and accelerations. After expanding Z, K, and M in Taylor series, the physical significance of the coefficients must be established, as well as some means to compute them.

In this work, we additionally assume that the pitch motion does not occur or its magnitude is negligible. This further simplifies the equations that we use to account for the nonlinearities in the roll mode and the coupling from heave, which is assumed to be described by a linear equation (nonlinear terms dropped out). The Taylor-series expansion for K contains polynomial approximations of the righting arm (from K_1) and the damping moment (from K_2). Both of these functions must be odd from symmetry considerations. The terms in K_3 contain what are known as the added masses and moments of inertia which take into account the inertia of the mass of water near the hull. After neglecting higher order terms in (5.5), we reduce the remaining equations to

$$\begin{aligned} &\dot{z} + 2\mu_z\dot{z} + \omega_z^2 z = Z(t) \\ &\dot{\phi} + (2\mu_\phi + \mu_3\dot{\phi}^2 + \cdots)\dot{\phi} + \omega_\phi^2(1 + \alpha_3\phi^2 + \alpha_5\phi^4 + \cdots)\phi - K_{\phi z}\phi z = K(t) \end{aligned} \tag{5.9}$$

The functions $Z(t)$ and $K(t)$ are usually assumed to be harmonic functions representing the wave amplitude and the waveslope respectively, and $K_{\phi z}$ represents the coefficient $\frac{\partial^2 K}{\partial\phi\partial z}$, which can be associated [72] with geometrical properties of the hull giving rise to a coupling between heave and roll.

5.2 Equations of motion : Variational approach

Nayfeh, Mook and Marshal [73] have shown that in some cases the Newtonian approach based on the use of Taylor-series expansions of the forces and moments can lead to equations that sustain self-oscillatory behavior which is unrealistic. They have proposed a more general alternative approach to derive the equations of motion. This method considers the ship and water as a single dynamical system and uses a Lagrangian formulation that starts from properly assumed expressions for the kinetic, potential, and dissipation energies.

In this case there is no need to assume that the body axes are aligned in the direction of the principal axes of inertia. We still consider the principal plane of symmetry as well as the Euler angles that describe the motion to be the same. The state of the system is described by the vector $\eta = \{x, y, z, \phi, \theta, \psi\}^T$. The velocities are better expressed in terms of their components referred to the body axes $\Pi = \{u, v, w, p, q, r\}^T$, where η and Π are related by

$$\{\Pi\} = [\alpha]\{\dot{\eta}\} \tag{5.10}$$

$$[\alpha]=\begin{bmatrix} c\psi c\theta & s\psi c\theta & -s\theta & 0 & 0 & 0 \\ -s\psi c\phi + c\psi s\theta s\phi & c\psi c\phi + s\psi s\theta s\phi & c\theta s\phi & 0 & 0 & 0 \\ s\psi s\phi + c\psi s\theta c\phi & -c\psi s\phi + s\psi s\theta c\phi & c\theta c\phi & 0 & 0 & 0 \\ 0 & 0 & 0 & 1 & 0 & -s\theta \\ 0 & 0 & 0 & 0 & c\phi & c\theta s\phi \\ 0 & 0 & 0 & 0 & -s\phi & c\theta c\phi \end{bmatrix} \tag{5.11}$$

The kinetic energy of the ship alone is given by

$$T=\frac{1}{2}m(u^2+v^2+w^2)+\frac{1}{2}(I_{xx}p^2+I_{yy}q^2+I_{zz}r^2)-I_{xz}pr \tag{5.12}$$

The components of Π are quasi-coordinates so that Lagrange's equation takes the special form

$$\frac{d}{dt}\{\frac{\partial T}{\partial \Pi}\}+[\Gamma]\{\frac{\partial T}{\partial \Pi}\}-[\beta]^T\{\frac{\partial T}{\partial \eta}-\frac{\partial V}{\partial \eta}\}+\{\frac{\partial D}{\partial \Pi}\}=\{Q\} \tag{5.13}$$

where $[\beta]=[\alpha]^{-1}$ and Γ is

$$[\Gamma]=\begin{bmatrix} 0 & -r & q & 0 & 0 & 0 \\ r & 0 & -p & 0 & 0 & 0 \\ -q & p & 0 & 0 & 0 & 0 \\ 0 & -w & v & 0 & -r & q \\ w & 0 & -u & r & 0 & -p \\ -v & u & 0 & -q & p & 0 \end{bmatrix} \tag{5.14}$$

The scalar D represent the damping function, the vector $\{Q\}$ represents the generalized forces and moments produced by the wave action and the control surfaces (assumed to be zero in this case).

To consider the ship and sea as a single system we must assume the functional form of the energy terms T and V and the damping function D. The requirements imposed on these functions are that T and D must be positive definite for every motion, and V must increase with every displacement from the equilibrium position. All three functions must account for the lateral symmetry of the ship. Following this variational approach we can obtain the appropriate equations of motion to the desired order of approximation.

5.3. *Static stability concepts*

To have a ship in static equilibrium in still water we need the weight of the ship to be supported by a resultant buoyancy force, which is equal in magnitude and acts in the opposite direction. The buoyancy force acts through the center of buoyancy whose position depends on the geometry of the underwater body. When the ship is heeled, the shape of this volume changes and consequently the position of the center of buoyancy changes accordingly. Figure 5.2 illustrates the situation where the center of gravity of a ship is located at G and the center of buoyancy is located at B. The buoyancy force is not along the line of action of the weight so that a couple would result with a magnitude proportional to the effective arm of the buoyancy force, which is known as the righting arm ($\overline{GZ}$). The moment produced by the buoyancy force in this case tends to bring the ship to the equilibrium position so that the righting arm is called positive. In the case of unstable equilibrium the righting arm is negative and the ship capsizes. The sign of the righting arm depends on the relative position of the center of gravity. The limiting location where the arm of the force is zero is the metacenter point M. Therefore, when the metacenter is above the center of gravity the position is stable.

For small angles the position of the metacenter remains fixed and the ship actually behaves like a pendulum hanging from the metacenter. For angles greater than approximately seven degrees the metacenter is no longer a fixed point so that the concept loses validity.

It is common to use the metacenter height ($\overline{GM}$) as an indication of the initial stability of a vessel. The larger this quantity is, the more stable the ship is to resist initial heel. For small angle of inclination, $\overline{GZ}$ is equal to $\overline{GM}\sin\phi$. Another practical relation is that for $\overline{BM}$, which can be obtained by considering the location of the buoyancy center for small angles:

$$\overline{BM} = \frac{I}{\nabla} \tag{5.15}$$

where I is the moment of inertia of the waterline plane about the longitudinal center line, of the ship and ∇ is the volume of displacement.

A way to characterize the static stability of a ship is by plotting the righting moments or righting arms for several displacements (volume of water displaced). Each of these figures is a static stability curve such as the one shown in Figure 5.3. For a specific loading condition the righting arm is given as a function of the angle of inclination. For the purpose of using these curves in dynamic analysis we approximate them with polynomials using the method of least squares. The polynomial used can be of any degree, but to reflect the symmetry for positive and negative angles, it must be an odd function.

The Intergovernmental Maritime Consultative Organization (IMCO) is in charge of issuing design regulations for ships and marine vehicles. The design specifications related to capsize have been largely based on the shape of the static stability curve and a large statistical data bank on casualties with the corresponding investigations. IMCO is aware that the current regulations are deficient, but due to the complexity of the dynamics of capsizing, more precise specifications have become impractical for wide spread use. In 1982 Bird and Morrall [74] reflected this spirit in their description of deficiencies in the existing design codes and the motivations to start the project SAFESHIP, as an major scientific effort to improve understanding of ship stability. Mathematical modeling and nonlinear analysis are very high on the list of issues related to risk assessment and understanding of capsizing in this on-going project. Toward this goal is that the applications of this work are directed.

5.4 Nonlinear damping in rolling

A ship that oscillates is subject to resistance from both air and water. In the absence of strong winds the resistance comes primarily from the interaction between the hull and the water. Three different mechanisms are usually associated with energy dissipation between the hull and the water : frictional forces within the boundary layer, generation of propagating waves on the surface of the water, and formation of eddies or vortices in the wake. Cardo et al. [75] have compared different mathematical models with experimental results and shown the complexities involved in fitting experimental data with some predefined analytical function. In general nonlinear damping in rolling has been modeled in the following forms :

$$\begin{aligned} D(\phi, \dot{\phi}) &= d_1\dot{\phi} + d_2 \mid \phi \mid \dot{\phi} + d_3 \mid \dot{\phi} \mid \dot{\phi} \\ D(\phi, \dot{\phi}) &= d_1\dot{\phi} + d_2\phi^2\dot{\phi} + d_3\dot{\phi}^3 \\ D(\dot{\phi}) &= d_1\dot{\phi} + d_2 \mid \dot{\phi} \mid \dot{\phi} \\ D(\dot{\phi}) &= d_1\dot{\phi} + d_2\dot{\phi}^3 \end{aligned} \tag{5.16}$$

We have selected the last model because it has been shown to be reasonably good [76] and the coefficients were available [77]. Additionally, it is convenient for analytical treatment.

Chapter 6

STABILITY AND COMPLICATED ROLLING RESPONSES OF SHIPS IN BEAM SEAS

6.1. Introduction

Nonlinear roll motion has long been recognized as a key factor in the study of capsizing of vessels in a seaway [78]. Nevertheless, the complicated nature of the dynamics has precluded this factor from being incorporated into safety codes and design regulations to protect life at sea [79]. A good deal of understanding has been gained from rather simple mathematical models that seem to capture the essential aspects of the dynamics [80]. Unfortunately, the nonlinear nature of the resulting differential equations that govern the motion has impaired the finding of exact closed-form solutions. However, approximate analytical and numerical solutions have been found that closely describe the physical phenomena [77].

The nonlinear roll response of a ship in beam seas has been successfully approximated using perturbation techniques and digital- and analog-computer simulations [e.g.,14,15,77,81]. The maximum rolling amplitude can then be obtained as a function of the characteristic parameters of the craft and the sea conditions. The approximate solutions determined by using, for example, the method of multiple scales [4,5] can account not only for the primary resonance (i.e., the encounter frequency is near the linear natural frequency of the system), but also for other nonlinear resonances of the system [82], such as subharmonic and superharmonic resonances.

Complicated behaviors not found in the linear predictions [83] have been observed when modeling nonlinear rolling through digital- and analog-computer simulations. As early as 1975 Wellicome [80] reported results of analog-computer simulations of a ship displaying what he described as a gap in the frequency response where "the analogue computer response shows no steady state response". This coincides with what four years later Huberman and Crutchfield [8] presented as one of the first observations of chaotic responses in physical systems. More recently, a variety of exotic phenomena has been shown to appear [e.g., 14,15,83,84] in the response of biased and unbiased ships in regular seas. This includes multistability of solutions; period-doubling, symmetry-breaking, and saddle-node bifurcations;

hysteretic loops; chaotic responses; fractal boundaries in the domains of attraction; and capsizing. The importance of these behaviors is that in many instances they provide information about qualitative changes in the solutions leading to catastrophic instabilities. Therefore, the naval architect must be able to recognize such phenomena and use the predicting tools through the design stages to insure the seaworthiness and safety of the vessel.

Our aim is to show that through the use of analytical tools a great deal of information on the seaworthiness and the intact stability of a vessel can be obtained. We expand on the work of Nayfeh and Khdeir [14,15] and apply Floquet theory and elementary concepts of bifurcation theory in the analysis of the stability of approximate solutions obtained by perturbation methods in the neighborhoods of the nonlinear resonances of the system. Although many of these concepts have been previously considered [e.g., 85-87], we concentrate on the analysis of qualitative changes of the solutions as some parameters are varied, more along the lines set by Guckenheimer and Holmes [36].

To illustrate the procedure, we consider in Sections 6.2 to 6.4 the rolling motion of unbiased and biased ships in regular beam seas. We present second-order perturbation solutions for the relative roll angle, and then we investigate the stability of these solutions for a broad portion of a parameter space composed of the waveslope and encounter frequency. The analytical predictions are verified by using digital- and analog-computer simulations to assess the effectiveness of the prediction technique. In Section 6.5, we present additional results from analog-computer simulations illustrating the effects of damping on the stability and seaworthiness of ships.

6.2. *Nonlinear Rolling in Beam Seas*

We follow Wright and Marshfield [77] and derive the equation of motion as a function of the relative motion of ship and wave. We let ϕ be the absolute roll angle and θ be the relative roll angle with respect to the local waveslope α. Applying Newton's second law, we find that the equation of motion can be written as

$$(I + \delta I)\ddot{\theta} + D(\dot{\theta}) + K(\theta) = B - I\ddot{\alpha} \tag{6.1a}$$

$$\theta = \phi - \alpha \tag{6.1b}$$

where I is the roll moment of inertia, δI is the added moment of inertia, which is assumed to be constant [77], and B is a constant bias moment, which might be due to a steady wind, or a shift in cargo, or water or ice on deck. The righting moment (restoring moment) K(θ) is approximated by an odd polynomial of the form

$$K(\theta) = \omega_0^2\theta + \alpha_3\theta^3 + \alpha_5\theta^5 + \cdots \tag{6.2}$$

The damping moment $D(\dot{\theta})$ is expressed as

$$D(\dot{\theta}) = 2\mu\dot{\theta} + \mu_3\dot{\theta}^3 \tag{6.3}$$

Assuming that the wavelength is large compared with the ship beam, we can write the waveslope of a regular beam sea as a harmonic function $\alpha = \alpha_m \cos \Omega t$, where α_m is the maximum waveslope. Using (6.1b)-(6.3), we rewrite (6.1a) as

$$\ddot{\theta} + 2\mu\dot{\theta} + \mu_3\dot{\theta}^3 + \omega_0^2\theta + \alpha_3\theta^3 + \alpha_5\theta^5 = \omega_0^2\theta_s + \alpha_3\theta_s^3 + \alpha_5\theta_s^5 + f\ \cos \Omega t \tag{6.4}$$

where θ_s is the still water bias angle and

$$(I + \delta I)f = I\alpha_m\Omega^2 \tag{6.5}$$

Nayfeh and Khdeir [14,15] demonstrated (a) the importance of including the quintic term in the polynomial fitting of the righting-arm curve and (b) the accuracy gain obtained when an approximate perturbation solution is carried out to second order. Equation (6.4) has been shown to display complicated behaviors [e.g.,14,15,83,84] for a variety of parameter values. These behaviors include competing attractors, period-multiplying bifurcations, chaotic motions, and sensitivity of response to initial conditions.

We used the physical characteristics of the low-freeboard model of Wright and Marshfield [77], listed in Table 1, to illustrate the resulting complicated dynamics and the effectiveness of the analytical prediction technique. The coefficients α_3 and α_5 shown in Table 1 were obtained by fitting the righting-arm curve with the polynomial in (6.2) by the method of least squares and then multiplying the result by the appropriate constant to obtain the righting moment. Figure 6.1 shows the potential function corresponding to the conservative part of (6.4) for this ship model when $\theta_s = 0$. It is evident that for some initial conditions the response becomes large and the ship will capsize. Furthermore, it is possible for a stable bounded oscillatory solution of (6.4) to become large when a parameter is slightly changed. We are particularly interested in this case due to the catastrophic implications that this event carries.

6.3. *Unbiased ship*

In this case the bias angle θ_s in (6.4) is equal to zero. The response in the neighborhood of the primary resonance $(\Omega^2 = \omega_0^2 + \varepsilon\sigma)$ can be found by recasting (6.4) as

$$\ddot{\theta} + \Omega^2\theta + \varepsilon[2\mu\dot{\theta} + \mu_3\dot{\theta}^3 + \alpha_3\theta^3 + \alpha_5\theta^5 - \sigma\theta] = \varepsilon f \cos \Omega t \tag{6.6}$$

where ε represents a bookkeeping parameter that can be later set equal to unity. A second-order approximate solution for this differential equation is given in reference [14] as

$$\theta = a\cos(\Omega t+\beta)+\varepsilon\left[\left(\frac{\alpha_3}{32\Omega^2}a^3+\frac{5\alpha_5}{128\Omega^2}a^5\right)\cos(3\Omega t+3\beta)\right.$$
$$\left.+\frac{\alpha_5}{384\Omega^2}a^5\cos(5\Omega t+5\beta)+\frac{\mu_3\Omega}{32}a^3\sin(3\Omega t+3\beta)\right]+O(\varepsilon^2) \tag{6.7}$$

where a and β are determined from

$$\dot{a} = \varepsilon\left(-\frac{f}{2\Omega}\sin\beta-\mu a-\frac{3}{8}\mu_3\Omega^2a^3\right)+\varepsilon^2\Bigg]\left(\frac{3}{8}\sigma\mu_3+\frac{3\mu\alpha_3}{8\Omega^2}\right)a^3$$
$$+\left(\frac{5\mu\alpha_5}{8\Omega^2}-\frac{3}{32}\alpha_3\mu_3\right)a^5+\frac{15\mu_3\alpha_5}{256}a^7 \tag{6.8}$$
$$\left.+\left(\frac{9f\alpha_3}{32\Omega^3}a^2+\frac{25f\alpha_5}{64\Omega^3}a^4-\frac{f\sigma}{8\Omega^3}\right)\sin\beta+\left(\frac{f\mu}{4\Omega^2}+\frac{15}{32}\mu_3fa^2\right)\cos\beta\right]$$

$$a\dot{\beta} = \varepsilon\left(-\frac{\sigma}{2\Omega}a+\frac{3\alpha_3}{8\Omega}a^3+\frac{5\alpha_5}{16\Omega}a^5-\frac{f}{2\Omega}\cos\beta\right)+\varepsilon^2\left[-\left(\frac{\sigma^2}{8\Omega^3}+\frac{\mu^2}{2\Omega}\right)a\right.$$
$$+\frac{3\sigma\alpha_3}{16\Omega^3}a^3+\left(\frac{5\alpha_5\sigma}{32\Omega^3}+\frac{9\mu_3^2\Omega^3}{256}-\frac{15\alpha_3^2}{256\Omega^3}\right)a^5-\frac{5\alpha_3\alpha_5}{64\Omega^3}a^7$$
$$-\frac{55\alpha_5^2}{3072\Omega^3}a^9+\left(\frac{3}{32}\mu_3fa^2-\frac{f\mu}{4\Omega^2}\right)\sin\beta \tag{6.9}$$
$$\left.+\left(\frac{3f\alpha_3}{32\Omega^3}a^2+\frac{5f\alpha_5}{64\Omega^3}a^4-\frac{f\sigma}{8\Omega^3}\right)\cos\beta\right]$$

For steady-state periodic responses $a = 0$ and $\beta = 0$ so that (6.8) and (6.9) become a set of algebraic equations that can be solved numerically to determine a and β.

Figure 6.2 shows a typical frequency-response curve for the ship whose coefficients are shown in Table 1 and a sea characterized by $\alpha_m = 0.2$. The circles show the results of direct numerical integration of (6.4). The dashed curve represents an unstable portion of the solution. In spite of the fact that μ, μ_3, α_3, α_5, and f are not relatively small compared with unity, the agreement between the analytical and numerical solutions is remarkable.

To ascertain the stability of the motion predicted by the approximate solution (6.7), we examine the time evolution of the periodic motion after the application of an arbitrary infinitesimal disturbance ξ(t) in the form

$$\tilde{\theta}(t) = \theta(t) + \xi(t) \tag{6.10}$$

The stability of θ(t) depends on whether ξ(t) grows or decays as $t \rightarrow \infty$. Substituting $\tilde{\theta}(t)$ into (6.4), setting $\theta_s = 0$, and keeping only linear terms in ξ(t), we obtain

$$\ddot{\xi} + (2\mu + 3\mu_3\dot{\theta}^2)\dot{\xi} + [\omega_0^2 + 3\alpha_3\theta^2 + 5\alpha_5\theta^4]\xi = 0 \tag{6.11}$$

which is a linear ordinary-differential equation with periodic coefficients. From expression (6.7), we observe that $\theta(t + T) = \theta(t)$ and $\theta(t + \frac{1}{2}T) = -\theta(t)$, where $T = \frac{2\pi}{\Omega}$, and hence the coefficients of (6.11) are periodic with the period $\frac{1}{2}T$. Therefore, it follows from Floquet theory [6] that (6.11) has solutions of the form

$$\xi(t + \frac{1}{2}T) = \lambda\xi(t) \tag{6.12}$$

where λ is an eigenvalue of the monodromy matrix C associated with a fundamental-matrix solution Φ(t) of (6.11) through the relation

$$\Phi(t + \frac{1}{2}T) = \Phi(t)C \tag{6.13}$$

The solution is then stable provided that ξ(t) does not grow with t. This requires that $|\lambda| < 1$. Thus, the eigenvalues of C must remain inside the unit circle in the complex plane for the solution given by (6.7) to be asymptotically stable.

For the dissipative one-degree-of-freedom system described by (6.4), there are two ways in which λ can leave the unit circle, which create independent patterns of instability in the T-periodic solution. An eigenvalue can leave the unit circle through the real axis at -1 , originating a tangent instability (see Chapter 3). A second way to exit the unit circle is through the real axis at $+1$, originating a pitchfork instability, which results in a symmetry-breaking bifurcation. The above patterns of instability allow us to predict the stability of the T-periodic solution (6.7) when the maximum waveslope α_m or the encounter frequency Ω is being changed. Therefore, the dynamic behavior of the ship under a wide variety of conditions can be determined.

The stability characteristics of a solution are determined by the eigenvalues of C, which in turn can be found by choosing a fundamental-matrix solution with the initial conditions $\Phi(0) = I$, where I is the identity matrix, so that (6.13) becomes

$$C = \Phi(\frac{1}{2}T) \tag{6.14}$$

The matrix Φ can be computed numerically by integrating (6.11) in the interval $[0, \frac{1}{2}T]$ subject to the two sets of initial conditions: (a) $\xi(0) = 1.0$ and $\dot{\xi}(0) = 0$ and (b) $\xi(0) = 0$ and $\dot{\xi}(0) = 1.0$ for each set of parameters (f, Ω) . We evaluate the periodic coefficients in (6.11) that depend on $\theta(t)$ and $\dot{\theta}(t)$ by using the approximate solution (6.7).

To apply this method to the frequency-response curve in Figure 6.2, we latch onto the upper-branch solution and slowly decrease Ω, computing the eigenvalues at each step to determine the stability. At location 1, we encounter a tangent instability. Similarly, if we latch onto the lower branch and slowly increase Ω, we encounter another tangent instability at location 2. In this case the presence of these instabilities only confirms the well known fact that the solutions at these points in the lower and upper branches lose stability and a jump to the stable branch is observed. By repeating this analysis in an iterative fashion for a large number of solutions with different values of the parameters α_m and Ω, we generated Figure 6.3, which shows the locus of the instability points in the (α_m, Ω) plane. In this case there are three attractors (long-term steady-state solutions which are qualitatively different): two shown in inserts (a) and (b) correspond to the lower and upper branches of the response curve and the third corresponds to a very large amplitude response. Because we are interested only in transitions occurring from the former two attractors, we assume that the initial conditions are set appropriately to reach any of the first two attractors, and then we change one of the parameters until an instability is observed. The two curves shown in Figure 6.3 represent tangent instabilities and there are transitions only between the upper and lower branches. Therefore, these curves can be interpreted as signaling a jump up (curve U) and a jump down (curve D). The direction in which the instabilities are active is indicated with arrow and the parameter space can be considered to be divided into the two regions A and B. In region A the large attractor in insert (a) (upper branch) is obtained, given the proper initial conditions, and we observe a jump to the smaller attractor in insert (b) (lower branch) when the parameters are varied to cross curve D. In region B the lower attractor is obtained (with suitable initial conditions) and we observe a jump to the larger attractor when the parameters are changed across curve U. For parameter values falling between curves U and D (where A and B overlap), it is possible to obtain either attractor depending on the prescribed initial conditions. At very low values of α_m the two attractors merge (no resonant branch) and no instability is observed as Ω is changed.

The black circles in Figure 6.3 show the results from direct numerical integration of (6.4). Although good agreement is obtained, we find an increasing degree of difficulty in latching onto one of the bounded attractors as α_m is increased. Figure 6.4 illustrates the dependence of the solution on the initial conditions and the importance of their proper selection. The white and black regions correspond to the domains of attraction of bounded and large-amplitude motions, respectively, as found by integrating (6.4) for a grid of 500x500 initial conditions when $\Omega = 0.7$ and $\alpha_m = 0.2$. The domain of bounded motions decreases as α_m is increased.

As a means to verify the behaviors predicted above, we used an analog computer to model the system described by (6.4). In spite of its moderate accuracy, this type of simulation provides insight into the behavior of the physical system that is being modeled and facilitates the study of parameter variations and bifurcations. Figure 6.5 shows the results of the analog-computer simulations obtained by using a system equipped with a very accurate electronic wave generator, a frequency analyzer (FFT), and oscilloscopes. These results are in complete agreement with those in Figure 6.3.

6.4. Biased Ship

In this case θ_s is in general nonzero. Nayfeh and Khdeir [15] used the transformation

$$\theta = \theta_s + u \tag{6.15}$$

to transform (6.4) into

$$\ddot{u} + 2\mu\dot{u} + \mu_3\dot{u}^3 + \omega_0^2 u + b_1 u + b_2 u^2 + b_3 u^3 + b_4 u^4 + b_5 u^5 = f \cos \Omega t \tag{6.16}$$

where

$$\begin{array}{lll} b_1 = 3\alpha_3\theta_s^2 + 5\alpha_5\theta_s^4 \quad , & b_2 = 3\alpha_3\theta_s + 10\alpha_5\theta_s^3 \quad , & b_3 = \alpha_3 + 10\alpha_5\theta_s^2 \\ b_4 = 5\alpha_5\theta_s \quad , & b_5 = \alpha_5 & \end{array}$$

By recasting (6.16) as a perturbed linear oscillator, they derived the following second-order perturbation solution valid in the neighborhood of the primary resonance of the system ($\Omega^2 = \omega_0^2 + \varepsilon\sigma$):

$$\begin{aligned} \theta = \theta_s + a\cos(\Omega t + \beta) + \varepsilon \Bigg[& -\frac{b_2}{2\Omega^2} a^2 - \frac{3b_4}{8\Omega^2} a^4 \\ & + \left(\frac{b_2}{6\Omega^2} a^2 + \frac{b_4}{6\Omega^2} a^4 \right) \cos(2\Omega t + 2\beta) \\ & + \left(\frac{b_3}{32\Omega^2} a^3 + \frac{5b_5}{128\Omega^2} a^5 \right) \cos(3\Omega t + 3\beta) + \frac{\mu_3 \Omega}{32} a^3 \sin(3\Omega t + 3\beta) \\ & + \frac{b_4}{120\Omega^2} a^4 \cos(4\Omega t + 4\beta) + \frac{b_5}{384\Omega^2} a^5 \cos(5\Omega t + 5\beta) \Bigg] + O(\varepsilon^2) \end{aligned} \tag{6.17}$$

where a and β are determined from

$$\begin{aligned}\dot{a} = \varepsilon\left(-\frac{f}{2\Omega}\sin\beta - \mu a - \frac{3}{8}\mu_3\Omega^2 a^3\right) + \varepsilon^2\Bigg[&\left(\frac{3}{8}b_0\mu_3 + \frac{3\mu b_3}{8\Omega^2}\right)a^3 \\ &+ \left(\frac{5\mu b_5}{8\Omega^2} - \frac{3}{32}b_3\mu_3\right)a^5 + \frac{15\mu_3 b_5}{256}a^7 \\ &+ \left(\frac{9fb_3}{32\Omega^3}a^2 + \frac{25fb_5}{64\Omega^3}a^4 - \frac{fb_0}{8\Omega^3}\right)\sin\beta + \left(\frac{f\mu}{4\Omega^2} + \frac{15}{32}\mu_3 fa^2\right)\cos\beta\Bigg]\end{aligned} \tag{6.18}$$

$$\begin{aligned}a\dot{\beta} = \varepsilon\left(-\frac{b_0}{2\Omega}a + \frac{3b_3}{8\Omega}a^3 + \frac{5b_5}{16\Omega}a^5 - \frac{f}{2\Omega}\cos\beta\right) + \varepsilon^2\Bigg[&-\left(\frac{b_0^2}{8\Omega^3} + \frac{\mu^2}{2\Omega}\right)a \\ &+ \left(\frac{3b_0b_3}{16\Omega^3} - \frac{5b_2^2}{12\Omega^3}\right)a^3 + \left(\frac{5b_5b_0}{32\Omega^3} + \frac{9\mu_3^2\Omega^3}{256} - \frac{15b_3^2}{256\Omega^3} - \frac{7b_2b_4}{8\Omega^3}\right)a^5 \\ &- \left(\frac{5b_3b_5}{64\Omega^3} + \frac{63b_4^2}{160\Omega^3}\right)a^7 - \frac{55\alpha_5^2}{3072\Omega^3}a^9 + \left(\frac{3}{32}\mu_3 fa^2 - \frac{f\mu}{4\Omega^2}\right)\sin\beta \\ &+ \left(\frac{3fb_3}{32\Omega^3}a^2 + \frac{5fb_5}{64\Omega^3}a^4 - \frac{fb_0}{8\Omega^3}\right)\cos\beta\Bigg]\end{aligned} \tag{6.19}$$

and $b_c = \sigma - b_1$. For steady-state solutions, again we set $\dot{a} = 0$ and $\dot{\beta} = 0$ to obtain a set of algebraic equations that can be solved numerically.

Figure 6.6 shows a typical frequency-response curve for a ship with the coefficients given in Table 1, a sea with the maximum waveslope $\alpha_m = 0.2$, and a positive bias angle θ_s of 6 degrees. In this figure, again we compare the analytical results with those obtained by direct numerical integrations of (6.4). The agreement between the analytical and numerical solutions is good except near 1. We note that contrary to the unbiased case this time we observe the solution growing large at 2, and consequently the ship is expected to capsize.

To determine the stability of the approximate solution (6.17), we follow the same procedure presented in the previous section. In this case we perturb $u(t)$ with an arbitrary infinitesimal disturbance $\zeta(t)$ and observe its time evolution, which is described by the differential equation

$$\ddot{\zeta} + (2\mu + 3\mu_3\dot{u}^2)\dot{\zeta} + [\omega_0^2 + b_1 + 2b_2u + 3b_3u^2 + 4b_4u^3 + 5b_5u^4]\zeta = 0 \quad (6.20)$$

This linear ordinary-differential equation has periodic coefficients with the period $T = \frac{2\pi}{\Omega}$. Therefore, we expect solutions of the form

$$\zeta(t + T) = \lambda\zeta(t) \quad (6.21)$$

where again λ is an eigenvalue of the monodromy matrix C associated with a fundamental-matrix solution Φ through the relation

$$\Phi(t + T) = \Phi(t)C \quad (6.22)$$

In this case the matrix Φ is computed by numerically integrating (6.20) in the interval [0,T] subject to the same initial conditions used in the previous section. The coefficients in (6.20) that depend on $u(t)$ and $\dot{u}(t)$ are evaluated by using (6.15) and (6.17).

Because the period of the coefficients of (6.20) is T, the instabilities generated when λ leaves the unit circle have an interpretation that is different from that in Section 6.3. In this case as λ crosses $+1$ we observe a tangent instability, and when λ goes through -1 we observe that the period of the solution doubles; that is, a period-doubling bifurcation.

Applying the above procedure to the frequency-response curve in Figure 6.6, we again latch onto the upper branch and decrease Ω until a period-doubling bifurcation is found at location 1. On the lower branch a tangent instability is found at location 2. As in Figure 6.2 the tangent instability causes a jump to another solution, but this time for the same value of Ω there is only a very large-amplitude solution, so the ship capsizes. The period-doubling bifurcation is the first in a sequence of events that leads to chaotic motions [29]. However, this fact is only confirmed in the digital- and analog-computer simulations. Because our analysis detects only the first bifurcation, we can simply say that the system is likely to have complicated behavior in this region. The circles indicate the results from direct numerical integration. The agreement between the analytical and numerical solutions is good except near location 1 where period-doubling bifurcations and chaotic solutions occur, two phenomena that are unaccounted for in the analytical solution.

Repeating the stability analysis for a large number of solutions with different parameter values α_m and Ω, we generated Figure 6.7, which similar to Figure 6.3 shows the locus of the instabilities in the (α_m, Ω) plane. In this case, in addition to the transitions between the attractors corresponding to the upper and lower branches of the response curve, we have instabilities that take the system to a large-amplitude solution, which we associate with capsizing (region C). The curves marked T_1 and T_2 (tangent instabilities) correspond to the ones shown as U and D in Figure 6.3. In addition, we have the curve marked with a P which denotes period-doubling instabilities. The arrows show the direction in which the instabilities are active. Region A is bordered by the curves T_2 and P. In this region, given appropriate initial conditions, we have solutions that are attracted to the upper branch. In region B, given the appropriate initial conditions, we can reach the lower branch. This region is bordered by T_1, so that the two regions overlap in a portion of the space enclosed by T_1,T_2, and P, where it is possible to reach either the upper or lower branch with suitable initial conditions.

We note in Figure 6.7 that there are transitions into the large-amplitude-solution region C when the parameters are varied across P and T_1. These events are of special importance because we know the ship capsizes in this transition. Therefore, the location of this region in the parameter space (α_m, Ω) provides a criterion for the deterioration of the seaworthiness of the vessel under particular sea conditions. If the location of this dangerous region is unacceptable, the ship's design can be modified and the process is repeated with a new set of coefficients in the governing equation. Another point of importance in Figure 6.7 is the qualitative nature of the transitions into the dangerous region. We mentioned two scenarios: (a) a transition from the upper-branch attractor to a large-amplitude one via a period-doubling sequence and (b) a transition from the lower-branch attractor through a tangent instability, which is more dangerous. In the latter the ship goes from a small-periodic oscillation to capsizing without any warnings.

The black circles in Figure 6.7 show the results from direct numerical integration of (6.16). The qualitative agreement between the digital-computer simulations and the analytical predictions is very good, but as shown in the figure, the instabilities in the upper branch (P and T_2) occur at slightly different locations. This might be due to the large sensitivity of the system to approximation errors in the neighborhoods of these instabilities. The sensitivity to initial conditions again complicates mapping of the instability regions. Figure 6.8 shows the shape and changes in the domains of attraction of oscillatory and unbounded solutions (white and black respectively) for $\Omega = 1.0$ when (a) $\alpha_m = 0.15$ and (b) $\alpha_m = 0.18$. They were obtained from numerical integration by using a grid of 500x500 initial conditions. In this case the changes in the domains of attraction are very drastic. We observe the boundaries of the domains losing their smoothness and possibly becoming fractal [63].

Figure 6.9 shows a summary of the analog-computer simulations for the biased model. We can identify the bifurcation curves T_1 , T_2, and P predicted by the stability analysis and shown in Figure 6.7. However, the analog-computer simulations show not only the first instability but a complete picture of the events taking place. We observe a new bifurcation curve marked E that runs close to P. Between these two curves, a sequence of period-doubling bifurcations takes place leading the system into chaotic motion, characterized by a broad-band frequency content in the power spectra (from the FFT analyzer). Figure 6.10 shows one of such sequences for $\Omega = 0.944$: (a) shows the asymmetric attractor for $\alpha_m = 0.197$, (b) a 2T-periodic attractor for $\alpha_m = 0.199$, (c) a 4T-periodic attractor for $\alpha_m = 0.213$, (d) an 8T-periodic attractor for $\alpha_m = 0.214$, and (e) and (f) show chaotic attractors for α_m 0.215 and 0.216. The corresponding power spectra of the solutions (a)-(f) in Figure 6.10 are shown in Figure 6.11, including (g), the power spectrum of the wave. Once the parameters are varied across curve E, the chaotic response becomes unstable and the system goes to another attractor, which in this case could be either the lower-branch response or the large-amplitude solution, depending on the portion of the parameter space where the crossing occurs and the state of the system at that point (location in the domains of attraction). For this system we note that if E or T_1 are crossed into the dotted region C of Figure 6.9, the ship capsizes. Additionally, if E is crossed into region B to the right of point I_2 or T_1 is crossed into A to the left of point I_1 the ship also capsizes. These points truly mark the dangerous region of the curves, in which subtle changes in the parameters can cause catastrophic consequences.

We can directly relate the appearance of the above complicated behavior in the upper-branch attractor to the early observations of Wellicome [80] and the phenomena that at the time were not understood and in many instances were considered to be due to errors introduced during the process of simulation.

6.5. Effect of Damping

The damping moment in (6.4) has a linear and a cubic term in the velocity. To investigate the influence of the coefficients μ and μ_3 on the dynamics of the ship, we performed analog-computer simulations by halving each time the value of the linear, nonlinear, or both damping coefficients, and comparing the resulting responses with those obtained for the original damping coefficients given in Table 1. Figure 6.12 shows the results for the unbiased ship and Figure 6.13 shows the results for the biased ship: (a) shows the cases with the original damping coefficients, (b) shows the results when the linear damping coefficient is halved, (c) shows the results when the cubic damping coefficient is halved, and (d) shows the results when both coefficients are halved.

The sequence (a)-(d) of Figure 6.12 shows the changes in the instability regions of the solutions of (6.4) for the unbiased case due to the variations in the damping coefficients. The first observation is that the location of the tangent instability T_1 of the lower-branch is almost insensitive to variations in damping. Therefore, no matter how crude our estimate of the damping coefficients is, the approximation of this instability would be good. This fact has been verified by digital-computer simulations. A second observation is that the instability curves for the higher-branch move down in the diagram as the damping coefficients decrease to the point that capsizing becomes possible in cases (b)-(d). The locations of the points I_1 and I_2 also move down, and apparently the nonlinear damping coefficient has a greater influence on this aspect. In cases (c) and (d), we can begin to see the instability curves P and E do not exist in (a): they show the presence of the period-doubling and chaotic phenomena.

Figure 6.13 (a)-(d) shows the corresponding variation of the instability regions when $\theta_s = 6$ degrees and the damping coefficients are sequentially halved as before. The observations for the unbiased case are also valid this time. The instability curves for the higher-branch attractor rotate down (see trend in figure) and T_1 remains in the same location as pointed out in the unbiased case.

This simple analysis shows the important role played by the damping in the stability and seaworthiness of ships. Lowering the damping coefficients shifts the instability curves for the higher-branch attractor down and makes the ship capsize at lower waveslopes. However, the instability of the lower-branch attractor remains unaffected. Moreover, lowering the damping coefficients increases the likelihood of complicated responses and hence deteriorates the seaworthiness of the vessel.

The domains of attraction are also severely affected by changes in the damping coefficients. Figure 6.14 shows the domains of attraction for the unbiased ship when $\Omega=0.7$ and $\alpha_m=0.2$ and the damping coefficients are one-half the values given in Table 1. Comparing these results with those in Figure 6.4, we see that the domains have become entangled and the boundaries are no longer smooth. This effect greatly increases the sensitivity to initial conditions and the possibility of capsizing.

Chapter 7

NONLINEAR ROLLING MOTIONS OF SHIPS IN LONGITUDINAL WAVES

7.1. Introduction

Since the early observations of Froude [20] on the undesirable seakeeping characteristics of a ship whose natural frequency in heave is twice its natural frequency in roll, the possibility of exciting large-amplitude oscillations and even capsizing a ship in longitudinal regular waves began to be recognized. The work of Grim [22] and Kerwin [23] showed that the periodic encounter of a ship with a wave result in a time-varying restoring moment and the roll motion is described by a Mathieu equation. The resonances of this equation reveal the unstable regions and the dangerous frequencies of encounter obtained for small roll angles, where linear approximations are valid. Paulling and Rosenberg [24] showed that the underlying mechanism for energy transfer from the longitudinal wave to the transverse rolling motion is a nonlinear coupling between the modes. Particularly, coupling between either the heave and roll modes or the pitch and roll modes was shown to generate time-varying coefficients in the roll equation of a ship in longitudinal waves, which takes the form of the Mathieu equation. More recently, a number of studies [69,72,78,80,88] on the roll equation with a parametric excitation (i.e., with time-varying coefficients) included nonlinear terms because large-amplitude oscillations and capsizing cannot be modeled by linearized equations.

As presented in Chapter 6, we had success in predicting the stability and complicated nonlinear rolling motion of a ship in beam seas. The procedure analyzes the stability of an approximate analytical solution by using Floquet theory and elementary concepts of bifurcation theory. The amplitude or frequency of the excitation was used as the bifurcation parameter. The results were summarized in a bifurcation diagram in a parameter space composed of the amplitude and frequency of excitation. This diagram clearly locates the regions of the parameter space where different responses, including capsizing, occur. All predictions were verified by using analog- and digital-computer simulations, which confirm the effectiveness of the scheme.

In this chapter, our aim is to apply the above procedure to the nonlinear response of a ship rolling in longitudinal waves (i.e., the waves crests are oriented at right angles to the vessel's centerline). We seek a qualitative understanding of the responses and their instabilities, rather than an accurate analysis of any specific case. We follow Blocki [72] and obtain the following equation for the nonlinear rolling of a ship due to heave - roll coupling :

$$\ddot{\theta} + 2\hat{\mu}\dot{\theta} + \hat{\mu}_3\dot{\theta}^3 + \omega_0^2\left[1 + \hat{\alpha}_3\theta^2 + \hat{\alpha}_5\theta^4 + h\cos(\hat{\Omega}\tau)\right]\theta = 0 \tag{7.1}$$

where τ is time, dots represent derivatives with respect to τ, and

$$h = \frac{K_{\theta z} a_z}{2\omega_0^2} \tag{7.2}$$

represents the amplitude of the parametric excitation. It depends on the magnitude of the coupling coefficient $K_{\theta z}$ and the amplitude of the heaving motion a_z. In this case the heaving motion is assumed to be harmonic with maximum amplitude a_z and encounter frequency $\hat{\Omega}$. The parametric term in (7.1) basically accounts for the time-dependent variation of the metacentric height. The coefficients $\hat{\alpha}_3$ and $\hat{\alpha}_5$ can be obtained by fitting the righting arm with a polynomial. The damping coefficients $\hat{\mu}$ and $\hat{\mu}_3$ are also obtained through the fit of experimental data. Equation (7.1) has been shown to govern the rolling motion of a ship in head or following seas [69,72,80] in the absence of heeling moments and pitch - roll coupling.

In order to make the analytical treatment more general, we introduce the time scale $t = \omega_0\tau$, which transforms (7.1) into

$$\ddot{\theta} + 2\mu\theta + \mu_3\dot{\theta}^3 + \theta + \hat{\alpha}_3\theta^3 + \hat{\alpha}_5\theta^5 + h\theta\cos(\Omega t) = 0 \tag{7.3}$$

where dots represent time derivatives with respect to t and the coefficients have been scaled appropriately. This transformation scales the natural frequency to unity, making the results easier to interpret. The traditional treatment of this problem has been to linearize (7.3) to obtain the Mathieu equation. This procedure determines conditions for the stability of the trivial solutions. Above these conditions, the roll angle grows exponentially with time, which is unrealistic. We are interested in not only identifying the regions of parameter space where trivial solutions lose their stability, but also determining what kind of motions are generated inside these regions and in characterizing the danger that these behaviors pose to the overall seaworthiness of a vessel. Furthermore, we show that some regions of very dangerous high-amplitude oscillations elude detection through the linearized procedure. In Sections 7.2 and 7.3, we develop approximate analytical solutions in the neighborhoods of the resonances of the system. In Section 7.4, we determine the stability of these solutions in the parameter space $h - \Omega$ and generate a bifurcation diagram that illustrates qualitative changes in the response. As a means to verify and complement our predictions, we present in Sections 7.5 and 7.6 the results of analog- and digital-computer simulations.

7.2. *Fundamental parametric resonance (FPR)*

An approximate analytical solution of (7.3) can be obtained by assuming that the coefficients μ, μ_3, $\hat{\alpha}_3$, $\hat{\alpha}_5$, and h are small. This smallness can be characterized by a single coefficient ε, which is used as a bookkeeping device and will be set equal to one in the final result. Thus, we rewrite (7.3) as

$$\ddot{\theta} + \theta + \varepsilon[2\mu\dot{\theta} + \mu_3\dot{\theta}^3 + \hat{\alpha}_3\theta^3 + \hat{\alpha}_5\theta^5 + h\theta\cos(\Omega t)] = 0 \qquad (7.4)$$

Carrying out a second-order straightforward expansion [4-6], we find that resonances occur when $\Omega \simeq 1, 2, 4$, and 6. The first two cases are known as the fundamental and principal parametric resonances, respectively. The first resonance is treated in this section and the second resonance is treated in Section 7.3. The method of multiple scales, as presented by Nayfeh [57], is used to determine second-order uniform solutions, which are considerably more accurate than first-order solutions. The analytical solutions are found to be in close agreement with digital-computer simulations. The other resonances were found to produce oscillation amplitudes, which are smaller than those produced by the fundamental and principal parametric resonances. Therefore, they were excluded from the frequency interval considered.

For the fundamental parametric resonant case, the proximity of Ω to unity is expressed as

$$\Omega^2 = 1 + \varepsilon\sigma_1 \tag{7.5}$$

where σ_1 is a detuning parameter. The natural frequency of the linear oscillator defined in (7.4) can be written in terms of Ω by using (7.5), resulting in the form

$$\ddot{\theta} + \Omega^2\theta = -\varepsilon[-\sigma_1\theta + 2\mu\dot{\theta} + \mu_3\dot{\theta}^3 + \hat{\alpha}_3\theta^3 + \hat{\alpha}_5\theta^5 + h\theta\cos(\Omega t)] \tag{7.6}$$

We let

$$\theta(t;\varepsilon) = \theta_0(T_0, T_1, T_2) + \varepsilon\theta_1(T_0, T_1, T_2) + \varepsilon^2\theta_2(T_0, T_1, T_2) + \ldots \tag{7.7}$$

where $T_0 = t$ is a fast scale, characterizing motions occurring at the frequency Ω, and $T_1 = \varepsilon t$ and $T_2 = \varepsilon^2 t$ are slow scales, characterizing the modulation of the amplitude and phase caused by the nonlinearity, damping, and resonances. The time derivatives become

$$\frac{d}{\mathrm{dt}} = D_0 + \varepsilon D_1 + \varepsilon^2 D_2 + \ldots \tag{7.8}$$

$$\frac{d^2}{dt^2} = D_0^2 + 2\varepsilon D_0 D_1 + \varepsilon^2(2D_0D_2 + D_1^2) + \ldots \tag{7.9}$$

where $D_n = \dfrac{\partial}{\partial T_n}$. Substituting (7.7)-(7.9) into (7.6) and equating coefficients of like powers of ε, we obtain

$$D_0^2\theta_0 + \Omega^2\theta_0 = 0 \tag{7.10}$$

$$\begin{aligned} D_0^2\theta_1 + \Omega^2\theta_1 = & -2D_0D_1\theta_0 - 2\mu D_0\theta_0 + \sigma_1\theta_0 - \mu_3(D_0\theta_0)^3 \\ & - \hat{\alpha}_3\theta_0^3 - \hat{\alpha}_5\theta_0^5 - h\theta_0\cos(\Omega T_0) \end{aligned} \tag{7.11}$$

$$\begin{aligned} D_0^2\theta_2 + \Omega^2\theta_2 = & -2D_0D_1\theta_1 - 2D_0D_2\theta_0 - D_1^2\theta_0 - 2\mu D_0\theta_1 - 2\mu D_1\theta_0 + \sigma_1\theta_1 \\ & - 3\mu_3(D_0\theta_0)^2D_0\theta_1 - 3\mu_3(D_0\theta_0)^2D_1\theta_0 - 3\hat{\alpha}_3\theta_0^2\theta_1 \\ & - 5\hat{\alpha}_5\theta_0^4\theta_1 - h\theta_1\cos(\Omega T_0) \end{aligned} \tag{7.12}$$

It is convenient to express the solution of (7.10) in the complex form

$$\theta_0(T_0, T_1, T_2) = A(T_1, T_2)e^{i\Omega T_0} + \bar{A}(T_1, T_2)e^{-i\Omega T_0} \tag{7.13}$$

where $\bar{A}$ is the complex conjugate of A, which is an arbitrary complex function of T_1 and T_2 at this level of approximation. It is determined by imposing the solvability conditions at the next levels of approximation.

Substituting (7.13) into (7.11) yields

$$\begin{aligned} D_0^2\theta_1 + \Omega^2\theta_1 = & -[2i\Omega(D_1A + \mu A) - \sigma_1 A + (3i\Omega^3\mu_3 + 3\hat{\alpha}_3)A^2\bar{A} \\ & + 10\mu_5A^3\bar{A}^2]e^{i\Omega T_0} - \frac{1}{4}h(A + \bar{A}) - \frac{1}{2}hAe^{2i\Omega T_0} \\ & + [(i\Omega^3\mu_3 - \hat{\alpha}_3)A^3 - 5\hat{\alpha}_5A^4\bar{A}]e^{3i\Omega T_0} - \hat{\alpha}_5A^5e^{5i\Omega T_0} + cc \end{aligned} \tag{7.14}$$

where cc stands for the complex conjugate of the preceding terms. Depending on the function A, the particular solutions of (7.14) may contain secular terms. The condition for the elimination of these secular terms is

$$2i\Omega(D_1A + \mu A) - \sigma_1 A + (3i\Omega^3\mu_3 + 3\hat{\alpha}_3)A^2\bar{A} + 10\mu_5 A^3\bar{A}^2 = 0 \tag{7.15}$$

Then, the particular solution of (7.14) can be written as

$$\begin{aligned}\theta_1 = & -\frac{1}{4\Omega^2}h(A+\bar{A}) + \frac{1}{6\Omega^2}hAe^{2i\Omega T_0} + \left[-\frac{1}{8\Omega^2}(i\Omega^3\mu_3 - \hat{\alpha}_3)A^3\right.\\ & \left.+\frac{5\hat{\alpha}_5}{8\Omega^2}A^4\bar{A}\right]e^{3i\Omega T_0} + \frac{\hat{\alpha}_5}{24\Omega^2}A^5e^{5i\Omega T_0} + cc\end{aligned} \tag{7.16}$$

Substituting (7.13) and (7.16) into (7.12) yields

$$\begin{aligned}D_0^2\theta_2 + \Omega^2\theta_2 = & \Big[-2i\Omega D_2A - D_1^2A - 2\mu D_1A - 6\Omega^2\mu_3A\bar{A}D_1A\\ & + 3\Omega^2\mu_3A^2D_1\bar{A} + \frac{h^2}{6\Omega^2}A + \frac{h^2}{4\Omega^2}\bar{A}\\ & + \left(\frac{9}{8}\Omega^4\mu_3^2 + \frac{3}{2}i\Omega\mu_3\hat{\alpha}_3 - \frac{3}{8\Omega^2}\hat{\alpha}_3^2\right)A^3\bar{A}^2\\ & + \left(i\frac{15}{2}\Omega\mu_3\hat{\alpha}_5 - \frac{5\hat{\alpha}_3\hat{\alpha}_5}{\Omega^2}\right)A^4\bar{A}^3 - \frac{95\hat{\alpha}_5^2}{6\Omega^2}A^5\bar{A}^4\Big]e^{i\Omega T_0} + NST + cc\end{aligned} \tag{7.17}$$

where NST stands for terms that do not produce secular terms. Eliminating secular terms from (7.17), we obtain

$$\begin{aligned}& -2i\Omega D_2A - D_1^2A - 2\mu D_1A - 6\Omega^2\mu_3A\bar{A}D_1A + 3\Omega^2\mu_3A^2D_1\bar{A}\\ & + \frac{h^2}{6\Omega^2}A + \frac{h^2}{4\Omega^2}\bar{A} + \left(\frac{9}{8}\Omega^4\mu_3^2 + \frac{3}{2}i\Omega\mu_3\hat{\alpha}_3 - \frac{3}{8\Omega^2}\hat{\alpha}_3^2\right)A^3\bar{A}^2\\ & + \left(i\frac{15}{2}\Omega\mu_3\hat{\alpha}_5 - \frac{5\hat{\alpha}_3\hat{\alpha}_5}{\Omega^2}\right)A^4\bar{A}^3 - \frac{95\hat{\alpha}_5^2}{6\Omega^2}A^5\bar{A}^4 = 0\end{aligned} \tag{7.18}$$

To solve (7.15) and (7.18), we find it convenient to combine them into a single first-order ordinary-differential equation. This procedure is usually referred to as the method of reconstitution [57] and gives

$$
\begin{aligned}
&2i\Omega\dot{A} + \varepsilon\Big[(-\sigma_1 + 2i\Omega\mu)A + (3i\Omega^3\mu_3 + 3\hat{\alpha}_3)A^2\bar{A} + 10\hat{\alpha}_5 A^3\bar{A}^2\Big] \\
&\quad + \varepsilon^2\Bigg[-\left(\frac{\sigma_1^2}{4\Omega^2} + \mu^2 + \frac{h^2}{6\Omega^2}\right)A - \frac{h^2}{4\Omega^2}\bar{A} \\
&\quad - \Bigg(i\frac{3\mu\hat{\alpha}_3}{\Omega} + i3\Omega\mu_3\sigma_1 - \frac{3\hat{\alpha}_3\sigma_1}{2\Omega^2}\Bigg)A^2\bar{A} + (-i\frac{20\mu\hat{\alpha}_5}{\Omega} + \frac{9}{8}\Omega^4\mu_3^2 \\
&\quad + 3i\Omega\mu_3\hat{\alpha}_3 - \frac{15\hat{\alpha}_3^2}{8\Omega^2} + \frac{5\hat{\alpha}_5\sigma_1}{\Omega^2})A^3\bar{A}^2 \\
&\quad - \Bigg(i\frac{15}{2}\Omega\mu_3\hat{\alpha}_5 + \frac{10\hat{\alpha}_3\hat{\alpha}_5}{\Omega^2}\Bigg)A^4\bar{A} - \frac{55\hat{\alpha}_5^2}{6\Omega^2}A^5\bar{A}^4\Bigg] = 0
\end{aligned}
\tag{7.19}
$$

Next, we express the function A in the polar form

$$
A = \frac{1}{2}ae^{i\beta} \tag{7.20}
$$

where a and β are the amplitude and phase of the fundamental component of the response. Substituting (7.20) into (7.19) and separating real and imaginary parts, we obtain

$$
\begin{aligned}
\dot{a} &= \varepsilon\Big[-\mu a - \frac{3}{8}\Omega^2\mu_3 a^3\Big] + \varepsilon^2\Bigg[-\frac{h^2}{8\Omega^3}a\sin(2\beta) + (\frac{3\mu\hat{\alpha}_3}{8\Omega^2} \\
&\quad + \frac{3\mu_3\sigma_1}{8})a^3 + \left(-\frac{3\mu_3\hat{\alpha}_3}{32} + \frac{5\mu\hat{\alpha}_5}{8\Omega^2}\right)a^5 + \frac{15\mu_3\hat{\alpha}5}{256}a^7\Bigg]
\end{aligned}
\tag{7.21}
$$

$$
\begin{aligned}
a\dot{\beta} = \varepsilon\left[-\frac{\sigma_1}{2\Omega} a + \frac{3\hat{\alpha}_3}{8\Omega} a^3 + \frac{5\hat{\alpha}_5}{16\Omega} a^5 \right] + \varepsilon^2 \Bigg[& -\Big(\frac{\mu^2}{2\Omega} + \frac{\sigma_1^2}{8\Omega^3} + \frac{h^2}{12\Omega^3} \\
& + \frac{h^2}{8\Omega^3}\cos(2\beta)\Big)a + \frac{3\hat{\alpha}_3\sigma_1}{16\Omega^3} a^3 + \left(\frac{9\Omega^3\mu_3^2}{256} - \frac{15\hat{\alpha}_3^2}{256\Omega^3} + \frac{5\hat{\alpha}_5\sigma_1}{32\Omega^3} \right) a^5 \\
& - \frac{5\hat{\alpha}_3\hat{\alpha}_5}{64\Omega^3} a^7 - \frac{55\hat{\alpha}_5^2}{3072\Omega^3} a^9 \Bigg]
\end{aligned}
\tag{7.22}
$$

Substituting (7.13), (7.16), and (7.20) into (7.7), we find that to the second-order approximation, the solution of (7.3) for the case of fundamental parametric resonance ($\Omega \simeq 1$) is

$$
\begin{aligned}
\theta_f(t) = a\cos(\Omega t + \beta) + \varepsilon \Bigg[& \frac{h}{6\Omega^2} a\cos(2\Omega t + \beta) + \frac{\Omega\mu_3}{32} a^3 \sin(3\Omega t + 3\beta) \\
& + \left(\frac{\hat{\alpha}_3}{32\Omega^2} a^3 + \frac{5\hat{\alpha}_5}{128\Omega^2} a^5 \right) \cos(3\Omega t + 3\beta) \\
& + \frac{\hat{\alpha}_5}{384\Omega^2} a^5 \cos(5\Omega t + 5\beta) - \frac{h}{2\Omega^2} a\cos(\beta) \Bigg] + \cdots
\end{aligned}
\tag{7.23}
$$

where a and β are given by (7.21) and (7.22). For steady-state periodic responses $a = 0$ and $\beta = 0$ so that (7.21) and (7.22) become a set of algebraic equations that can be solved numerically to determine a and β.

7.3. Principal parametric resonance (PPR)

In this case $\Omega \simeq 2$ and we introduce a detuning parameter σ_2 defined according to

$$\frac{1}{4}\Omega^2 = 1 + \varepsilon\sigma_2 \tag{7.24}$$

Using (7.24) to express the natural frequency of the linear oscillator defined in (7.4), we obtain

$$\ddot{\theta} + \frac{1}{4}\Omega^2\theta = -\varepsilon[-\sigma_2\theta + 2\mu\dot{\theta} + \mu_3\dot{\theta}^3 + \hat{\alpha}_3\theta^3 + \hat{\alpha}_5\theta^5 + h\theta\cos(\Omega t)] \tag{7.25}$$

Following the procedure used in the previous section, we substitute (7.7)-(7.9) into (7.25), equate coefficients of like powers of ε, and obtain

$$D_0^2\theta_0 + \frac{1}{4}\Omega^2\theta_0 = 0 \tag{7.26}$$

$$\begin{aligned} D_0^2\theta_1 + \frac{1}{4}\Omega^2\theta_1 = {} & -2D_0D_1\theta_0 - 2\mu D_0\theta_0 + \sigma_2\theta_0 \\ & - \mu_3(D_0\theta_0)^3 - \hat{\alpha}_3\theta_0^3 - \hat{\alpha}_5\theta_0^5 - h\theta_0\cos(\Omega T_0) \end{aligned} \tag{7.27}$$

$$\begin{aligned} D_0^2\theta_2 + \frac{1}{4}\Omega^2\theta_2 = {} & -2D_0D_1\theta_1 - 2D_0D_2\theta_0 - D_1^2\theta_0 - 2\mu D_0\theta_1 - 2\mu D_1\theta_0 + \sigma_2\theta_1 \\ & - 3\mu_3(D_0\theta_0)^2D_0\theta_1 - 3\mu_3(D_0\theta_0)^2D_1\theta_0 - 3\hat{\alpha}_3\theta_0^2\theta_1 \\ & - 5\hat{\alpha}_5\theta_0^4\theta_1 - h\theta_1\cos(\Omega T_0) \end{aligned} \tag{7.28}$$

The solution of (7.26) is expressed in the form

$$\theta_0(T_0, T_1, T_2) = A(T_1, T_2)e^{\frac{1}{2}i\Omega T_0} + \overline{A}(T_1, T_2)e^{-\frac{1}{2}i\Omega T_0} \tag{7.29}$$

Substituting (7.29) into (7.27) yields

$$\begin{aligned} D_0^2\theta_1 + \frac{1}{4}\Omega^2\theta_1 = & -\Big[i\Omega(D_1A + \mu A) - \sigma_2 A + \Big(i\frac{3}{8}\Omega^3\mu_3 + 3\hat{\alpha}_3\Big)A^2\overline{A} \\ & + 10\mu_5 A^3\overline{A}^2 + \frac{1}{2}h\overline{A}\Big]e^{\frac{1}{2}i\Omega T_0} \\ & + \Big[\Big(i\frac{1}{8}\Omega^3\mu_3 - \hat{\alpha}_3\Big)A^3 - 5\hat{\alpha}_5 A^4\overline{A} - \frac{1}{2}hA\Big]e^{\frac{3}{2}i\Omega T_0} \\ & - \hat{\alpha}_5 A^5 e^{\frac{5}{2}i\Omega T_0} + cc \end{aligned} \tag{7.30}$$

Eliminating the terms that produce secular terms in (7.30) yields

$$\begin{aligned} i\Omega(D_1A + \mu A) - \sigma_2 A + (i\frac{3}{8}\Omega^3\mu_3 + 3\hat{\alpha}_3)A^2\overline{A} + 10\mu_5 A^3\overline{A}^2 & \\ + \frac{1}{2}h\overline{A} = 0 & \end{aligned} \tag{7.31}$$

This leaves (7.30) with the particular solution

$$\begin{aligned} \theta_1 = & \Big[\Big(-i\frac{\Omega\mu_3}{16} + \frac{\hat{\alpha}_3}{2\Omega^2}\Big)A^3 + \frac{5\hat{\alpha}_5}{2\Omega^2}A^4\overline{A} + \frac{h}{4\Omega^2}A\Big]e^{\frac{3}{2}i\Omega T_0} \\ & + \frac{\hat{\alpha}_5}{6\Omega^2}A^5 e^{\frac{5}{2}i\Omega T_0} \end{aligned} \tag{7.32}$$

Substituting (7.29) and (7.32) into (7.28), we find that elimination of secular terms from θ_2 requires that

$$
\begin{aligned}
& i\Omega D_2 A + D_1^2 A + 2\mu D_1 A + \frac{h^2}{8\Omega^2} A + \frac{3\mu_3}{2\Omega^2} A\overline{A} D_1 A - \frac{3\Omega^2\mu_3}{4} A^2 D_1 \overline{A} \\
& + \left(\frac{3\hat{\alpha}_3 h}{4\Omega^2} - i\frac{9\Omega\mu_3 h}{32} \right) A\overline{A}^2 + \frac{5\hat{\alpha}_5 h}{\Omega^2} A^2\overline{A}^3 + \left(\frac{\hat{\alpha}_3 h}{4\Omega^2} - i\frac{\Omega\mu_3 h}{32} \right) A^3 \\
& - \left(\frac{9\Omega^4\mu_3^2}{128} + i\frac{3}{4}\Omega\mu_3\hat{\alpha}_3 - \frac{3\hat{\alpha}_3^2}{2\Omega^2} \right) A^3\overline{A}^2 \\
& + \left(\frac{20\hat{\alpha}_3\hat{\alpha}_5}{\Omega^2} - i\frac{15}{4}\Omega\mu_3\hat{\alpha}_5 \right) A^4\overline{A}^3 + \frac{5\hat{\alpha}_5 h}{2\Omega^2} A^4\overline{A} + \frac{190\hat{\alpha}_5^2}{3\Omega^2} A^5\overline{A}^4 = 0
\end{aligned}
\tag{7.33}
$$

Combining (7.31) and (7.33) in the manner mentioned in the preceding section, we obtain

$$
\begin{aligned}
& i\Omega\dot{A} + \varepsilon\left[(-\sigma_2 + i\Omega\mu)A + \frac{1}{2}h\overline{A} + \left(i\frac{3}{8}\Omega^3\mu_3 + 3\hat{\alpha}_3 \right) A^2\overline{A} + 10\hat{\alpha}_5 A^3\overline{A}^2 \right] \\
& + \varepsilon^2\left[\left(-\frac{\sigma^2}{\Omega^2} - \mu^2 + \frac{3h^2}{8\Omega^2} \right) A + \left(\frac{6\hat{\alpha}_3\sigma_2}{\Omega^2} - i\frac{3}{2}\Omega\mu_3\sigma_2 - i\frac{6\mu\hat{\alpha}_3}{\Omega} \right) A^2\overline{A} \right. \\
& - \left(i\frac{3}{32}\Omega\mu_3 h + \frac{3\hat{\alpha}_3 h}{4\Omega^2} \right) A\overline{A}^2 - \frac{5\hat{\alpha}_5 h}{\Omega^2} A^2\overline{A}^3 + \left(i\frac{17}{32}\Omega\mu_3 h + \frac{7\hat{\alpha}_3 h}{4\Omega^2} \right) A^3 \\
& + \left(\frac{9}{128}\Omega^4\mu_3^2 + i\frac{3}{2}\Omega\mu_3\hat{\alpha}_3 + \frac{20\hat{\alpha}_5\sigma_2}{\Omega^2} - \frac{15\hat{\alpha}_3^2}{2\Omega^2} - i\frac{40\mu\hat{\alpha}_5}{\Omega} \right) A^3\overline{A}^2 \\
& \left. + \frac{25\hat{\alpha}_5 h}{2\Omega^2} A^4\overline{A} + \left(-i\frac{15}{4}\Omega\mu_3\hat{\alpha}_5 - \frac{40\hat{\alpha}_3\hat{\alpha}_5}{\Omega^2} \right) A^4\overline{A}^3 - \frac{110\hat{\alpha}_5^2}{3\Omega^2} A^5\overline{A}^4 \right] = 0
\end{aligned}
\tag{7.34}
$$

Substituting (7.20) into (7.34) and separating real and imaginary parts, we have

$$
\begin{aligned}
\dot{a} = \varepsilon\Big[-\mu a - \frac{3}{32}\Omega^2\mu_3 a^3 + \frac{h}{2\Omega} a \sin(2\beta)\Big] + \varepsilon^2\Big[\Big(\frac{3\mu\hat{\alpha}_3}{2\Omega^2} + \frac{3}{8}\mu_3\sigma_2 \\
- \frac{5\hat{\alpha}_3 h}{8\Omega^3}\sin(2\beta) - \frac{7}{64}\mu_3 h \cos(2\beta)\Big) a^3 + \Big(\frac{5\mu\hat{\alpha}_5}{2\Omega^2} - \frac{3}{32}\mu_3\hat{\alpha}_3 \\
- \frac{35\hat{\alpha}_5 h}{32\Omega^3}\sin(2\beta)\Big) a^5 + \frac{15}{256}\mu_3\hat{\alpha}_5 a^7 \Big]
\end{aligned} \tag{7.35}
$$

$$
\begin{aligned}
a\dot{\beta} = \varepsilon\Big[-\frac{\sigma_2}{\Omega} a + \frac{3\hat{\alpha}_3}{4\Omega} a^3 + \frac{5\hat{\alpha}_5}{8\Omega} a^5 + \frac{h}{2\Omega} a \cos(2\beta)\Big] + \varepsilon^2\Big[-\Big(\frac{\mu^2}{\Omega} \\
+ \frac{\sigma^2}{\Omega^3} - \frac{3h^2}{8\Omega^3}\Big) a + \left(\frac{3\hat{\alpha}_3\sigma_2}{2\Omega^3} - \frac{5}{32}\mu_3 h \sin(2\beta) + \frac{\hat{\alpha}_3 h}{4\Omega^3}\cos(2\beta)\right) a^3 \\
+ \left(\frac{9}{2048}\Omega^3\mu_3^2 - \frac{15\hat{\alpha}_3^2}{32\Omega^3} + \frac{5\hat{\alpha}_5\sigma_2}{4\Omega^3} + \frac{15\hat{\alpha}_5 h}{32\Omega^3}\cos(2\beta) \right) a^5 \\
- \frac{5\hat{\alpha}_3\hat{\alpha}_5}{8\Omega^3} a^7 - \frac{55\hat{\alpha}_5^2}{384\Omega^3} a^9 \Big]
\end{aligned} \tag{7.36}
$$

Substituting (7.29), (7.32), and (7.20) into (7.7), we obtain the following approximate solution for the case of principal parametric resonance ($\Omega \simeq 2$) :

$$
\begin{aligned}
\theta_p(t) = a \cos\Big(\frac{1}{2}\Omega t + \beta\Big) + \varepsilon\Big[\frac{1}{64}\Omega\mu_3 a^3 \sin\Big(\frac{3}{2}\Omega t + 3\beta\Big) \\
+ \left(\frac{h}{4\Omega^2} a + \frac{\hat{\alpha}_3}{8\Omega^2} a^3 + \frac{5\hat{\alpha}_5}{32\Omega^2} a^5 \right) \cos\Big(\frac{3}{2}\Omega t + 3\beta\Big) \\
+ \frac{\hat{\alpha}_5}{96\Omega^2} a^5 \cos\Big(\frac{5}{2}\Omega t + 5\beta\Big) \Big] + \cdots
\end{aligned} \tag{7.37}
$$

where a and β are given by (7.35) and (7.36). In this case again, periodic responses correspond to $\dot{a} = 0$ and $\dot{\beta} = 0$ so that (7.35) and (7.36) become a set of algebraic equations that can be solved numerically to obtain a and β.

7.4. Stability analysis

7.4.1. Stability of the trivial solution near $\Omega = 1$

In the Sections 7.3 and 7.4, we developed expressions (7.23) and (7.37) to approximate the responses of the ship when Ω is near 1 and 2, respectively. Both $\theta_f\,(t)$ and $\theta_p(t)$ are functions of a and β, which in turn are described by the differential equations (7.21) and (7.22) and (7.35) and (7.36), respectively. Steady-state periodic solutions correspond to $\dot{a} = \dot{\beta} = 0$; that is, the fixed points of these equations. We note that $a = 0$ (i.e., the trivial response) is a possible solution for both sets of equations. To determine whether these solutions can be realized physically, we need to determine their stability. To this end, we analyze the behavior of the linearized differential equations (7.19) and (7.34), which determine the evolution of a.

Neglecting the nonlinear terms in (7.19), we obtain

$$2i\Omega\dot{A} + \varepsilon[(-\sigma_1 + 2i\Omega\mu)A] + \varepsilon^2\left[-\left(\frac{\sigma_1^2}{4\Omega^2} + \mu^2 + \frac{h^2}{6\Omega^2}\right)A\right] - \varepsilon^2\frac{h^2}{4\Omega^2}\bar{A} = 0 \tag{7.38}$$

A closed-form solution of (7.38) can be obtained by letting

$$A = B_r + iB_i \tag{7.39}$$

where B_r and B_i are real. Substituting (7.39) into (7.38) and separating real and imaginary parts, we have

$$2\Omega(\dot{B}_r + \varepsilon\mu)B_r + \left[-\left(\varepsilon\sigma_1 + \varepsilon^2\frac{\sigma_1^2}{4\Omega^2} + \varepsilon^2\mu^2 + \varepsilon^2\frac{h^2}{6\Omega^2}\right) + \varepsilon^2\frac{h^2}{4\Omega^2}\right]B_i = 0 \tag{7.40}$$

$$2\Omega(\dot{B}_i + \varepsilon\mu)B_i + \left[\left(\varepsilon\sigma_1 + \varepsilon^2\frac{\sigma_1^2}{4\Omega^2} + \varepsilon^2\mu^2 + \varepsilon^2\frac{h^2}{6\Omega^2}\right) + \varepsilon^2\frac{h^2}{4\Omega^2}\right]B_r = 0 \tag{7.41}$$

Equations (7.40) and (7.41) admit solutions of the form

$$(B_r, B_i) = (b_r, b_i)e^{\varepsilon\lambda t} \tag{7.42}$$

provided that

$$\lambda = -\mu \pm \sqrt{\varepsilon^2 \frac{h^4}{64\Omega^6} - \frac{1}{4\Omega^2}\left(\sigma_1 + \varepsilon \frac{\sigma_1^2}{4\Omega^2} + \varepsilon\mu^2 + \varepsilon \frac{h^2}{6\Omega^2}\right)^2} \qquad (7.43)$$

Hence, the trivial solution is stable if and only if the real part of each λ is negative or zero, and it is unstable if the real part of one of the λ's is positive. Thus, the vanishing of λ yields a curve in the h-Ω plane, which separates stable from unstable trivial solutions.

7.4.2. Stability of trivial solution near $\Omega = 2$

Linearization of (7.34) yields the following differential equation governing the stability of the null solution :

$$i\Omega\dot{A} + \varepsilon[(-\sigma_2 + i\Omega\mu)A + \frac{1}{2}h\bar{A}] + \varepsilon^2[(-\frac{\sigma_2^2}{\Omega^2} - \mu^2 + \frac{3h^2}{8\Omega^2})A] = 0 \quad (7.44)$$

Substituting (7.39) into (7.44) and separating real and imaginary parts, we obtain

$$\Omega(\dot{B}_r + \varepsilon\mu B_r) + [-(\varepsilon\sigma_2 + \varepsilon^2\frac{\sigma_2^2}{4\Omega^2} + \varepsilon^2\mu^2 - \varepsilon^2\frac{3h^2}{8\Omega^2}) - \frac{1}{2}\varepsilon h]B_i = 0 \quad (7.45)$$

$$\Omega(\dot{B}_i + \varepsilon\mu B_i) + [(\varepsilon\sigma_2 + \varepsilon^2\frac{\sigma_2^2}{4\Omega^2} + \varepsilon^2\mu^2 - \varepsilon^2\frac{3h^2}{8\Omega^2}) - \frac{1}{2}\varepsilon h]B_r = 0 \quad (7.46)$$

Equations (7.45) and (7.46) admit solutions of the form (7.42) provided that

$$\lambda = -\mu \pm \sqrt{\frac{h^2}{4\Omega^2} - \left(\frac{\sigma_2}{\Omega} + \varepsilon\frac{\sigma_2^2}{\Omega^3} + \varepsilon\frac{\mu^2}{\Omega} - \varepsilon\frac{3h^2}{8\Omega^3}\right)^2} \qquad (7.47)$$

In this case, again $\lambda = 0$ gives the equation of the curve separating stable from unstable trivial solutions.

7.4.3. Orbital stability of the fundamental parametric response

To ascertain the stability of the motion predicted by the approximate solution (7.23), we examine the time evolution of the periodic motion after the application of an arbitrary infinitesimal disturbance ξ(t) in the form

$$\tilde{\theta}(t) = \theta_f(t) + \xi(t) \qquad (7.48)$$

The stability of $\theta_f(t)$ depends on whether ξ(t) grows or decays as t → ∞. Substituting $\tilde{\theta}(t)$ into (7.3) and keeping only linear terms in ξ(t), we obtain

$$\ddot{\xi} + [2\mu + 3\mu_3\dot{\theta}_f^2(t)]\dot{\xi} + [1 + 3\hat{\alpha}_3\theta_f^2(t) + 5\hat{\alpha}_5\theta_f^4(t) + h\cos\Omega t]\xi = 0 \qquad (7.49)$$

which is a linear ordinary-differential equation with periodic coefficients. It follows from (7.23) that the coefficients of (7.49) have the period $T = \frac{2\pi}{\Omega}$. Therefore, it follows from Floquet theory [6] that (7.49) has solutions of the form

$$\xi(t+T) = \lambda\xi(t) \qquad (7.50)$$

where λ is called a Floquet multiplier. It is is an eigenvalue of the monodromy matrix C associated with a fundamental matrix solution Φ(t) of (7.49) through the relation

$$\Phi(t+T) = \Phi(t)C \qquad (7.51)$$

The solution θ_f is then asymptotically stable provided that ξ(t) decays with t. This requires that $|\lambda| < 1$. Thus, the eigenvalues of C must remain inside the unit circle in the complex plane for the solution given by (7.23) to be asymptotically stable.

For the dissipative one-degree-of-freedom system described by (7.3), there are two ways in which λ can leave the unit circle, which create independent patterns of instability in the T-periodic solution [36]. First, eigenvalue can leave the unit circle through the real axis at +1 , originating a tangent instability. As second, an eigenvalue can leave the unit circle through the real axis at -1, originating a period-doubling bifurcation and resulting in a 2T-periodic solution. The above patterns of instability allow us to predict the stability of the T-periodic solution (7.23) when the excitation level h or the encounter frequency Ω is being changed. Therefore, the dynamic behavior of the ship under a wide variety of conditions can be determined.

The stability characteristics of a solution are determined by the eigenvalues of C, which in turn can be found by choosing a fundamental matrix solution with the initial conditions $\Phi(0) = I$, where I is the identity matrix, so that (7.51) yields

$$C = \Phi(T) \tag{7.52}$$

The matrix Φ can be computed numerically by integrating (7.49) in the interval $[0,T]$ subject to the two sets of initial conditions: (a) $\xi(0) = 1.0$ and $\dot{\xi}(0) = 0$ and (b) $\xi(0) = 0$ and $\dot{\xi}(0) = 1.0$ for each set of parameters $(h\,,\Omega)$. The periodic coefficients in (7.49) that depend on $\theta_t\,(t)$ and $\dot{\theta}_t\,(t)$ are evaluated from (7.23).

7.4.4. Orbital stability of the principal parametric response

As in the preceding case, to ascertain the stability of the principal parametric resonant solution, we apply an arbitrary infinitesimal disturbance $\zeta(t)$ and obtain

$$\tilde{\theta}(t) = \theta_p\,(t) + \zeta(t) \tag{7.53}$$

Substituting (7.53) into (7.3) and keeping only linear terms in ζ(t), we obtain

$$\ddot{\zeta} + [2\mu + 3\mu_3\dot{\theta}_p^2(t)]\dot{\zeta} + [1 + 3\hat{\alpha}_3\theta_p^2(t) + 5\hat{\alpha}_5\theta_p^4(t) + h\cos\Omega t]\zeta = 0 \tag{7.54}$$

It follows from (7.37) that the period of $\theta_p(t)$ is $T = \frac{4\pi}{\Omega}$, but the period of the coefficients of (7.54) is still $\frac{2\pi}{\Omega}$ or $\frac{1}{2}T$. Furthermore, it follows from (7.37) that $\theta_p(t + \frac{1}{2}T) = -\theta(t)$; that is, (7.37) is symmetric. Then, it follows from Floquet theory that (7.54) has solutions of the form

$$\zeta(t + \frac{1}{2}T) = \lambda\zeta(t) \tag{7.55}$$

This implies that when λ leaves the unit circle through $+1$, $\theta_p(t)$ undergoes a pitchfork bifurcation and loses symmetry. On the other hand when λ leaves the unit circle through -1, $\theta_p(t)$ undergoes a saddle-node bifurcation, resulting in a jump. The matrix C in this case is computed by integrating (7.54) in the interval $[0, \frac{1}{2}T]$ subject to the two sets of initial conditions: (a) $\zeta(0) = 1.0$ and $\dot{\zeta}(0) = 0$ and (b) $\zeta(0) = 0$ and $\dot{\zeta}(0) = 1.0$.

7.4.5 Bifurcation diagram

In the preceding sections, we analyzed the stability of the trivial and periodic solutions of (7.3) in the neighborhoods of the fundamental ($\Omega \simeq 1$) and principal ($\Omega \simeq 2$) parametric resonances. Expressions (7.43) and (7.47) provide the equations of the bifurcation curves of the trivial solutions in the parameter space. The bifurcation curves for the nontrivial periodic solutions are generated by iteratively solving the algebraic equations for a and β and then applying Floquet analysis to determine the stability of the solutions $\theta_f(t)$ and $\theta_p(t)$.

To illustrate the preceding procedure, we consider the low-freeboard model treated by Wright and Marshfield [77], which has the physical characteristics listed in Table 1 ($\hat{\alpha}_i = \frac{\alpha_i}{\omega_0^2}$). The coefficients α_3 and α_5 shown in Table 1 are obtained by fitting the righting-arm curve with a quintic polynomial by using the least-squares method, and then multiplying the expression by the appropriate constant to obtain the righting moment. The angle of vanishing stability θ_v for this model is near 0.93 radians. Figure 7.1 shows a frequency-response curve when $h = 0.3$. The solid curve is obtained by numerically integrating (7.3) using a Runge-Kutta routine with double precision arithmetics. Because the threshold for the FPR is at a higher excitation amplitude, this figure shows only the response for the PPR. The black dots on the solid curve represent the analytical predictions obtained from (7.37) after solving the two algebraic equations generated from (7.35) and (7.36) by putting $a = 0$ and $\beta = 0$. The agreement between the numerical simulation and the analytical predictions is excellent.

Figure 7.1 shows some important qualitative changes in the response. When we sweep the frequency from right to left beginning at 3.0, we initially obtain the trivial response. This solution loses stability at the location T_1, where a nontrivial solution is first observed. As we continue decreasing the frequency the amplitude of the response grows rapidly and at point S we observe a symmetry-breaking bifurcation characterized by the appearance of even frequency harmonics in the response spectrum. Shortly afterwards, we observe a period-doubling bifurcation. However, our analytical predictions based on (7.37) can only account for the symmetry-breaking bifurcation because after this point the solution is qualitatively different. At the bifurcation point one of the Floquet multipliers goes through $+1$. Once the first period-doubling bifurcation takes place, a sequence of period-doubling bifurcations takes place in a narrow interval, leading to a chaotic response. Chaotic responses characterized by broad-band frequency content and its Poincaré map displays what is known as a strange attractor [36]. All these behaviors occur in the interval between points S and J. By the time we reach point J the chaotic solution loses its stability and a jump to the trivial solution is observed. When we sweep the frequency from left to right, the trivial solution loses its stability at point T_2 and a jump to a finite-amplitude periodic solution is observed.

Figure 7.2 shows a frequency-response curve when $h = 0.8$. For this level of excitation both the PPR and FPR resonances are excited. When we sweep the frequency down, the trivial solution loses it stability at T_1, where the PPR is excited. The amplitude of oscillation grows rapidly until point S is reached where a symmetry-breaking bifurcation occurs. However this time, after the chaotic attractor loses its stability at point J_1, the response can only be unbounded because the trivial solution is not stable for this value of Ω. The ship capsizes at this point. Furthermore, when the trivial solution loses its stability during forward sweeps, the jump point at T_2 again leads to capsizing because no other solution is stable for this value of Ω. The FPR covers a very narrow frequency range. In the downsweeps, we find that the nontrivial response begins at point T_3. The response amplitude increases rapidly and at point P a period-doubling bifurcation occurs. Between points P and J_2 we observe a sequence of period-doubling bifurcations, ending in a chaotic attractor. This attractor becomes unstable at point J_2 and capsizing takes place again. When the frequency is swept up, the trivial solution loses its stability at point T_4 and a jump takes place, changing the response from a trivial to an unbounded motion.

We are most interested in the locations where the solutions undergo qualitative changes when the parameters h and Ω are slowly varied. Figures 7.1 and 7.2 show the nature of the changes taking place for two levels of excitation. By performing the stability analysis for a large number of values of h, we generate the bifurcation diagram shown in Figure 7.3, where the results for a large number of excitation levels h and encounter frequencies Ω are summarized. The solid curves T_1, T_2, T_3, and T_4 represent the locations where the trivial solution loses its stability. These curves are generated from (7.43) and (7.47). Inside these tongues the principal and fundamental parametric resonances are excited and the steady-state response of the system is given by (7.23) and (7.37) in the neighborhoods of $\Omega = 1$ and $\Omega = 2$, respectively. The orbital stability analysis of $\theta_p(t)$ generates the bifurcation curves J_1, which represents a jump to the trivial solution, and S, which represents a symmetry-breaking bifurcation and a precursor to period-doubling bifurcations. It is important to point out that as we trace the bifurcation curves, we move out of the tongue predicted by linear theory and observe large-amplitude oscillations in the tip that protrudes out of the tongue bordered by a curve (J_1) of saddle-node bifurcations and a curve (S) of symmetry-breaking bifurcations. Arrows show the directions in which the bifurcations are active, indicating qualitative changes observed in the system as we cross the bifurcation curves.

Figure 7.3 also shows the bifurcation curves for $\theta_f(t)$. Higher excitation levels are needed to activate this resonance. The qualitative behavior of this solution is similar to that of $\theta_p(t)$. We observe the trivial solution losing stability across T_3 and T_4 . Inside this tongue, we have nontrivial oscillations that are given by (7.23). The stability analysis predicts that the nontrivial solution undergoes saddle-node bifurcations across J_2 and period-doubling bifurcations across P. We note again a tip that protrudes out of the tongue in which nontrivial oscillations take place.

Figure 7.3 indicates the regions of the parameter space where the solutions lose stability. Some particularly interesting regions are those denoted by C_1 and C_2, where the trivial solutions are unstable and at the same time the period-T periodic solutions are also unstable. In these regions it is likely to observe complicated behavior including capsizing. It is shown in the next section that in a narrow region the periodic solution undergoes symmetry-breaking bifurcations, period-doubling sequences, and a jump to another attractor, which in this case could be only an unbounded solution. This diagram provides us with a general picture of the dynamics of the ship model for a broad portion of the parameter space.

7.5. Analog-computer simulations

To verify our analytical predictions, we performed analog-computer simulations of the solutions of (7.3). Because our aim was to study the stability of the motion, we concentrated on obtaining a very detailed bifurcation diagram. Figure 7.4 shows the bifurcation diagram obtained after carefully observing the changes in the response brought about by slowly varying the frequency or the amplitude of the excitation. The power spectrum from a FFT (Fast Fourier Transform) signal analyzer and the Poincaré map were used to identify the qualitative changes that occurred in the solution.

Figure 7.4 shows the instabilities of the principal parametric resonant solution. The curves T_1 and T_2 mark the locations where the trivial solution loses stability. Across T_1 the nontrivial solution grows slowly while across T_2 there is a jump to the nontrivial solution. The nontrivial solution loses stability through a saddle-node instability across J_1, jumping to the trivial attractor.

Across P_1, we observe a period-doubling bifurcation followed by a sequence of period-doubling bifurcations. Then, the solution displays broad-band frequency components and a strange attractor in the Poincaré map, which are indications of a chaotic behavior [34,89]. This sequence of events is shown in more detail in Figure 7.5 (a)-(i), where the phase portraits and the power spectra of the solutions are displayed. The period-doubling sequence to chaos is observed in the narrow region between the curves P_1 and E_1 in Figure 7.4. When E_1 is crossed the chaotic attractor suddenly disappears in what is known as a crises [90] and a jump is observed. The system jumps to another stable solution, which in this case can be the trivial solution or an unbounded solution that would produce capsizing. The basins of attraction of these solutions and the state of the system at the crossing point would determine the final solution. During the simulations the system went to capsizing for crossings that took place with values of h larger than those corresponding to point X_1. In the dotted region the system always capsizes because no other solution is stable.

Figure 7.4 also shows the instabilities of the fundamental parametric resonant solution. In this case the trivial solution loses stability across the curves T_3 and T_4. As T_3 is crossed the nontrivial solution begins to slowly grow. As T_4 is crossed the small-amplitude solution shown in Figure 7.6 develops. This solution loses its stability across J_4 and a jump to the FPR or to capsizing is observed, depending on the location of the crossing point and the state of the system. Crossing J_4 with values of h larger than those corresponding to the black dot shown on the curve results in capsizing. Inside the fundamental parametric resonant region, we observed two attractors that are inversions of each other and undergo bifurcations similar to those observed for the case of principal parametric resonance. We observe jumps to the trivial solution across J_2 and period-doubling sequences that lead to chaos in a narrow region near P_2 . In Figures 7.7 and 7.8, we show qualitative changes in the two coexisting attractors. Capsizing is observed for crossings taking place above X_3 in the directions indicated by the arrows. The mechanism for the transition is again the disappearance of the chaotic attractor.

For values of Ω below 0.6, Figure 7.4 shows a small tongue that corresponds to the bifurcation curves for the attractor shown in Figure 7.9, which is a superharmonic resonant response. At lower frequencies, we found more of these superharmonic resonances at higher levels of excitation. The structure of the bifurcation curves for these solutions is remarkably similar to those for the PPR and FPR, but occur in a much smaller frequency range at larger levels of excitation.

Figure 7.4 gives an important qualitative description of the dynamics of the ship model. However, to completely characterize the behavior of the vessel it is necessary to also consider the influence of the other coefficients in (7.3), which are not associated with the excitation. These coefficients pertain to the specific features of a particular design and loading conditions. Of special significance is the understanding of the role of damping because it is known [6] to alter the stability regions of the Mathieu equation.

Figure 7.10 shows a set of four bifurcation diagrams for various damping parameters. Figure 7.10a shows the results previously displayed in Figure 7.4, which correspond to the damping coefficients given in Table 1, Figure 7.10b shows a simplified version of the bifurcation diagram after halving the linear damping coefficient (i.e., taking $\frac{1}{2}\mu$), Figure 7.10c shows the results obtained after halving the nonlinear damping coefficient (i.e., taking $\frac{1}{2}\mu_3$), and Figure 7.10d shows the results obtained when both damping coefficients are halved (i.e, taking $\frac{1}{2}\mu$ and $\frac{1}{2}\mu_3$). From these figures, we observe that lowering the damping coefficients has a considerable influence on the boundaries of the nontrivial solutions; they move down, thereby making the ship susceptible to capsizing at lower excitation levels. However, the effect of the damping coefficients on the stability boundaries of the trivial solutions seems to be small for the PPR and of some importance for the FPR. The location of the points x_1, x_2, x_3, and x_4, which mark the limit values of h for which crossings lead to capsizing, seems to be most affected by variations in μ_3.

7.6. Digital-computer simulations

Figures 7.1 and 7.2 show the excellent agreement obtained between the analytical predictions and the results from a direct numerical integration of (7.3) by using a Runge-Kutta routine with double precision arithmetics. An important aspect of the behavior of the system that can be also investigated numerically is the effect of the initial conditions on the steady-state response. This effect is best portrayed by mapping the basins of attraction of the attractors of interest. Because we are interested in the prediction of capsizing, our objective is to identify domains of attraction for capsizing and noncapsizing solutions (trivial or oscillatory). This is achieved by numerically integrating (7.3) with a grid of 500x500 initial conditions and determining which initial conditions lead to capsizing. This process requires extensive computation, but there are techniques such as cell-to-cell mapping [64] that reduce the number of computations required when a systematic survey is needed.

Figure 7.11 shows the results obtained for two levels of excitation ($h = 0.6$ and $h = 0.8$) in the neighborhood of the fundamental parametric resonance ($\Omega = 0.8$). We observe the changes in the basins of attraction as the amplitude of excitation is increased. The basin of attraction of capsizing solutions grows and undergoes changes. When the excitation amplitude enters the dotted region shown in Figure 7.4 for $\Omega = 0.8$, all initial conditions lead to capsizing and therefore the basin of attraction of noncapsizing solutions shrinks to zero.

Figure 7.12 shows the basins of attraction for two levels of excitation ($h = 0.5$ and $h = 0.6$) in the neighborhood of the principal parametric resonance ($\Omega = 1.8$). In this case the qualitative changes in the basins (also known as metamorphoses) display what is called fractal boundaries [63]. The result is an extreme sensitivity to initial conditions. We observe for this resonance also the disappearance of the basin of attraction of noncapsizing solutions when the amplitude reaches the dotted region shown in Figure 7.4.

Chapter 8

EFFECT OF PARAMETRIC EXCITATION ON THE ROLL MOTION OF A BIASED SHIP

8.1. Introduction

In the study of the roll motion of a vessel it is common to have an equation of motion with time-varying coefficients, which arise from time-dependent restoring moments due to the ship's position on the wave [6,23] or to changes in the displacement volume resulting from coupling with other modes [69]. These time-varying coefficients constitute what is known as parametric excitations [24]. A considerable number of roll studies [e.g., 6,23,69,72,78,80,88] have studied the influence of these excitations on the stability of a ship in the presence of resonances, which can lead to capsizing under rather mild sea conditions (see Chapter 7).

In Chapters 3-7, we presented and applied an analytical-numerical procedure to characterize the stability of the steady-state response of a ship when a parameter is slowly varied. The procedure analyzes the stability of an approximate analytical solution by using Floquet theory and elementary concepts of bifurcation theory. In Chapter 7, we have shown that a ship model under purely parametric excitation, which is the case of rolling in longitudinal waves in the absence of heeling moments and pitch-roll coupling, displays self-similar behavior near the resonances. Instabilities can lead to capsizing through two scenarios: one evolving from a large oscillation through the disappearance of a chaotic attractor (crises) and a second, potentially more dangerous, developing from a small oscillation through a sudden tangent instability. Similar behaviors occur for excitation frequencies near the linear natural frequency, twice the natural frequency, and the superharmonic frequencies (at higher excitation levels). In Chapter 6, we treated the behavior of the same ship model under an external excitation; that is, the case of rolling in beam seas. In this case we also found a qualitatively similar behavior in the neighborhood of the primary resonance ($\Omega \approx \omega_0$). These results are in agreement with the conjecture of Parlitz and Lauterborn [12] that this behavior represents a manifestation of some fundamental physical structure and should be observed in the neighborhood of every resonance of the system if the excitation amplitude is sufficiently large.

Wellicome [80] and Féat and Jones [69], among others, considered a second-order equation with parametric and external excitations. It models the rolling motion of a ship (a) in beam seas when the coupling with heave or the Smith effect is included or (b) in longitudinal waves when bias is included. One of the important features of the nonlinear motion observed in these studies [69] is the difference in stability characteristics between ships with positive and negative bias angles, which confirms the experimental observations of Right and Marshfield [77].

In this Chapter we expand the above studies by analyzing the nonlinear rolling response of a biased ship to both parametric an external excitations. Our aim is to gain general understanding of the dynamics by identifying the instabilities that appear when a parameter is slowly varied and characterize the locus of these instabilities in a parameter space of physical significance. We present the results of analog-computer simulations in a broad portion of the amplitude and frequency of the external excitation, keeping the level of the parametric excitation fixed. The analytic predictions could have been obtained by using the method presented in the previous chapters.

Following Wright and Marshfield [77] and Féat and Jones [69], we derive the equation of motion as a function of the relative motion of the ship and the wave. We let ϕ be the absolute roll angle and θ be the relative roll angle with respect to the local waveslope α hat.. Applying Newton's second law, we find that the equation of motion can be written as

$$(I + \delta I)\ddot{\theta} + D(\dot{\theta}) + K(\theta, \tau) = B - I\ddot{\alpha} \tag{8.1a}$$

$$\theta = \phi - \alpha \tag{8.1b}$$

where the dots represent derivatives with respect to the time τ, I is the roll moment of inertia, δI is the added moment of inertia, which is assumed to be constant [77], and B is a constant bias moment, which might be due to a steady wind, or a shift in cargo, or water or ice on deck. The righting moment K(θ,τ) has an explicit time dependence, which might come from two sources [69]: the position of the ship on the wave or variations in the displacement volume due to heave coupling. We are mostly interested in the latter effect; however, consideration of the first effect only changes the numerical values of the coefficients. The righting-moment function is approximated as [72,77]

$$K(\theta, t) = \omega_0^2 \left[\theta + \hat{\alpha}_3\theta^3 + \hat{\alpha}_5\theta^5 + h\theta\cos(\hat{\Omega}\tau)\right] \tag{8.2}$$

where the odd polynomial fits the ship's righting-moment curve and the parametric term represents heave - roll coupling expressed by the coefficient

$$h = \frac{K_{\theta z} a_z}{2\omega_0^2} \tag{8.3}$$

Here, $K_{\theta z}$ is the magnitude of the coupling coefficient and a_z is the amplitude of the heaving motion, which is assumed to be harmonic with frequency $\hat{\Omega}$. The damping moment $D(\dot{\theta})$ is expressed as

$$D(\dot{\theta}) = 2\hat{\mu}\dot{\theta} + \hat{\mu}_3\dot{\theta}^3 \tag{8.4}$$

Assuming that the wavelength is large compared with the ship's beam, we can write the waveslope of a regular beam sea as a harmonic function $\alpha = \alpha_m \cos \hat{\Omega} t$, where α_m is the maximum waveslope. Using (8.1b)-(8.4), we rewrite (8.1a) as

$$\begin{aligned} \ddot{\theta} + 2\hat{\mu}\dot{\theta} + \hat{\mu}_3\dot{\theta}^3 + \omega_0^2\left[\theta + \hat{\alpha}_3\theta^3 + \hat{\alpha}_5\theta^5 + h\theta\cos(\hat{\Omega}\tau)\right] &= \\ \omega_0^2\left[\theta_s + \hat{\alpha}_3\theta_s^3 + \hat{\alpha}_5\theta_s^5\right] + \frac{\alpha_m I\hat{\Omega}^2}{(I + \delta I)} \cos(\hat{\Omega}\tau + \gamma) \end{aligned} \tag{8.5}$$

where γ represents a phase angle between the wave and heave motions and θ_s is the bias angle produced by the moment B. To simplify the governing equation, we introduce the time scaling $t = \omega_0\tau$, which transforms (8.5) into

$$\begin{aligned} \ddot{\theta} + 2\mu\dot{\theta} + \mu_3\dot{\theta}^3 + \theta + \hat{\alpha}_3\theta + \hat{\alpha}_5\theta^5 + h\theta\cos(\Omega t) &= \theta_s + \hat{\alpha}_3\theta_s^3 + \hat{\alpha}_5\theta_s^5 \\ &+ \hat{f}_1\cos(\Omega t) - f_2\sin(\Omega t) \end{aligned} \tag{8.6}$$

where the dot represents the derivative with respect to t,

$$\hat{f}_1 = \frac{\alpha_m I\Omega^2}{(I + \delta I)} \cos\gamma \tag{8.7}$$

and

$$f_2 = \frac{\alpha_m I\Omega^2}{(I + \delta I)} \sin\gamma \tag{8.8}$$

Using the transformation

$$\theta = \theta_s + u \tag{8.9}$$

we rewrite (8.6) as

$$\begin{aligned} \ddot{u} + 2\mu\dot{u} + \mu_3\dot{u}^3 + u + b_1 u + b_2 u^2 + b_3 u^3 + b_4 u^4 + b_5 u^5 \\ + hu\cos(\Omega t) = f_1\cos(\Omega t) - f_2\sin(\Omega t) \end{aligned} \tag{8.10}$$

where

$$\begin{aligned} &b_1 = 3\hat{\alpha}_3\theta_s^2 + 5\hat{\alpha}_5\theta_s^4 \quad , \quad b_2 = 3\hat{\alpha}_3\theta_s + 10\hat{\alpha}_5\theta_s^3 \quad , \quad b_3 = \hat{\alpha}_3 + 10\hat{\alpha}_5\theta_s^2 \\ &b_4 = 5\hat{\alpha}_5\theta_s \quad , \quad b_5 = \hat{\alpha}_5 \end{aligned}$$

and

$$f_1 = \hat{f}_1 - h\theta_s \tag{8.11}$$

Equation (8.10) is general and can model the roll motion of biased and unbiased ships in a variety of regular sea conditions, including beam seas, head or following seas, and quartering seas. The cases treated in the two previous chapters are particular forms of this equation. When $\gamma = 0$ and $h = 0$, (8.10) models the rolling of a biased or an unbiased ship in beam seas, depending on whether θ_s is zero or nonzero. Similarly, when $\alpha_m = 0$ and $\theta_s = 0$, (8.10) models the rolling motion of a biased or an unbiased ship in head or following seas. The natural frequency has been scaled to unity to make the results easily applicable to a wide number of cases. Because of the generality of the cases covered, we have a large number of excitation parameters to consider, namely, Ω, γ, h, θ_s, and α_m. Because our goal is to study the effect of the parametric amplitude h, we study primarily the stability boundaries in the α_m-Ω parameter space at a set level of h. The phase angle γ is set at zero because this angle produces large amplitudes near $\Omega = 1$. The bias angle is taken to be either +6 or -6 degrees. The effect of the parametric term complements the results of Chapters 6 and 7 obtained for the cases of either a purely parametric or a purely external excitation.

8.2. Bifurcation diagrams

Analog-computer simulation of (8.5) for $\gamma = 0$, $\theta_s = 0°$, $h = 0.3$, and the other coefficients as given in Table 1 ($\hat{\alpha}_i = \frac{\alpha_i}{\omega_0^2}$) yields the bifurcation diagram shown in Figure 8.1. In this diagram, we present the bifurcations of three basic attractors which are stable near $\Omega = 1$ and $\Omega = 2$. Figure 8.2 shows a phase diagram of the two attractors at $\Omega = 0.856$ and $\alpha_m = 0.048$. The small attractor loses its stability when the parameters are varied across S_1, which is the locus of saddle-node bifurcations that produce a jump to another attractor. If the crossing occurs for values of $\alpha_m > I_2$, the ship capsizes. For crossings with values of $\alpha_m < I_2$, the jump is to the large attractor in Figure 8.2. The curve S_2 is the locus of saddle-node bifurcations that produce a jump from the large to the small attractor. The large attractor also undergoes a period-doubling sequence to chaos in the region between P_1 and J_1. Figure 8.3 shows phase diagrams and power spectra of various attractors at selected locations in this region. In the dotted region all initial conditions lead to capsize. When J_1 is crossed the chaotic attractor loses stability and the system jumps to an unbounded solution associated with capsizing or to the small attractor, depending on whether the crossing occurs above or below I_1. The large attractor in Figure 8.2 also loses stability near $\Omega = 2$. Between P_3 and P_4 this limit cycle is unstable. When P_3 is crossed from left to right the attractor undergoes a period-doubling bifurcation and a jump to the subharmonic response is observed. When P_4 is crossed from right to left another period-doubling bifurcation is observed. Therefore, the primary resonant response ($\Omega \approx 1$) is unstable in the region between P_3 and P_4.

The third attractor represented in the bifurcation diagram in Figure 8.1 is the subharmonic response near $\Omega = 2$, which is stable in the region between P_4 and J_2. Figure 8.4 shows selected attractors in this region: (a) shows the principal resonant response, (b) shows the subharmonic resonant response obtained after crossing P_4 from right to left, (c) and (d) show quantitative changes in the subharmonic response, (e) shows the subharmonic response after a period-doubling bifurcation across P_2, and (f) shows a chaotic attractor to the right of J_2

Figure 8.5 shows the bifurcation diagram obtained from an analog-computer simulation of (8.5) when the parameters are set at $\gamma = 0$, $\theta_s = +6°$, and h = 0.3. In this case the dotted region is much larger than that for the case of an unbiased ship. The region of stability of the subharmonic response shrank and the primary and subharmonic responses only coexist in a narrow region between $\Omega = 1.5$ and 2.0. The curves S_1 and S_2 represent saddle-node bifurcations of the large and small attractors of the primary resonant response, which produce jumps in the corresponding attractors. Figure 8.6 shows the two attractors for $\Omega = 0.768$ and $\alpha_m = 0.217$. In Figure 8.5, S_1 represents a jump from the large to the small attractor; S_2 represents a jump in the small attractor, which takes the system to the large attractor if α_m is below the black dot or to capsize if it is above this point; and P_1 represents period-doubling bifurcations, leading to either chaos in the portion of the curve enclosed by E_1 or directly to an instability in the rest of the curve. The instability results in either capsize when α_m is above the black dot on P_1 or a jump to the subharmonic attractor when it is below the black dot on P_1 . Figure 8.7 shows the coexisting attractors near the subharmonic resonance at $\Omega = 1.758$ and $\alpha_m = 0.046$. The curve E_1 in Figure 8.5 represents the point of capsize. For values of Ω below the black dot on E_1, a sequence to chaos such as the one shown in Figure 8.7 is observed. For crossings of E_1 between the black dot and the point of merge with P_1, a saddle-node bifurcation is observed, making the period-2T solution unstable and resulting in capsizing.

Figure 8.5 also shows the stability region of the subharmonic, which is narrower than that in Figure 8.1. Crossing P_3 from right to left causes the primary resonant response to lose stability and the subharmonic response becomes stable. Along P_2, the system undergoes period-doubling bifurcations leading to a chaotic attractor, which disappears when E_2 is reached causing the ship to capsize. Figure 8.9 shows selected phase portraits of the above changes in the solution : (a) shows the primary resonant response, (b) and (c) show the subharmonic response after crossing P_3, (d) shows a period-doubling bifurcation in the subharmonic response after crossing P_2, and (e) shows a second-period doubling bifurcation in the subharmonic response.

Figure 8.10 shows the bifurcation diagram obtained from analog-computer simulation of (8.5) when the parameters are set at: $\gamma = 0$, $\theta_s = -6°$, and h = 0.3. Figure 8.11 shows the attractors near the primary resonance. Across the curve S in Figure 8.10, the small attractor undergoes a saddle-node bifurcation that produces capsizing. Across P_1 the large attractor undergoes period-doubling bifurcations. In the portion of P_1 enclosed by E_1 a sequence of period-doubling bifurcations to chaos is observed, in the rest of the curve capsizing occurs after the first period-doubling bifurcation. The large attractor also undergoes period-doubling bifurcations across P_4. The subharmonic response undergoes period-doubling bifurcations across P_2, P_3, and P_5. Capsizing is observed after crossing P_2 and E_2. Figure 8.12 shows the coexisting attractors that are found between P_2 and P_4.

From the previous results we observe that the dynamics of the biased ship is different when the bias angle is positive than when it is negative, which confirms the experimental observations of Right and Marshfield [77]. However, it is difficult to conclude which of the two cases is more stable since that depends on the region of the parameter space under consideration. Nevertheless, it is clear that the motion is very sensitive to bias. We also found the bifurcation diagram to be sensitive to changes in the phase angle γ.

Chapter 9

CONCLUSIONS

9.1. *Current Work*

A procedure to generate an approximate bifurcation diagram for a single-degree-of-freedom system in a selected parameter space was developed. The procedure is based on Floquet analysis to determine the stability of a second-order perturbation approximation to the solution of the system in the neighborhood of specific resonances. As a control parameter is varied, we can use a combination of elementary concepts of bifurcation theory and the proposed method to detect the first bifurcation from the periodic solutions and hence infer the qualitative changes that the system experiences. From this information, we can iteratively trace the codimension one bifurcations of the approximate solution in a two-dimensional parameter space composed of the amplitude and frequency of the excitation. We applied the technique to a softening Duffing oscillator subject to either an external or a parametric excitation. Encouraged by the success in these two cases, we considered the case of rolling oscillations of ships in waves. Three cases were considered: rolling in beam seas, rolling in transverse waves, and finally, rolling in quartering waves.

As a means to verify the accuracy of the predictions, we used analog- and digital-computer simulations. These simulations revealed the complete bifurcation patterns of the systems. In general the agreement among the simulations and the analytic predictions is good. Although the predictions are based on the first bifurcation of the approximate solutions, they give a good estimate of the actual behavior of the system due to the fact that other behaviors are confined to narrow regions of the parameter space.

The stability regions in the parameter space display a self-similar pattern that is repeated near each resonance of the system. These patterns seem to form the superstructure that Parlitz and Lauterborn [12] found in another oscillator. This generic structure was observed in all the cases treated. The stability regions of the attractors of the system have tongue-like or wedge shapes in parameter space. The stable regions are bordered by saddle-node or period-doubling, or pitchfork bifurcation curves, depending on the symmetry properties of the system. The wedge typically has period-doubling bifurcations on the top side and saddle-node bifurcations on the bottom.

The physical implications of the bifurcation patterns become evident in the capsizing of ships. The dangerous regions of the parameter space where capsizing might occur can be identified for a given system. In this case, the system is a vessel with a given geometry and loading conditions rolling in a sea. The parameter space can be associated with the sea conditions that the vessel could encounter. Therefore, the seaworthiness of a particular design can be assessed according to the regions of the parameter space where capsizing or large-amplitude oscillations can occur.

An important observation is that capsizing was found to occur via two distinct scenarios: one evolving from a large oscillation through a disappearance of a chaotic attractor (crises) and a second, potentially more dangerous, developing from a small oscillation through a sudden tangent instability. The scenarios agree with what Paulling, Kastner, and Schaffran [84] called mode 1 and mode 2 of capsizing in their 1972 experimental studies in the San Francisco Bay. Therefore, important information, which could be related to experimental observations, can be derived from the instability regions in the bifurcation diagrams.

9.2 Future work

In direct relation to the technique presented, the most important aspect will be to check its applicability to higher-order systems. The first step should be to test it with a two degree-of-freedom system. The system should have complicated solutions confined to small regions of the parameter space. This is not always the case, but it might be possible to derive the general conditions under which this constraint holds.

The sensitivity to initial conditions was portrayed by numerically integrating the governing equation to locate the basin of attraction of unbounded solutions. It was shown that drastic basin metamorphoses occur as a parameter is changed; they can affect the global behavior of the ship model. These simulations were performed at very selected locations. However, it would be very interesting to carry out a complete analysis of the metamorphoses of the basins of attraction to identify conditions for global bifurcations, such as the disappearance of the chaotic attractors. Due to the tremendous computational effort required, such a study would benefit from the use of efficient mapping techniques, such as the cell-to-cell mapping [64].

Many other aspects of ship dynamics could be analyzed such as modal interactions. Nevertheless, experimental verification of the predictions for the one degree-of-freedom problem should be a first priority.

REFERENCES

1. Abraham, N. B., Gollub, J. P., and Swinney, H. L. , "Meeting report: testing nonlinear dynamics," Physica 11D, 252 (1984).

2. Zeeman, E. C., "Chairman's introduction," Proceedings from the Royal Society of London, A 413, 3 (1987).

3. Poincaré, H., "Les méthodes nouvelles de la mécanique céleste II," Gauthiers-Villars, Paris, 1893.

4. Nayfeh, A. H., **Perturbation Methods**, Wiley-Interscience, New York, 1973.

5. Nayfeh, A. H., **Introduction to Perturbation Techniques**, Wiley-Interscience, New York, 1981.

6. Nayfeh, A. H. and Mook, D. T., **Nonlinear Oscillations**, Wiley-Interscience, New York, 1979.

7. Bogoliubov, N. N. and Mitropolky, Y. A., **Asymptotic methods in the theory of oscillations**, Hindustan Publishing Company, Delhi, 1961.

8. Huberman, B. A. and Crutchfield, J. P., ″Chaotic states of an harmonic systems in periodic fields,″ Physical Review Letters 43, 1743 (1979).

9. Morosov, A. D., ″Approach to a complete qualitative study of Duffing′s equation,″ USSR Journal of Mathematics and Mathematical Physics 13, 1134 (1973).

10. Morosov, A. D., ″A complete investigation of Duffing′s equation,″ Differential Equations 12, 164 (1976).

11. Huberman, B.A., Crutchfield, J. P., and Packard, N. H., ″Noise phenomena in Josephson junctions,″ Applied Physics Letters 37, 750 (1980).

12. Parlitz, U. and Lauterborn, W., ″Superstructure in the bifurcation set of the Duffing equation,″ Physics Letters 107A, 351 (1985).

13. Zavodney, L. D., Nayfeh, A. H., and Sanchez, N., ″The response of a single-degree-of-freedom system with quadratic and cubic non-linearities to a principal parametric resonance,″ Journal of Sound and Vibration 129, 417 (1989).

14. Nayfeh, A. H. and Khdeir, A. A., "Nonlinear rolling of ships in regular beam seas," International Shipbuilding Progress 33, 40 (1986).

15. Nayfeh, A. H. and Khdeir, A. A., "Nonlinear rolling of biased ships in regular beam waves," International Shipbuilding Progress 33, 84 (1986).

16. Dahle, E. and Kjæland, O., "The capsizing of M/S HELLAND-HANSEN," Transactions of the Royal Institution of Naval Architects 2, 51 (1980).

17. Thompson, J. M. T., "Chaotic dynamics and the Newtonian legacy," Applied Mechanical Reviews 42, 15 (1989).

18. Kuo, C and Welaya, Y., "A review of intact stability research and criteria," Ocean Engineering 8, 65 (1981).

19. Hamamoto, M. and Kensaku, N., "Transverse stability of ships in a following sea," Second International Conference on Stability of Ships and Ocean Vehicles, S iv-2b, p. 215, Tokyo, Oct. (1982).

20. Froude, W., "On the rolling of ships," Transactions of the Institution of Naval Architects, 2, 180 (1861).

21. Krilov, A. N., "Oscillations of Ships," Vol. 11 of Collected Works, Academy of Sciences, USSR (1951).

22. Grim, O., "Rollschwingungen, Stabilität, und Sicherheit im Seegang," Schiffstechnik 1, 10 (1952).

23. Kerwin, J. E., "Notes on rolling in longitudinal waves," International Shipbuilding Progress 2, 597 (1955).

24. Paulling, J. R. and Rosenberg, R. M., "On unstable ship motions resulting from nonlinear coupling," Journal of Ship Research, 3, p. 36, (1959).

25. Nayfeh, A. H., Mook, D. T., and Marshall, L., "Nonlinear coupling of pitch and roll modes in ship motions," Journal of Hydronautics 7, 145 (1973).

26. Liapunov, A. M., "Probleme general de la stabilite du mouvement," Annals of Mathematical Studies, Vol. 17, Princeton University Press, Princeton, NJ, 1949.

27. Birkhoff, G. D., **Dynamical Systems** , American Mathematical Society, Providence, RI, 1927.

28. Andronov, A. A. and Pontryagin, L., "Systemes Ggossiers," Dokl. Adad. Navk. SSSR, 14, 247 (1937).

29. Kolmogorov, A. N., "General theory of dynamical systems and classical mechanics," Proceedings of the 1954 International Congress of Mathematics, p. 315, North-Holland, Amsterdam, 1957.

30. Moser, J., "On invariant curves of area-preserving mappings on an Annulus," Nachr. Akad. Wiss Gottingen. Math. Phys. K1, 1 (1962).

31. Arnold, V. I., "Proof of A. N. Kolmogorov's theorem on the preservation of quasiperiodic motions under small perturbations of the Hamiltonian," Russ. Math. Surv., 18, 85 (1963).

32. Smale, S., **Diffeomorphisms with many periodic points** , in Differential and Combinational Topology, edited by S. S. Cairns, p. 63, Princeton University Press, Princeton, NJ, 1963.

33. Eckmann, J.-P., "Roads to turbulence in dissipative dynamical systems," Reviews of Modern Physics 53, 643 (1981).

34. Bergé, P., Pomeau, Y. and Vidal, C., **Order Within Chaos**, Wiley-Interscience, New York, 1984.

35. Kubicek, M. and Marek, M., **Computational Methods in Bifurcation Theory and Dissipative Structures**, Springer-Verlag, New York, 1983.

36. Guckenheimer, J. and Holmes, P. J., **Nonlinear Oscillations, Dynamical Systems and Bifurcations of Vector Fields**, Springer-Verlag, New York, 1983.

37. Thompson, J. M. T., **Nonlinear Dynamics and Chaos : Geometrical Methods for Engineers and Scientist**, Wiley, New York, 1986.

38. Jordan, D. W. and Smith, P., **Nonlinear Ordinary Differential Equations**, Clarendon Press, Oxford, 1983.

39. Arnold, V. I., **Mathematical Methods of Classical Mechanics**, Springer-Verlag, New York, 1978.

40. Seydel, R., **From Equilibrium to Chaos : Practical Bifurcation and Stability Analysis**, Elsevier, New York, 1988.

41. Lichtenberg, A. J. and Lieberman, M. A., **Regular and Stochastic Motion**, Springer-Verlag, New York, 1983.

42. Iooss, G. and Joseph, D., **Elementary Stability and Bifurcation Theory**, Springer-Verlag, New York, 1980.

43. Schuster, H. G., **Deterministic Chaos**, Physik-Verlag, Weinheim, 1984.

44. Newhouse, S., Ruelle, D., and Takens, F., "Occurrence of strange Axiom A attractors near quasiperiodic flows on T^m , $m \geq 3$.," Communications in Mathematical Physics 64, 35 (1978).

45. Ruelle, D. and Takens, F., "On the nature of turbulence," Communications in Mathematical Physics 20, 167 (1971).

46. Carr, J., **Applications of Center Manifold Theory**, Springer-Verlag, New York, 1981.

47. Räty, R., von Boehm, J., and Isomäki, H. M., "Absence of inversion-symmetric limit cycles of even periods and the chaotic motion of Duffing's oscillator," Physics Letters 103A, 289 (1984).

48. Rahman, Z. and Burton, T. D., "Large amplitudes primary and superharmonic resonances in the Duffing oscillator," Journal of Sound and Vibration 110, 363 (1986).

49. Liu, K. L. and Young, K., "Stability of forced nonlinear oscillators via Poincare map," Journal of Mathematical Physics 27, 502 (1986).

50. Bhattacharyya, R., **Dynamics of Marine Vehicles**, Wiley, New York, 1978.

51. Kautz, R. L. and MacFarlane, J. C., "Onset of chaos in the rf-biased Josephson junction," Physical Review A33, 498 (1986).

52. Rasband, S. N., "Marginal stability boundaries for some driven, damped, non-linear oscillators," International Journal of Non-Linear Mechanics 22, 477 (1987).

53. Arnold, V. I., **Geometrical Methods in the Theory of Ordinary Differential Equations** , Springer-Verlag, New York, 1983.

54. D"Humiere, D., Beasley, M. R., Huberman, B. A., and Libchaber, A., "Chaotic states and routes to chaos in the forced pendulum," Physical Review 26A, 3483 (1982).

55. Thompson, J. M. T., Bishop, S. R. and Leung, L. M., "Fractal basins and chaotic bifurcations prior to escape from a potential well," Physics Letters A121, 116 (1987).

56. Glass, L. and Perez, R., "Fine structure of phase locking," Physical Review Letters 48, 1171 (1982).

57. Nayfeh, A. H., "Perturbation Methods in Nonlinear Dynamics," in Lecture Notes in Physics, Proceedings of the Joint US-CERN School on Particle Accelerators, edited by J. M. Jowett, M. Month and S. Turner, Springer-Verlag, New York, 1985.

58. Swift, J. and Wiesenfeld, K., "Suppression of period doubling in symmetric systems," Physical Review Letters 52, 705 (1984).

59. Wiesenfeld, K. and McNamara, B., "Small-signal amplification in bifurcating dynamical systems," Physical Review A33, 629 (1986).

60. Novak, S. and Frehlich, R. G., "Transition to chaos in the Duffing oscillator," Physical Review A26, 3660 (1982).

61. Szemplinska-Stupnicka, W., "Secondary resonances and approximate models of routes to chaotic motions in non-linear oscillators," Journal of Sound and Vibration 113, 155 (1987).

62. Decker, D. W. and Keller, H. B., "Solution branching, a constructive technique," in **NEW APPROACHES TO NONLINEAR PROBLEMS IN DYNAMICS** , edited by P. J. Holmes, SIAM, Philadelphia, 33 (1980).

63. Grebogi, C., Ott, E., and Yorke, J., "Metamorphoses of basin boundaries in nonlinear dynamical systems," Physics Review Letters 56, 1011 (1986).

64. Hsu, C. S., **Cell-to-Cell Mapping: A Method of Global Analysis for Nonlinear Systems**, Springer Verlag, New York, 1987.

65. Nayfeh, A. H. and Sanchez, N. E., "Bifurcations in a forced softening Duffing oscillator," to appear International Journal of Non-Linear Mechanics, 1989.

66. Ibrahim, R. A., **Parametric Random Vibrations**, Wiley, New York, 1985.

67. Schmidt, G. and Tondl, A., **Non-linear Vibrations**, Akademi-Verlag, Berlin, 1986.

68. Zavodney, L. D., and Nayfeh, A. H., "The response of a single-degree-of-freedom system with quadratic and cubic non-linearities

to a fundamental parametric resonance," Journal of Sound and Vibration 120, 63 (1988).

69. Feat, G. and Jones, D., "Parametric excitation and the stability of a ship subjected to a steady heeling moment," International Shipbuilding Progress 28, 263 (1984).

70. Koch, B. P. and Leven, R. W., "Subharmonic and homoclinc bifurcations in a parametrically forced pendulum," Physica 16D, 1 (1985).

71. "Nomenclature for treatment the motion of a submerged body through a fluid," Technical and Research Bulletin No 1-5, SNAME, 1950.

72. Blocki, W., "Ship safety in connection with parametric resonance of the roll," International Shipbuilding Progress 27, (1980).

73. Nayfeh, A. H., Mook, D. T., and Marshall, L. R., "Perturbation energy approach for the development of the nonlinear equations of ship motion," Journal of Hydronautics 8, 130 (1974).

74. Bird, H. and Morrall, A., "Ship stability - A research strategy," Second International Conference on Stability of Ships and Ocean Vehicles, p. 663, Tokyo, October 1982.

75. Cardo, A., Francescutto, A., and Nabergoj, R., "TECHNICAL NOTE : On damping models in free and forced rolling motion," Ocean Engineering 9, 171 (1982).

76. Mathisen, J. B. and Price, W. G., "Estimation of ship roll damping coefficients," Royal Institution of Naval Architects, p. 295 (1985).

77. Right, J. H. G. and Marshfield, W. B., "Ship roll response and capsize behavior in beam seas," Transactions Royal Institution of Naval Architects 122, 129 (1980).

78. Abicht, W., "On capsizing of ships in regular and irregular seas," Proceedings of the International Conference on Stability of Ships and Ocean Vehicles, Glasgow, (1975).

79. Kuo C. and Welaya, Y., "A review of intact ship stability research and criteria," Ocean Engineering 8, 65 (1981).

80. Wellicome. J. F., "An analytical study of the mechanism of capsizing," Proceedings of the International Conference on Stability of Ships and Ocean Vehicles, Glasgow (1975).

81. Cardo A. and Trincas, G., "A multiscale analysis of nonlinear rolling," Ocean Engineering 14, 83 (1987).

82. Cardo, A., Francescutto, A., and Nabergoj, R., ″Subharmonic oscillations in nonlinear rolling,″ Ocean Engineering 11, 663 (1984).

83. Nayfeh, A. H. and Sanchez, N. E., ″Chaos and dynamic instabilities in the rolling motion of ships,″ Proceedings of the Seventeenth Symposium on Naval Hydrodynamics, The Hague, The Netherlands (1988).

84. Virgin, L. N., ″The nonlinear rolling response of a vessel including chaotic motions leading to capsize in regular seas,″ Applied Ocean Research 9, 89 (1987).

85. Kuo, C. and Odabasi, A. Y., ″Application of dynamic systems approach to ship and ocean vehicle stability,″ International Conference on Ship and Ocean Vehicles, Glasgow (1975).

86. Özkan, R. ″Total (practical) stability of ships,″ Ocean Engineering 8, 551 (1981).

87. Odabasi, A. Y., ″A morphology of mathematical stability theory and its application to intact ship and ocean stability assessment,″ Proceedings of the Second International Conference on Stability of Ships and Ocean Vehicles, p. 47, Tokyo (1982).

88. Skomedal, N. G., "Parametric excitation of roll motion and its influence on stability," Second International Conference on Stability of Ships and Ocean Vehicles, SIII-3a, October 1982.

89. Moon, F. C., **Chaotic Vibrations**, Wiley, New York, 1987.

90. Grebogi, C., Ott, E., and Yorke, J. A., "Chaotic attractors in crises," Physical Review Letters 48, 1507 (1982).

91. Paulling, J. R., Kastner, S. and Schaffran, S., "Experimental studies of capsizing of intact ships in heavy seas," Department of Naval Architecture, University of California, Berkeley, CA, 1972.

TABLES AND FIGURES

Table 1. Coefficients of ship model considered.

I	K	ω_0	μ	μ_3	$\frac{\alpha_3}{\omega_0^2}$	$\frac{\alpha_5}{\omega_0^2}$	δI
mK^2	$110.mm$	5.278	0.086	0.108	−1.402	0.271	$0.25I$

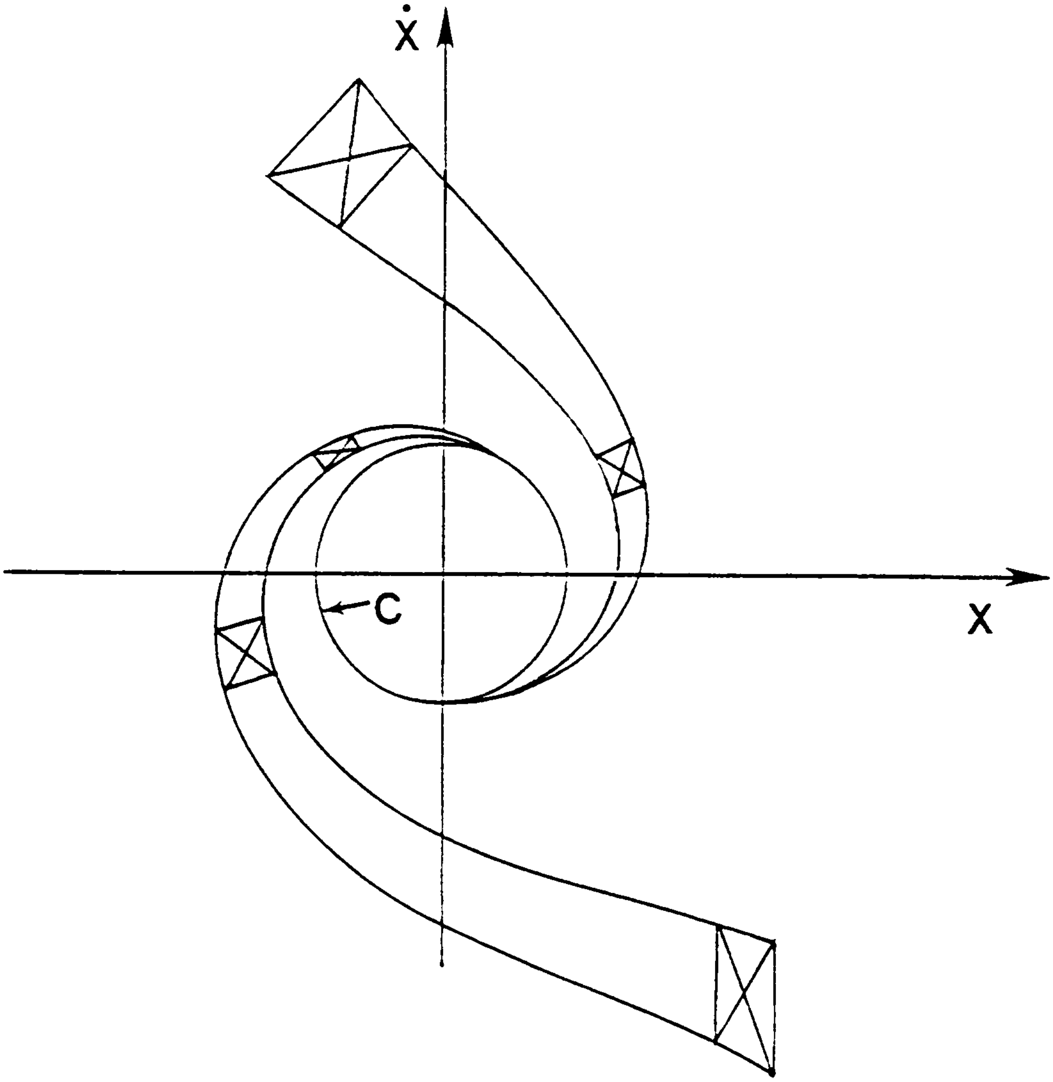

Figure 2.1 Limit cycle of a dissipative system. The contraction of areas of phase space is illustrated.

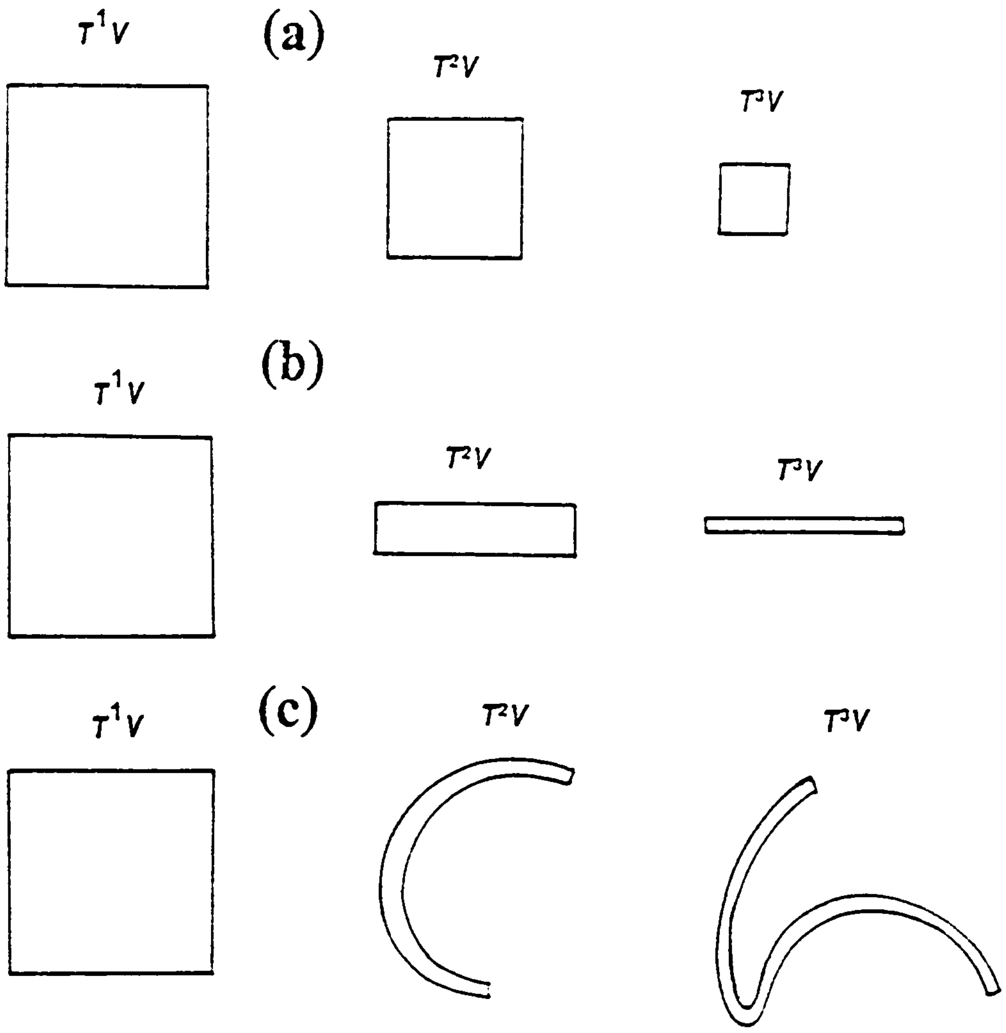

Figure 2.2 Contraction of volume in phase space ; (a) All legths are contracted, (b) Only one dimension is contracted, (c) There is stretching and folding.

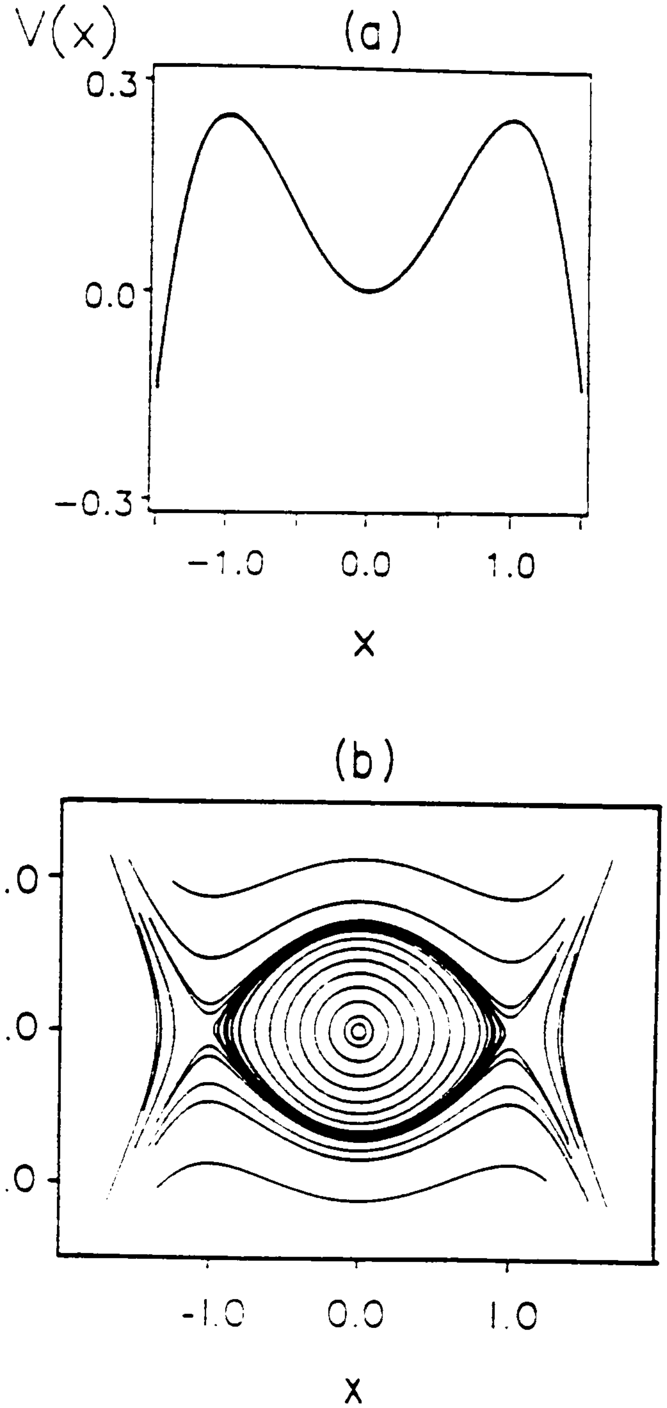

Figure 3.1 (a) Potential well $V(x) = \frac{1}{2}x^2 - \frac{1}{4}x^4$. (b) Phase diagram of oscillator $\ddot{x} + x - x^3 = 0$.

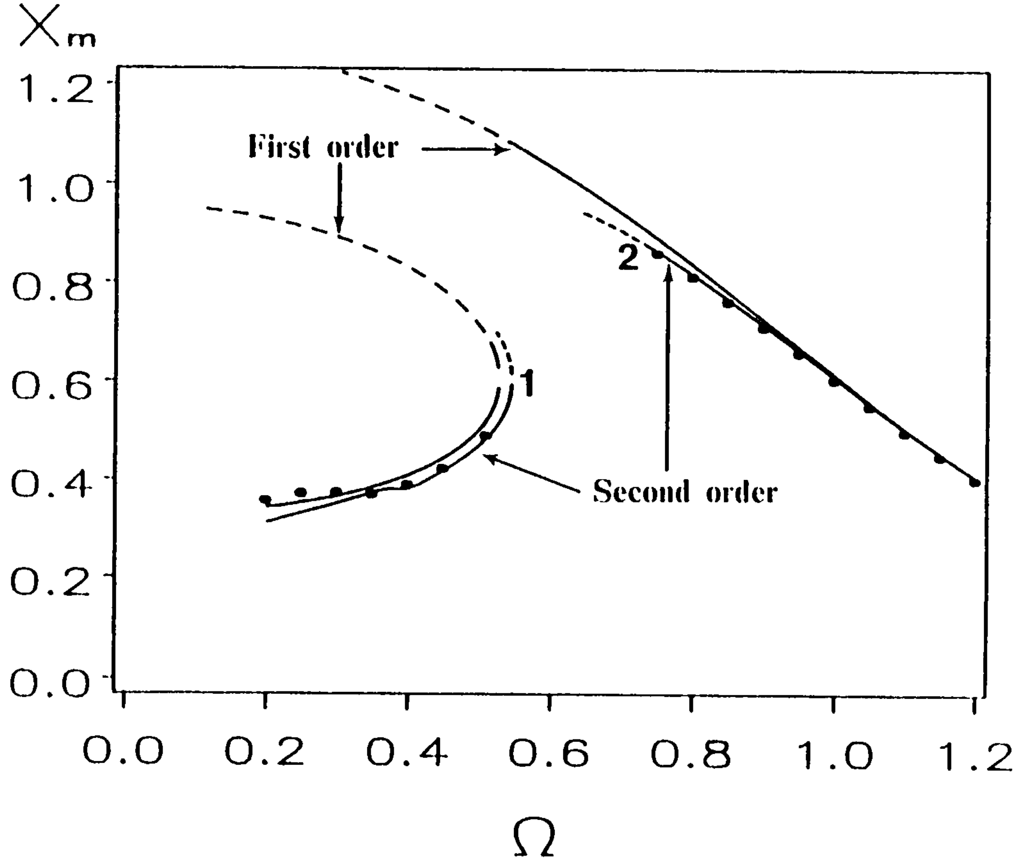

Figure 3.2 Frequency response curve calculated using the first- and second-order approximate solutions. Dashed curves represent unstable solutions. The circles show the results from numerical integration.

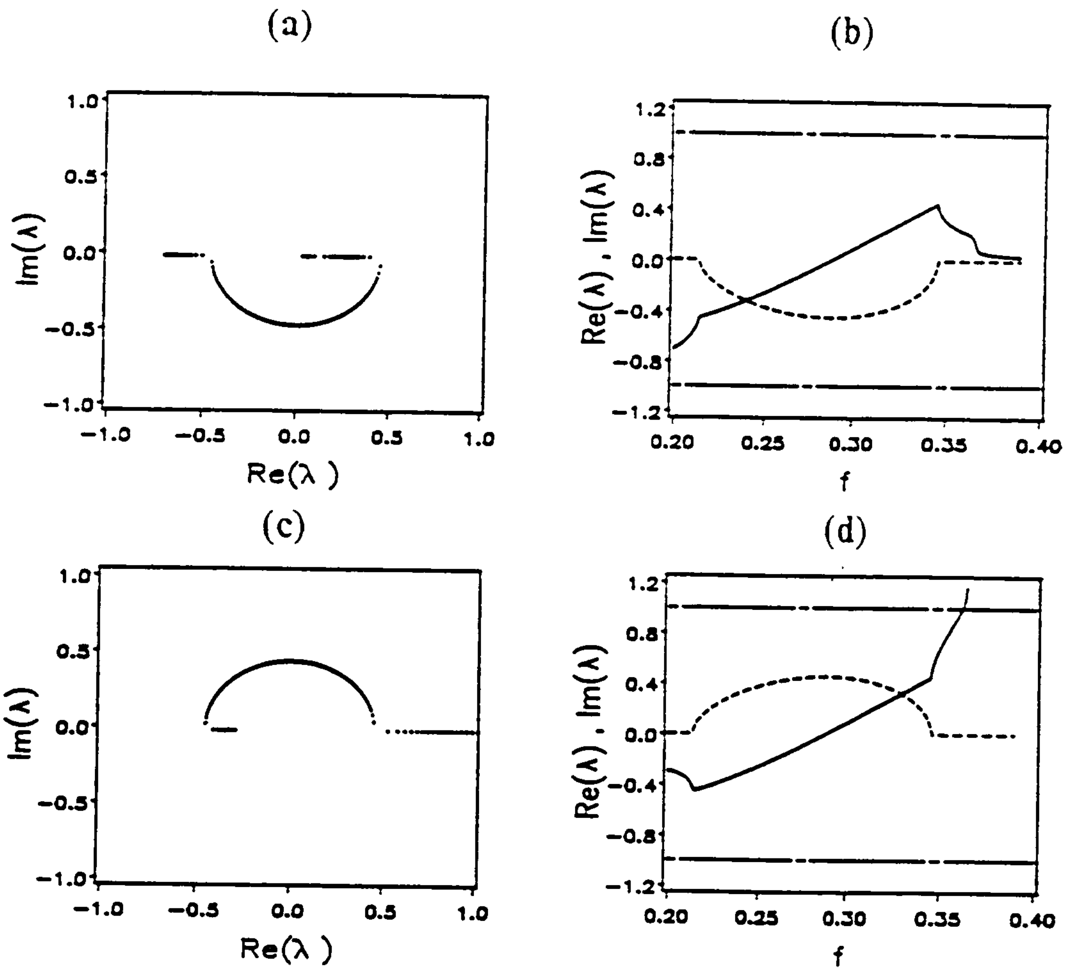

Figure 3.3 Floquet multipliers for $\Omega = 0.8$, $\mu = 0.2$, $\alpha = 1.0$, and increasing f : (a) behavior of λ_1 in the complex plane, (b) real (solid) and imaginary (dashed) parts of λ_1. The horizontal lines at +1 and -1 enclose the stable region, (c) λ_2 shows a pitchfork in the complex plane, and (d) real and imaginary parts of λ_2.

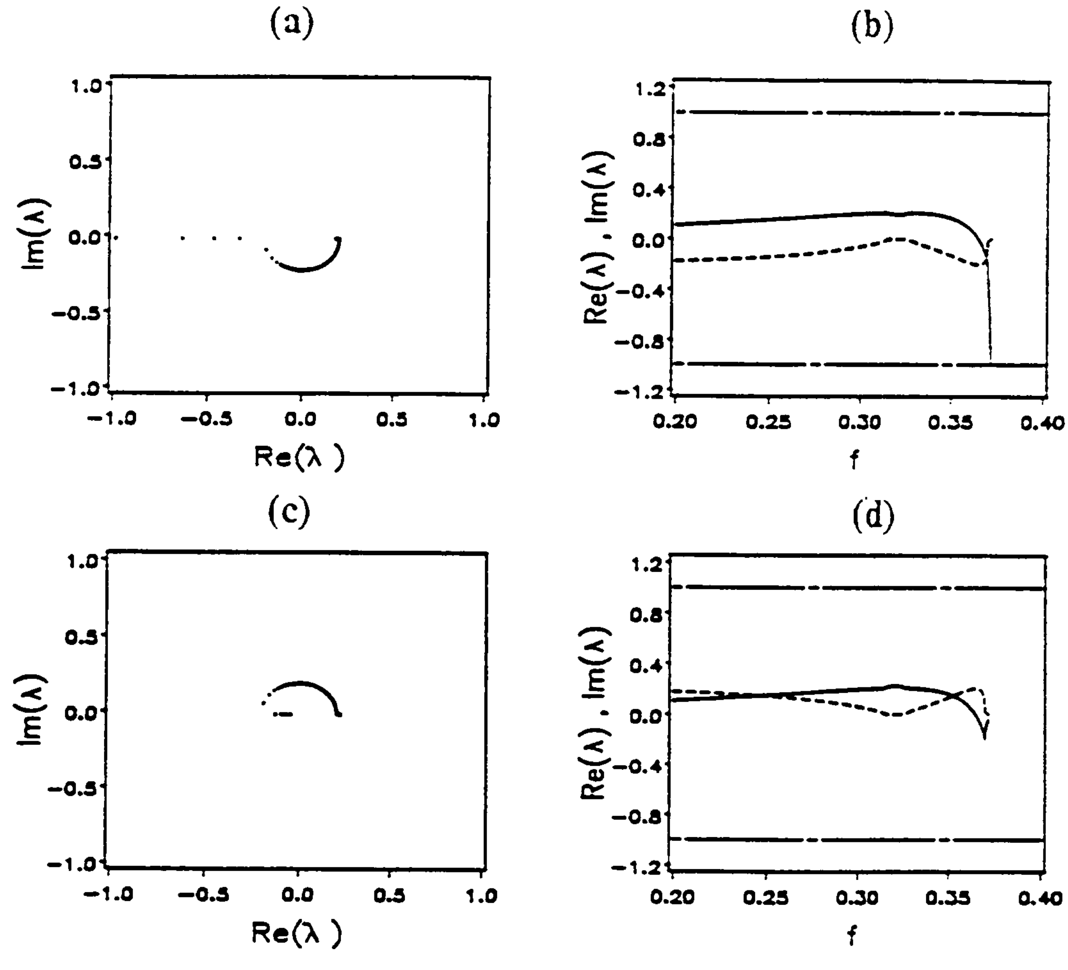

Figure 3.4 Floquet multipliers for $\Omega = 0.4$, $\mu = 0.2$, $\alpha = 1.0$, and increasing f: (a) λ_1 shows a saddle-node behavior in the complex plane, (b) real (solid) and imaginary (dashed) parts of λ_1, (c) behavior of λ_2 in the complex plane, and (d) real and imaginary parts of λ_2.

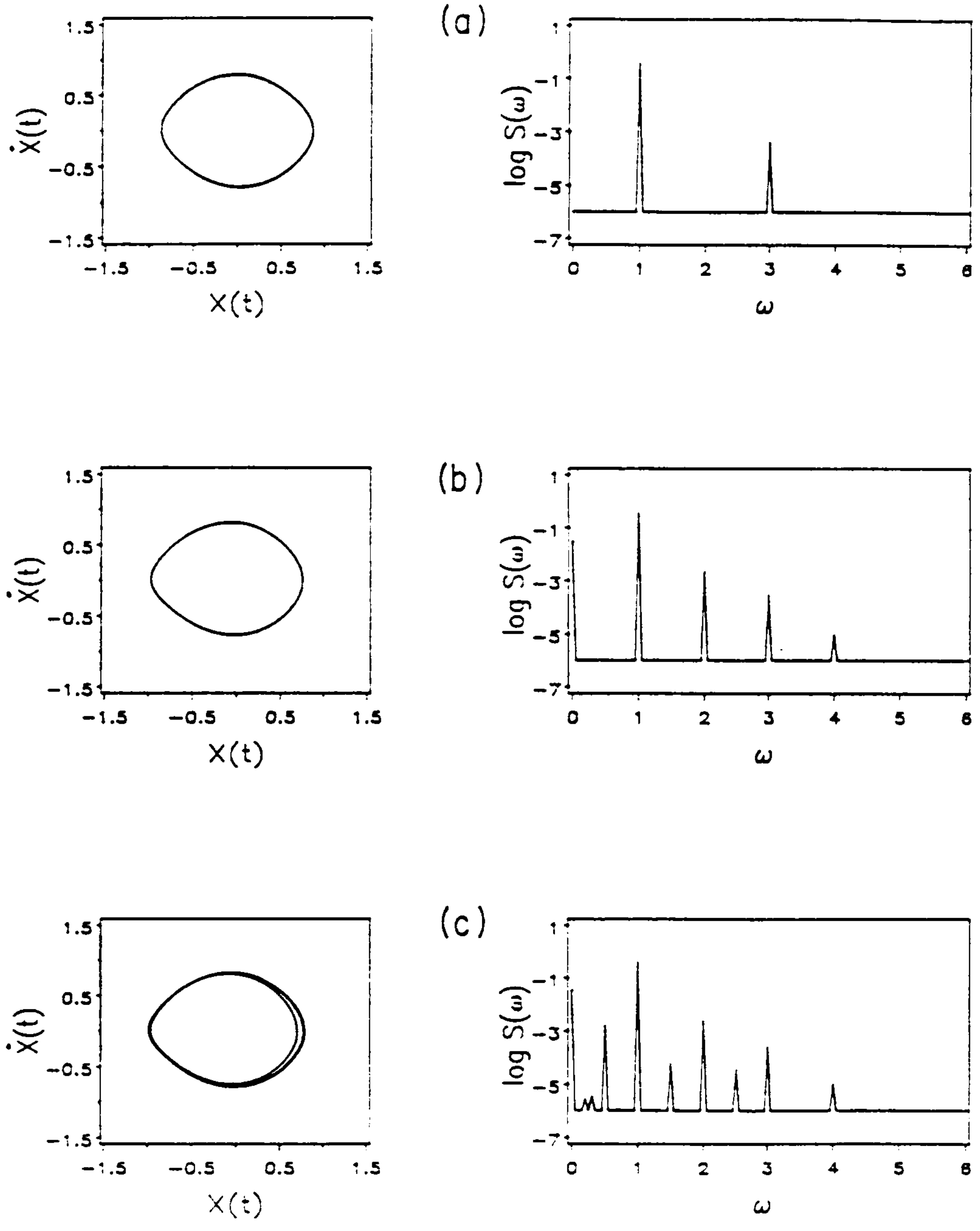

Figure 3.5 Typical orbits and spectra for $\Omega = 0.8$, $\mu = 0.2$, $\alpha = 1.0$: (a) f = 0.350, symmetric solution, (b) f = 0.380, asymmetric solution, and (c) f = 0.386, 2T-periodic solution.

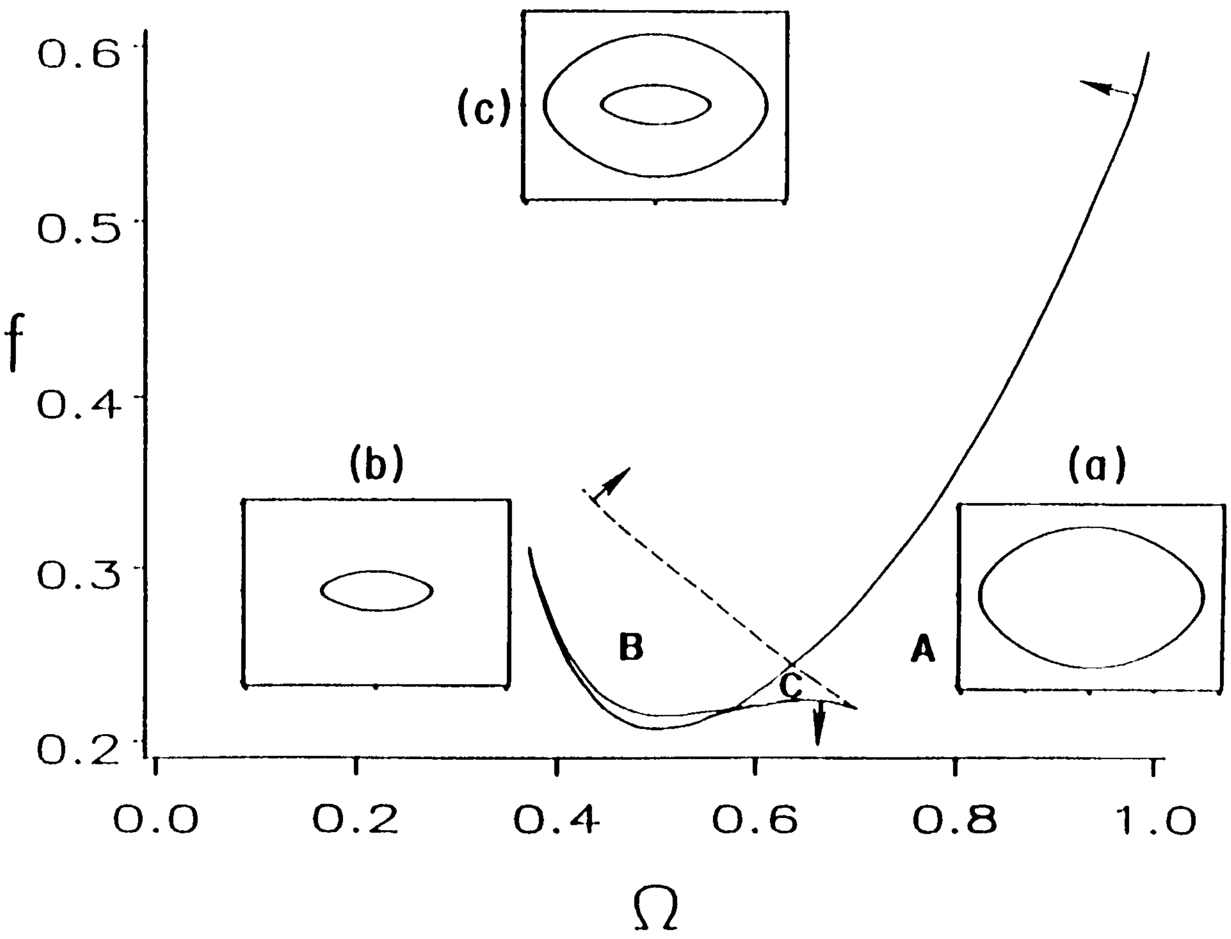

Figure 3.6 Bifurcation diagram of the approximate T-periodic multiple-scales solution for $\mu = 0.2$, $\alpha = 1.0$. All curves represent saddle-node or pitchfork bifurcations. Inserts show existing attractors in A, B, and C. Arrows point the direction in which the bifurcations are active.

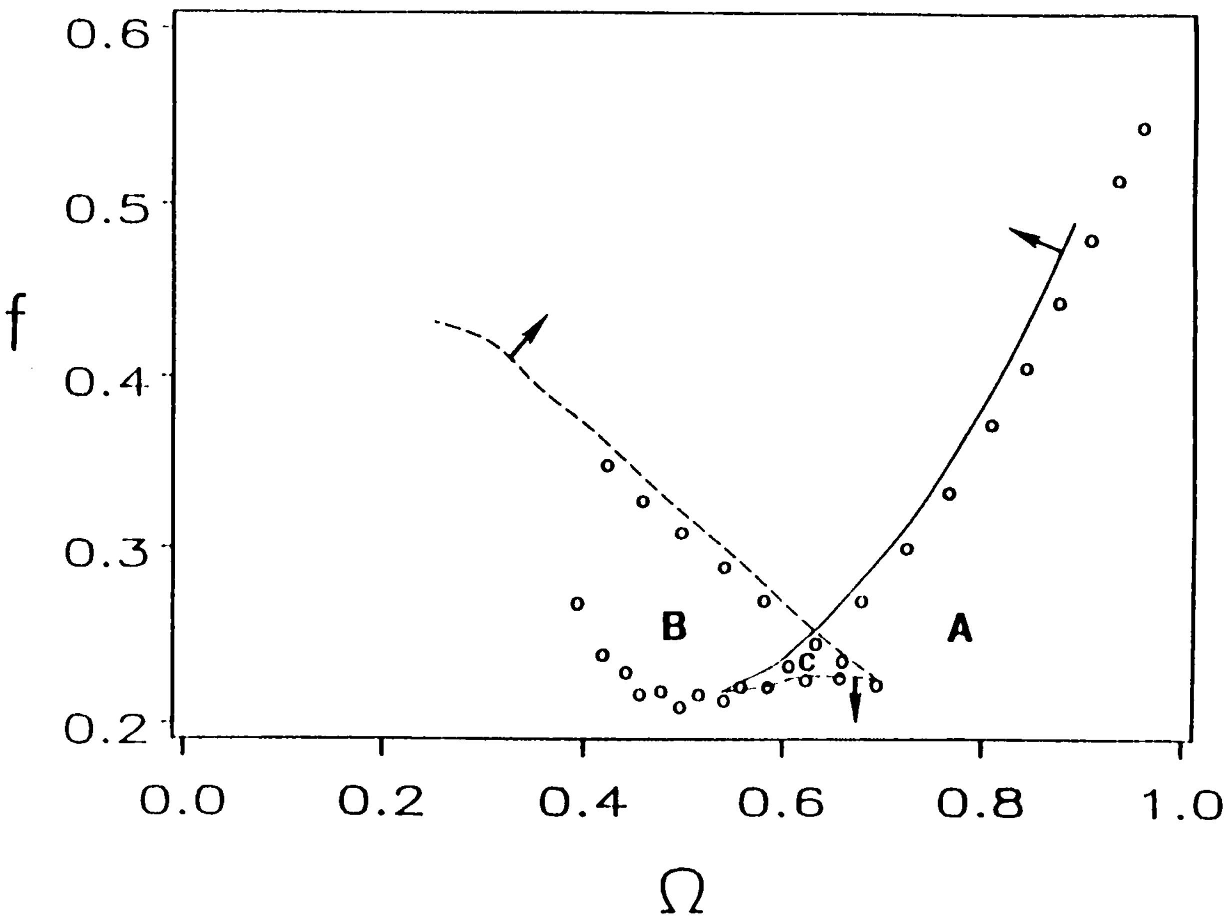

Figure 3.7 Bifurcation diagram of the approximate T-periodic asymmetric solution for $\mu = 0.2$, $\alpha = 1.0$. Harmonic balance results are shown in solid (period-doubling) and dashed (saddle-node) curves. Circles show the results in Figure 3.6.

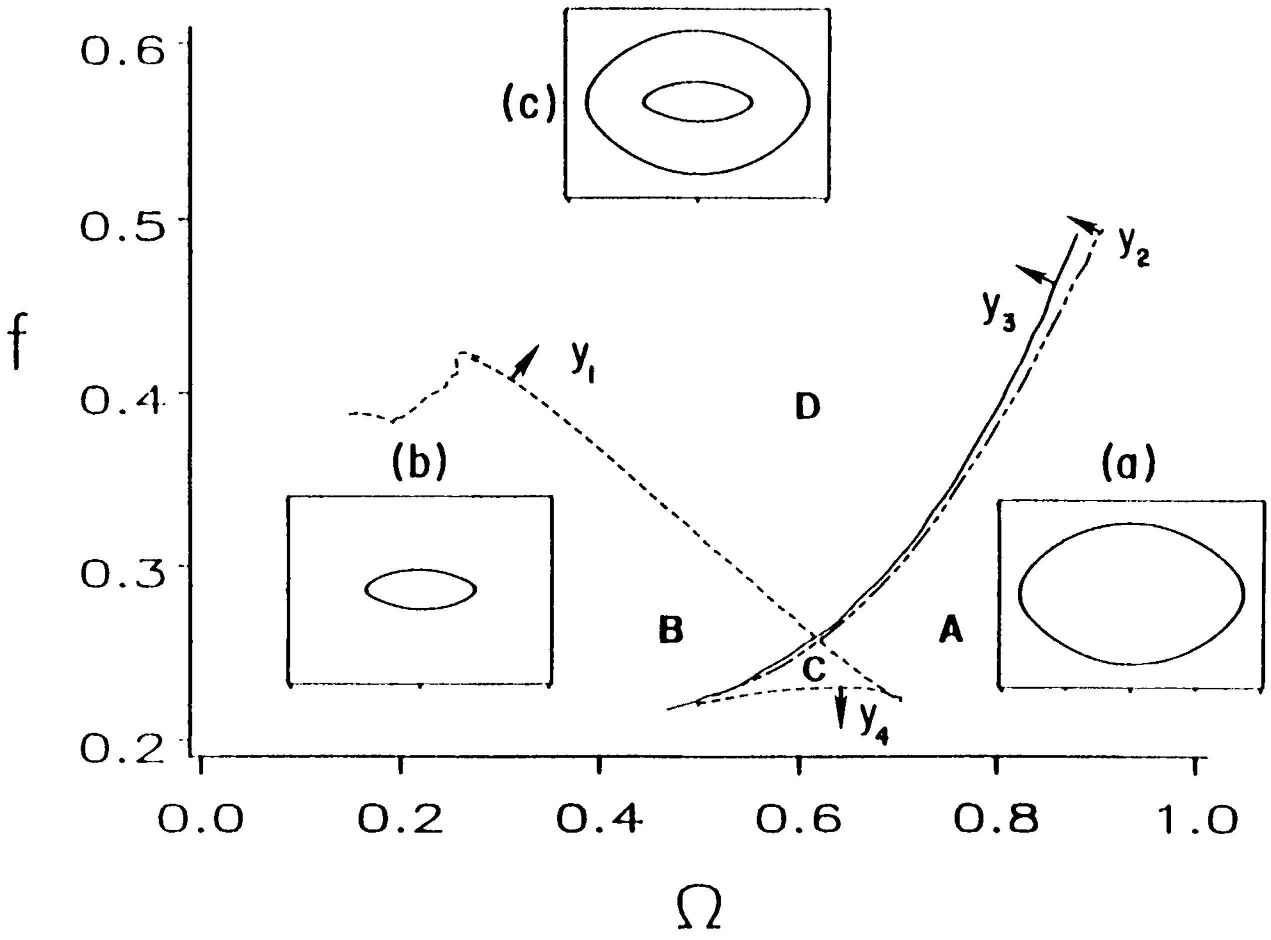

Figure 3.8 Bifurcation diagram generated from analog-computer simulations.

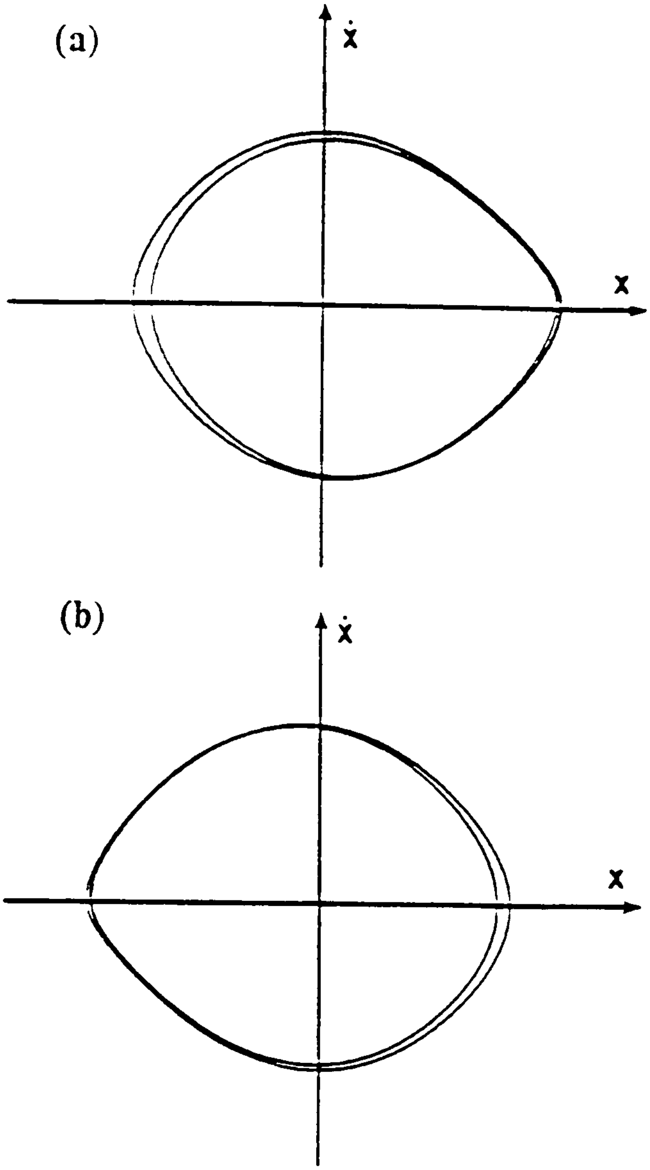

Figure 3.9 Asymmetric attractors observed in the analog-simulation.

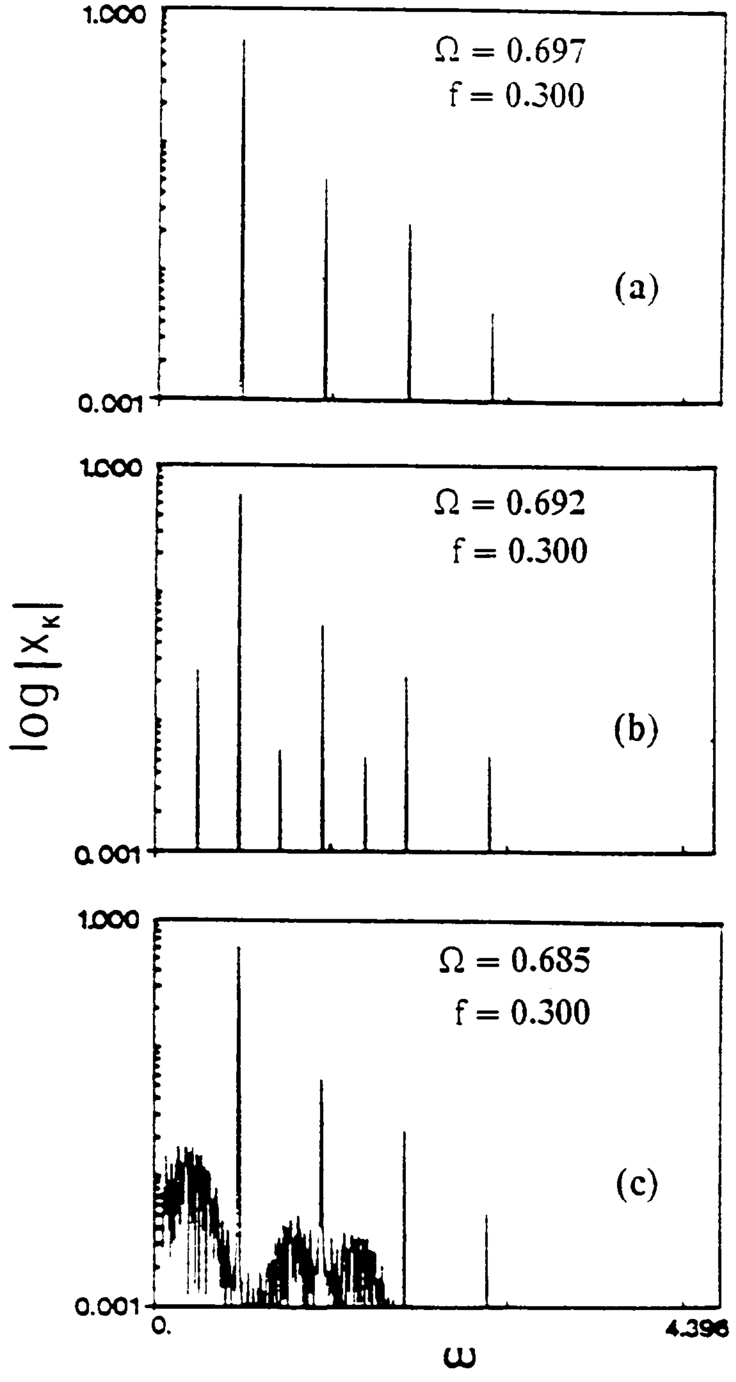

Figure 3.10 Spectra of solution in the transition to chaos: (a) T-periodic asymmetric solution, (b) 2T-periodic asymmetric solution, and (c) chaotic solution.

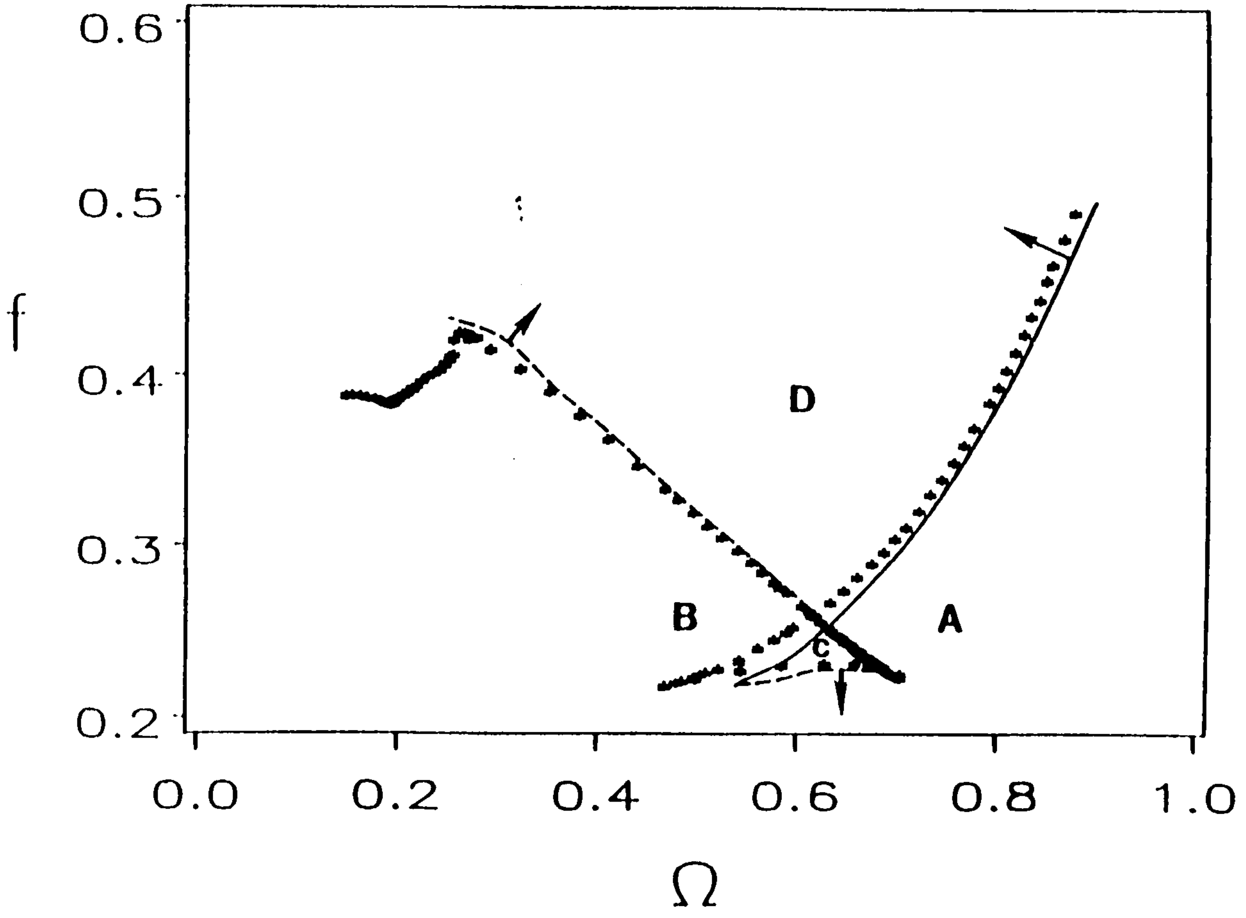

Figure 3.11 Bifurcation diagram shows predicted period-doubling curve (solid), saddle-node curves (dashed) and observed bifurcations from analog-computer simulation (stars).

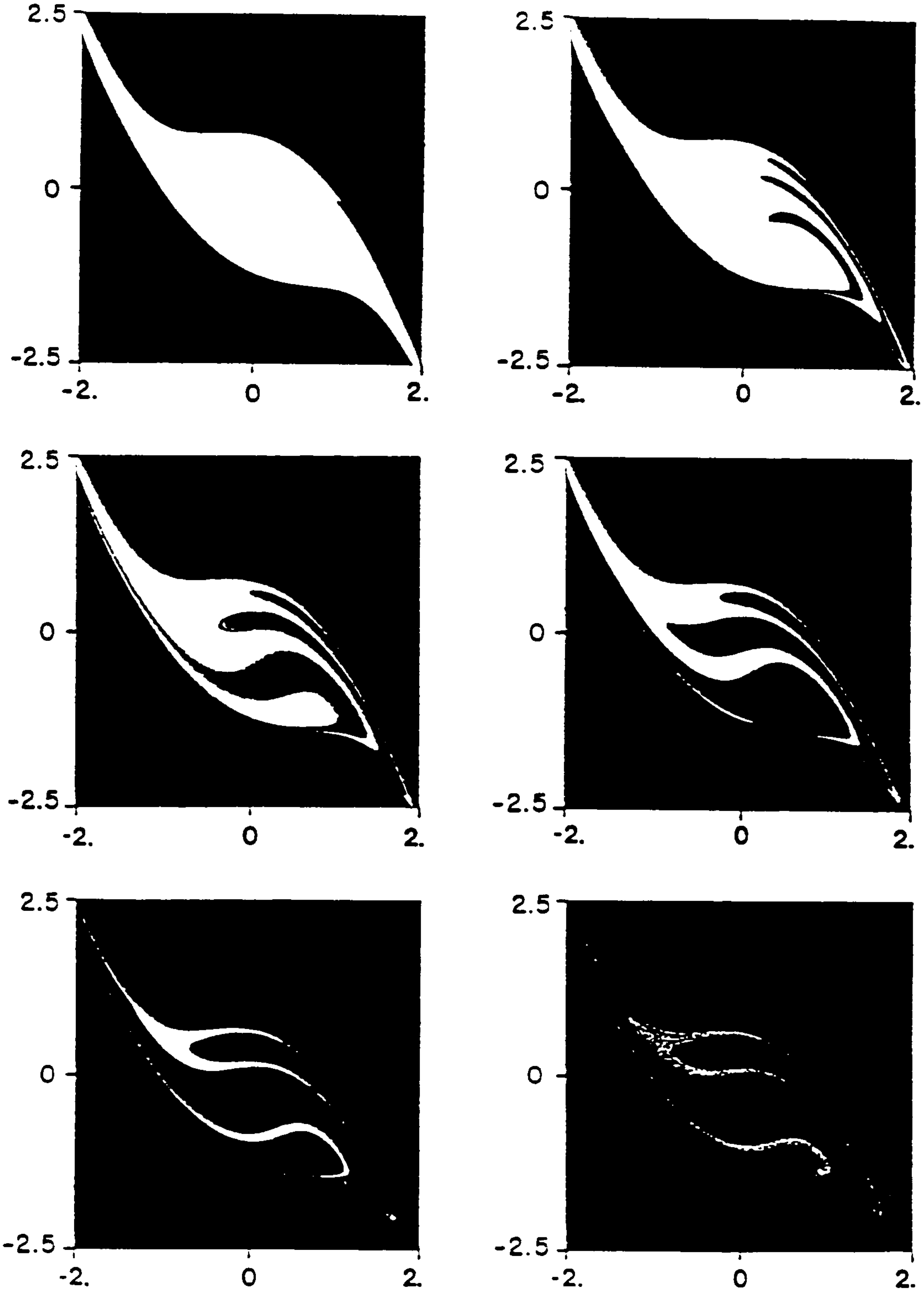

Figure 3.12 Basin boundary metamorphoses for $\Omega = 0.3$. f increases from left to right and from top to bottom in the sequence (0.30, 0.32, 0.33, 0.345, 0.38, 0.394).

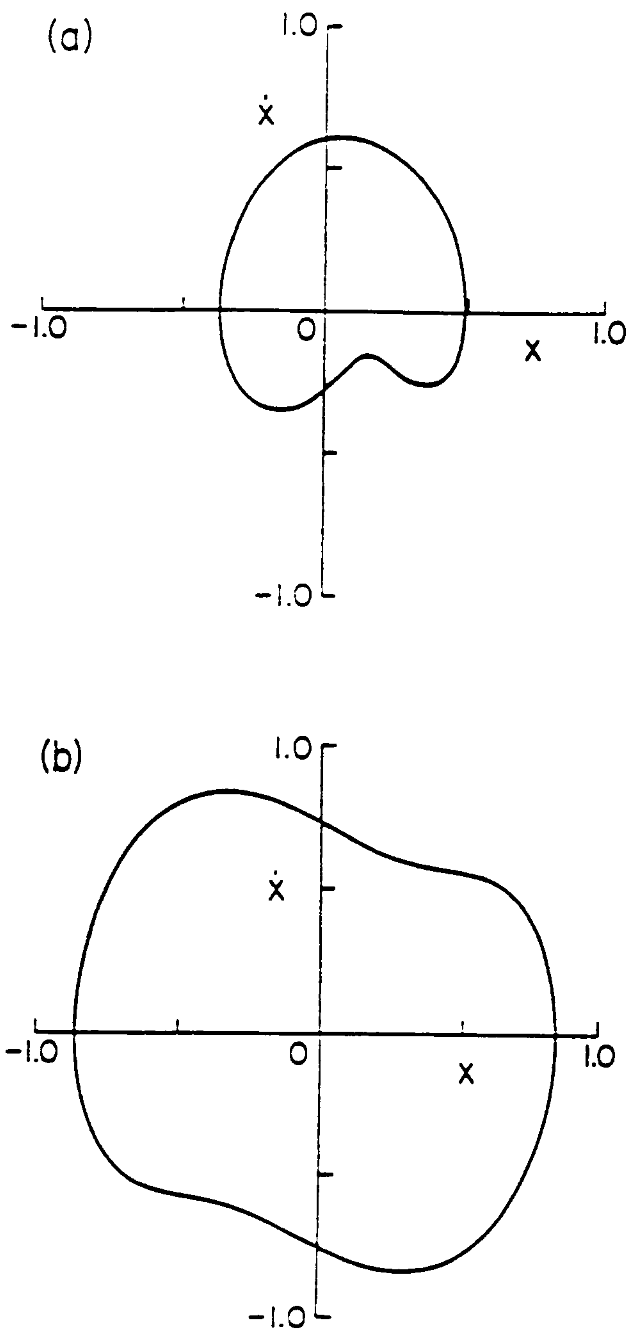

Figure 4.1 Perturbation solutions: (a) fundamental parametric response for $\Omega = 1.0$ and $g = 1.8$ and (b) principal parametric response for $\Omega = 2.0$ and $g = 1.27$.

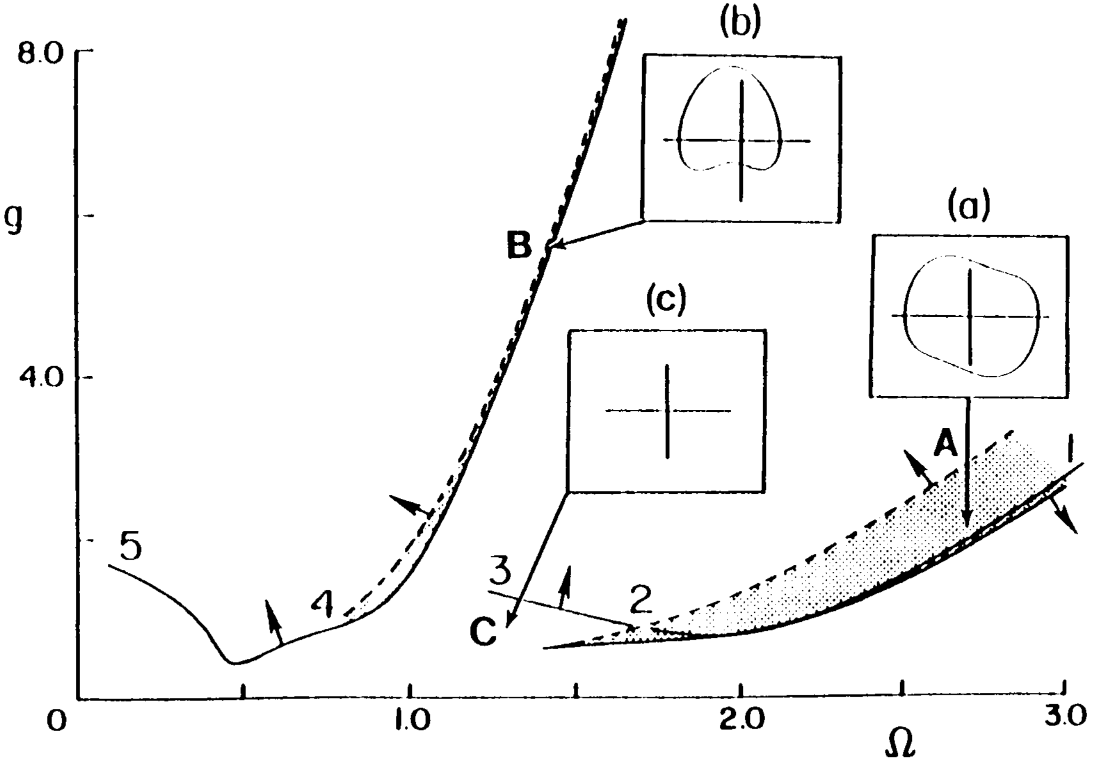

Figure 4.2 Predicted bifurcation diagram. Inserts (a)-(c) show the stable attractors in regions A, B, and C. Dotted areas represent stable domains for periodic attractors. All curves represent the locus of bifurcations.

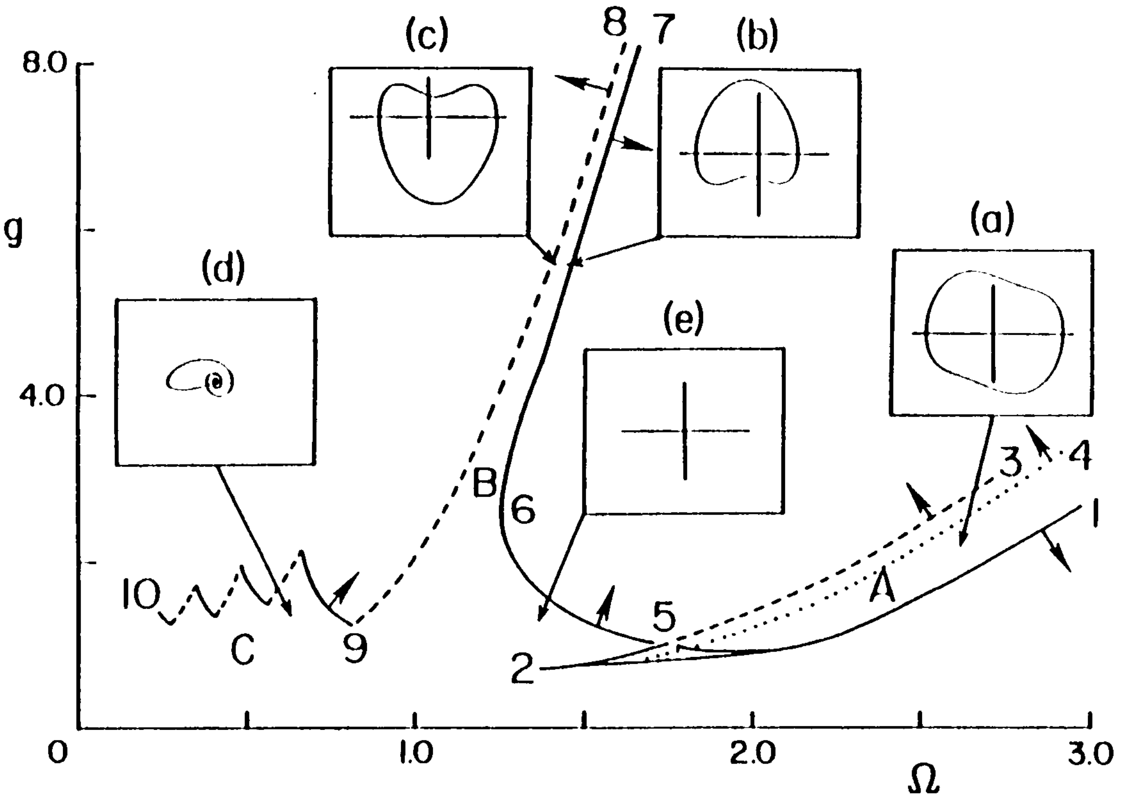

Figure 4.3 Bifurcation diagram obtained using analog-computer simulations. Inserts (a)-(d) show the types of attractor found. Dashed curves correspond to destruction of the chaotic attractor and escape. Dotted curves correspond to period-doubling bifurcations and solid curves represent saddle-node and pitchfork instabilities.

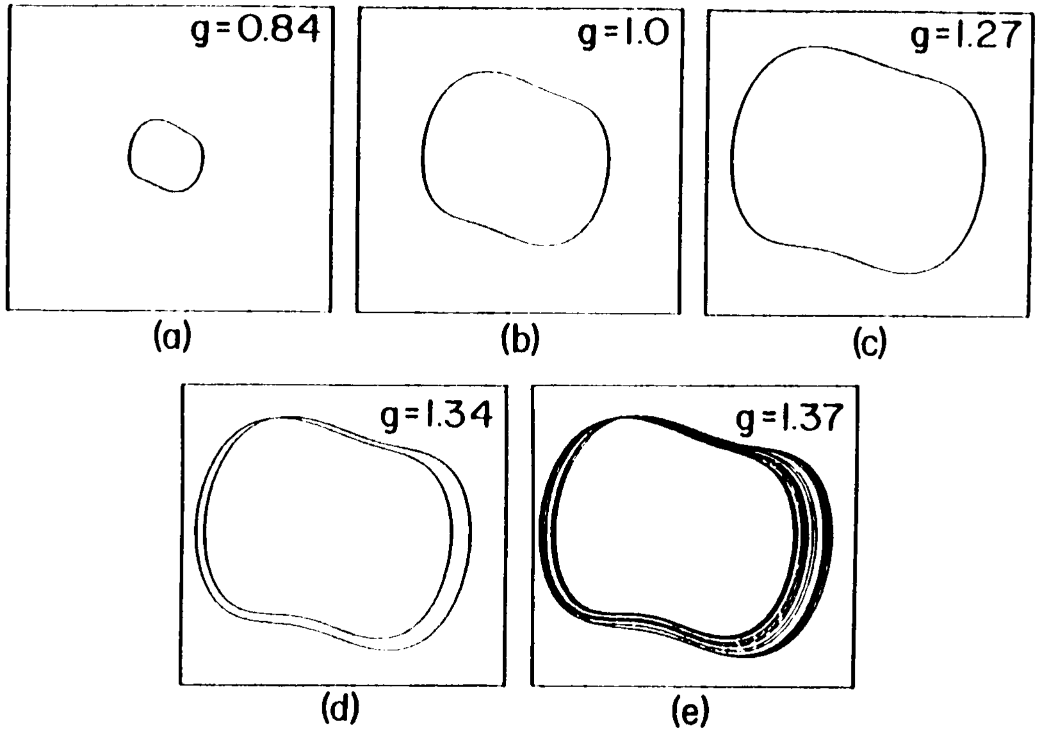

Figure 4.4 Principal parametric responses obtained using an analog-computer simulation for $\Omega = 2.0$: (a)-(c) increasing in amplitude of excitation, (d) period-doubling bifurcation, and (e) chaos.

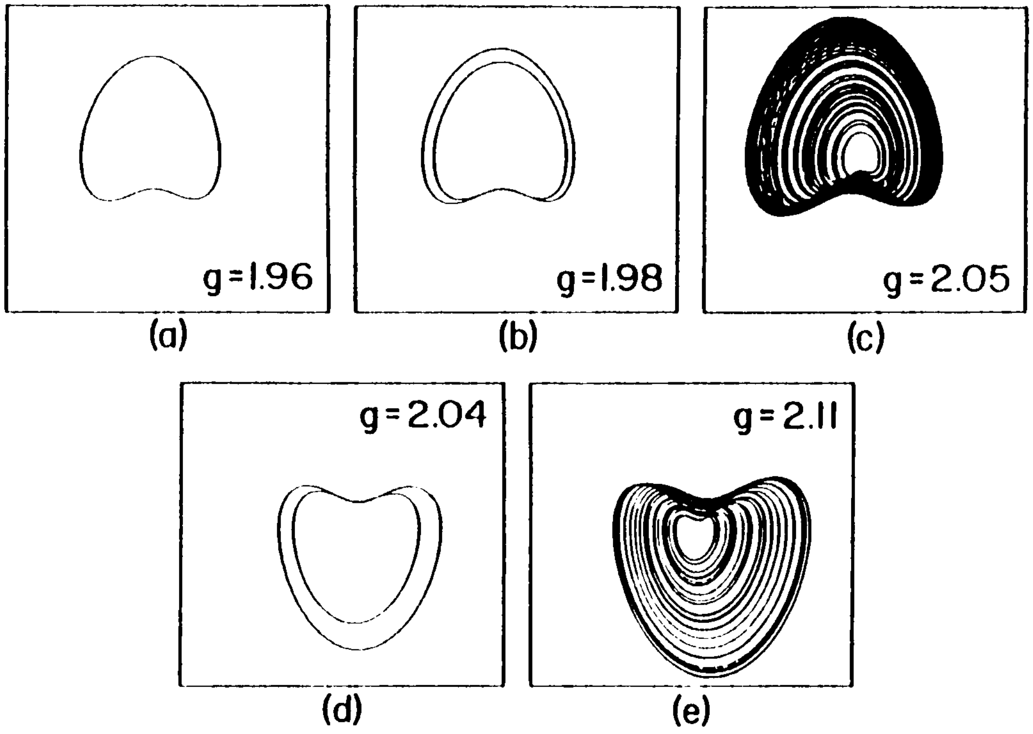

Figure 4.5 Fundamental parametric responses obtained using an analog- computer simulation for $\Omega = 1.0$: (a)-(c) period-doubling cascade leading to chaos and (d)-(e) second cascade on the inverted attractor.

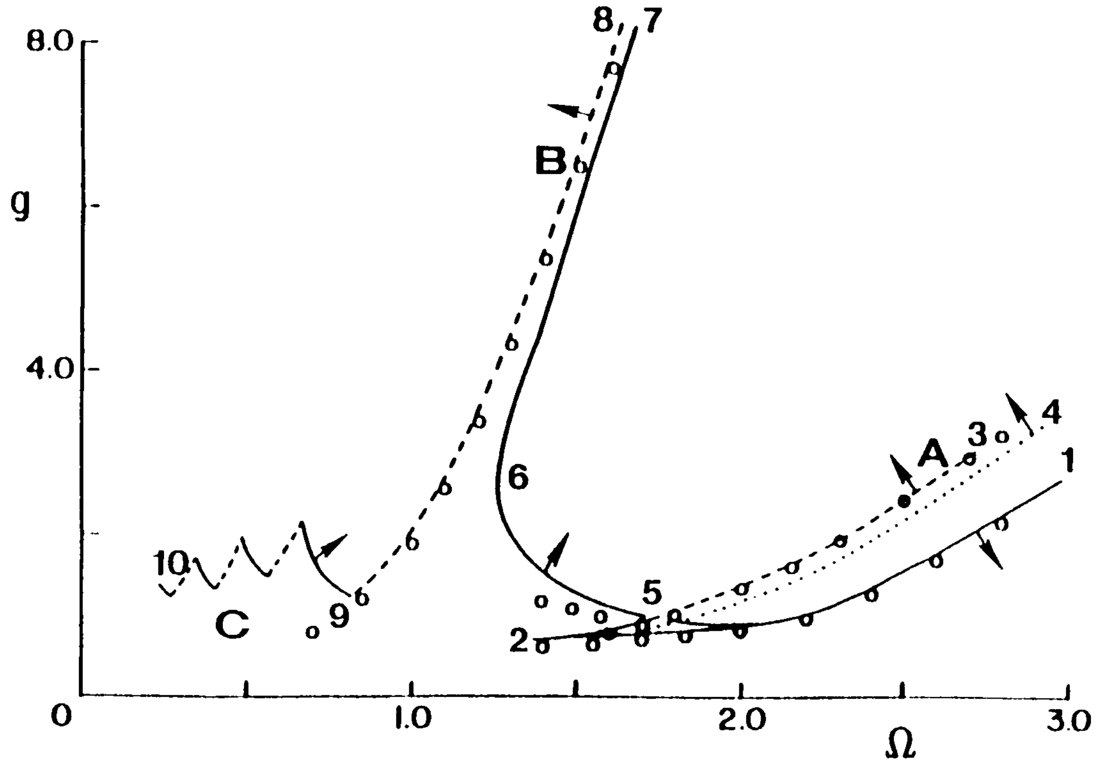

Figure 4.6 Comparison between the results of analog-computer simulation and the analytical predictions. Circles show the analytical predictions given in Figure 4.2, which have been superimposed on the analog-computer results of Figure 4.3.

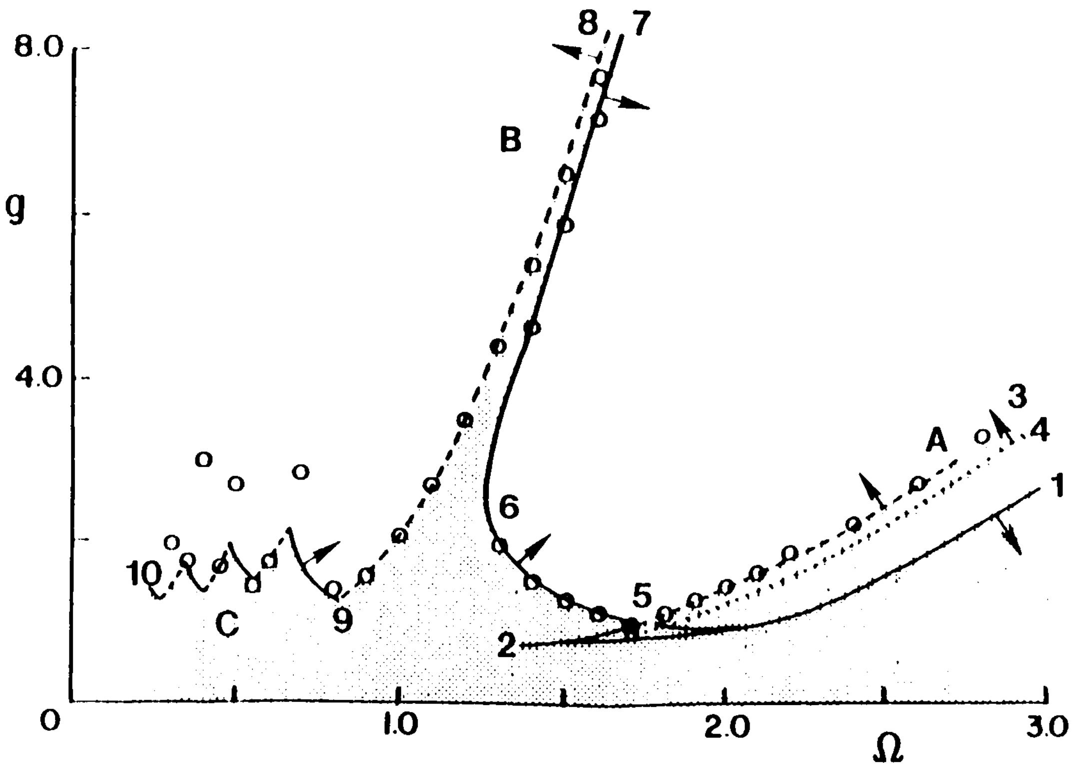

Figure 4.7 Digital-computer predictions of escape (represented by circles) are compared with the analog-computer results of Figure 4.2. Dotted area encloses the space of unbounded solutions.

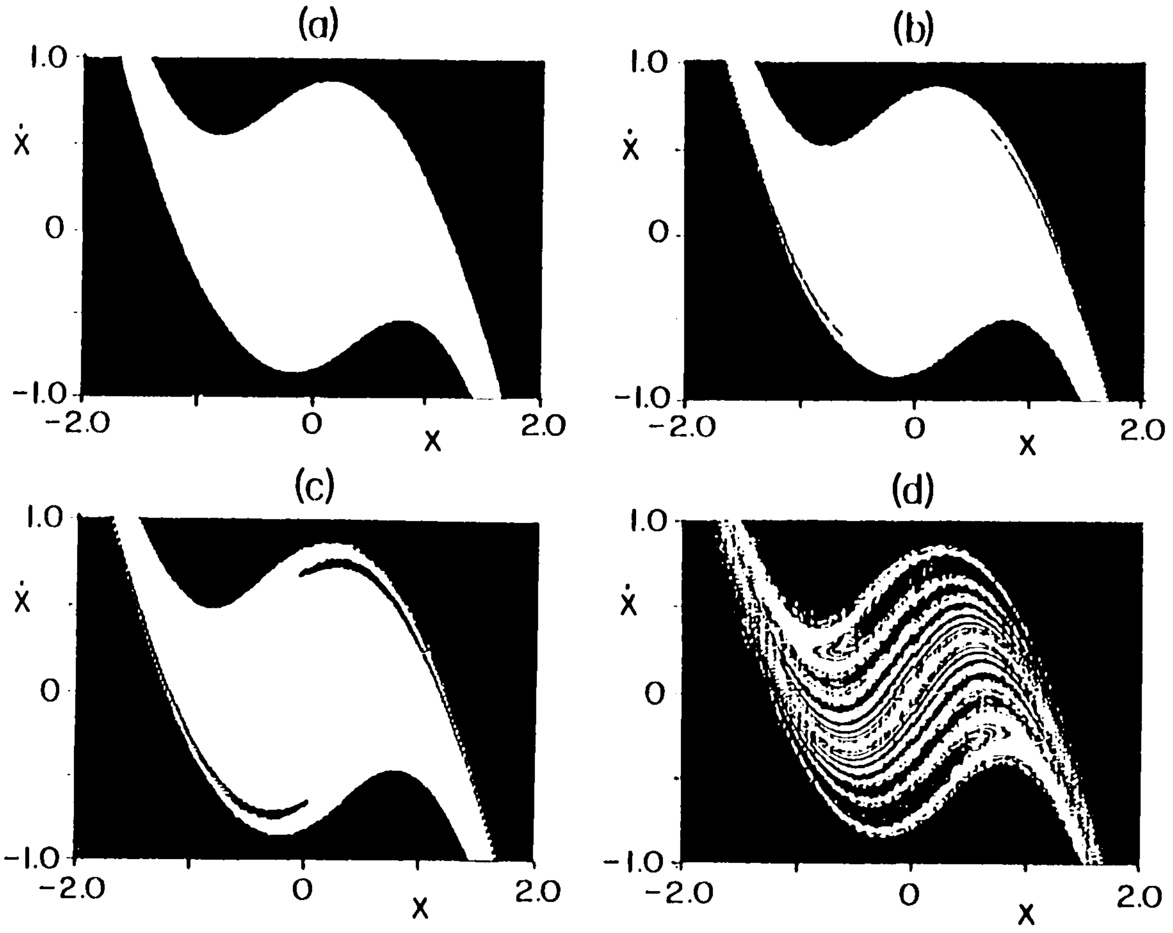

Figure 4.8 Basin-boundary metamorphoses for the principal parametric response for $\Omega = 2.0$. The white areas represent the basin of attraction of bounded solutions, whereas the black portions represent the basin of attraction of unbounded solutions for (a) $g = 1.15$, (b) $g = 1.21$, (c) $g = 1.3$, and (d) $g = 1.41$.

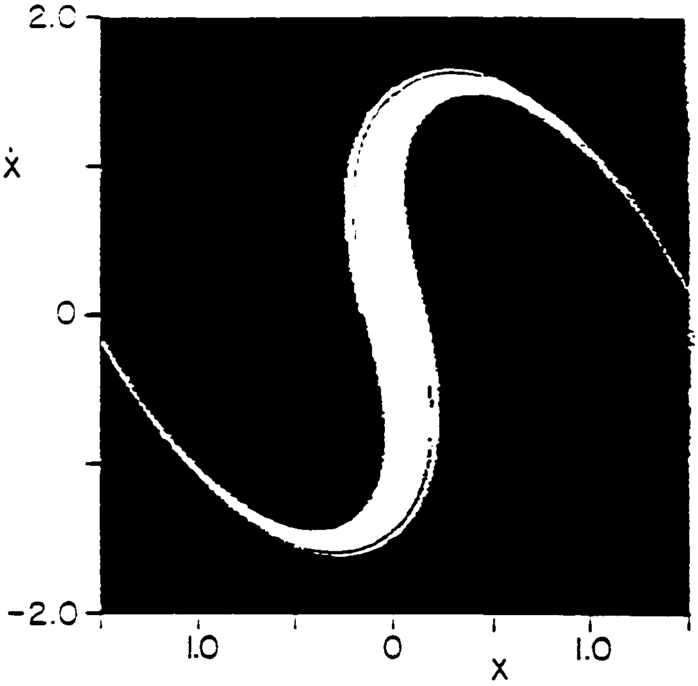

Figure 4.9 Basin of attraction for the fundamental parametric response for $\Omega = 1.0$ and $g = 2.0$. The black region represents the basin of attraction of unbounded solutions, whereas the white region represents the basin of attraction of bounded solutions.

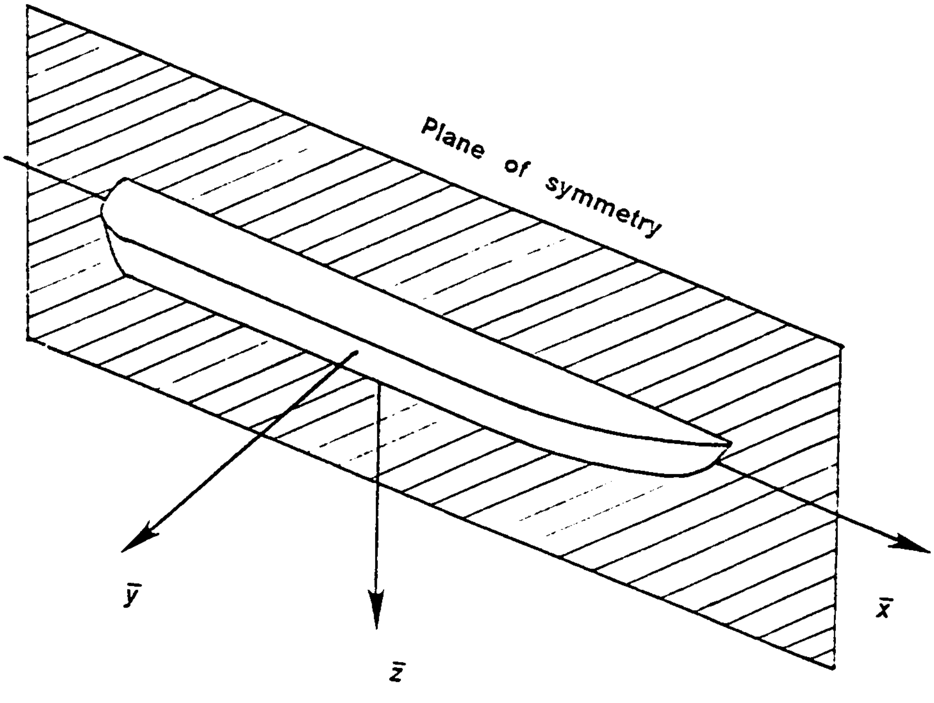

Figure 5.1 Body axes and plane of symmetry of ship

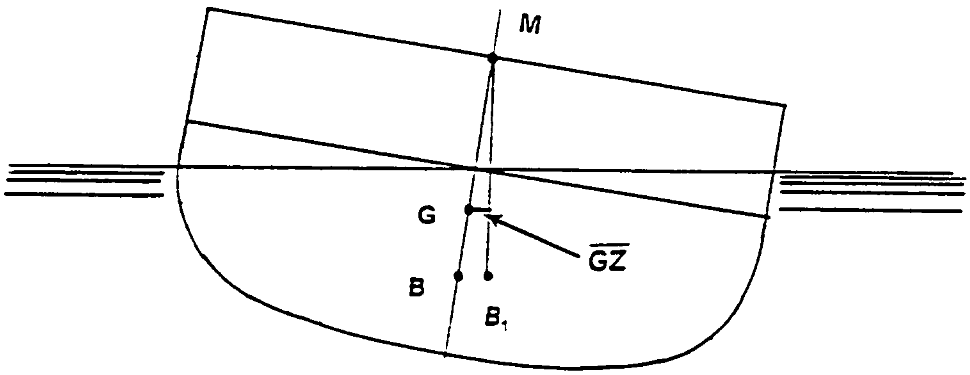

Figure 5.2 Stable equilibrium of inclined ship. The arm of the buoyancy force $\overline{GZ}$ is called righting arm.

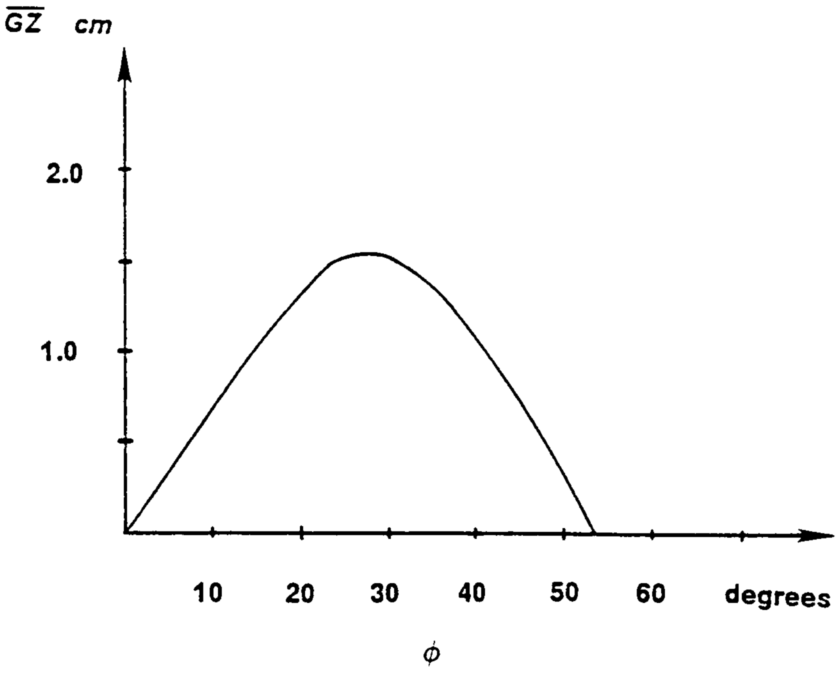

Figure 5.3 Static stability curve. or $\overline{GZ}$ curve.

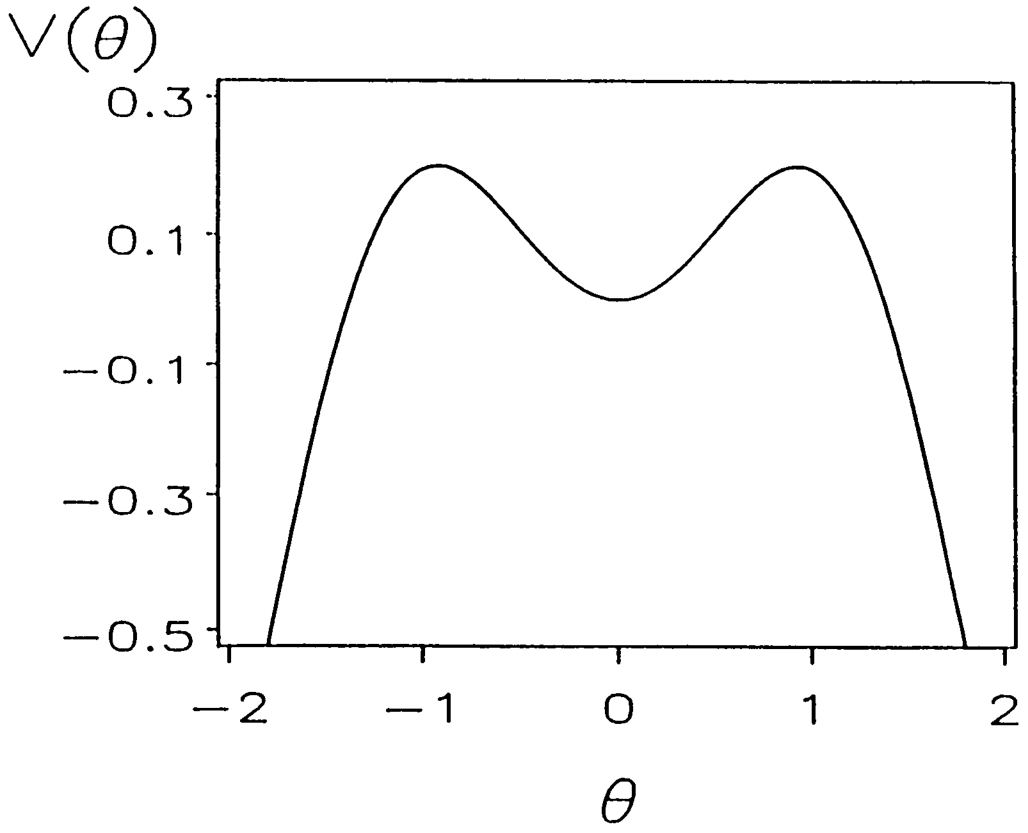

Figure 6.1. Potential function for the unbiased undamped rolling oscillation.

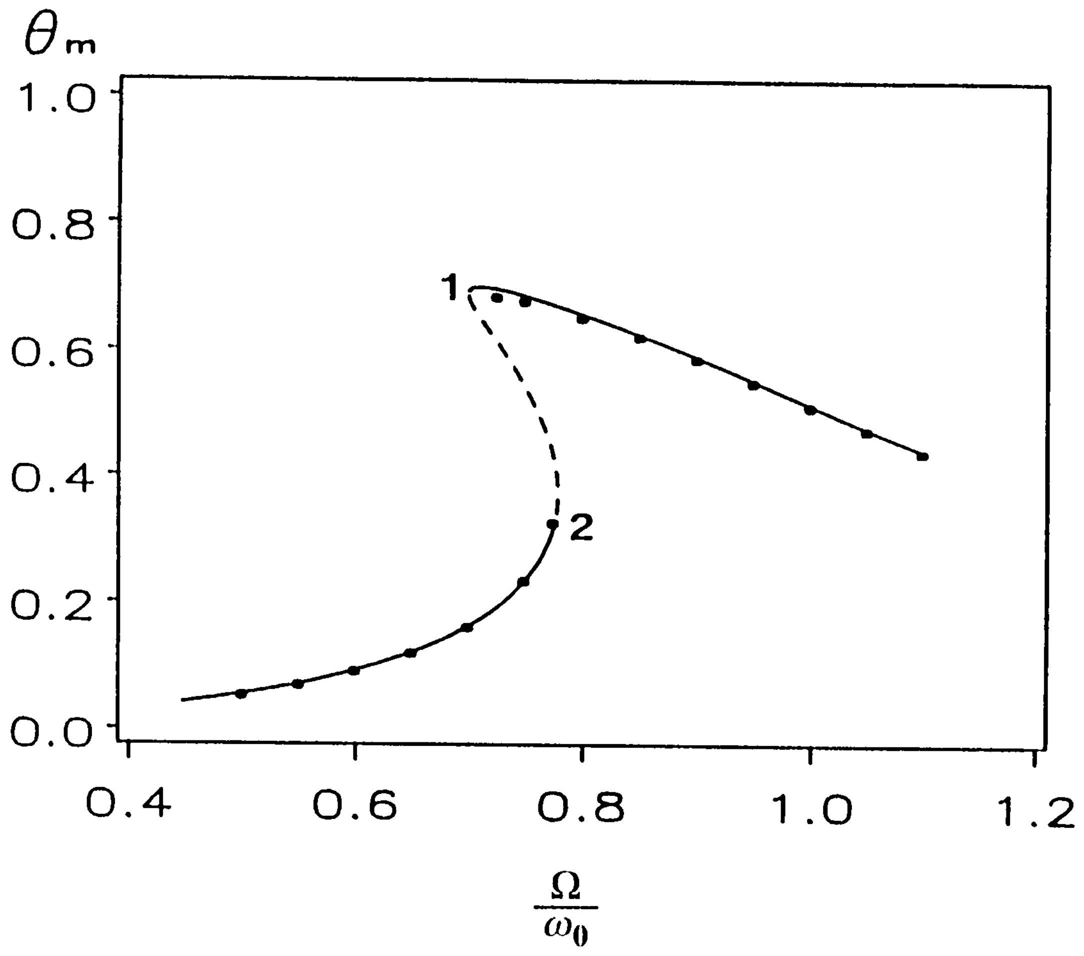

Figure 6.2. A frequency-response curve for the unbiased ship computed using the second-order approximate solution. Tangent instabilities are found at locations 1 and 2. The black circles indicate the results obtained from direct numerical integrations. The dashed curve represents unstable solutions.

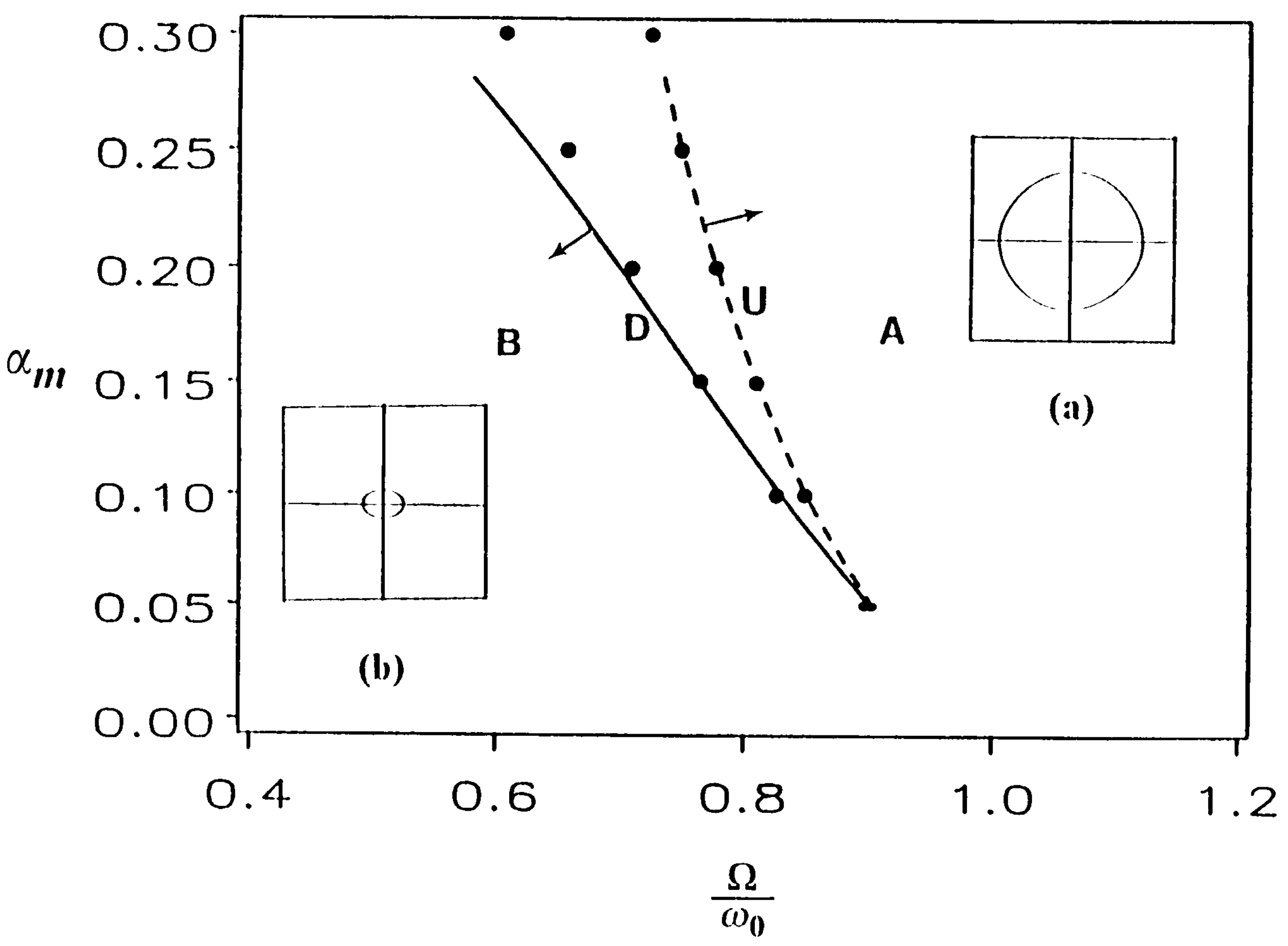

Figure 6.3. A bifurcation diagram for the unbiased ship computed from the stability analysis. It shows the locus of instabilities. The inserts show the attractors obtained in regions A and B when the initial conditions are set appropriately. The black circles indicate the results from direct numerical integrations.

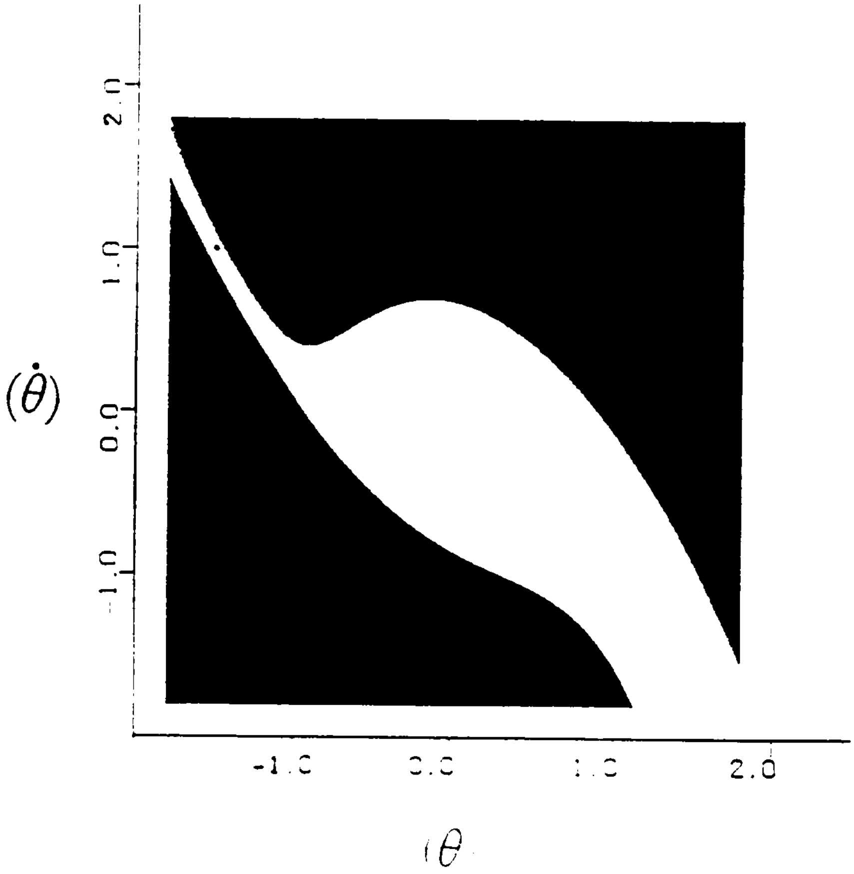

Figure 6.4. Domains of attraction of oscillatory (white) and capsizing (black) solutions for $\Omega = 0.7$ and $\alpha_m = 0.2$.

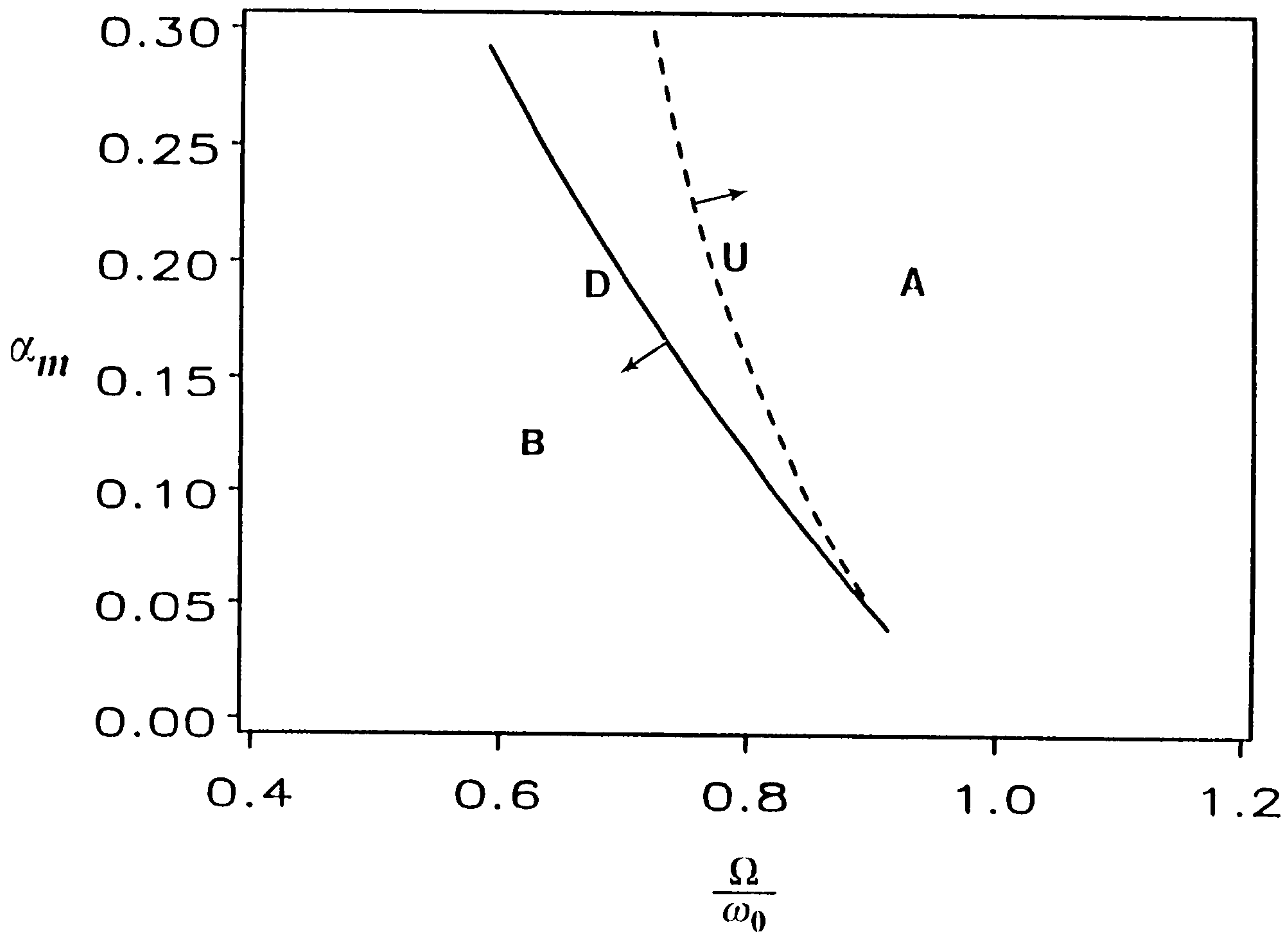

Figure 6.5. A bifurcation diagram for the unbiased ship obtained using analog-computer simulations.

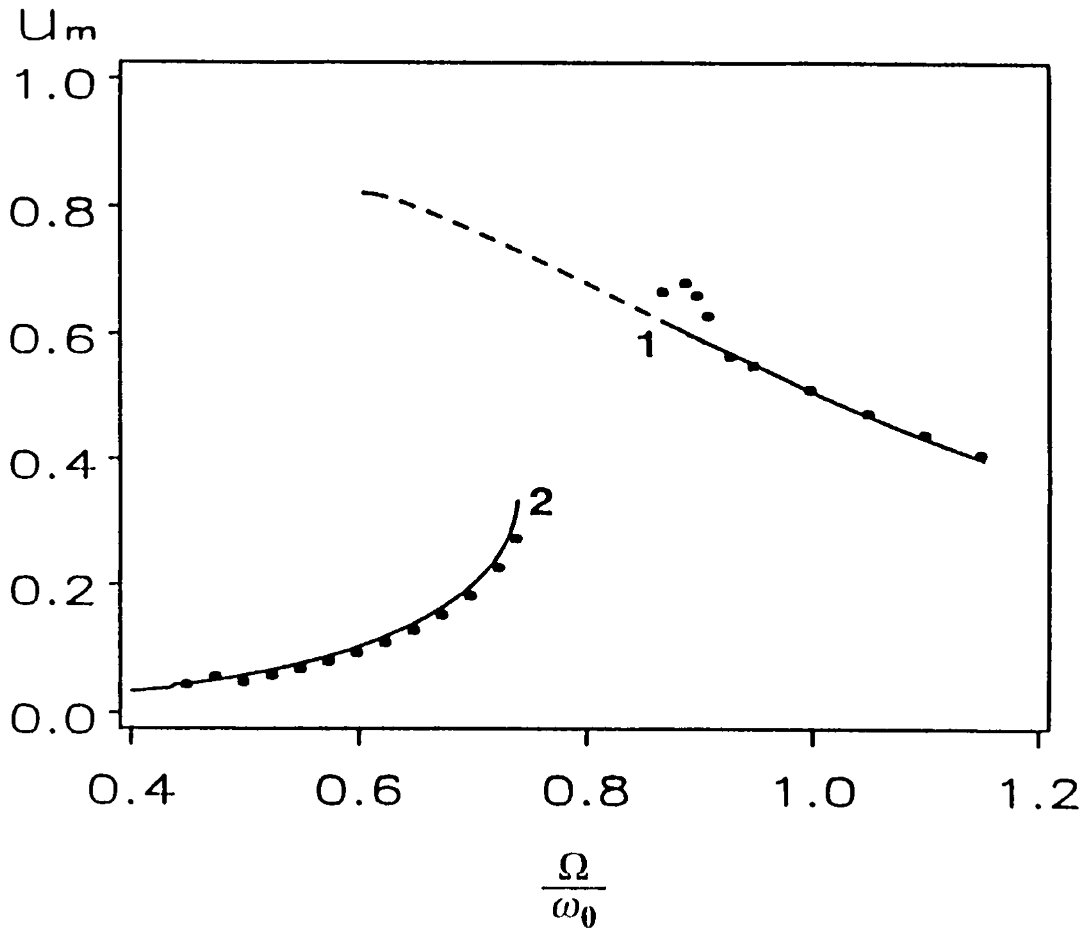

Figure 6.6. A frequency-response curve for the biased ship computed using the second-order approximate solution. The black circles mark the results of direct numerical integration. The dashed curve represents unstable solutions.

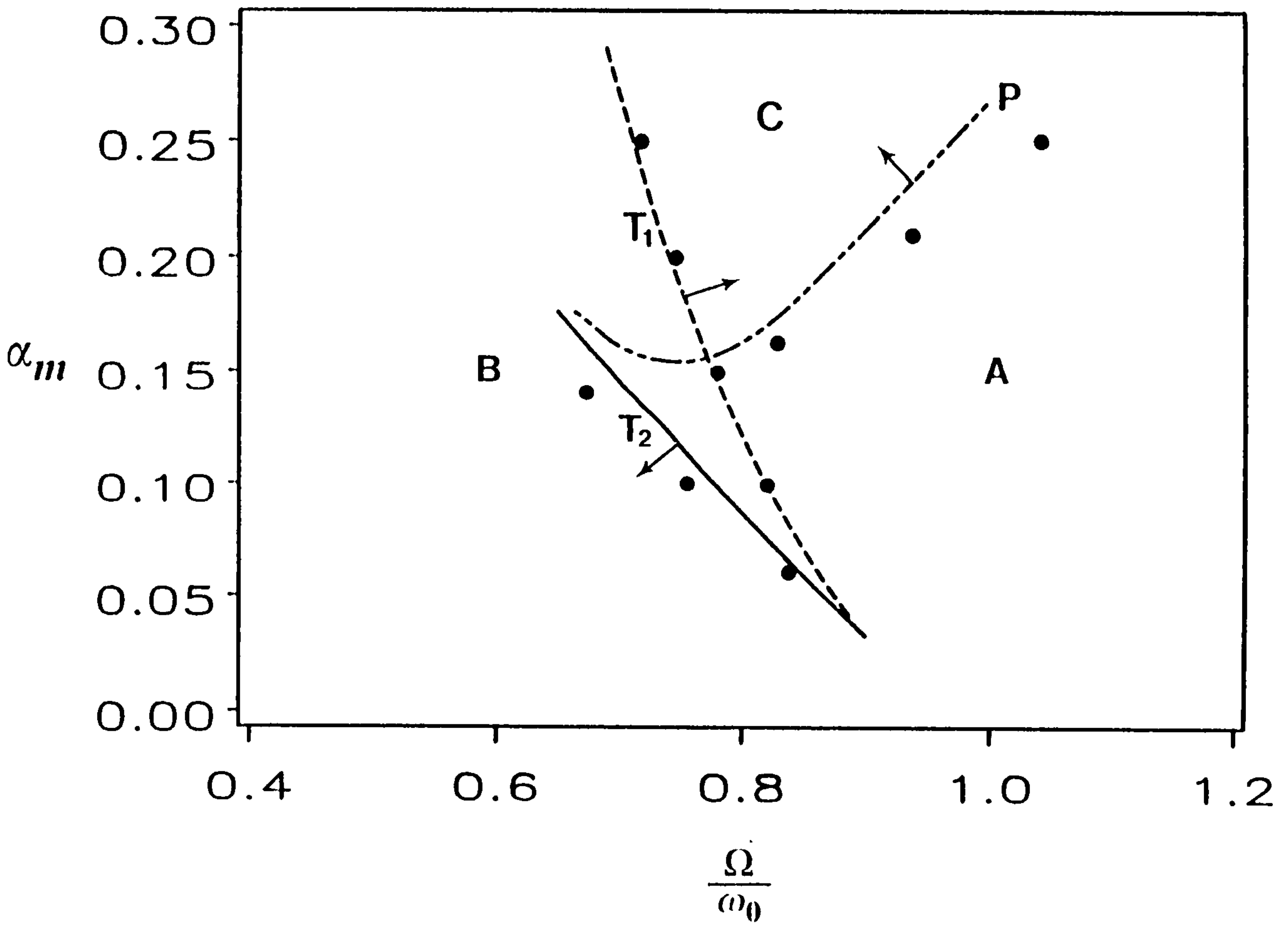

Figure 6.7. A bifurcation diagram for the biased ship computed from stability analysis: T_1 and T_2 represent tangent instabilities and P represents period-doubling instabilities. The black circles show the results obtained using direct numerical integrations.

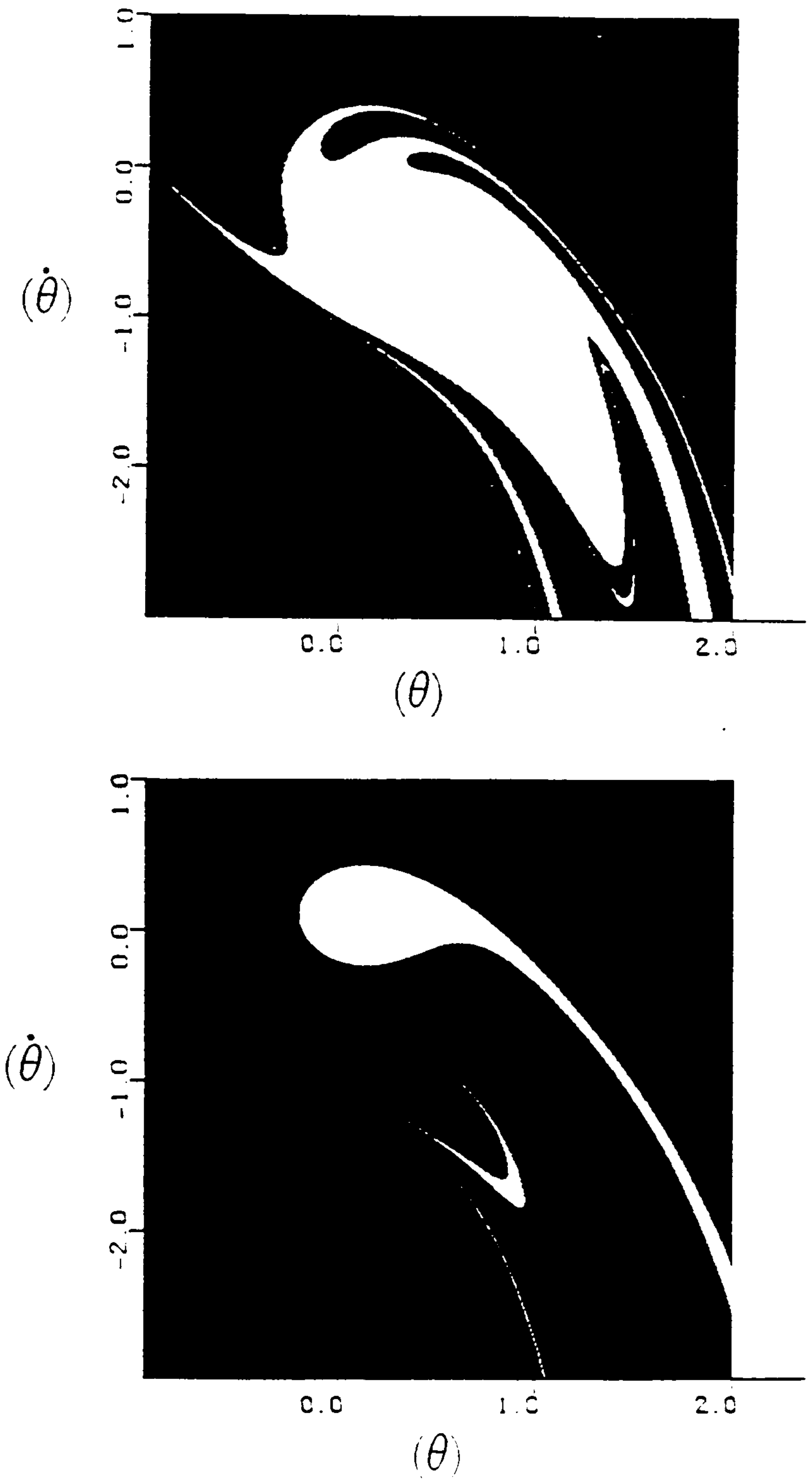

Figure 6.8. Domains of attraction of oscillatory (white) and capsizing (black) solutions for the biased ship for $\Omega = 1.0$: (a) $x_m = 0.15$ and (b) $x_m = 0.13$.

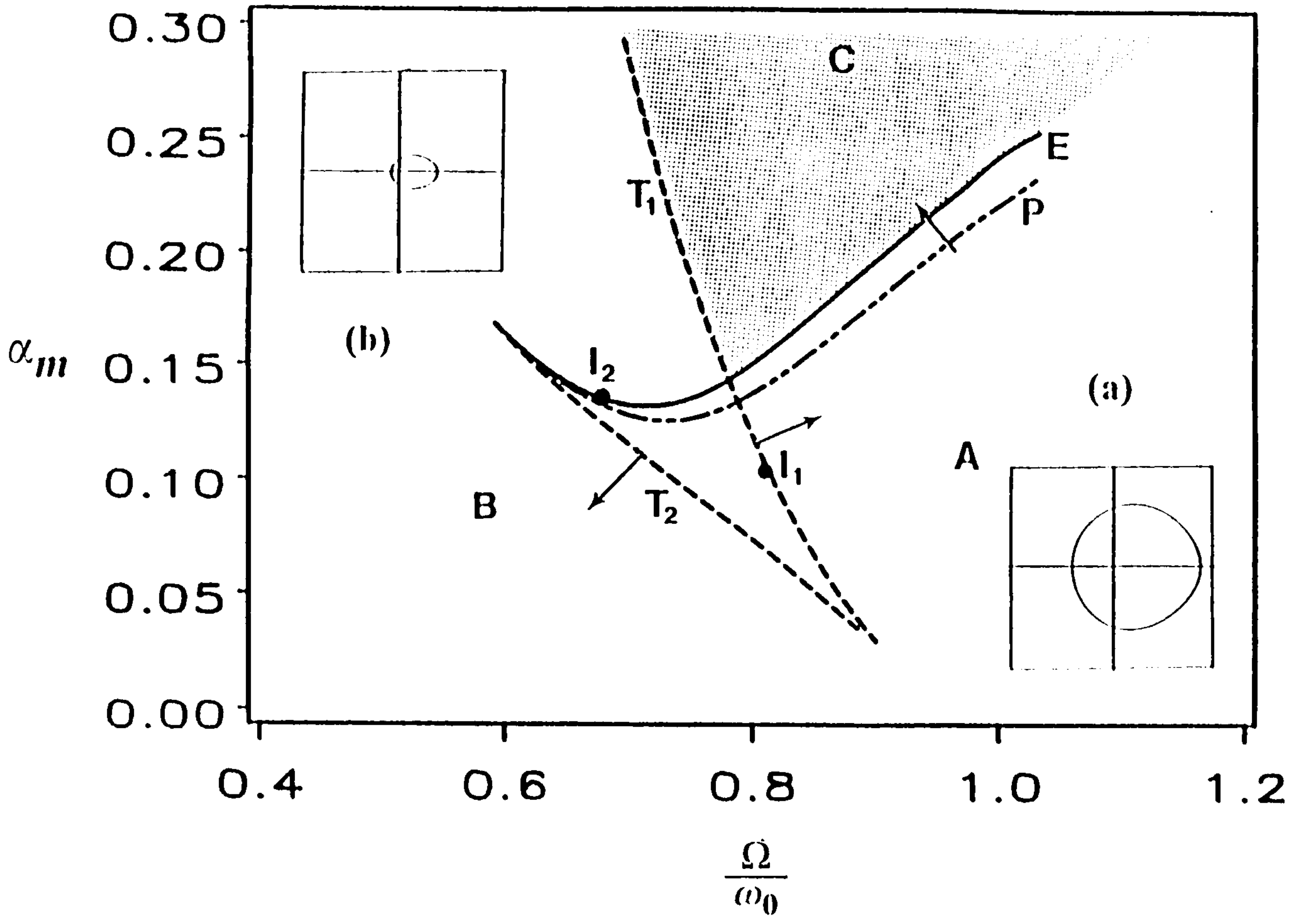

Figure 6.9. A bifurcation diagram for the biased ship computed using analog-computer simulations of the original governing equation. The inserts show the orbits of oscillatory solutions. In the dotted area only capsizing solutions can be obtained

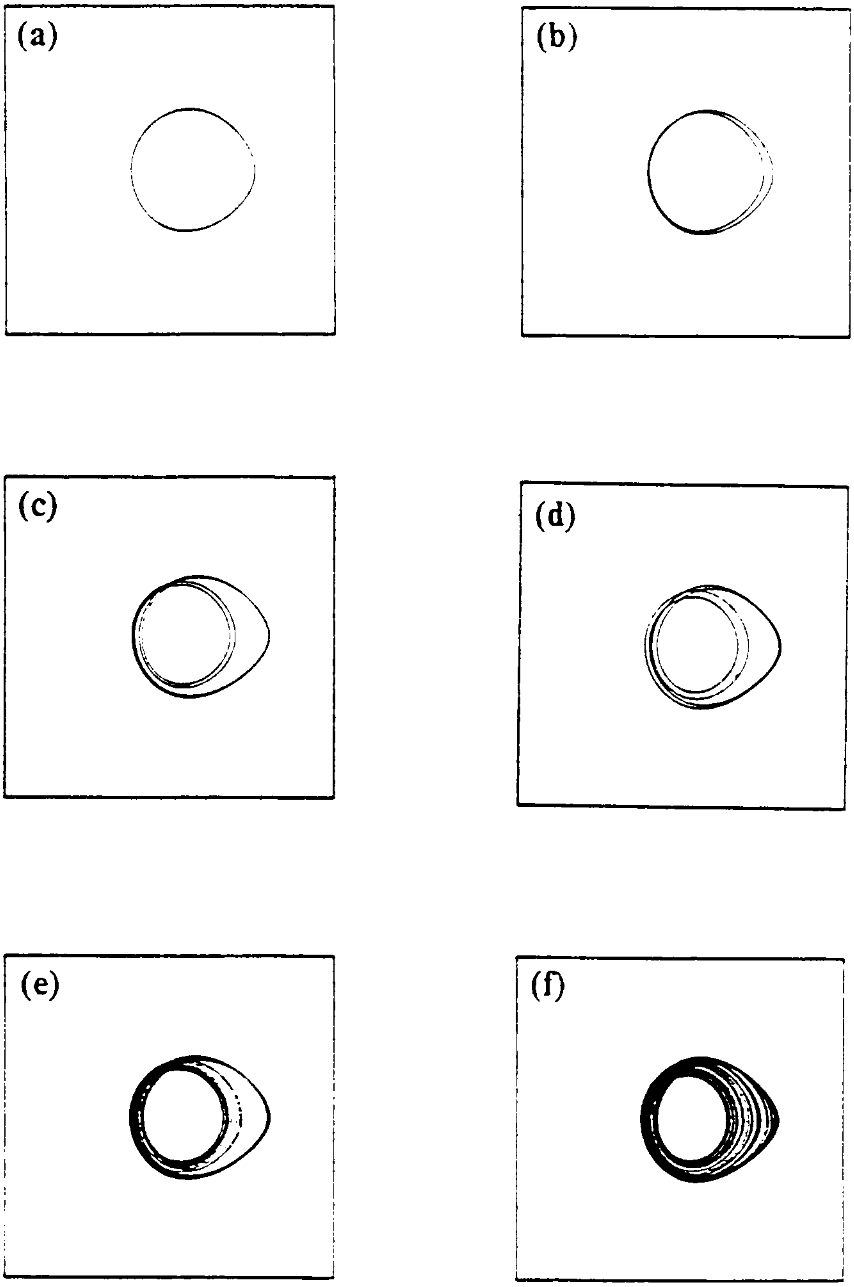

Figure 6.10. A period-doubling sequence to chaos for $\Omega = 0.944$: (a) asymmetric T-periodic solution for $\alpha_m = 0.197$, (b) 2T-periodic solution for $\alpha_m = 0.199$, (c) 4T-periodic solution for $\alpha_m = 0.213$, (d) 8T-periodic solution for $\alpha_m = 0.214$, and (e) and (f) are chaotic solutions for α_m 0.215 and 0.216.

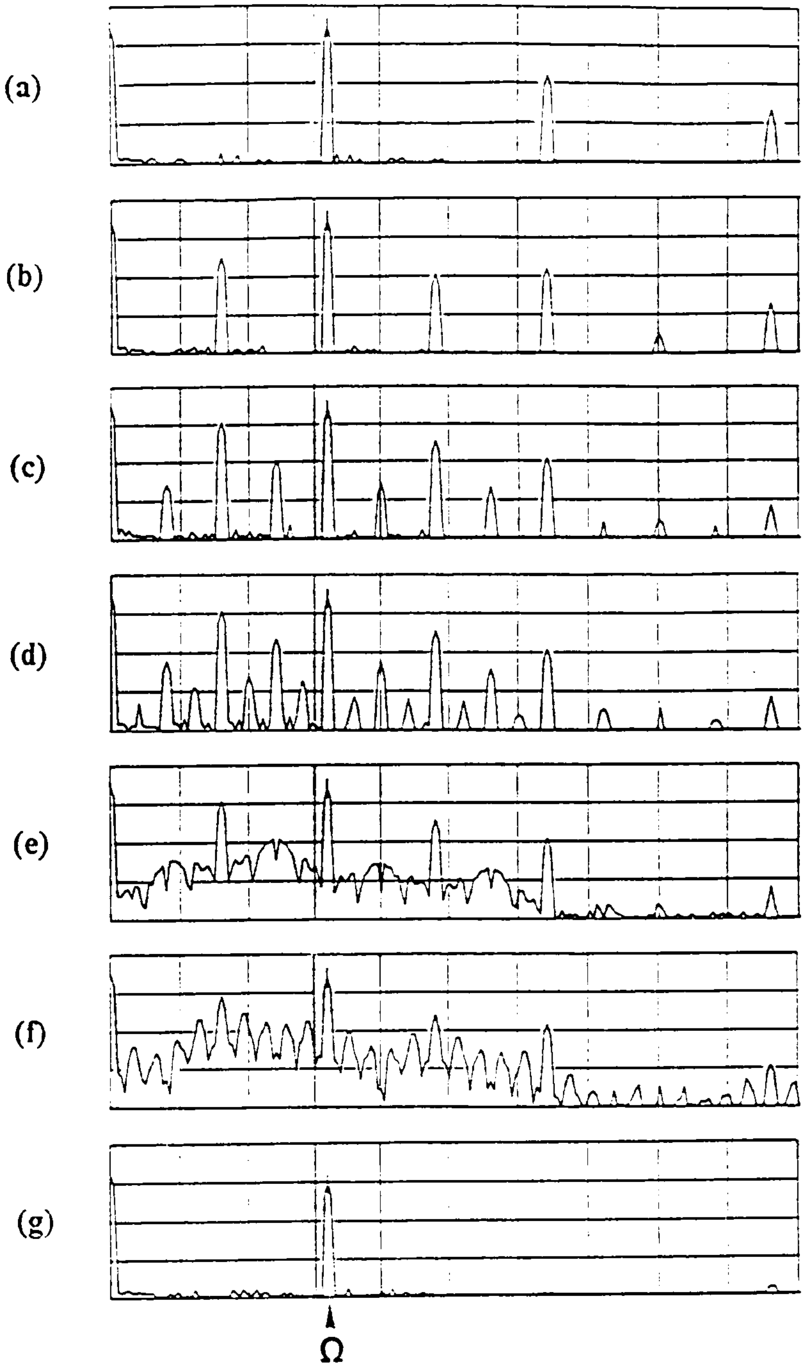

Figure 6.11. (a)-(f) Power spectra of the solutions in Figure 6.10; (g) spectrum of the wave, it shows a peak at the frequency Ω. The horizontal scale is linear and the vertical scales shows a maximum of 80 dB.

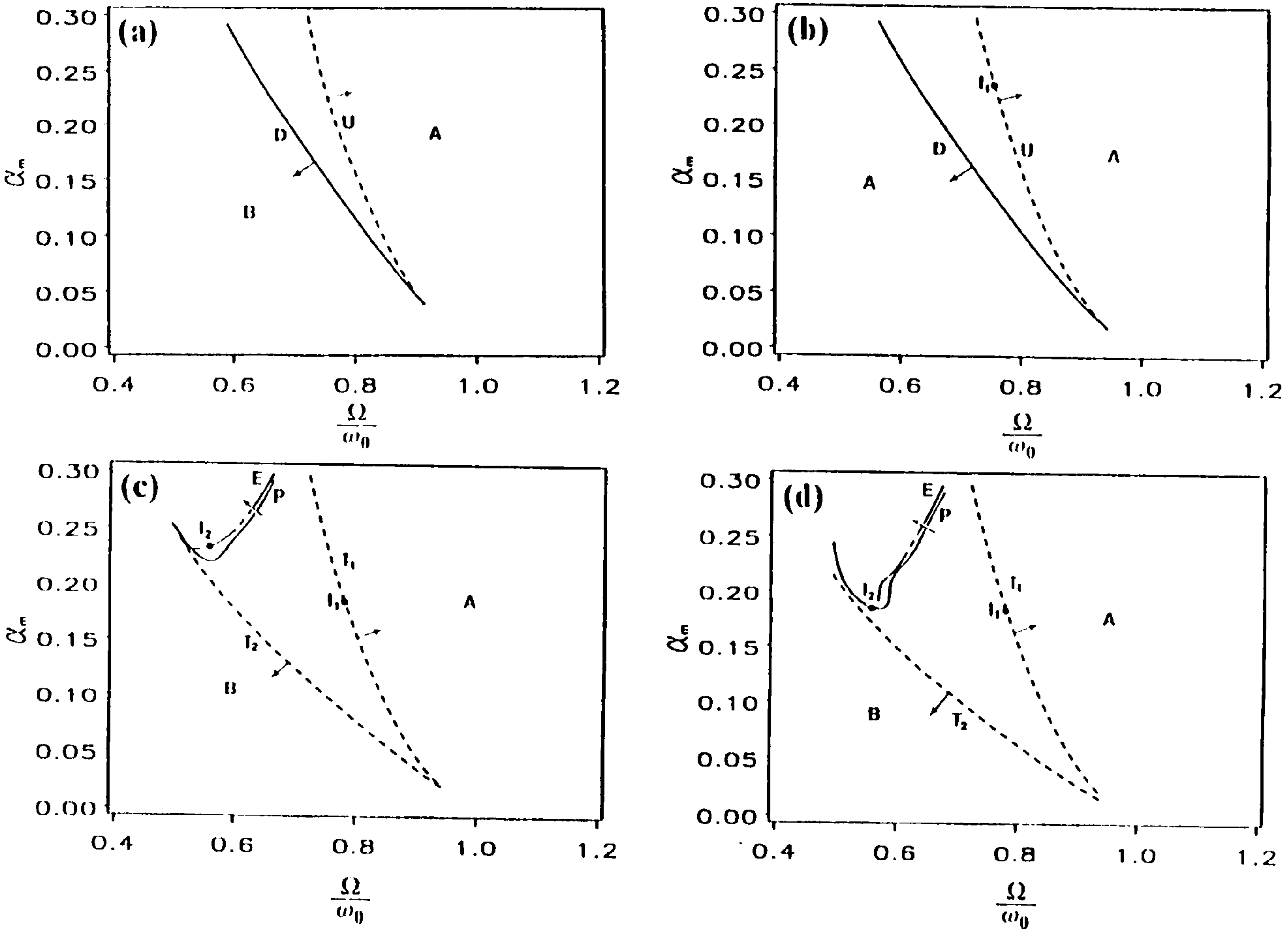

Figure 6.12. Bifurcation diagrams showing the effect of damping on the stability of the unbiased ship: (a) damping coefficients as given in Table 1, (b) the value of μ is halved, (c) the value of μ_3 is halved, and (d) the values of μ and μ_3 are halved.

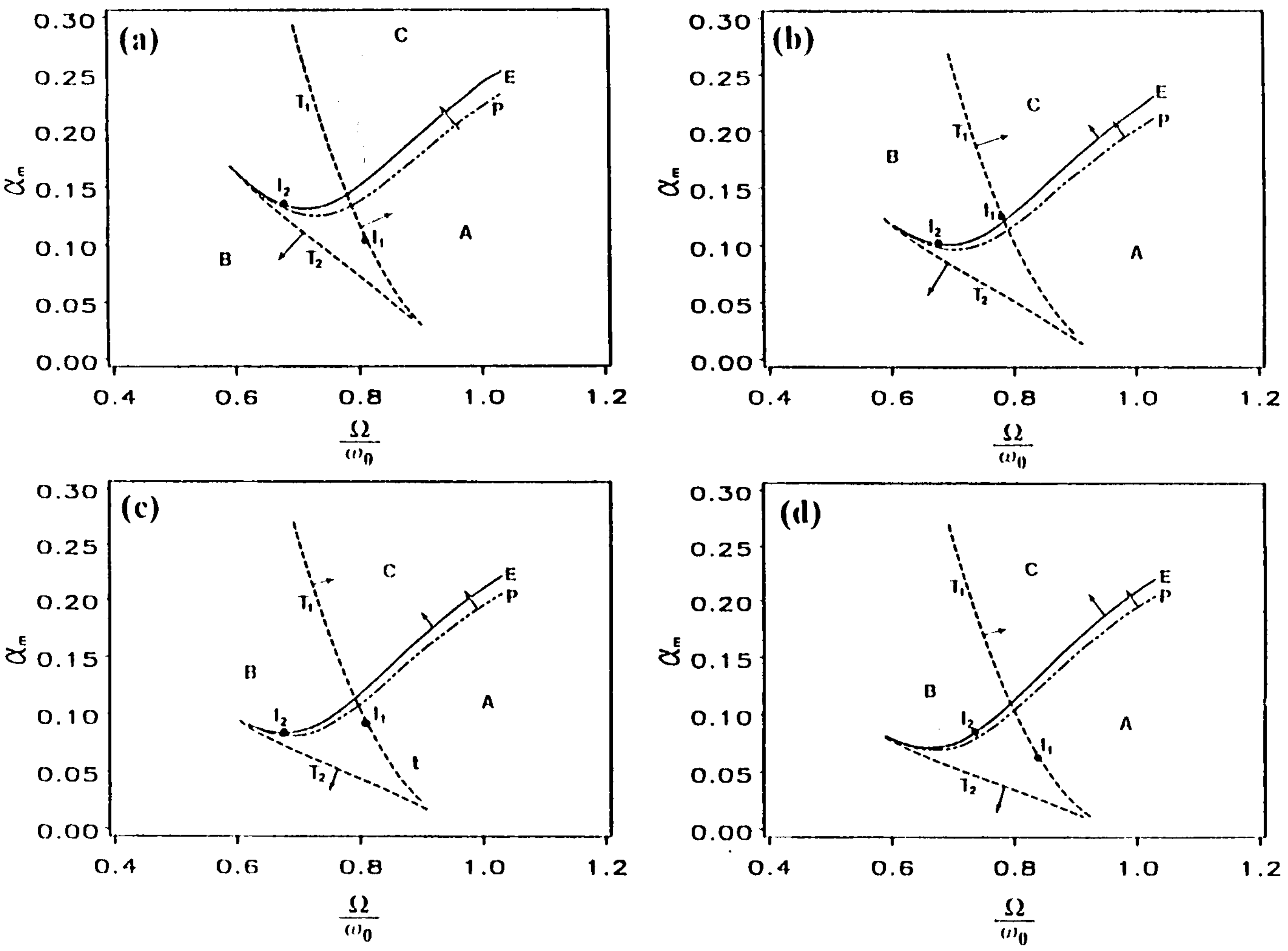

Figure 6.13. Bifurcation diagrams showing the effect of damping on the stability of the biased ship: (a) damping coefficients as given in Table 1, (b) the value of μ is halved, (c) the value of μ_3 is halved, and (d) the values of μ and μ_3 are halved.

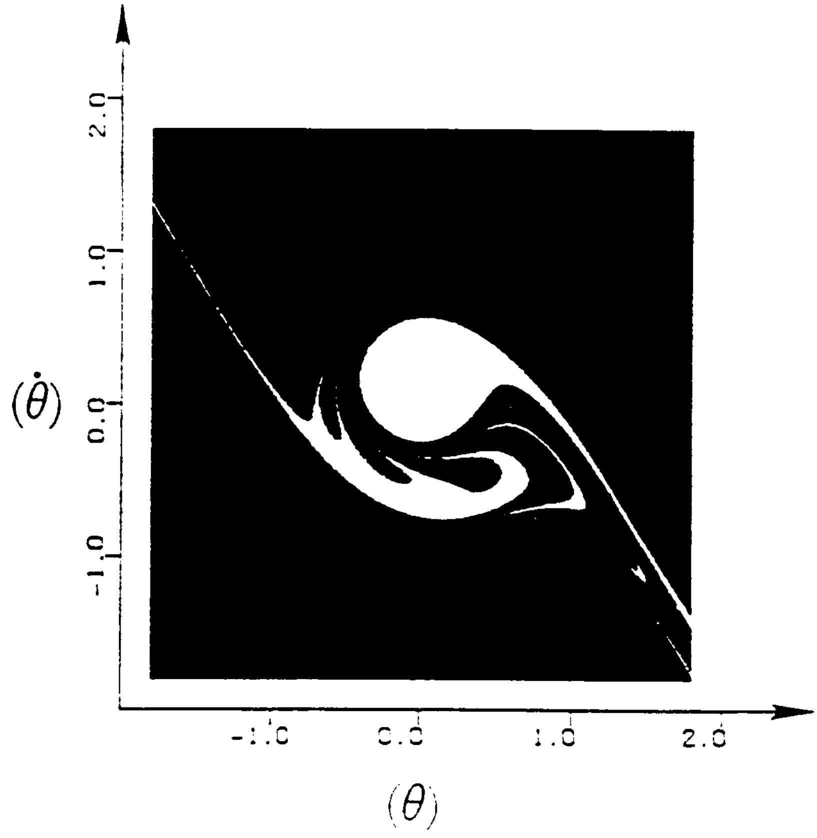

Figure 6.14. Domains of attraction of oscillatory (white) and capsizing (black) solutions for the unbiased ship when the linear and cubic damping coefficients are one-half the values given in Table 1.

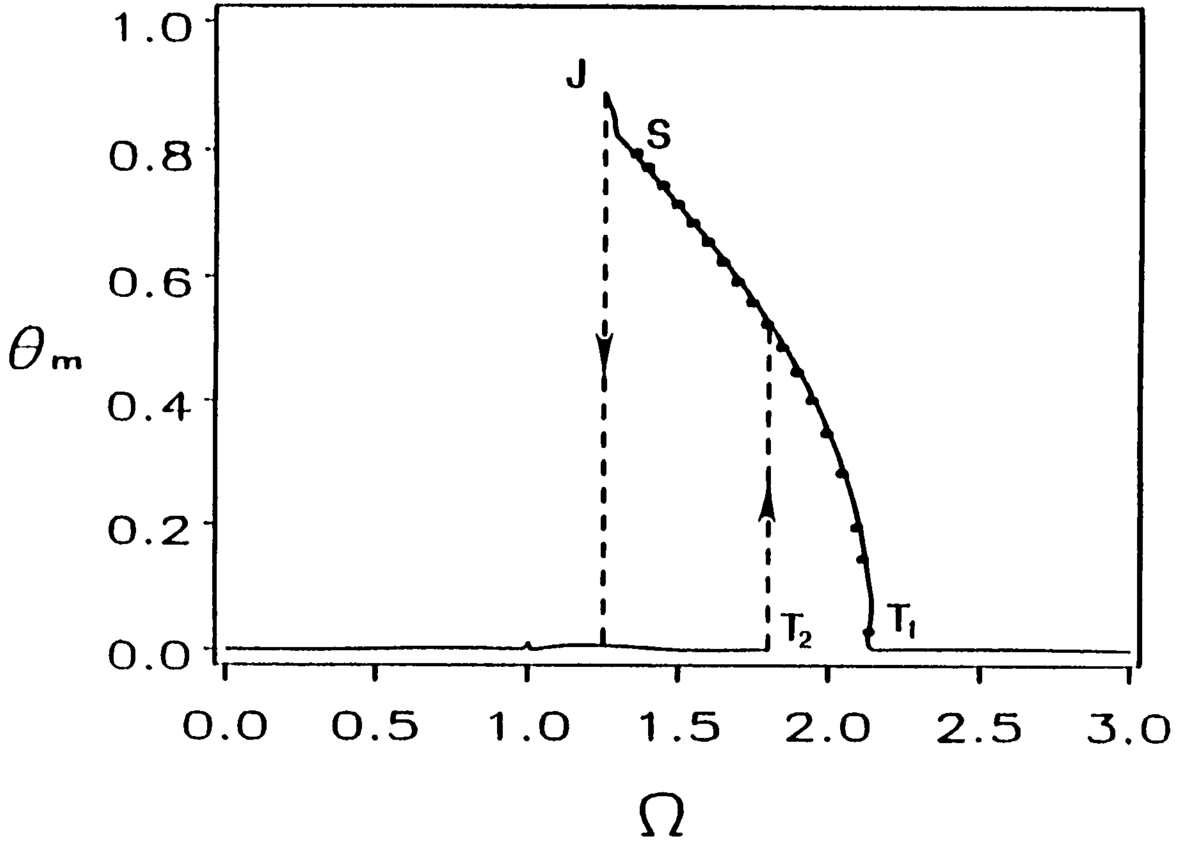

Figure 7.1. Frequency-response curve of the ship model for h = 0.3. The principal parametric response is shown.

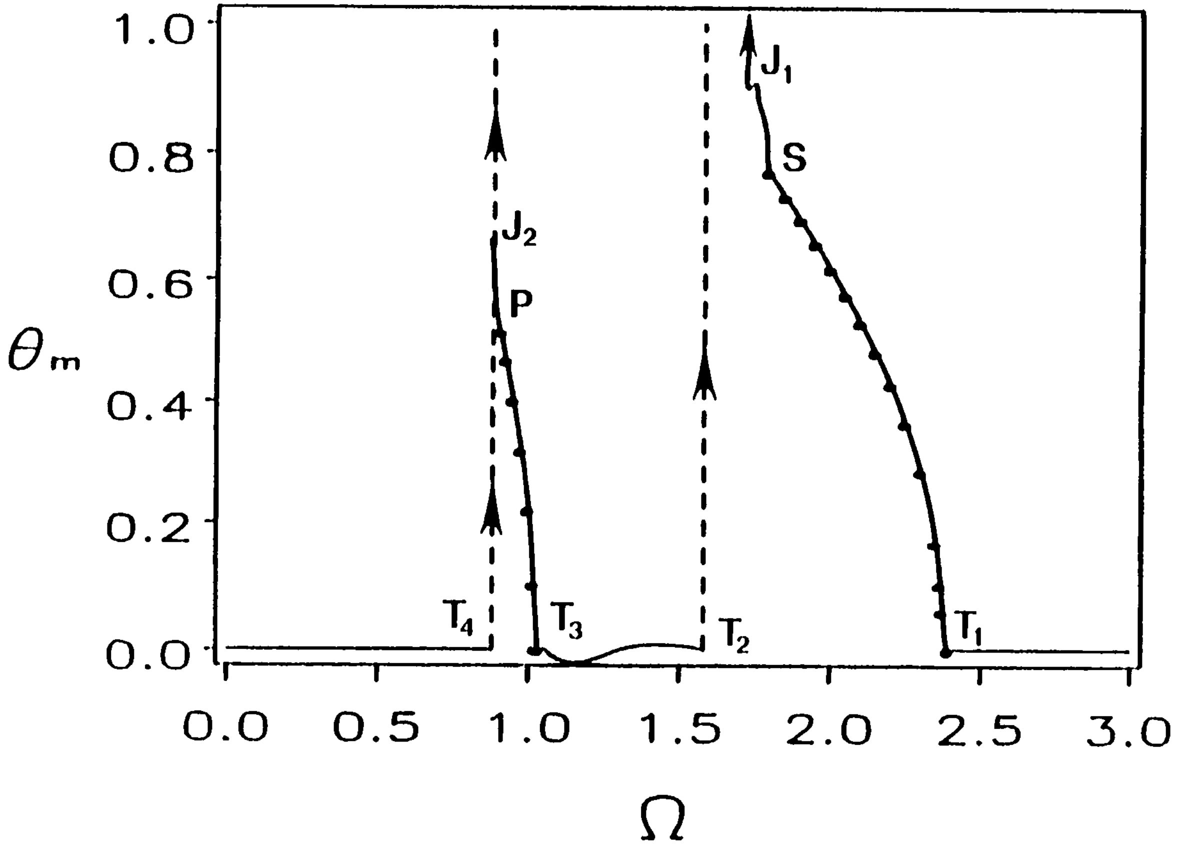

Figure 7.2. Frequency-response curve of ship model for h = 0.8. The principal and the fundamental parametric responses are excited.

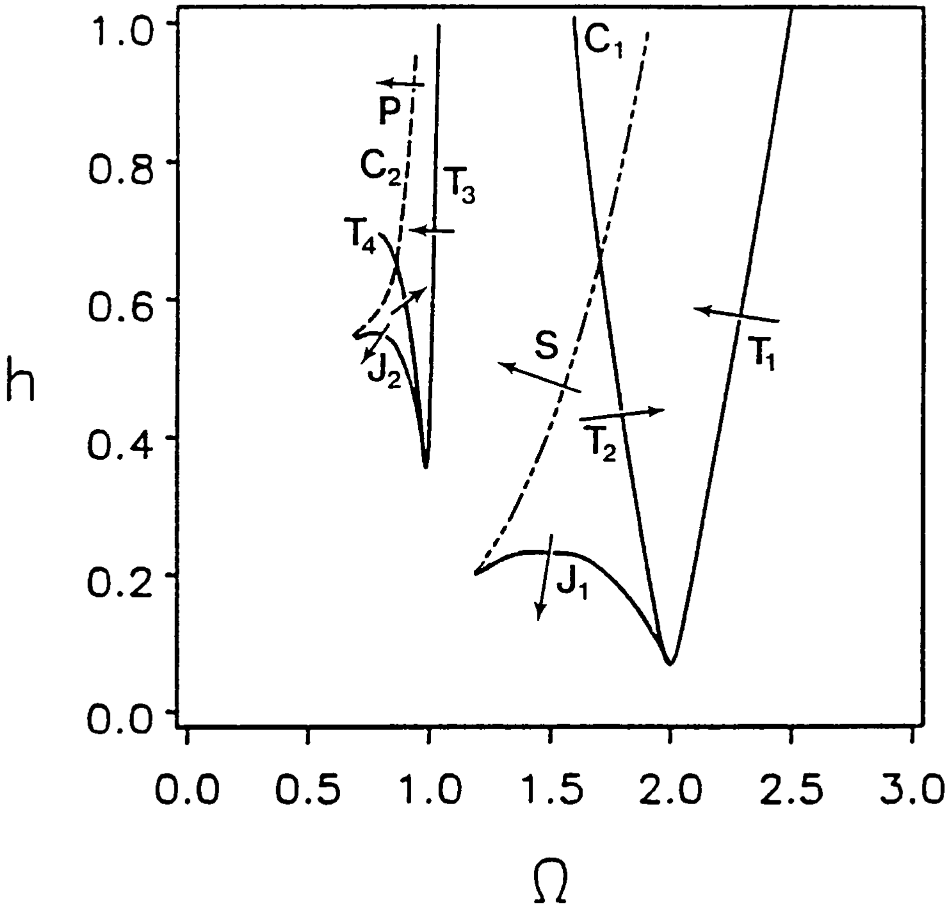

Figure 7.3. Bifurcation diagram obtained from the analysis of the stability of the perturbation solution. The regions of resonance are marked by tongues that exhibit self-similarity.

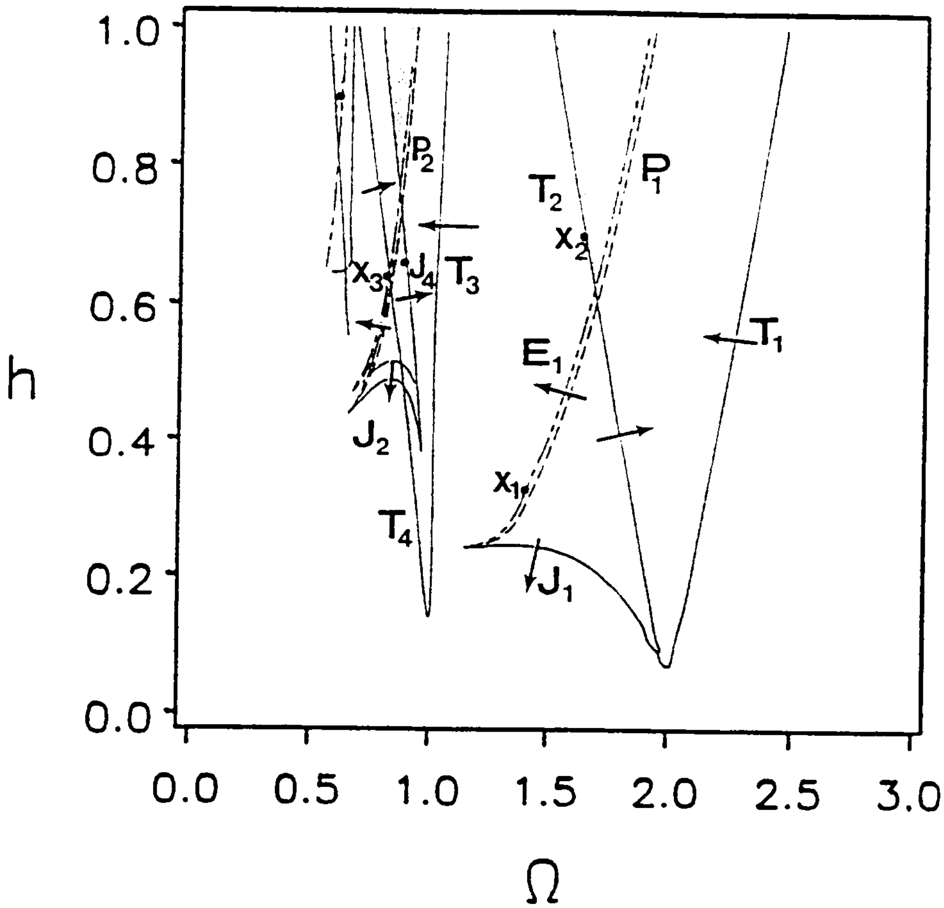

Figure 7.4. Bifurcation diagram obtained from analog-computer simulation.

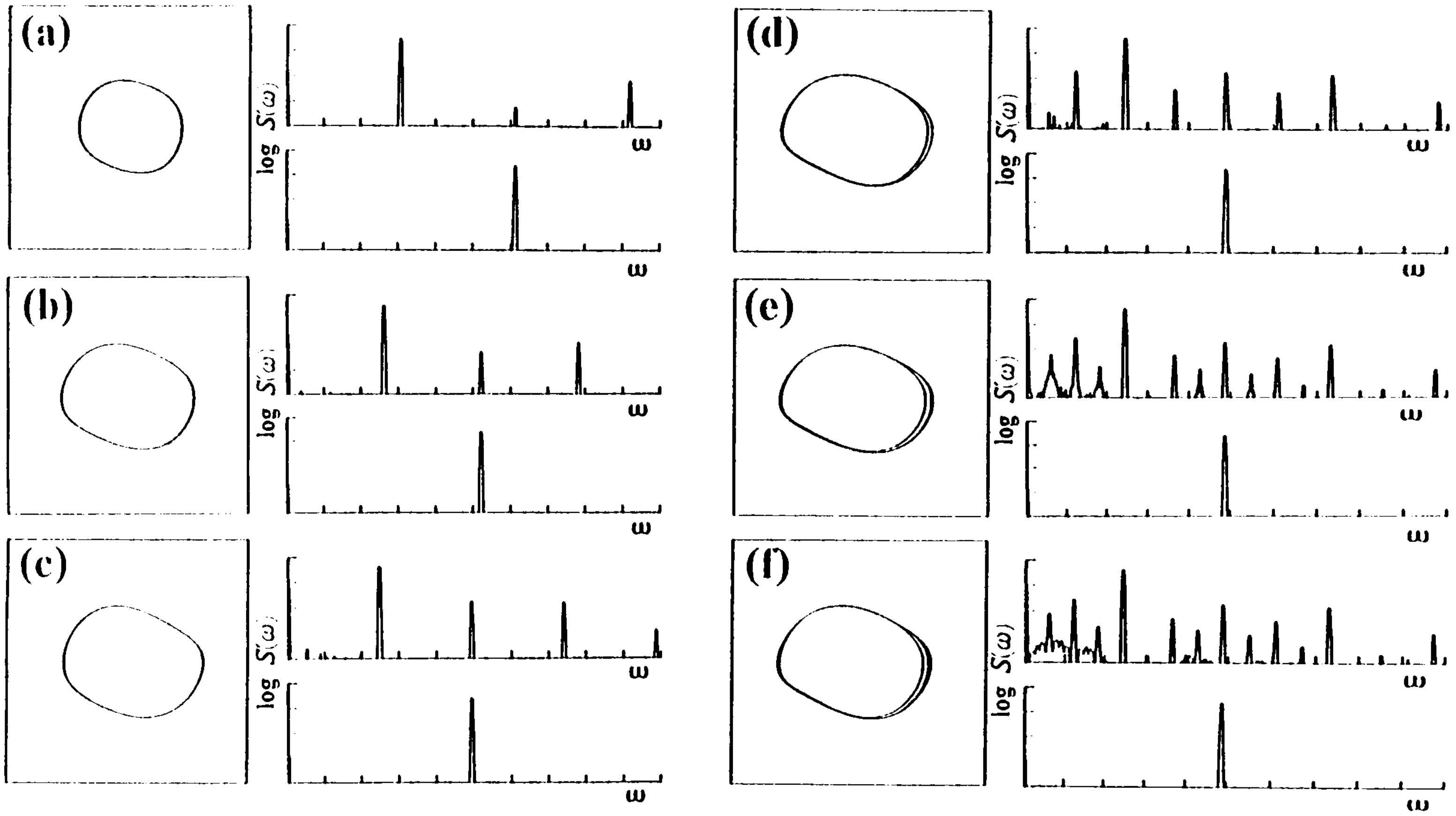

Figure 7.5. A period-doubling sequence of the principal parametric response for $h = 0.35$. (a) $\Omega = 1.83$, (b) $\Omega = 1.56$, (c) $\Omega = 1.47$, (d) $\Omega = 1.46$, (e) $\Omega = 1.451$, (f) $\Omega = 1.45$, (g) $\Omega = 1.449$, (h) $\Omega = 1.448$ (i) $\Omega = 1.446$. The power spectra of the response (top) and the excitation can be observed on the right side of the orbits.

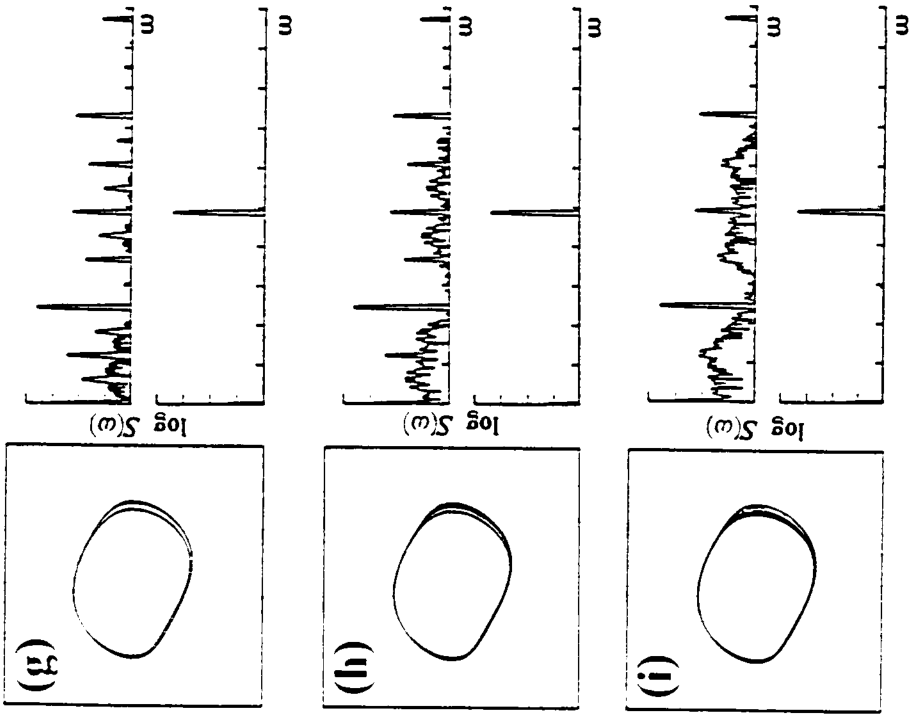
(g)
log S(ω)
ω
ω
(h)
log S(ω)
ω
ω
(i)
log S(ω)
ω
ω

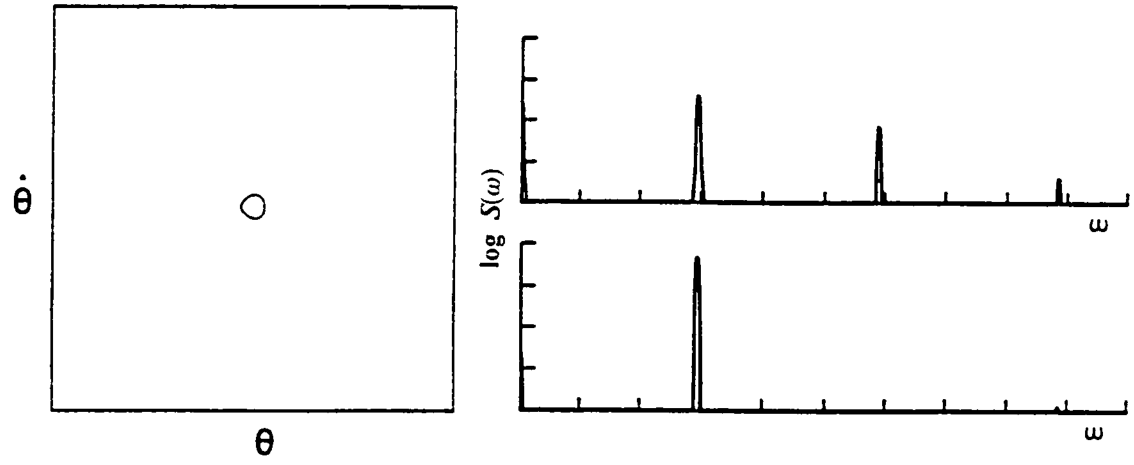

Figure 7.6. Small-amplitude attractor found inside the fundamental parametric resonant region for h = 0.7 Ω = 0.8785. The power spectra of the response (top) and excitation (bottom) can be observed on the right side of the orbit.

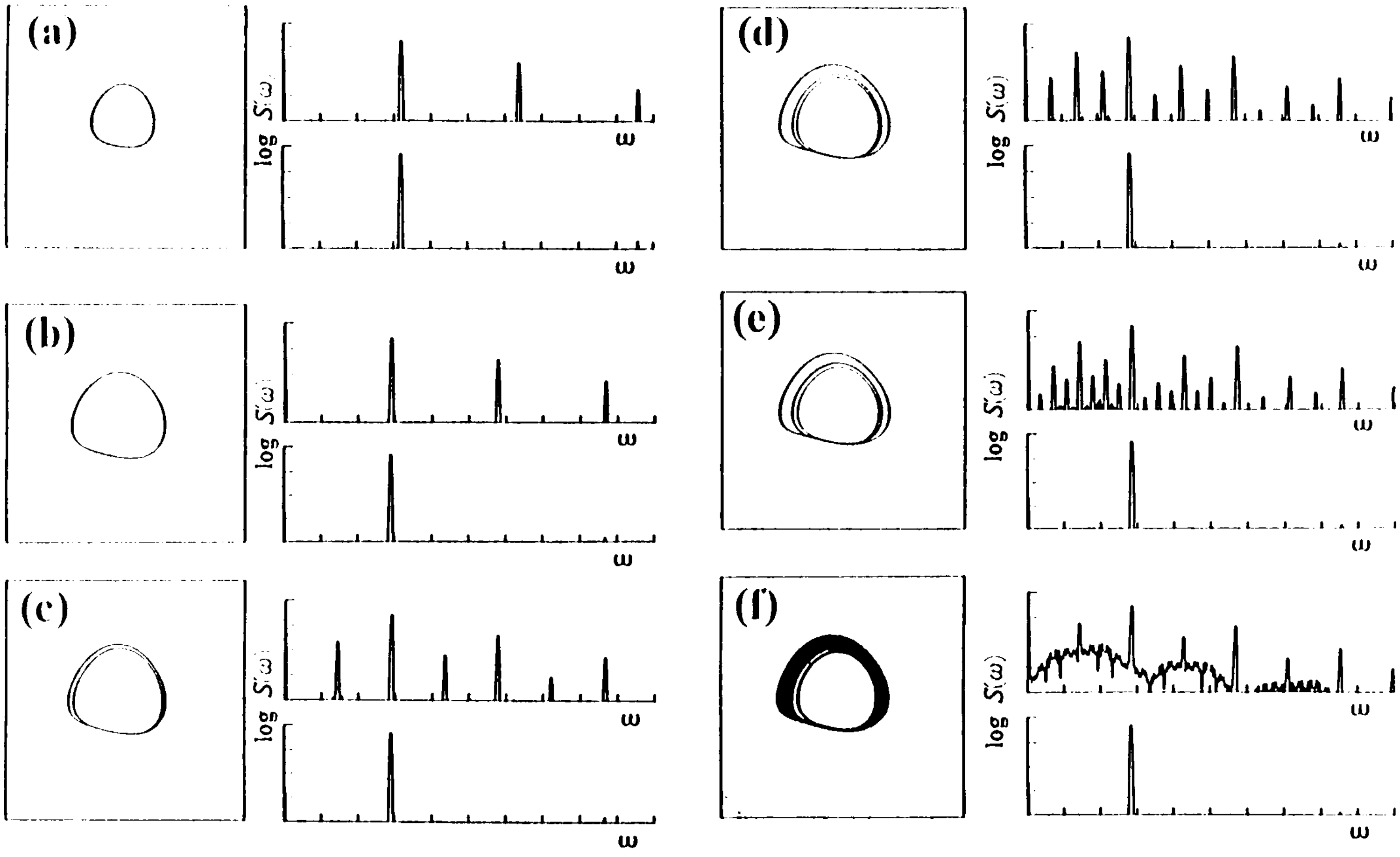

Figure 7.7. A period-doubling sequence of attractor 1 in the fundamental parametric resonant region for h = 0.7. (a) $\Omega = 0.952$, (b) $\Omega = 0.862$, (c) $\Omega = 0.860$, (d) $\Omega = 0.849$, (e) $\Omega = 0.848$, (f) $\Omega = 0.8472$. The power spectra of the response (top) and excitation (bottom) can be observed on the right side of the orbits.

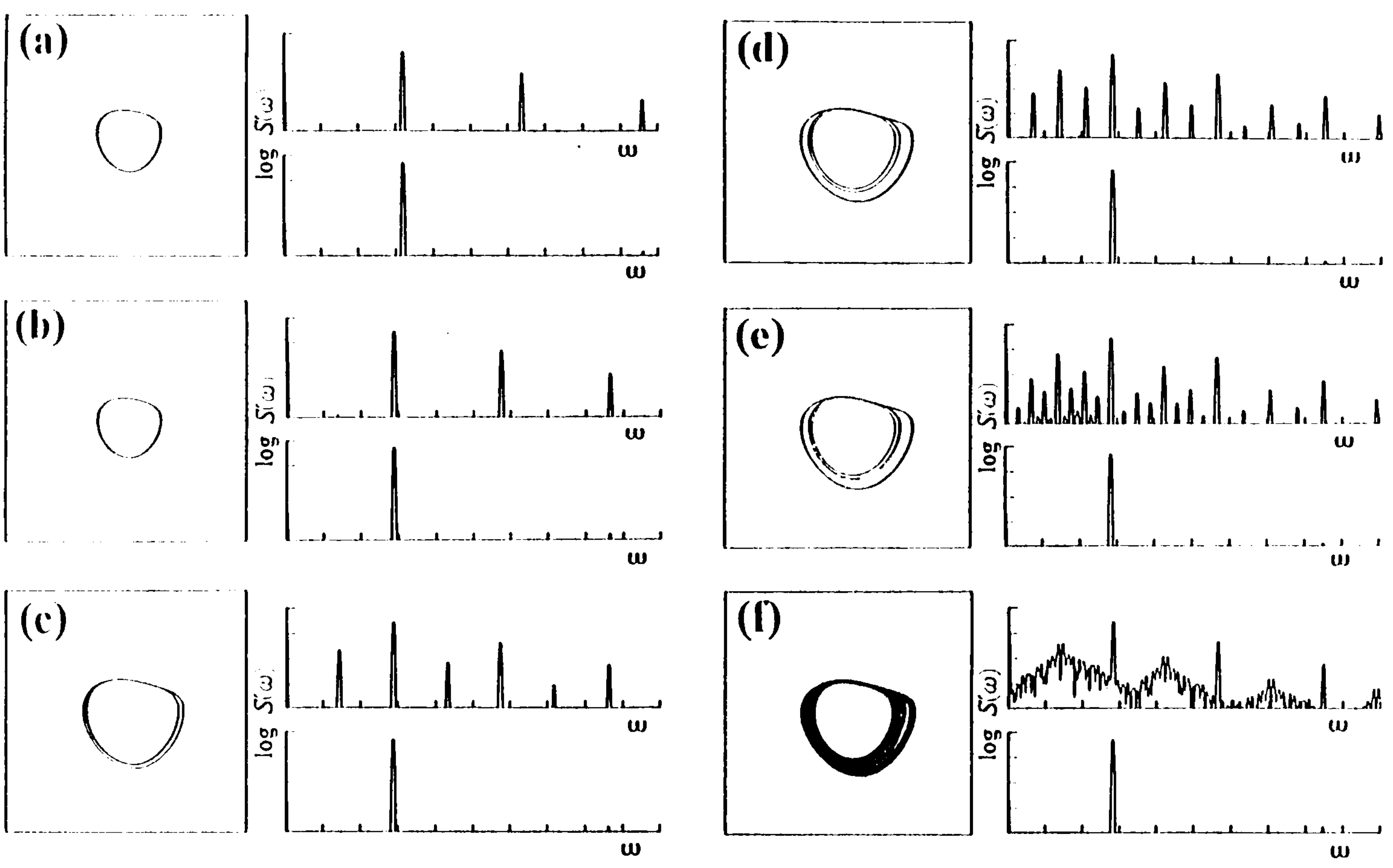

Figure 7.8. A period-doubling sequence of the attractor 2 in the fundamental parametric resonant region for $h = 0.7$. (a) $\Omega = 0.952$, (b) $\Omega = 0.858$, (c) $\Omega = 0.856$, (d) $\Omega = 0.8454$, (e) $\Omega = 0.8448$, (f) $\Omega = 0.8425$. The power spectra of the response (top) and excitation (bottom) can be observed on the right side of the orbits.

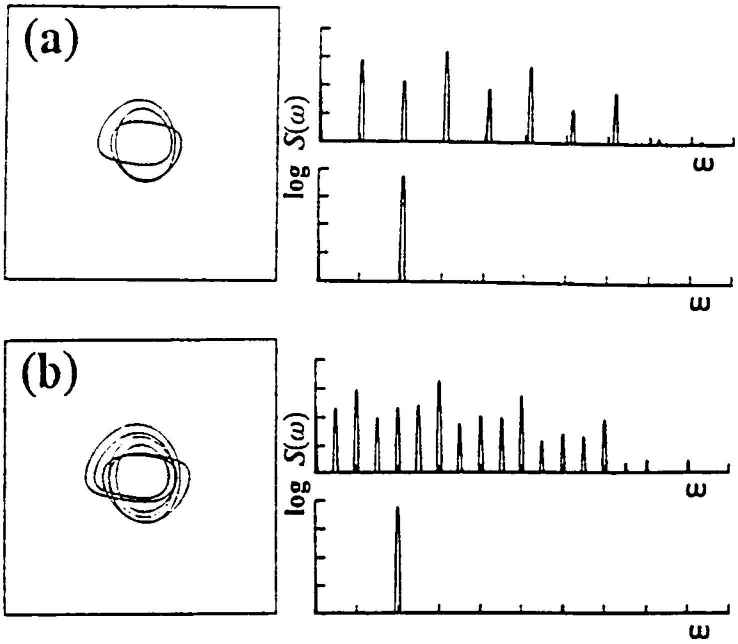

Figure 7.9. One of the superharmonic resonant responses found at h = 0.8: (a) periodic solution for Ω = 0.61, and (b) period-doubled solution for Ω = 0.598.

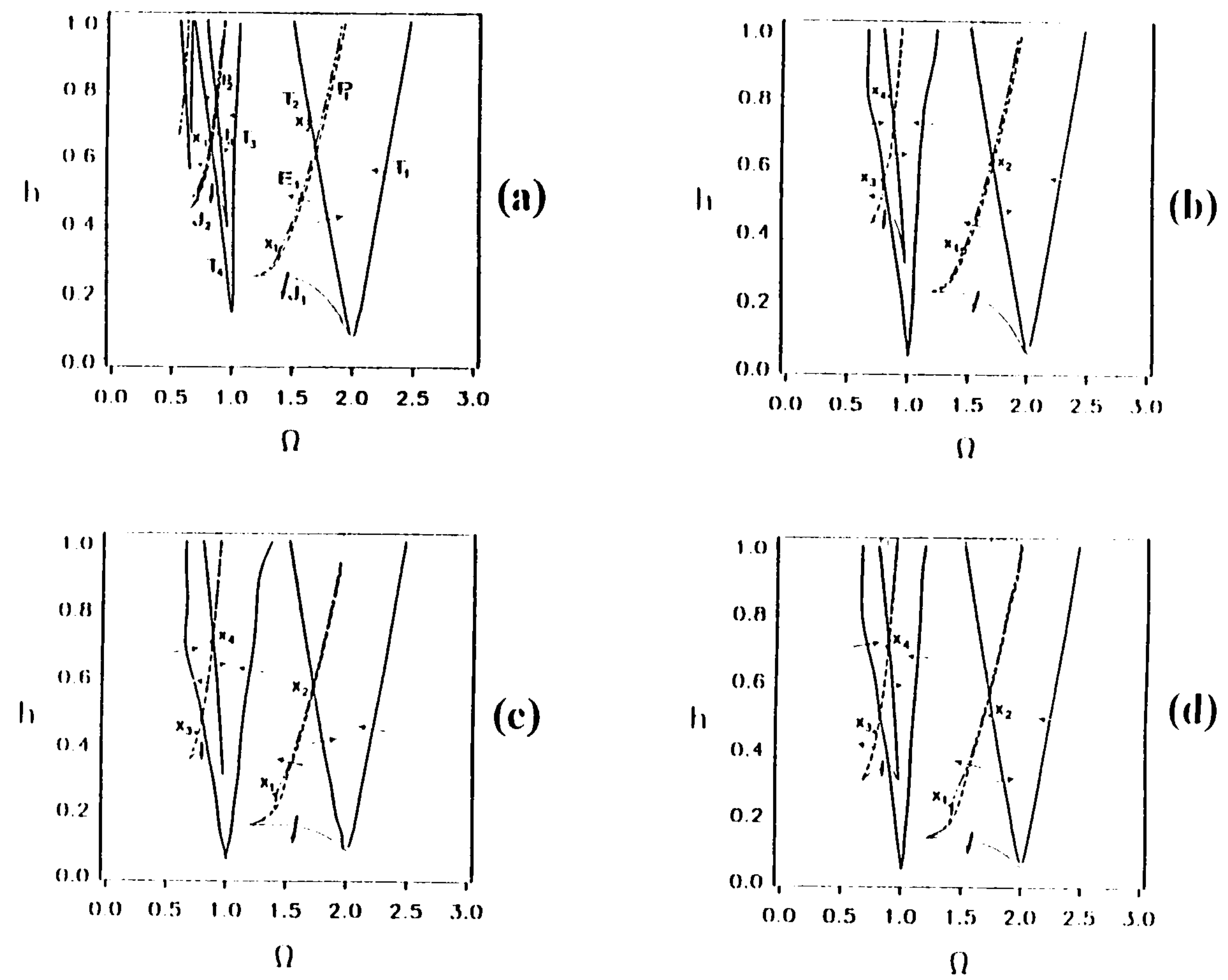

Figure 7.10. Influence of damping on the location of the bifurcations : (a) μ and μ_3 as given in Table 1, (b) $\frac{1}{2}\mu$, μ_3 , (c) μ, $\frac{1}{2}\mu_3$, and (d) $\frac{1}{2}\mu$, $\frac{1}{2}\mu_3$.

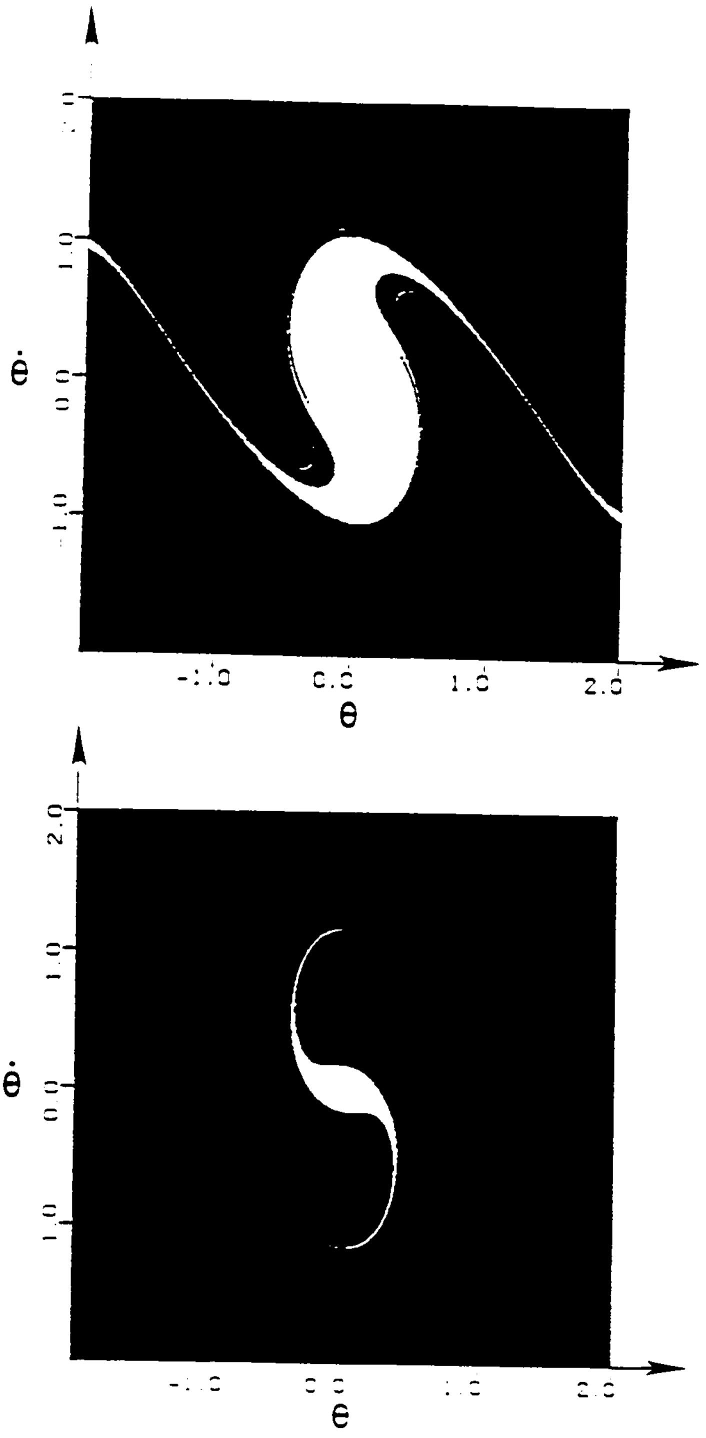

Figure 7.11. Basins of attraction of oscillatory (white) and capsizing (black) solutions computed by numerically integrating (7.3) with a grid of 500x500 initial conditions for $\Omega = 0.8$: (a) $h = 0.6$, and (b) $h = 0.3$.

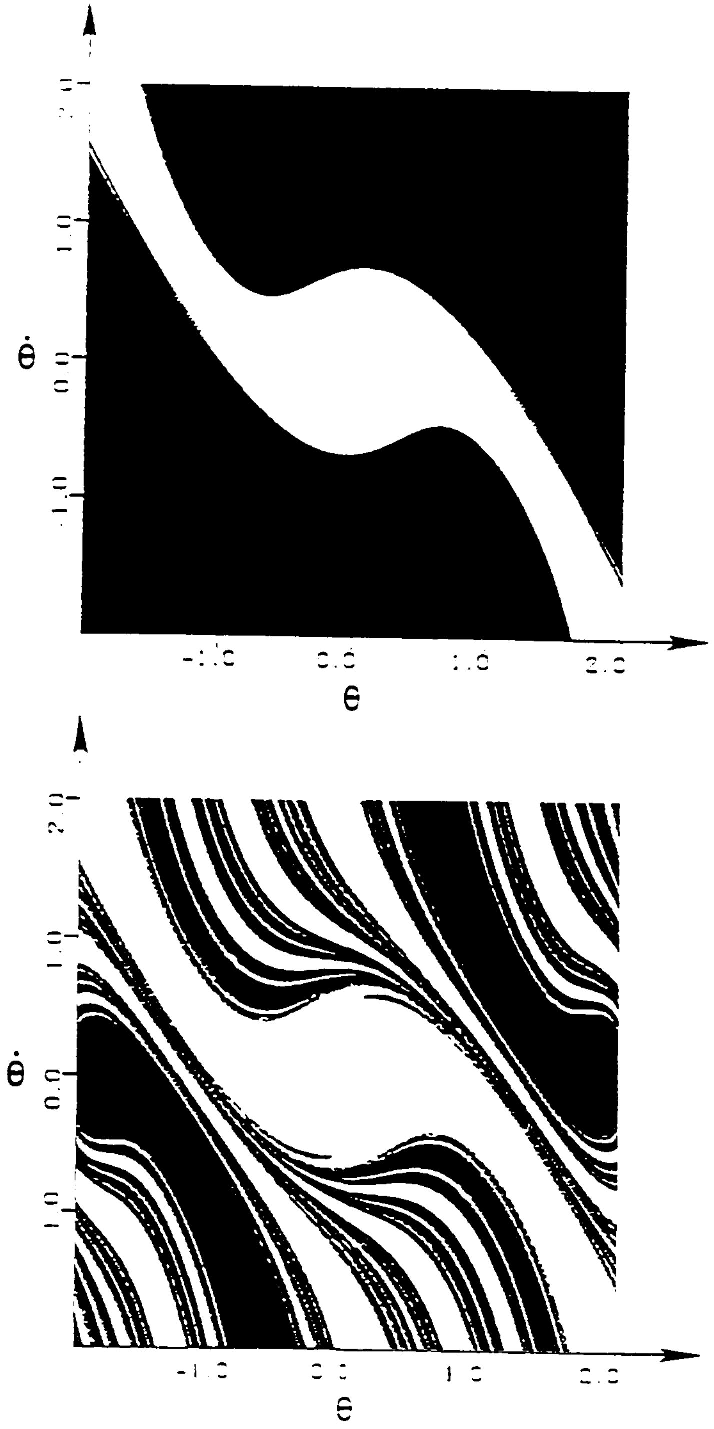

Figure 7.12. Basins of attraction of oscillatory (white) and capsizing (black) solutions computed by numerically integrating (7.3) with a grid of 500x500 initial conditions for $\Omega = 1.8$. (a) $h = 0.5$, and (b) $h = 0.6$.

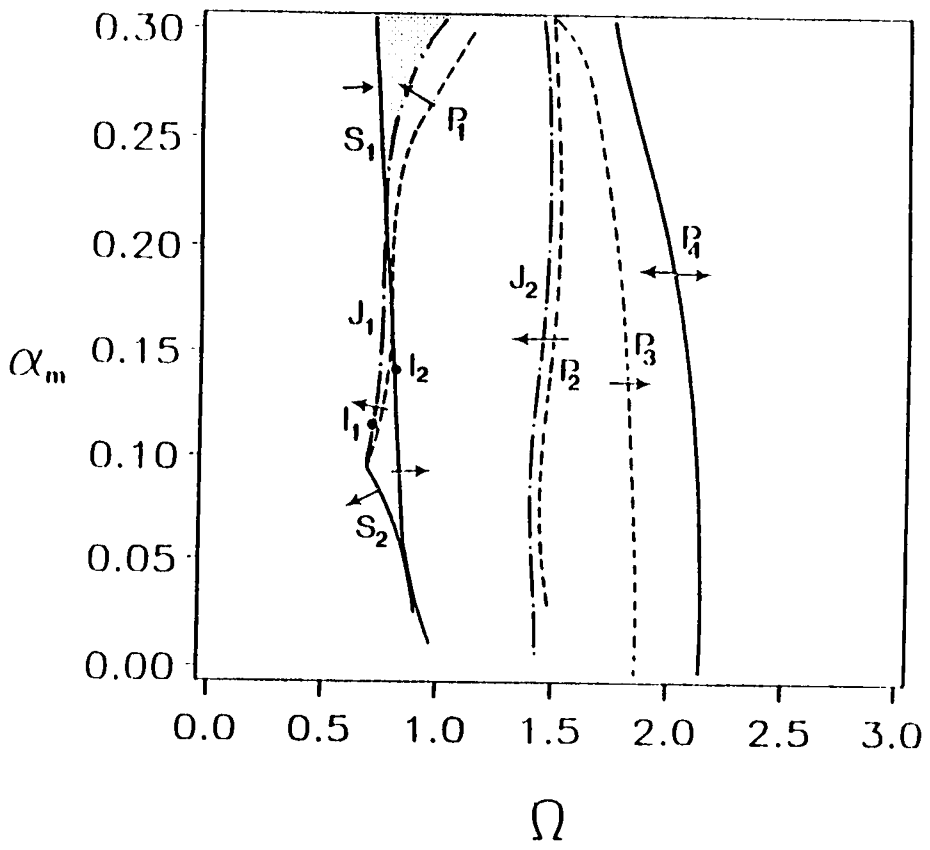

Figure 8.1. Bifurcation diagram from analog-computer simulations of (8.5) for $\gamma = 0$, $\theta_s = 0°$, $h = 0.3$.

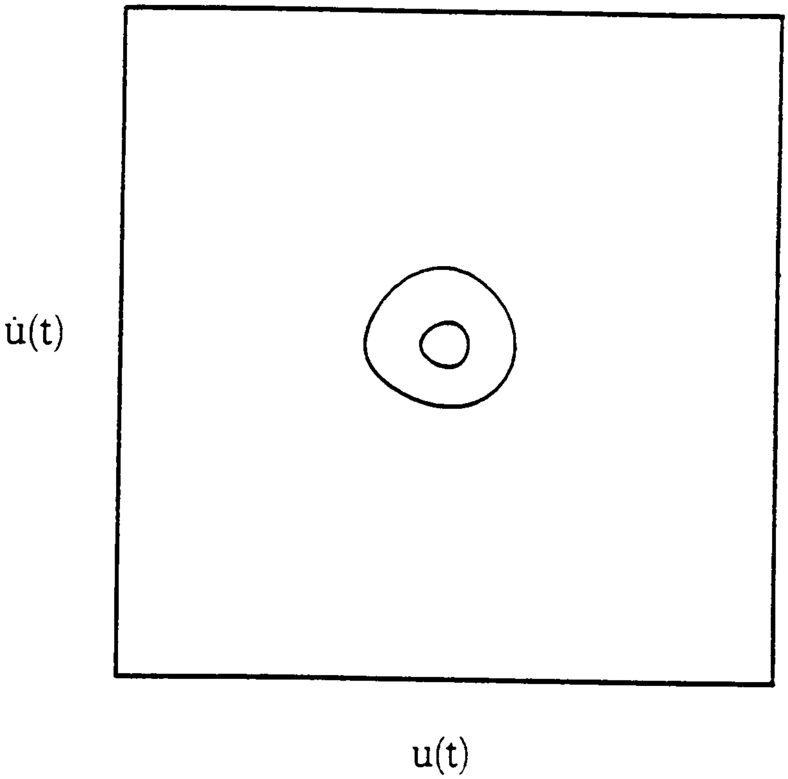

Figure 8.2. Phase portrait of coexisting attractors at $\Omega = 0.856$ and $x_m = 0.048$. Both attractors correspond to the primary resonance.

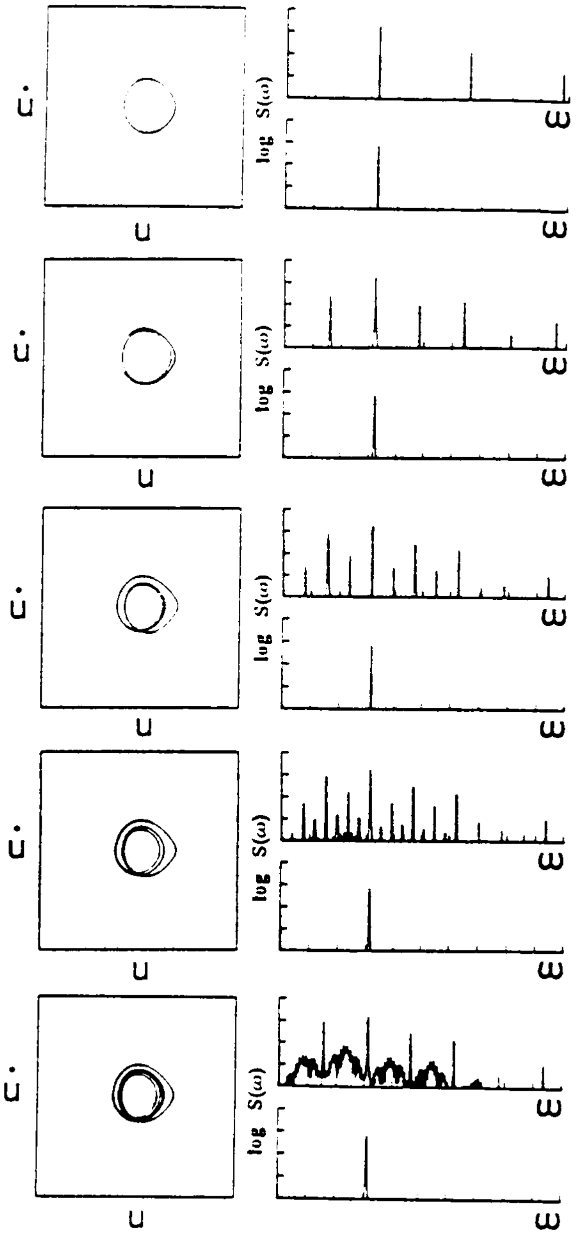

Figure 8.3. Phase portraits and power spectra of the attractor and the excitation at selected locations near the primary resonance : (a) T-periodic solution for $\Omega = 0.983$ and $x_m = 0.258$, (b) 2T-periodic solution for $\Omega = 0.966$ and $x_m = 0.268$, (c) 4T-periodic solution for $\Omega = 0.942$ and $x_m = 0.282$, (d) 8T-periodic solution for $\Omega = 0.939$ and $x_m = 0.284$, and (e) chaotic attractor for $\Omega = 0.937$ and $x_m = 0.285$.

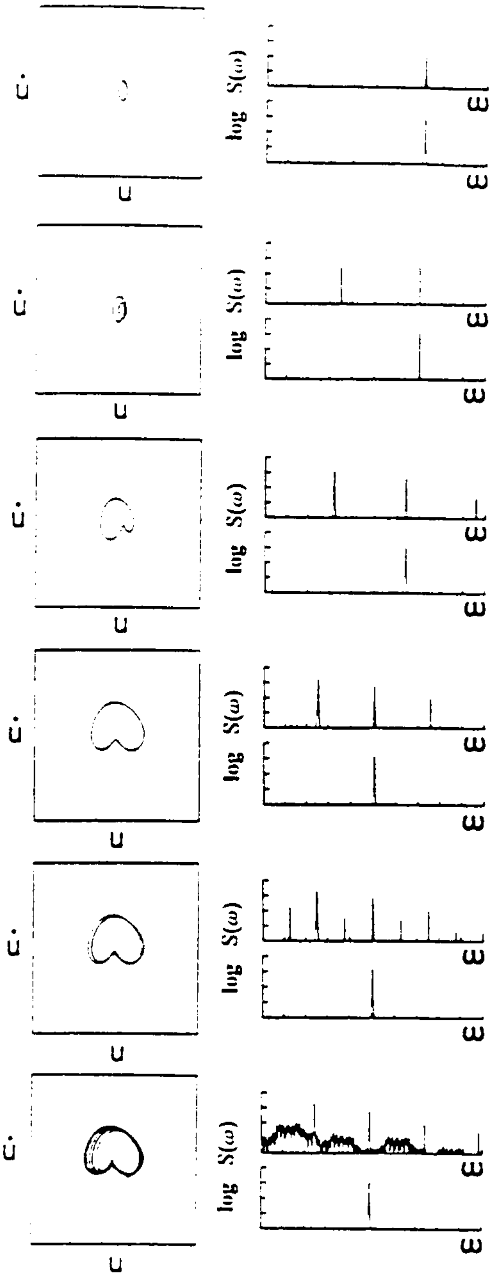

Figure 8.4. Phase portraits and power spectra of the attractor and the excitation at selected locations near the subharmonic resonance : (a) primary response for $\Omega = 2.158$ and $x_m = 0.107$, (b) subharmonic response for $\Omega = 2.102$ and $x_m = 0.113$, (c) subharmonic response for $\Omega = 1.920$ and $x_m = 0.136$, (d) subharmonic response for $\Omega = 1.514$ and $x_m = 0.218$, (e) 2T-periodic subharmonic response for $\Omega = 1.505$ and $x_m = 0.221$, and (f) chaotic attractor in the subharmonic response for $\Omega = 1.480$ and $x_m = 0.228$.

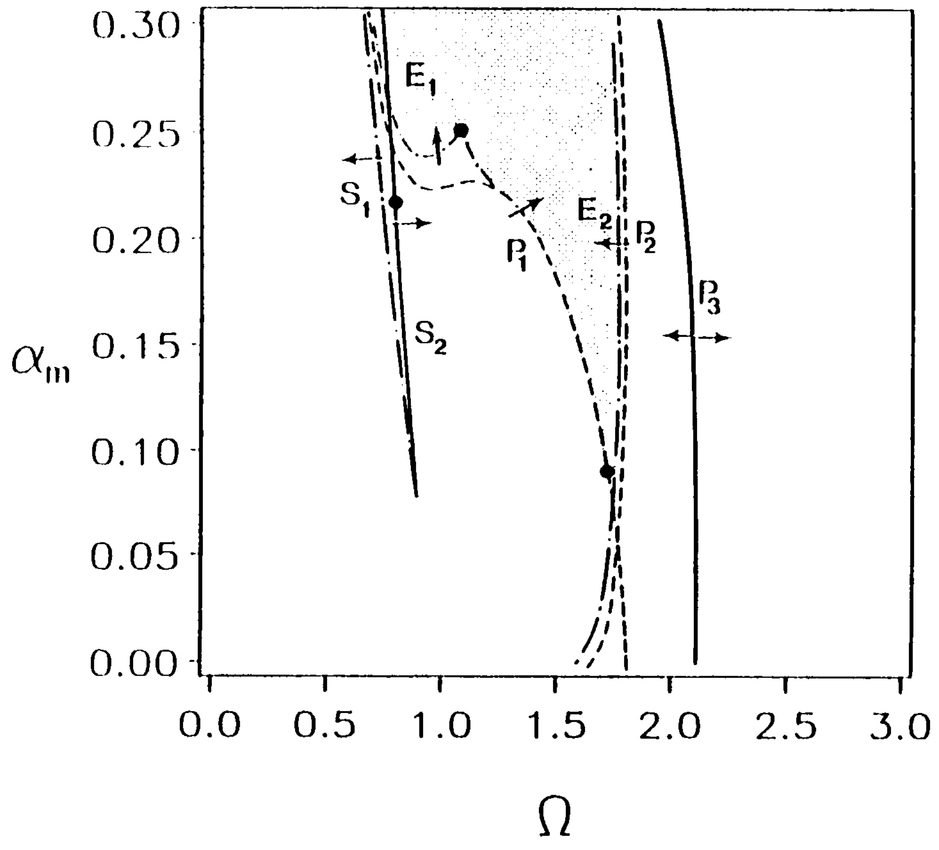

Figure 8.5. Bifurcation diagram from analog-computer simulations of (8.5) for $\gamma = 0$, $\theta_s = +6°$, $h = 0.3$

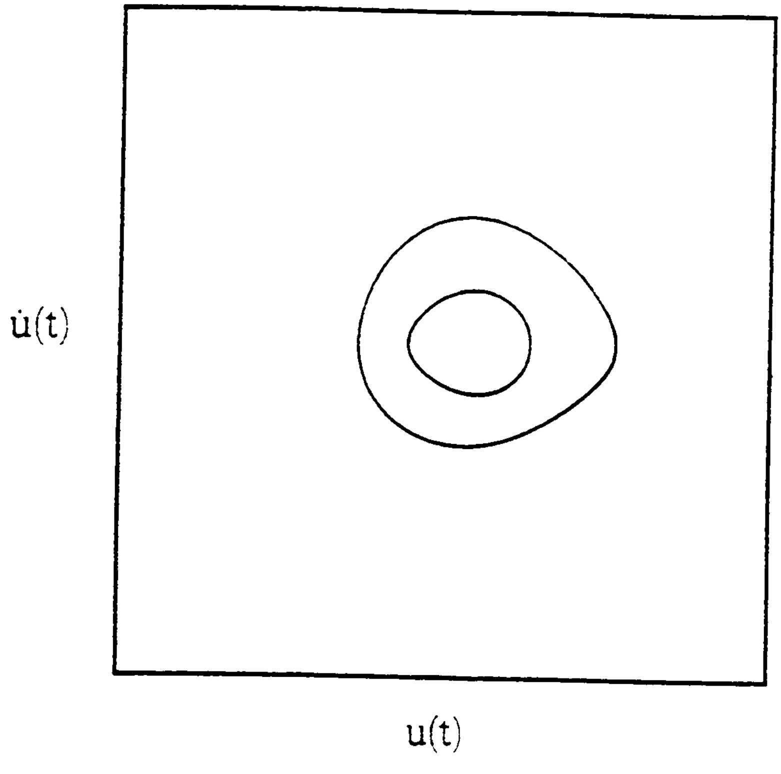

Figure 8.6. Coexisting attractors near the primary resonace for $\Omega = 0.768$ and $\alpha_m = 0.217$.

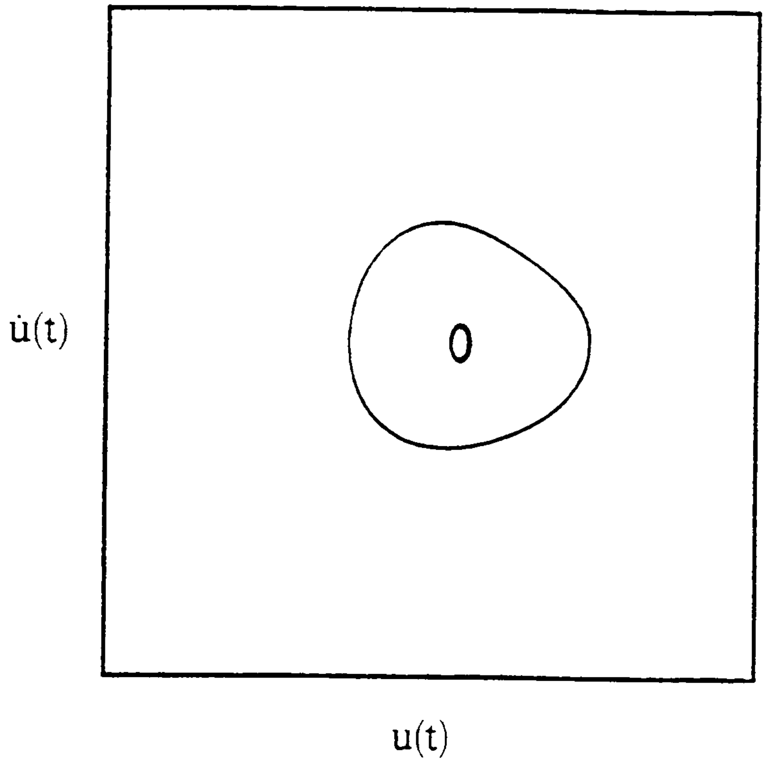

Figure 8.7. Coexisting attractors near the subharmonic resonance for $\Omega = 1.758$ and $\alpha_m = 0.046$.

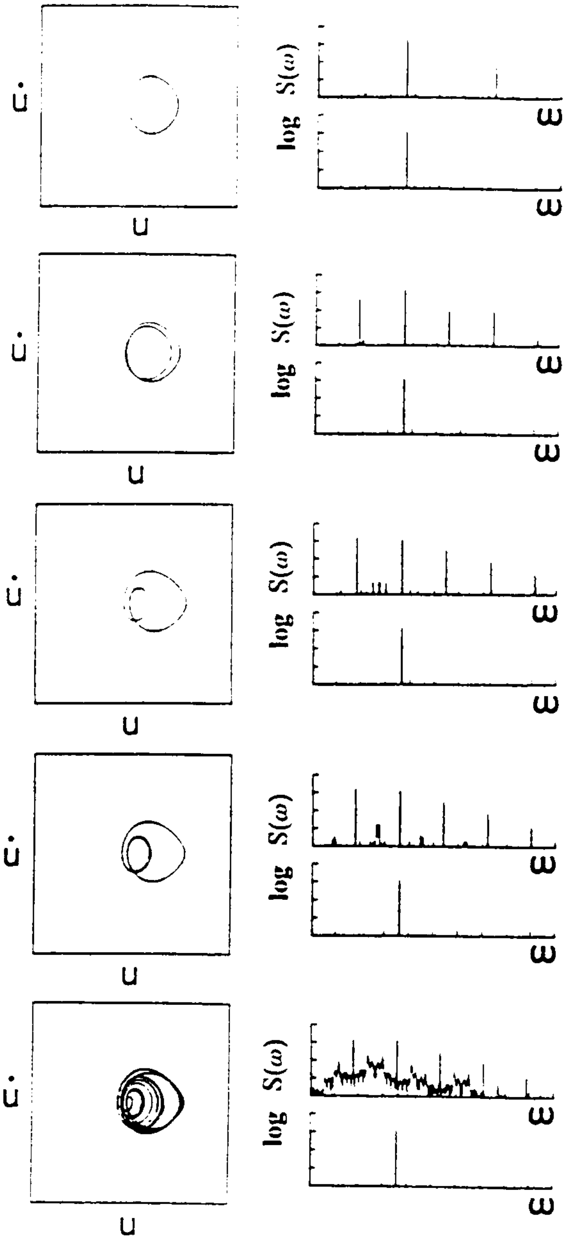

Figure 8.8. Phase portraits and power spectra of the response and the excitation near the primary resonance : (a) T-periodic response for $\Omega = 1.098$ and $x_m = 0.228$, (b) 2T-periodic response for $\Omega = 1.098$ and $x_m = 0.231$, (c) 2T-periodic response for $\Omega = 1.098$ and $x_m = 0.245$, (d) appearance of broad-band frequency content in the 2T-periodic response for $\Omega = 1.093$ and $x_m = 0.248$, and (e) chaotic attractor for $\Omega = 1.067$ and $x_m = 0.249$.

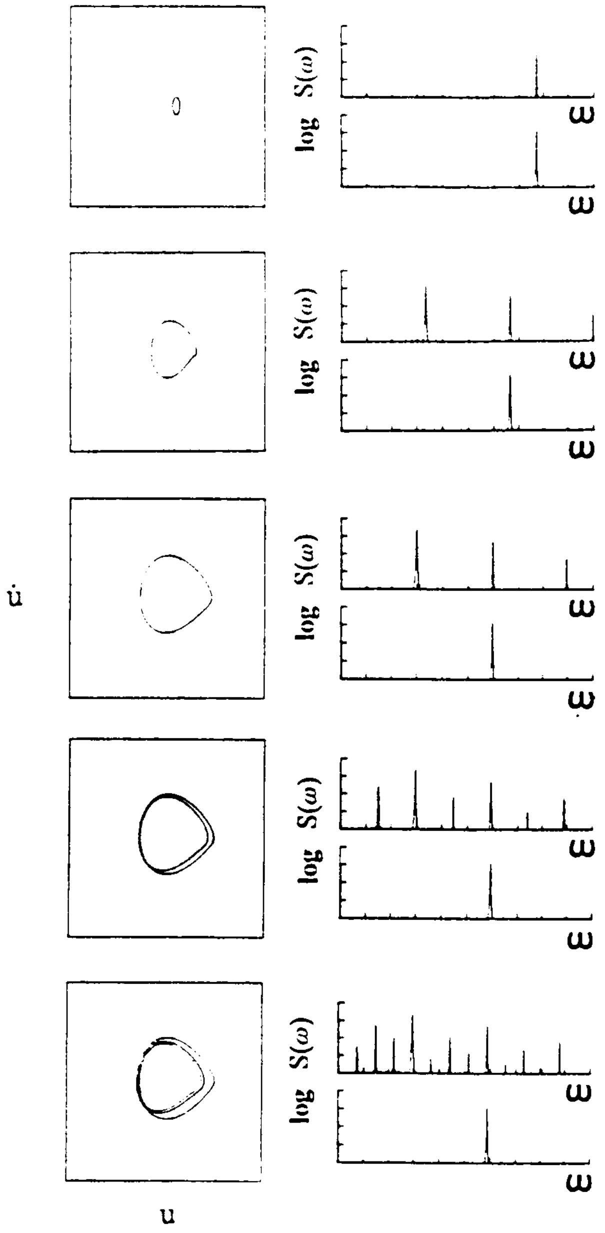

Figure 8.9. Phase portrait and power spectra of the response and the excitation near the subharmonic resonance : (a) primary response for $\Omega = 2.319$ and $\alpha_m = 0.058$, (b) subharmonic response for $\Omega = 1.997$ and $\alpha_m = 0.078$, (c) subharmonic response for $\Omega = 1.794$ and $\alpha_m = 0.097$, (d) 2T-periodic attractor of the subharmonic response for $\Omega = 1.780$ and $\alpha_m = 0.099$, (e) 4T-periodic attractor of the subharmonic response for $\Omega = 1.763$ and $\alpha_m = 0.100$.

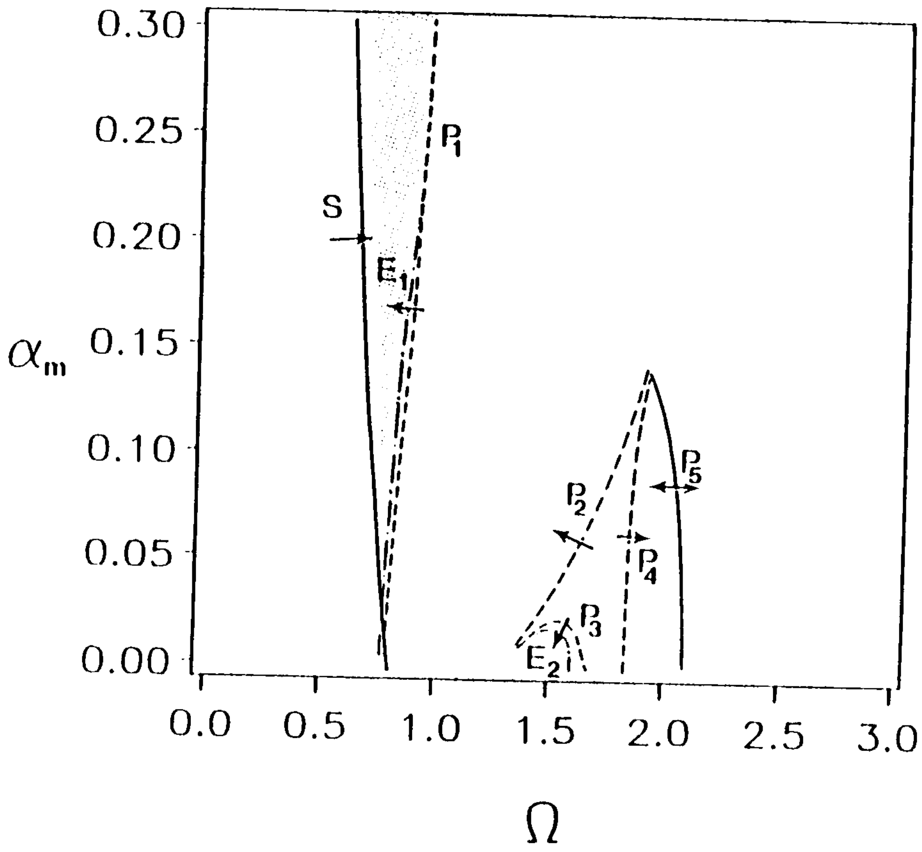

Figure 8.10. Bifurcation diagram from analog-computer simulations of (8.5) for $\gamma = 0$, $\theta_s = -6°$, $h = 0.3$

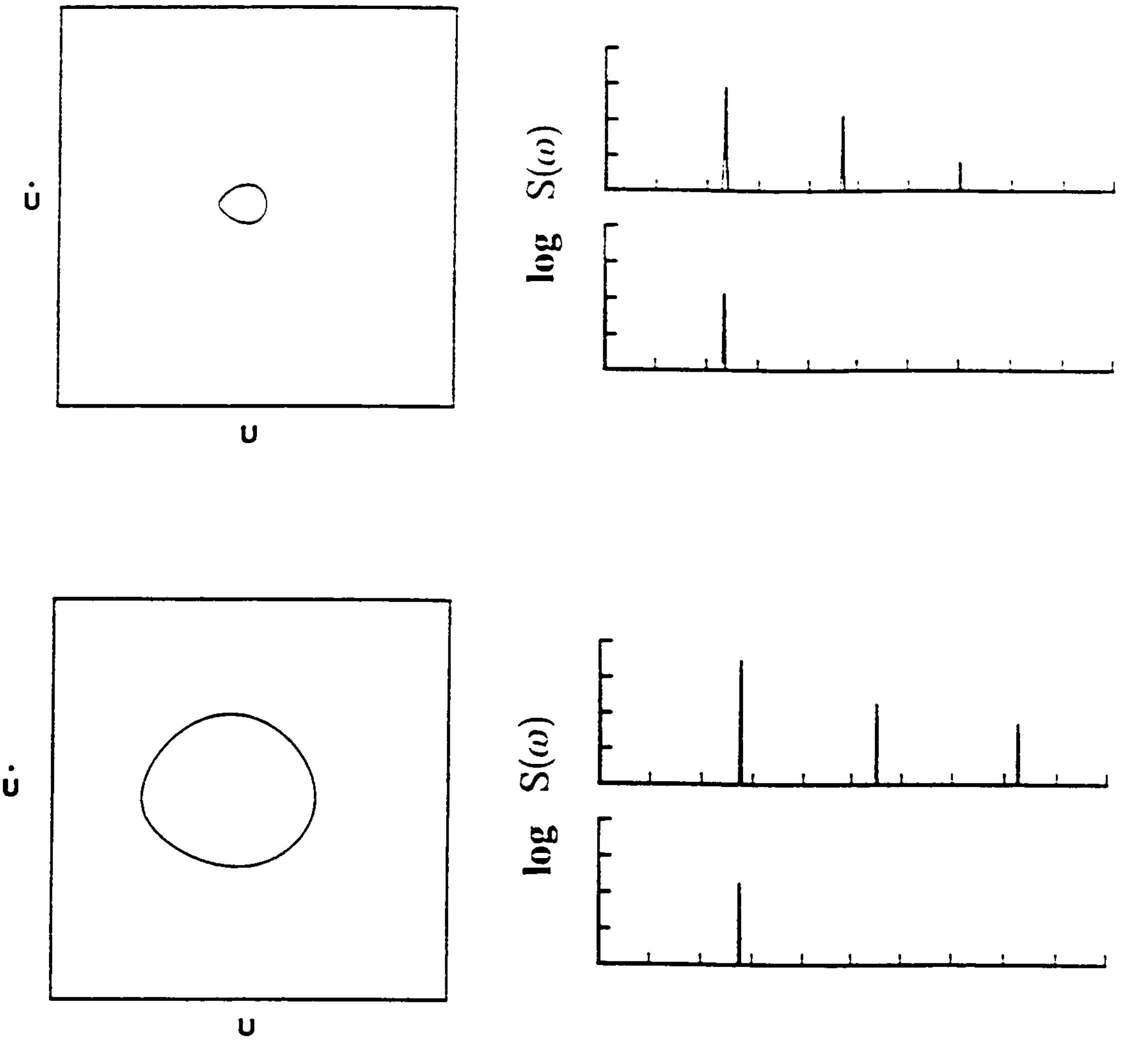

Figure 8.11. Phase portraits of the attractors near the primary resonance and the power spectra of the response and excitation : (a) $\Omega = 0.702$ and $\alpha_m = 0.063$, and (b) $\Omega = 0.827$ and $\alpha_m = 0.057$.

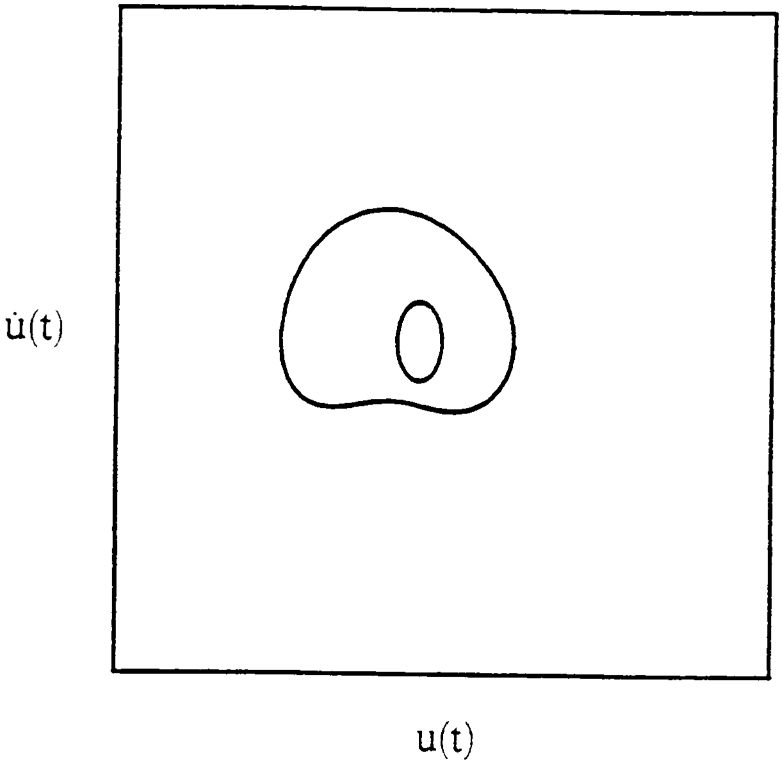

Figure 8.12. Coexisting attractors near the subharmonic resonance for $\Omega = 1.698$ and $\alpha_m = 0.061$.